LEABHARLANN CHOLÁISTE NA TRÍONÓIDE, BAILE ÁTHA CLIATH
Ollscoil Átha Cliath

TRINITY COLLEGE LIBRARY DUBLIN
The University of Dublin

Terms and Conditions of Use of Digitised Theses from Trinity College Library Dublin

Copyright statement

All material supplied by Trinity College Library is protected by copyright (under the Copyright and Related Rights Act, 2000 as amended) and other relevant Intellectual Property Rights. By accessing and using a Digitised Thesis from Trinity College Library you acknowledge that all Intellectual Property Rights in any Works supplied are the sole and exclusive property of the copyright and/or other IPR holder. Specific copyright holders may not be explicitly identified. Use of materials from other sources within a thesis should not be construed as a claim over them.

A non-exclusive, non-transferable licence is hereby granted to those using or reproducing, in whole or in part, the material for valid purposes, providing the copyright owners are acknowledged using the normal conventions. Where specific permission to use material is required, this is identified and such permission must be sought from the copyright holder or agency cited.

Liability statement

By using a Digitised Thesis, I accept that Trinity College Dublin bears no legal responsibility for the accuracy, legality or comprehensiveness of materials contained within the thesis, and that Trinity College Dublin accepts no liability for indirect, consequential, or incidental, damages or losses arising from use of the thesis for whatever reason. Information located in a thesis may be subject to specific use constraints, details of which may not be explicitly described. It is the responsibility of potential and actual users to be aware of such constraints and to abide by them. By making use of material from a digitised thesis, you accept these copyright and disclaimer provisions. Where it is brought to the attention of Trinity College Library that there may be a breach of copyright or other restraint, it is the policy to withdraw or take down access to a thesis while the issue is being resolved.

Access Agreement

By using a Digitised Thesis from Trinity College Library you are bound by the following Terms & Conditions. Please read them carefully.

I have read and I understand the following statement: All material supplied via a Digitised Thesis from Trinity College Library is protected by copyright and other intellectual property rights, and duplication or sale of all or part of any of a thesis is not permitted, except that material may be duplicated by you for your research use or for educational purposes in electronic or print form providing the copyright owners are acknowledged using the normal conventions. You must obtain permission for any other use. Electronic or print copies may not be offered, whether for sale or otherwise to anyone. This copy has been supplied on the understanding that it is copyright material and that no quotation from the thesis may be published without proper acknowledgement.

FINITE ELEMENT ANALYSIS & DIE PROFILE OPTIMISATION FOR A COLD FORGING PROCESS

Conor MacCormack

Submitted in fulfilment of the requirements for the award of the degree of Doctor of Philosophy to the University of Dublin, Trinity College, 6th October 2000.

Supervisor: **Professor John Monaghan**

The work presented in this thesis was conducted at the Department of Mechanical and Manufacturing Engineering, University of Dublin, Trinity College, Ireland.

Declaration

I declare that the present work has not been submitted as an exercise for a degree at any other University. This thesis consists entirely of my own work except where references indicate otherwise.

I agree that the library of the University of Dublin, Trinity College, Dublin, may lend or copy this thesis upon request.

Conor Mac Cormack

Conor MacCormack

Acknowledgements

There are a lot of people who helped in some shape or form in the completion of this thesis. Firstly I'd like to thank my supervisor Professor John Monaghan for his guidance, and help and all the 6:00am morning drives to Hi-Life Tools.

Special thanks to Mr Jim Ryall from Hi-Life Tools who offered much of his time to answer all my "one last question" e-mails. I am also very grateful to all the technical staff at T.C.D., Frank, Tom, Sean, Gerry, Gabriel, and Peter and last but not least Danny for all their help over the years.

The financial and technical support provided by Materials Ireland is gratefully acknowledged.

I am also grateful to all the postgraduates and staff at Trinity College for all the good times we've had over the years. In particular I would like to thank present MI staff: Toman, Michael, and Ray for all the good times, breaking machines and cups of coffee and past MI members Liam and Gavin I wish the greatest things for both of your careers. I'd like to wish the best of luck to Gabriel in his last year and for all the squash and tennis lessons, and to Karl who is finishing up also.

I'd like to thank my parents Dominic and Annie for all the help and guidance over the years, my mother for all the 'laps' and to my father for introducing me to the world of engineering; I can never thank you enough. I'd also like to express my thanks to Annette and Patsy who have treated me like one of their own. To my brothers Fintan and Dermot in America, thanks for all the advice and encouragement over the years, and to my sister Emer, best of luck to you in your last year at college (until the postgraduate studies!).

Finally, to my wife Deirdre, without you this thesis would not have been possible, thanks Dee, I dedicate this to you.

Abstract

Throughout the world, almost every machine that moves requires the use of bolts in one form or another. Bolts, or *Fasteners,* are made in bolt making machines by a process of cold forming. At a particular stage in the bolt making process a Trim Die is used to form the familiar hexagonal head on the bolt.

Hi-Life Tools based in Shannon together with the parent company SPS Technologies in the USA are the largest supplier of Trim Dies in the Western World. Customers of Hi-Life Tools reported erratic tool life compared to that achieved using competitors Trim Dies.

The objective of this study was to reduce the likelihood of Trim Die failure by establishing an ‘Optimum’ Trim Die profile. To that end the investigations performed in this project had to provide a better understanding of the trimming process than was currently available. A combination of finite element techniques, experimental testing and evaluation was undertaken to assist the design process in achieving the ‘optimum’ Trim Die profile. An analysis of failed Trim Dies enabled the prediction of the most likely failure mechanism. The Trim Die fracture was induced by fatigue, which originated at surface defects on the coating, and assisted by hard carbide particle segregation inherent within the trim die material.

The Trim Die failure investigation, coupled with the theoretical finite element analysis established the ‘Optimum’ Trim Die profile and a new and previously unconsidered profile developed by the author, which both significantly reduced the ‘critical’ stress component thought to promote Trim Die failure.

Table of Contents

Nomenclature

SYMBOL	UNIT	DEFINITION
E	MPa	Young's Modulus
f	----	A yield function
$\overline{F}_i$	N	Surface traction applied to surface S_F
{F}	N	Nodal force vector
G_{12}	MPa	Shear Modulus in the principal directions
$g(\sigma_{ij})$	----	Plastic Potential
J2	MPa	Von Mises criteria for yielding
K	N/mm	Stiffness Matrix
k	MPa	Yield stress in shear
Q	----	Large positive constant to penalise volume change
S_F	mm^2	Surface of deformation
{u}	M/sec	Vector representing the elemental velocity
V_i	M/sec	Velocity component on surface S_F
α	Degrees	Angle of Fractured surface
$\Delta\varepsilon$	----	Elastic strain tensor
Δt	sec	Change in time
δ_{ij}	----	Kronecker Delta
δV	mm^3	Small portion of the volume V
$\delta\Phi[u_{i0}]$	----	Rayleigh-Ritz formula
ε_t	----	Strain at time t
$\varepsilon_{t+\Delta t}$	----	Strain at time $t+\Delta t$
$\dot{\varepsilon}_t$	1/sec	Stain rate at time t
$\overline{\varepsilon}$	----	Effective strain
$\dot{\overline{\varepsilon}}$	1/sec	Effective stain rate

$\dot{\varepsilon}_{ij}$	1/sec	Strain rate deformation
$\dot{\varepsilon}_{ij}^{E}$	1/sec	Elastic strain rate
$\dot{\varepsilon}_{ij}^{P}$	1/sec	Plastic strain rate
μ	----	General coefficient of friction
m	----	Friction Factor
f_S	MPa	Frictional Shear Stress
p	Mpa	Compressive Normal Stress
$\dot{\lambda}$	----	Positive proportional constant
ν	-----	Poisson's ratio
$\dot{v}_{xy}^{P}$	1/sec	Plastic strain rate component on the xy plane
σ	MPa	Stress tensor
σ_m	MPa	Mean or hydrostatic stress
σ_X	MPa	Pure stress in the X direction
σ_Y	MPa	Pure stress in the Y direction
σ_Z	MPa	Pure stress in the Z direction
σ_1	MPa	1st principal direction
σ_2	MPa	2nd principal direction
σ_3	MPa	3rd principal direction
$\overline{\sigma}$	MPa	Flow Stress
σ^{1}_{ij}	MPa	Deviatoric Stress Component
$\frac{\delta\sigma_{ij}}{\delta x_j}$	----	Equilibrium condition
τ_{xy}	MPa	Shear stress on the Y plane in the X direction
τ_{yz}	MPa	Shear stress on the Z plane in the Y direction
τ_{xz}	MPa	Shear stress on the Z plane in the X direction

Part I

1 Introduction

Throughout the world, almost every machine that moves from aircraft, trains to automobiles requires the use of bolts in one form or another. Bolts, or *Fasteners*, are made in bolt making machines by a process of cold forging. Bolt making machines are fed coiled bar stock at one end and produce threaded bolts at the other. At a particular stage in the bolt making process a Trim Die is used to form the hexagonal head on the bolt. Figure 1-1 below illustrates a standard trim die showing the internal hexagonal hole.

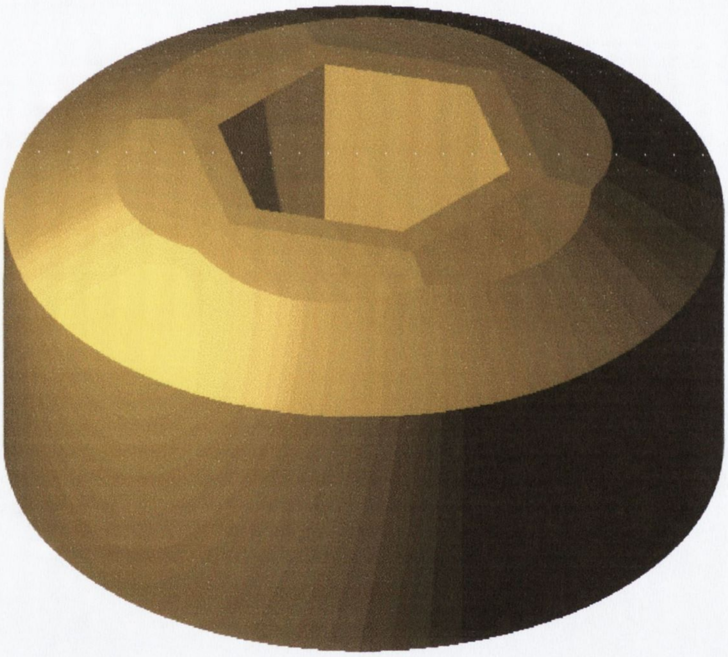

Figure 1-1: Standard Trim Die Showing Hexagonal Internal Hole

In the last few decades, the mass production of components by cold forging has increased dramatically. Cold forging has various advantages including little loss of material, improved strength, geometrically precise components and high production rates. A standard boltmaking machine can produce up to 5,500 bolts per hour. However considerable difficulties can be encountered due to the high stresses induced within the tooling because of the very large forming loads [1]. Reducing the stress level in cold forging tooling by modifications in the design has he greatest influence on tool life [1, 2].

Hi Life Tools based in Shannon, which is a division of the parent company SPS Technologies, located in Philadelphia, USA, is the largest supplier of Trim Dies in the Western World. Customers of Hi-Life Tools reported erratic tool life compared to that achieved using competitors Trim Dies. Life times ranging from 40,000 to 180,000 trimmed bolts has been reported. Figure 1-2 below shows a Scanning Electron Microscope (SEM) image of a failed trim die showing characteristic corner chipping.

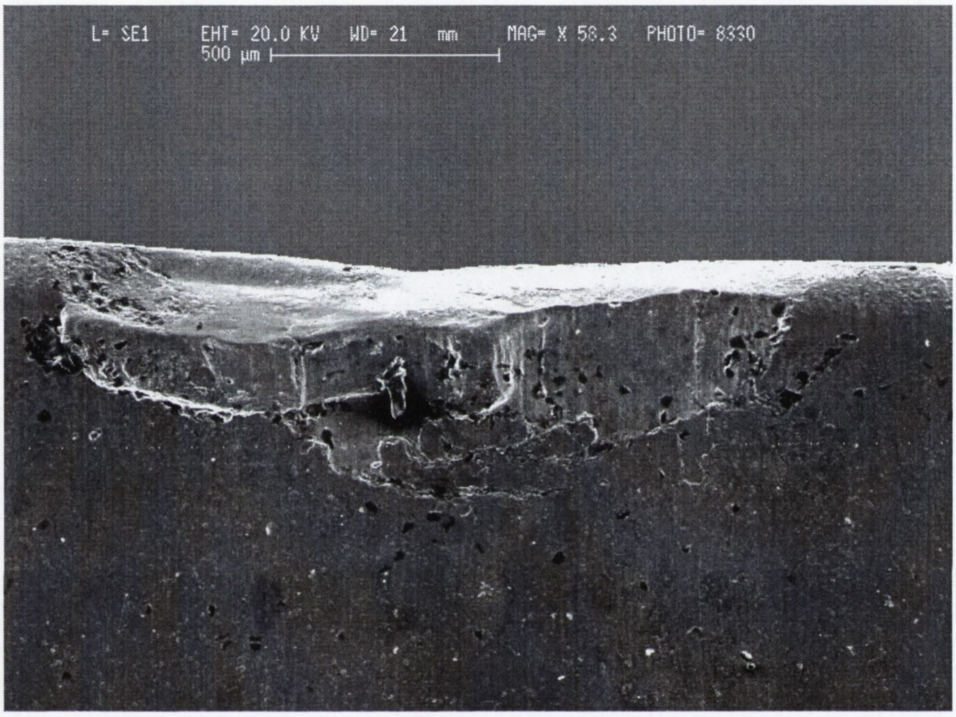

Figure 1-2: Corner Chipping on Trim Die

Because of this, in 1994 Hi-Life Tools in conjunction with Materials Ireland, T.C.D. initiated a project to examine the influence of corner geometry on the stresses within a cold forging trim die. The initial work carried out in 1994 produced good results [3], but at that time the Finite Element Analysis (FEA) packages were insufficiently developed and could not therefore provide a complete analysis. It is from this point that the research work for this project commenced. The work conducted in 1994 was used as a foundation to expand upon and obtain a complete understanding of the trimming process. With the recent advances in software development and more powerful computers, the FEA package DEFORM can now model the entire deformation of the trimming process while simultaneously predicting all the necessary stress components in both the trim die and workpiece.

The objectives for the work undertaken for this project are given in Section 2.6 on page 50.

Part II

2 Literature Review and Introduction to Trimming

2.1 Introduction To Trimming

This Section introduces the manufacturing process known as Trimming. The fundamentals of Trimming along with a description of the process required to manufacture the Trim Die will be explained. Finally the die coating process and heat treatment cycle will be discussed. Unfortunately there is very little literature available related to the trimming process, which makes this project somewhat unique. The trimming process is similar to the Broaching process, whereby a hexagonal shaped hole is formed within the head of the bolt to receive a hex key, however literature in the area of Broaching is also very scarce. Extensive research has been conducted in the area of Extrusion, combining finite element techniques and failure analysis to obtain a greater understanding of the process, which enables the design of an improved die profile. Section 2.5.9 on page 47 lists the research conducted in this area and also highlights why their method of approach could not be used in this body of work. To the author's knowledge, no other research has combined elastoplastic finite element analysis and experimental testing to determine the most likely mechanisms leading to failure and to derive an optimised die profile for this particular cold forging process. The following section provides a description of a trimming process and the trim die manufacture.

2.1.1 Fundamentals Of Trimming

Figure 2-1 on the following page shows a schematic representation of a four-station bolt-making machine. Most cold-bolt making machines used in production are fed with coiled wire stock. The bolt material analysed in this project was a medium carbon, low alloy steel having the designation SPS 0.9 and a yield stress of 680MPa. With reference to figure 2-1, the stock is fed into the machine by feed rolls to the cut-off station. The end of the wire stock butts against a wire stop or stock gage (not shown), which determines the length of the blank. The cut-off station essentially acts as a guillotine to shear off a predetermined blank length. A transfer mechanism, having 'fingers' in front of each die, enables the blank to be transferred from one station to the next. The transfer mechanism has been removed from the drawing for clarity.

Once the blank has been cut to the correct length, the transfer mechanism brings the blank to the Coining Station. The coining punch has been sectioned to show the profile inside the die. Coining (or Bulbing) punches are used before the Heading Station because they enable heading of a length of wire of up to six times the diameter of the blank material in only two strokes. The transfer mechanism 'picks up' the workpiece material and places it at the penultimate Heading Station. At the Heading station the die produces a preform known in the industry as the 'cheesehead'.

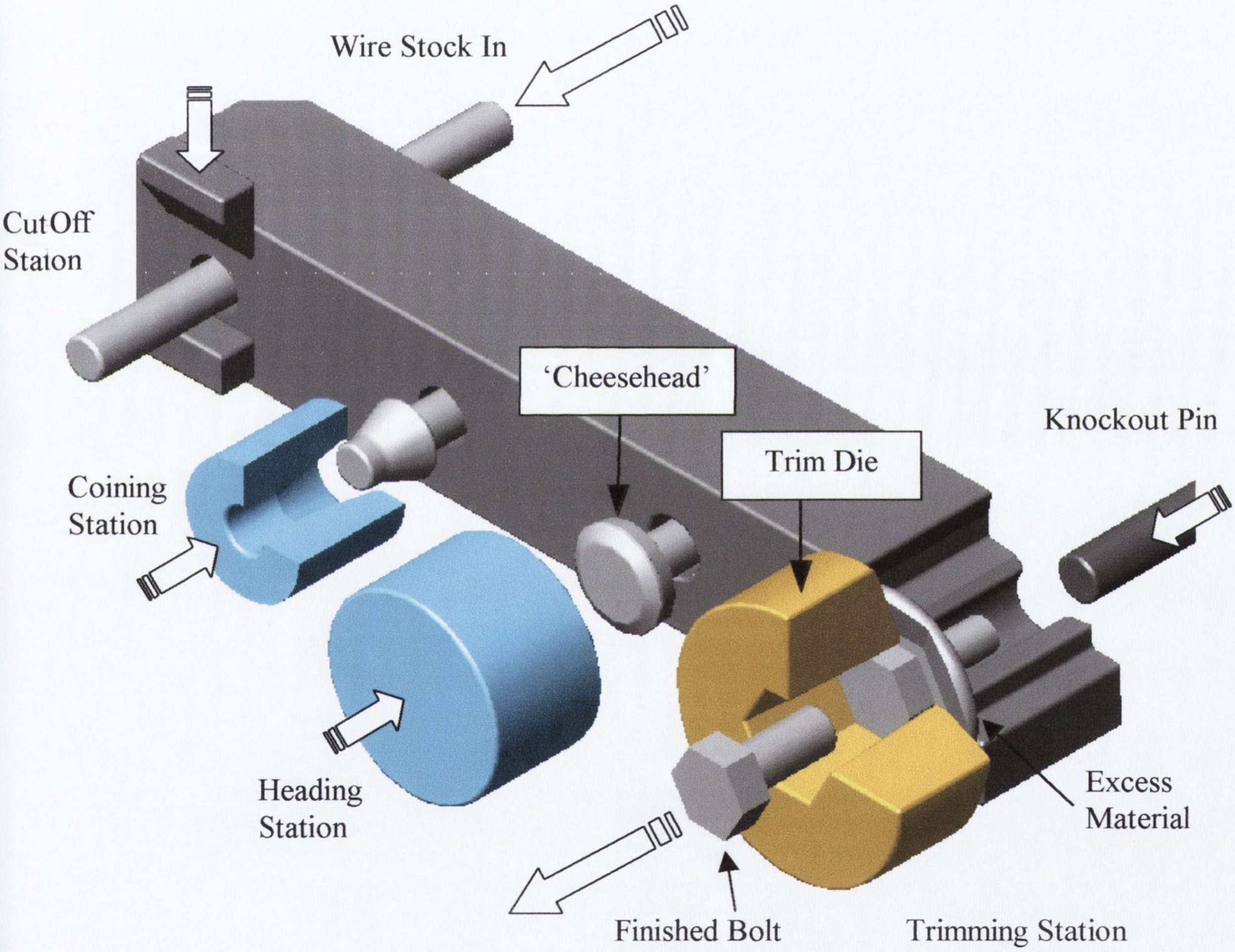

Figure 2-1: Schematic Of A Four-Station Bolt Making Machine

Finally the cheesehead preform is transferred to the trimming station. The trim die, illustrated by the golden colour to represent the titanium carbide outer coating, is forced onto the workpiece preform. Due to the hexagonal internal hole within the trim die, the standard hexagonal head is formed.

The excess material is still connected to the base of the bolt head. The trim die remains in this position, which allows a Knockout Pin to drive the bolt through the centre of the die thereby shearing of the excess material in the process. The finished bolt passes through the trim die where it is collected and orientated for the application of threads using a thread rolling process.

As mentioned in the introduction, the bolt making operation is a cold forming process, which induces high stresses within the tooling. In Section 4.5.4 on page 190, a failure analysis of the trim die is presented. Results from this analysis highlighted that the manufacturing process used to produce trim dies was responsible for some undesirable flaws. Therefore the following section will detail how the trim die is manufactured from the initial billet to the finished coated and heat treated component.

2.2 Trim Die Manufacture

2.2.1 Rotary Swaging

Rotary swaging is a process for reducing the cross-sectional area or changing the shape of bars, tubes or wires by repeated radial blows with two or more dies [2]. Swaging can produce straight and compound tapers, contours on the inside diameter of tubing and change round bars to square or other shapes.

The trim die is made from the high-speed steel AISI M2, the material characteristics of which are outlined in Appendix A on page 230. The M2 material is supplied to the factory floor in tubular form, with the internal hole being circular. As mentioned in the previous section, the trim die requires a hexagonal internal hole, to form the head on the bolt, see figure 2-1 on the previous page. Rotary Swaging is used to change the initial circular hole into a tapered hexagonal shape. The taper on the internal hexagonal hole is known as the 'Rake Angle', and its effects on the stress distribution within the trim die are discussed later in Section 4.1.5 on page 136. To form an internal shape in Rotary Swaging a mandrel is used. Swaging over a mandrel can produce a wide variety of internal shapes from ovals to the spirals used in gun barrels. Before the tubular M2 stock is swaged, it is induction heated to below 700°c, in order to reduce its yield stress and therefore the necessary swaging loads. Figure 2-2 shows the induction heating process applied to the M2 tubular stock.

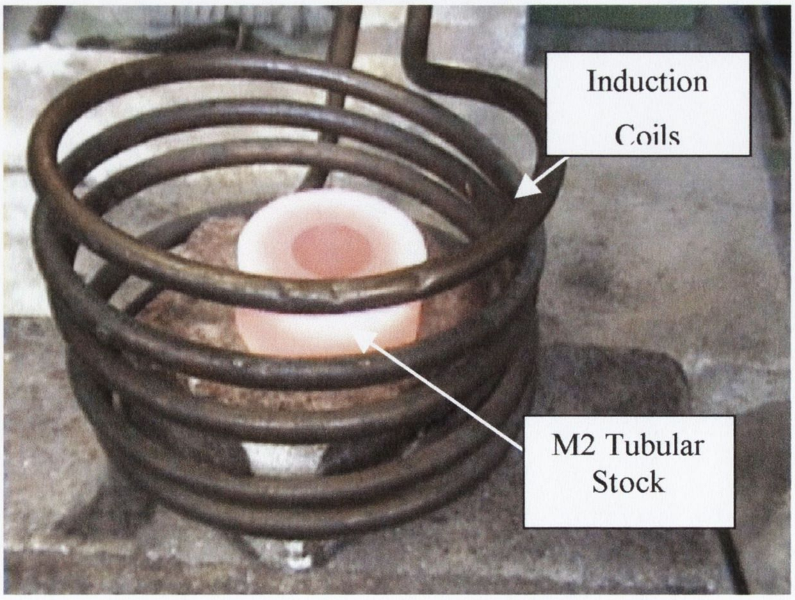

Figure 2-2: Induction Heating Of Tubular M2 Stock

Once the material has been raised to its swaging temperature, the tubular stock is placed onto the tapered hexagonal mandrel and both the M2 workpiece and the mandrel are placed into the four-jaw Rotary Swaging machine shown in figure 2-3 below.

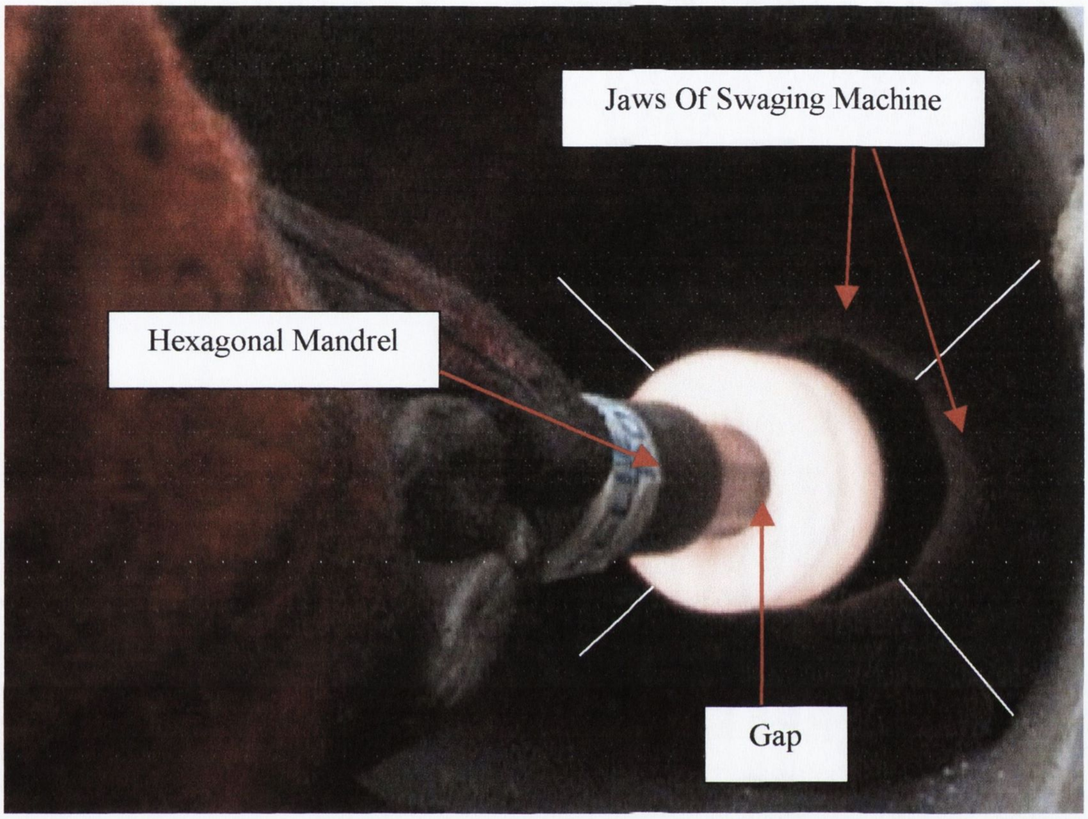

Figure 2-3: Heated Tubular M2 Stock on Tapered Hexagonal Mandrel

With respect to figure 2-3 above, the gap between the circular internal hole in the stock material and the hexagonal mandrel is clearly visible. The four jaws of the Rotary Swaging machine have been highlighted with the use of white lines.

Figure 2-4 on the following page shows the Tubular M2 stock swaged onto the hexagonal mandrel. Notice that the gap highlighted in figure 2-3 above has been removed due to the swaging action.

Although the swaging operation forms the internal hexagonal hole, the outside profile may not be perfectly circular. Therefore the mandrel and M2 material are then transferred to a CNC Lathe, for a machining operation, which produces the near finished trim, die geometry shown in figure 2-5.

In figure 2-5, the geometry of the die before and after the CNC lathe operation is illustrated.

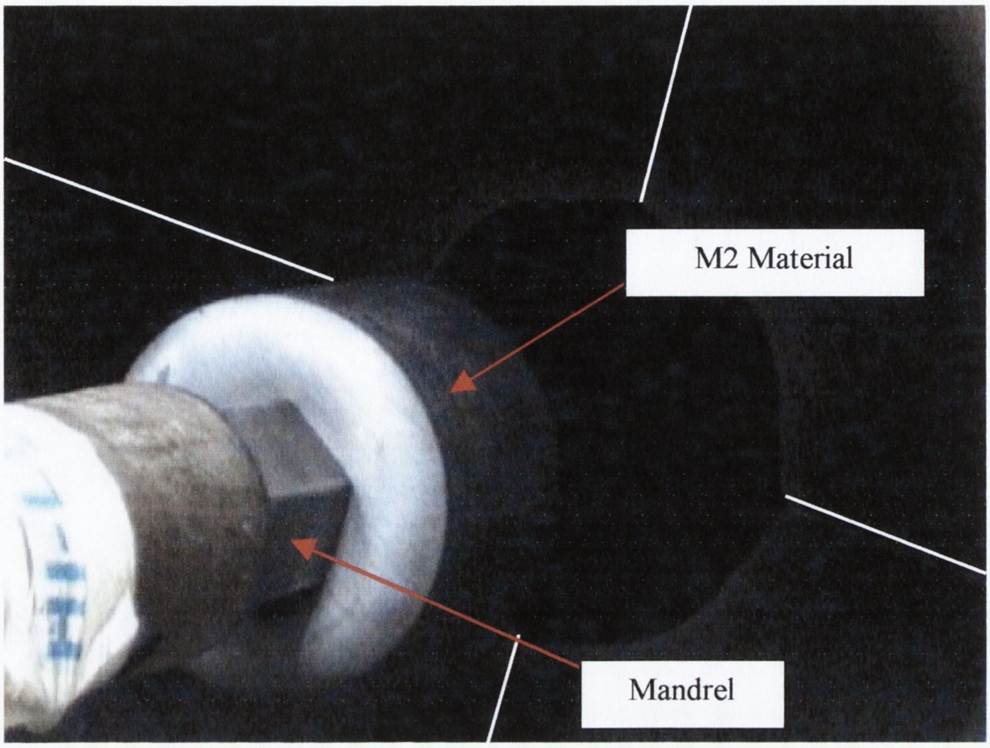

Figure 2-4: Tubular Stock Swaged Onto Hexagonal Stock

Figure 2-5: Trim Die Geometry Pre and Post CNC Lathe Operation.

The final machining operation is to grind the 'Petals' and corner radius onto the trim die.

2.2.2 Grinding

Figure 2-6 below shows the petals being ground onto the trim die. The grinding process produces a rough surface finish on the petals and the land surface. This rough finish is shown in figure 2-7.

Figure 2-6: Grinding of the Petal Angles onto the Trim Die

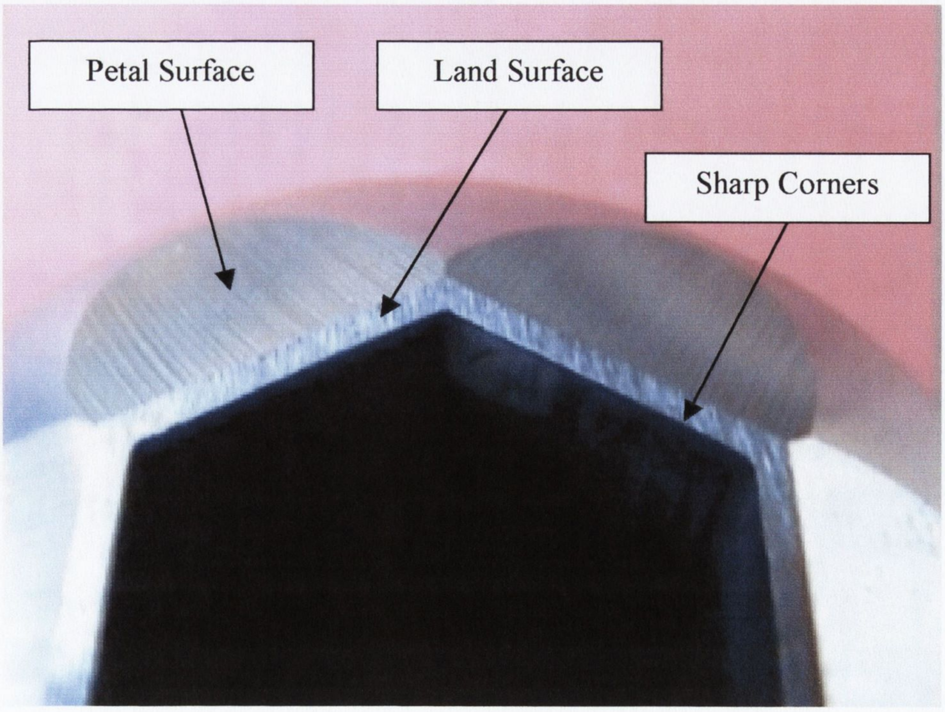

Figure 2-7: Rough Surface Finish after Grinding on the Petal and Land Surfaces

Figure 2-7 also highlighted that after the grinding process, the corners of the internal hexagonal hole have a sharp edge. To improve the rough surface finish on the land surface and petal angles, and to generate the required corner radius, an abrasive wheel is used. This process is known on the factory floor as 'edge preparation'. The wheel has abrasive strands, which make contact with the surface of the trim die. The trim die is rotated about its own centre causing the corner profile to be formed. Figure 2-8 below shows the abrasive wheel and the direction of rotation of the trim die.

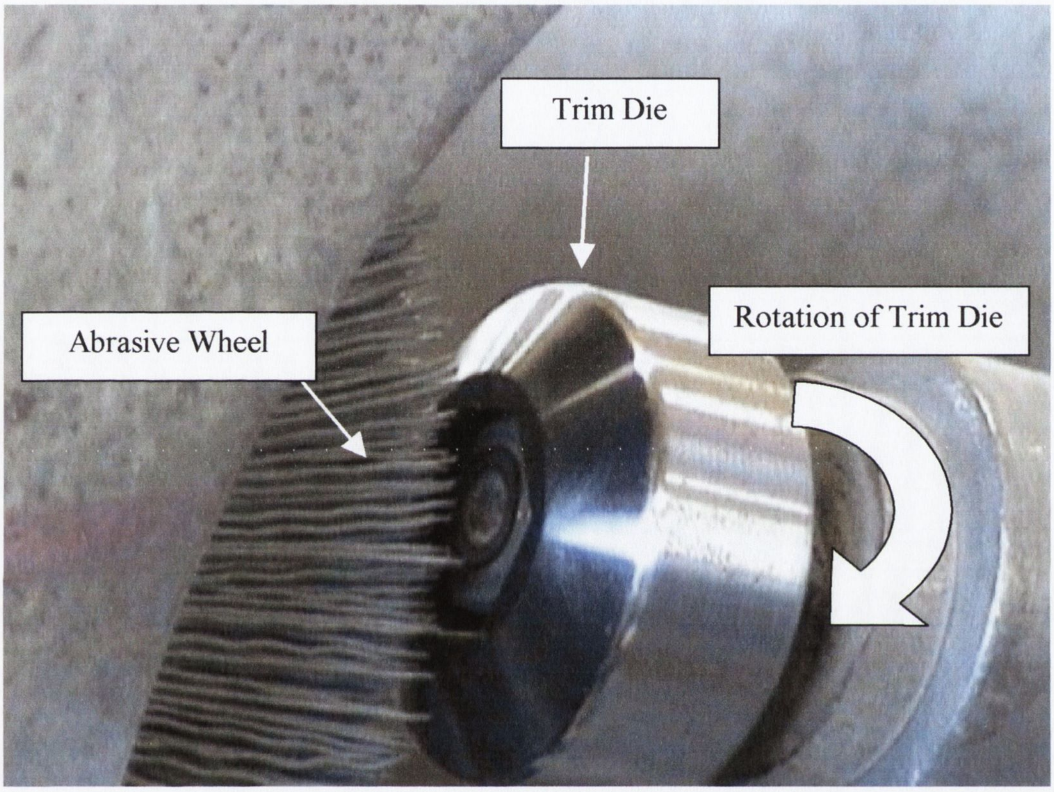

Figure 2-8: Edge Preparation of the Trim Die using an Abrasive Wheel

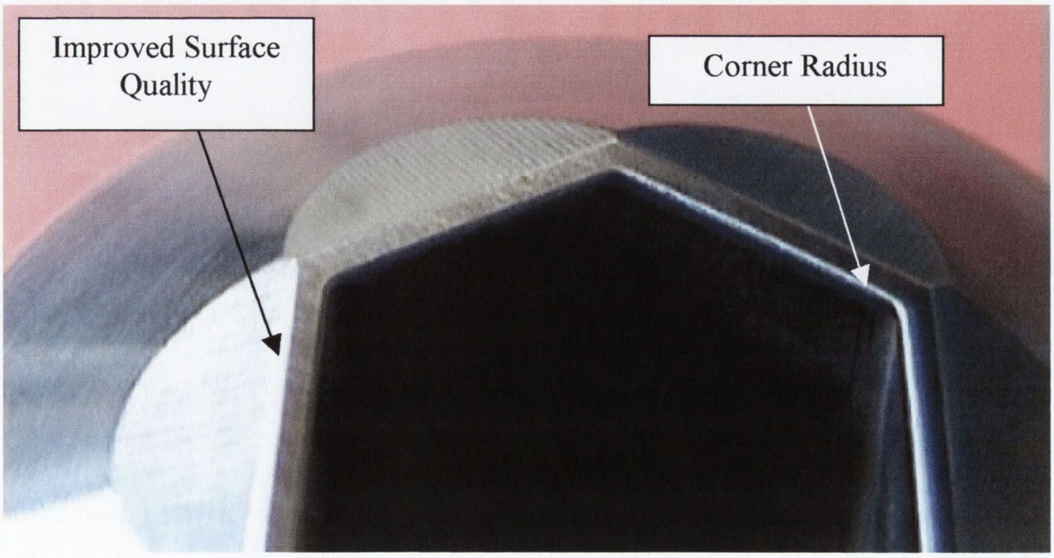

Figure 2-9: Improved Surface Finish and Formation of Corner Geometry

Figure 2-9 on the previous page shows the trim die surface after the ‘edge preparation’. The corner profile generated by the abrasive wheel is also visible.

Figure 2-10 below shows the trim die geometry before and after the grinding of the petals and the ‘edge preparation’.

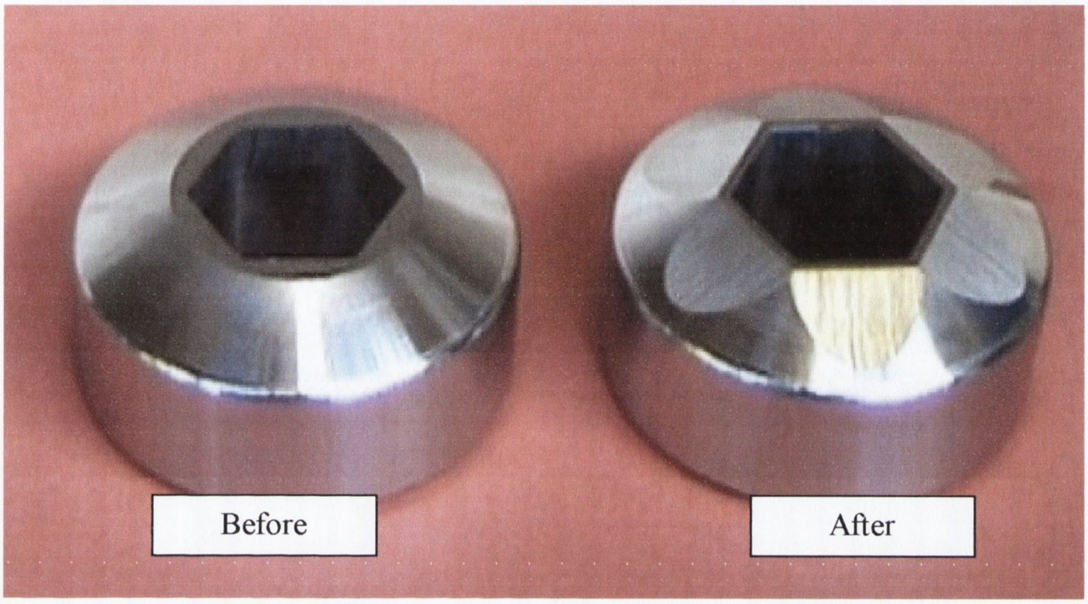

Figure 2-10: Trim Die Geometry Pre and Post Edge Preparation

The trim die profile shown above on the right now requires a hard surface coating.

2.2.3 Coating Application

Once the machining of the trim die shape is complete, a coating is applied to the surface using a process known as Chemical Vapour Deposition (CVD). An outline of the CVD coating process is given in Appendix B on page 231 and will not be detailed here.

2.2.4 Heat Treatment Cycle

Once the trim die has been coated it requires a Heat Treatment cycle. The heat treatment of tool steels is as important as the selection of the grade itself [4, 5]. Heat treatment can be applied to steel not only to harden it but also to improve its strength, toughness or ductility [6].

As mentioned in Section 2.2.1, and outlined in Appendix A, the trim die investigated in the project was made from AISI M2, High Speed Steel (HSS). The heat treatment cycle applied to the trim die consists of three main processes:

1) Austenitizing
2) Quenching
3) Tempering

2.2.4.1 Austenitizing

When a piece of steel, containing sufficient carbon, is cooled rapidly from above its upper critical temperature it becomes considerably harder than if it were allowed to cool slowly. In soft annealed tool steel, most of the alloying elements are bound up with carbon as carbides. When a steel is heated for hardening, the basic idea is to dissolve the carbides to such a degree that the matrix acquires an alloying content that gives the hardening effect, but without becoming coarse grained and brittle. Note that the carbides are partially dissolved. This means that the matrix becomes alloyed with carbon and carbide-forming elements. When the HSS is heated to the austenitizing temperature, the carbides are partially dissolved, and the matrix is changed from ferrite to austenite. This change of the matrix material from ferrite to austenite changes the atomic lattice from a Body-Centred Cubic (BCC) to a Face-Centred Cubic (FCC) structure. This change in the lattice 'makes room' for atoms of carbon and alloying elements. The carbon and alloying elements from the carbides are dissolved in the matrix.

At Hi-Life Tools, the application of the austenitizing temperature used is divided into two stages. The first in known as 'Preheat', where the trim die is elevated to 870°c and held there for 60 minutes (soak time). At this Preheat temperature, austenite begins to form. The second stage 'High-heat' increases this temperature to 1120°c for a soak time of 75 minutes. The Preheat stage is used to minimise thermal shock on the die [4, 5]. A vacuum furnace is used to prevent oxidisation of the coated trim die surface.

2.2.4.2 Quenching

Once the trim dies have reached the austenitizing temperature for the predetermined 'soak' time, the final quenching part of the hardening process is started.

If steel is quenched sufficiently fast, the carbon atoms do not have time to reposition themselves to allow the reformation of ferrite from austenite. Instead they are held in positions where there is insufficient space and as a result high microstresses are caused within the structure of the steel, which causes increased hardness. The hard material structure produced by quenching is known as Martensite. Thus, martensite can be viewed as a forced solution of carbon in ferrite. This 'forcing' of the carbon atoms into the ferrite BCC lattice causes distortion [7]. It has been stated that the presence of any carbon in excess of 0.02% will frustrate the formation of a simple BCC structure when steel is quenched from the austenite phase [6]. The degree of distortion is proportional to the overall carbon content. Consequently as carbon content increases so does hardness. The quenching medium used at Hi-Life Tools is Nitrogen pressurised between 3.5 to 6 bar. The combination of the Austenitizing and Quenching processes is commonly known as Hardening.

2.2.4.3 Tempering

When a steel is hardened, the matrix is not completely converted into martensite. Some austenite is always left and is called "Retained Austenite". Therefore after quenching, the steel has a microstructure consisting of martensite, retained austenite and carbides.

After quenching, HSS usually possess high residual stresses [4] that can easily cause distortion and cracking. Reheating the steel can prevent cracking, and it is good practice to commence this reheating before the steel cools to 65°c.

This reheating after hardening is called Tempering. Tool steels should always be double tempered because the first tempering process causes much of the retained austenite to transform to hard martensite and this may lead to the introduction of internal micro-stresses. This effect is typical in HSS and is known as 'secondary hardening'. It is for this reason that three tempers are advised for HSS components [7]. In Hi-life Tools, the temperature used for each of the three tempers is 560°c with a soak time of 150 minutes each.

Figure 2-11 below schematically representation of the trim die manufacturing process and the subsequent process temperatures.

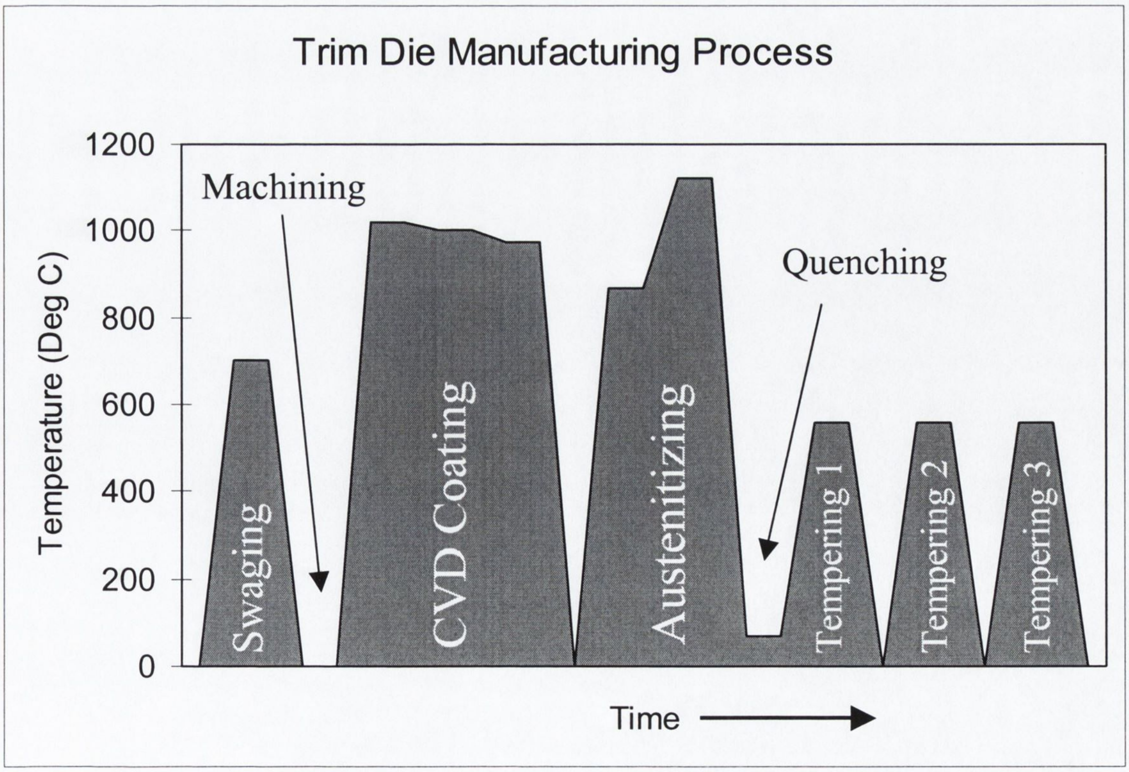

Figure 2-11: Temperatures Induced During The Trim Die Manufacturing Process

2.3 Coating Technology

2.3.1 Introduction

Generally, coating technology can be divided into the three following categories:

1) Hard Facing Coating Technologies
2) Liquid Phase Coating Technologies
3) Coating Deposition From The Vapour Phase

Hard facing coating technologies can be divided into three types namely, thermal spraying, welding and cladding. The important point to note about hard facing coating technologies is that they deposit relatively thick layers of material of the order of 0.1 to 5mm. Spray coatings can be used on precision components to build up worn parts, and this requires subsequent machining to obtain finished dimensions.

Electroplating and anodising are the best known examples of liquid phase coating technologies. Anodising is mainly used for corrosion resistance and aesthetic appearance. It has been stated that the electroplating industry in America is worth several billion dollars [8].

Vapour deposition processes can be divided into two principal types [9]:

- Chemical Vapour Deposition (CVD)
- Physical Vapour Deposition (PVD)

A detailed description of the CVD and PVD coating techniques is discussed in Appendix B on page 231, however the main advantages and disadvantages between the two processes will now be presented.

2.3.2 Advantages and Disadvantages of CVD and PVD

Chemical Vapour Deposition (CVD):

Advantages:

- Complex geometries such as tubes and blind holes can be coated
- Better adhesion between the coating and substrate than PVD
- PVD coatings are limited in thickness due to the high compressive stresses inherent in the coating process. Typical coating layers in PVD approximately 3μm, whereas CVD can deposit coatings up to 10μm.

Disadvantages:

- Due to the high temperatures required to apply the coating, approximately 1000°c, the substrate material has been changed and requires subsequent heat treatment. As will be shown in Section 4.5.4.3 on page 208, this heat treatment cycles causes damage onto the coating surface.
- Because of a mismatch between the coefficients of thermal expansion between the coating and the substrate, tensile residual stresses are induced within the coating layer. These tensile residual stresses have a detrimental effect on the fatigue limit of a material as will be outlined in Section 2.3.4.2 on page 19.
- Lower Deposition rate in comparison to PVD.
- Substrate must be able to withstand the high process temperatures.
- Process tends to 'blunt' sharp corners.
- Due to the large grained microstructure of the CVD coatings, the surface is generally rougher than PVD.
- If coating tungsten carbide insert with a layer of TiN, carbon atoms are 'pulled' from the substrate tungsten leaving behind a brittle 'eta-phase'.

Physical Vapour Deposition (PVD):

Advantages:

- Due to the relatively low process temperatures (550°c), no additional heat treatment of the substrate is required.
- The bombardment of the coating atoms onto the substrate induces compressive residual stresses, which can be a disadvantage because it limits the coating thickness. It will be outlined however in Section 2.3.4.2 on page 19, that compressive residual stresses play an important role in delaying of crack initiation.
- The PVD process allows a sharp edge to be retained.

Disadvantages:

- PVD process is a 'line of sight' technique. For this reason tubes and blind holes with a depth to width ratio greater than one cannot be coated. Also because of the 'line of sight' process, complex shapes have to be manipulated in front of the vapour source to get good all round coverage.

Obviously the above description becomes a little blurred, as some of the disadvantages of the CVD process are advantages of the PVD process and vice versa. The significance of the above points become more apparent when the fatigue endurance of a coated steel component is considered, as will be outlined in Section 2.3.4 on page 18.

2.3.3 Trim Die Coatings

As previously mentioned in Section 2.2.3 on page 12, once the trim dies have been machined to the correct dimensions, a CVD coating is applied to the surface of the tool. This coating typically consists of three layers, which are:

1. Titanium Carbide (TiC). Thickness 3-4μm.
2. Titanium Carbon Nitride (Ti (CN)). Thickness 1-1.5μm.

3. Titanium Nitride (TiN). Thickness 3-4μm.

Figure 2-12 below shows an image taken with a light microscope of the M2 substrate and the triple coatings on the trim die surface.

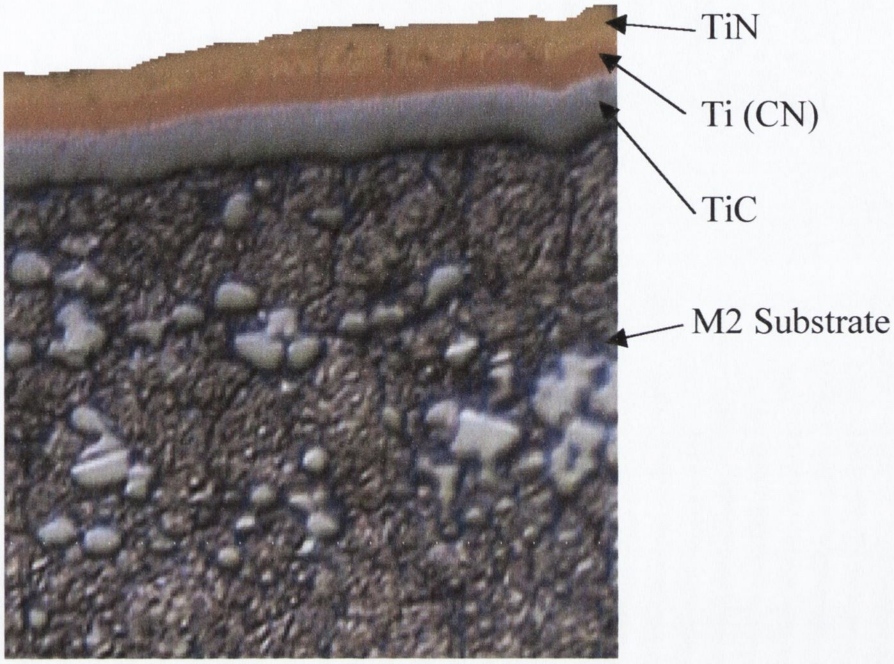

Figure 2-12: Triple Coating on the M2 Substrate

2.3.4 Coatings and Fatigue Endurance

A surface coating is often applied on cold working dies to improve its wear characteristics. However, the application of a coating can be detrimental in terms of its fatigue resistance [10, 11, 12]. For example, when coating tungsten carbide, carbon atoms are 'pulled' from the substrate to combine with the titanium on the first layer to make TiC. The absence of carbon atoms in the tungsten carbide substrate produces a brittle layer commonly known as the 'eta-phase' [13]. To overcome this problem, when coating tungsten carbide tools, the atmosphere is 'spiked' with an excess of hydrogen gas. This problem however does not arise when coating steels, in fact the 'pulling' of carbon atoms from the steel will actually soften the substrate and thereby increase its toughness. It has been stated by other researchers [12] that the various mechanisms by which ceramic coatings can effect the fatigue behaviour have yet to be documented in a systematic way. Very little information is available about the effect of a coating film on the fatigue behaviour of metals [14]. Some results on the area of fatigue and coatings seem to be contradictory [10], stating that coatings improve the fatigue characteristics. However a closer examination of some of the research work available reveals the probable reason why these improved fatigue results were obtained.

2.3.4.1 Contradictory Results

Research conducted by R. Ebara et al in 1987 [15] investigated the coating of steam turbine blades using an Ion-Plating PVD process. The turbine blades were made from martensitic stainless steel. Rotational bending fatigue tests revealed that a test specimen coated with a Cr-TiN layer produced a higher fatigue endurance limit. The term 'Fatigue Endurance' is explained in Section 2.4.3.3 on page 31, but it is sufficient to say at this stage that a specimen with a superior fatigue endurance limit is capable of withstanding a higher cyclic stress before failure occurs. Therefore the research by R. Ebara et al concludes that a coating improves the components fatigue resistance.

R. Murakami et al [12] conducted research on TiN coated steel fatigue specimens. As in the previous research mentioned above [15], the coating was deposited using ion-plating technology, which is a form of PVD coating. This research [12] also stated that the fatigue life of the component was greater once the coating was applied.

Unfortunately, research work considering the fatigue endurance of steels coated by CVD techniques [10, 11, 14, 16] produced contradictory results to work done by R. Ebara et al [15] and R. Murakami et al [12], stating the fatigue endurance was reduced by the application of a coating. Considering the residual stresses within the coating layer helps to understand how these contradictory results were obtained.

2.3.4.2 Residual Stresses

A closer examination the research conducted by R. Ebara et al [15] and R. Murakami et al [12] reveal that the method used to deposit the coating was Ion-plating, which is a PVD technique. As outlined in the advantages and disadvantages of CVD and PVD techniques, the Physical Vapour Deposition (PVD) process, imparts a compressive residual stress on the surface of the coating, while the CVD process tends to create tensile residual stresses due to a mismatch of the coefficients of thermal expansion between the coatings and the steel substrate [8, 16, 17].

Figure 2-13 and 2-14 below show the residual stress distributions generated by a PVD and CVD coating process respectively [16].

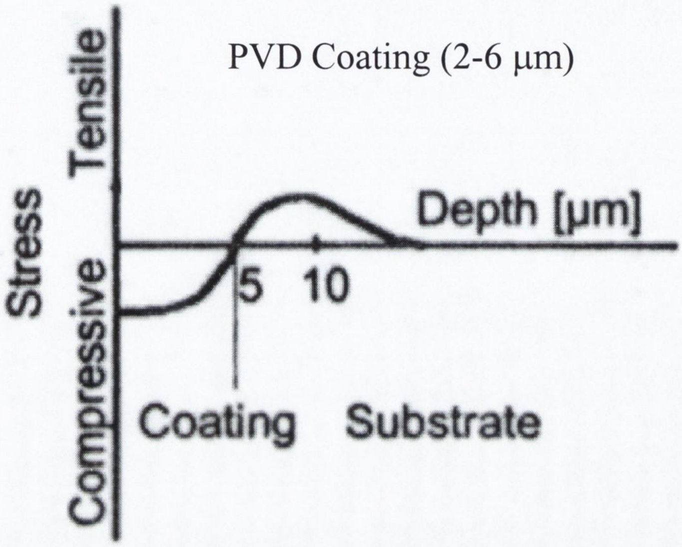

Figure 2-13: Residual Stress Distribution in Coating and Substrate Caused by a PVD Coating Process

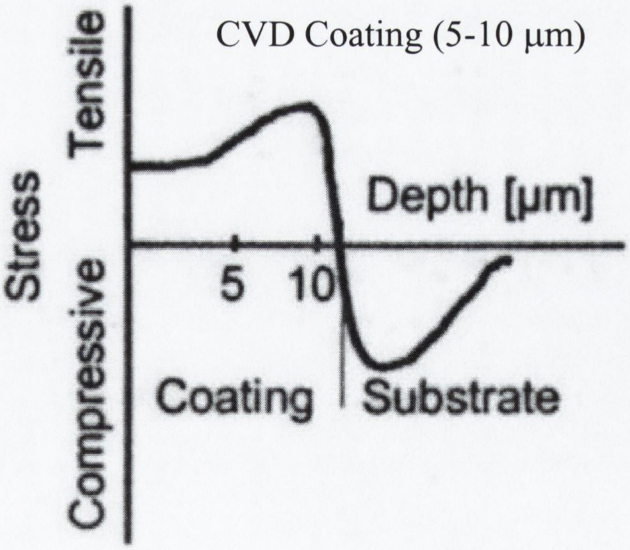

Figure 2-14: Residual Stress Distribution in Coating and Substrate Caused by a CVD Coating Process

Comparing figures 2-13 and 2-14 clearly indicate that the PVD process induces compressive residual stresses within the coating, while the CVD process induces tensile residual stresses. It has been stated that compressive residual stresses at the external surfaces generally enhance fatigue life, while tensile stresses are detrimental [18].

Therefore as Ion-plating technology generates compressive residual stresses within the coating, this could cause the improvements in the fatigue endurance of the PVD coated specimens.

2.3.4.3 Fatigue Tests

In Section 4.5.4 on page 190 it will be outlined why the fatigue properties of the trim die material M2 along with the triple coating were required in an effort to clarify the situation in relation to coatings and fatigue.

M. Geiger et al [10] conducted research on CVD and PVD coated AISI M2 specimens. The results from these fatigue tests proved that a CVD coating lowered the fatigue endurance of the M2 substrate. Unfortunately, the results from that research could not be used in this project because:

- Once the CVD coating was applied, the material characteristics of the M2 substrate changed due to the high coating temperatures. A heat treatment cycle was not conducted on the fatigue specimens to return the substrate to its original conditions. As outlined in Section 2.2.4 on page 12, the Hi-Life Tools trim dies are heat treated after the CVD coating, therefore to obtain as accurate results as possible the coated fatigue specimens require a heat treatment.

- The tests only considered a single layer on TiN on an M2 substrate.

- Due to the close collaboration between Hi-Life Tools and Materials Ireland, TCD, it was possible to manufacture fatigue specimens using exactly the same machines and conditions as the actual trim die themselves.

A. Kocanda [19] conducted fatigue tests on AISI M2, however the results from these tests could not be used either because:

- The fatigue tests were conducted at the elevated temperatures of 350°c, 500°c and 650°c.
- The effect of coating was not considered
- The hardness of the M2 fatigue specimens was not given

2.3.4.4 Corrosion

It is generally understood that corrosion on the surface of a material can cause stress concentrations, which lead to a reduction in fatigue endurance [20].

Research into the effect of coatings and corrosion [14, 15, 20, 21] has proposed the mechanism of decrease in corrosion fatigue strength. It has been stated that corrosion pits are likely to form on the substrate metal due to saline solution penetrating throughout the flaws in the coating [14]. The corrosion fatigue life for a coated tool is shorter than that of an uncoated tool because the coating is electrochemically nobler than the substrate, making the coating cathodic and the substrate anodic in a corrosion cell [21]. These corrosion pits act as initiation sites for fatigue cracks to propagate and will generally reduce the fatigue endurance of a component [15, 20].

2.3.4.5 Fatigue Crack Arrest

A keynote paper by F. Klocke et al [16] stated that a number of layers in a coating are thought to provide a barrier against crack propagation. However it was not clarified if the coatings were deposited by the PVD or CVD method. The method of deposition becomes important because of the differences in coating temperature. As previously mentioned, a PVD coating is deposited at around 550°C where as the CVD process operates at around 1000°C. Therefore in a CVD coating the interface between the coating layers become diffused and 'blend' together. Section 4.5.4.3 on page 208 considers the crack arrest properties of the triple layered trim die.

2.4 Failure Mechanisms in Cold Forging Dies

Extensive research has shown that the reduction in tool costs and reduction in the down times of expensive machine are of major importance for the cold forging industry [1, 22 - 28]. The improvement and prediction of tool fracture behaviour represents one of the major objectives for the economical application of cold forging technology [22]. Tooling costs contribute significantly to the overall cost of a cold forged component [27]. In the case of cold extrusion, the total cost of die production is approximately 5-15% of the overall production cost [24].

The author conducted an extensive research for literature related to trim die failure, but unfortunately it did not prove successful. Numerous studies in bulk forming operations [1, 22, 24 - 32] have been conducted and have shown that the die life is mainly influenced by the following three failure mechanisms:

- Wear
- Plastic Deformation
- Fracture

2.4.1 Wear

It has been stated that thermal load and contact time with hot metal, during the deformation process, makes wear the most frequent reason for failure in warm and hot forging [1]. Typical failure rates for tools in cold extrusion, for example, are 80% failure by fracture but only 20% of tool replacement is due to wear [25,27].

In terms of tool steels, such as AISI M2, there are four basic mechanisms of wear:

- Abrasion
- Adhesion
- Corrosion
- Contact fatigue

As wear is predominately a failure mechanism in warm and hot forging, only a brief outline of the four wear mechanisms will be given.

An important point to note is that although wear is the dominant mechanism of failure in warm and hot forging, it always takes place even in cold forging despite the high hardness of the tools or the application of coatings [25].

2.4.1.1 Abrasion

Abrasive wear, as defined by ASTM [33], is due to hard particles or hard protuberances that are forced together and move along a solid surface. Wear, in turn, is defined as damage to a solid surface that generally involves progressive loss of material and is due to relative motion between surfaces and a contacting substance. The cost of abrasion is high and has been estimated as ranging from 1 to 4% of the gross national product of an industrialised nation [9].

Several mechanisms have been proposed to explain how material is removed from a surface during abrasion. These mechanisms include fracture and fatigue. Because of the complexity of abrasion, no one mechanism completely accounts for all the loss.

A tool steel with a large volume fraction of large hard carbides will have reduced wear characteristics [9]. During abrasion the large carbides can be torn from the steel matrix and will increase wear on the tool steel by adding abrasive carbide particles to the wear debris.

2.4.1.2 Adhesion

Adhesion wear between tool steel and workpiece can result when direct contact occurs because of lubricant breakdown, high pressures, or process design. This type of wear arises as a result of cold welding of microscopic asperities between the tool and the workpiece.

2.4.1.3 Corrosion Wear

Corrosion wear is not a major cause of wear in tool steel, but it can become a most important mechanism at high temperatures.

2.4.1.4 Contact Fatigue Wear

Repeated sliding or rolling of one component over another, leads to spalling or microcracking and causes contact fatigue wear. This type of wear often manifests itself as cutting or punch edge chipping. Figure 2-15 below shows the surface of a tool steel punch, AISI D2, used to cut austenitic stainless steel [9]. The white arrow indicates the direction of material sliding. It has been stated that the cracks shown in figure 2-15 are primarily caused by friction force. Spalling begins to accelerate the wear after a certain number of cuts. Finally, one of the transverse cracks initiates a large-scale fracture of the punch edge, instantly ending tool life.

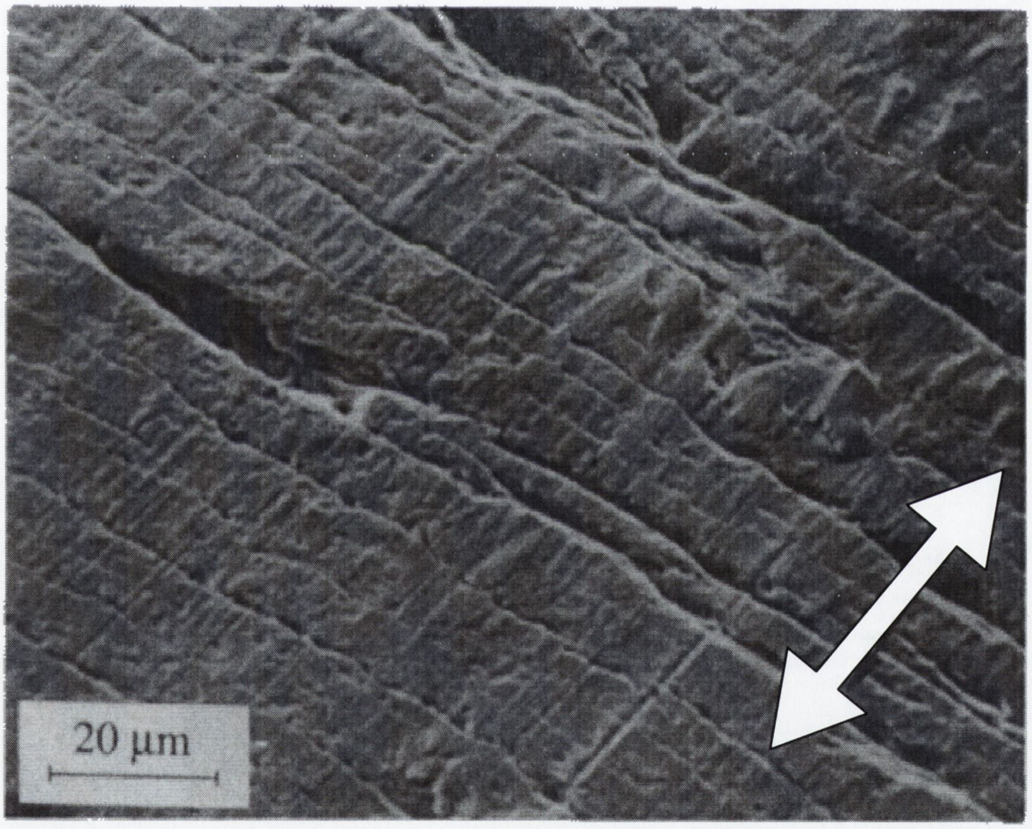

Figure 2-15: Cracks in an AISI D2 Punch, Transverse to the Direction of Material Sliding [9]

Numerous studies have shown that the application of a coating onto a die, whose life is controlled by wear, can produce dramatic improvements in output [1, 9, 25, 32]. One study in particular [9] compared the life of three press forming dies, each made from a hot-work tool steel AISI H29, but having different surface treatments. Figure 2-16 plots the results from the tests. With reference to figure 2-16, the obvious improvement in die life when coated with titanium nitride in comparison to the chromium and uncoated dies is clear.

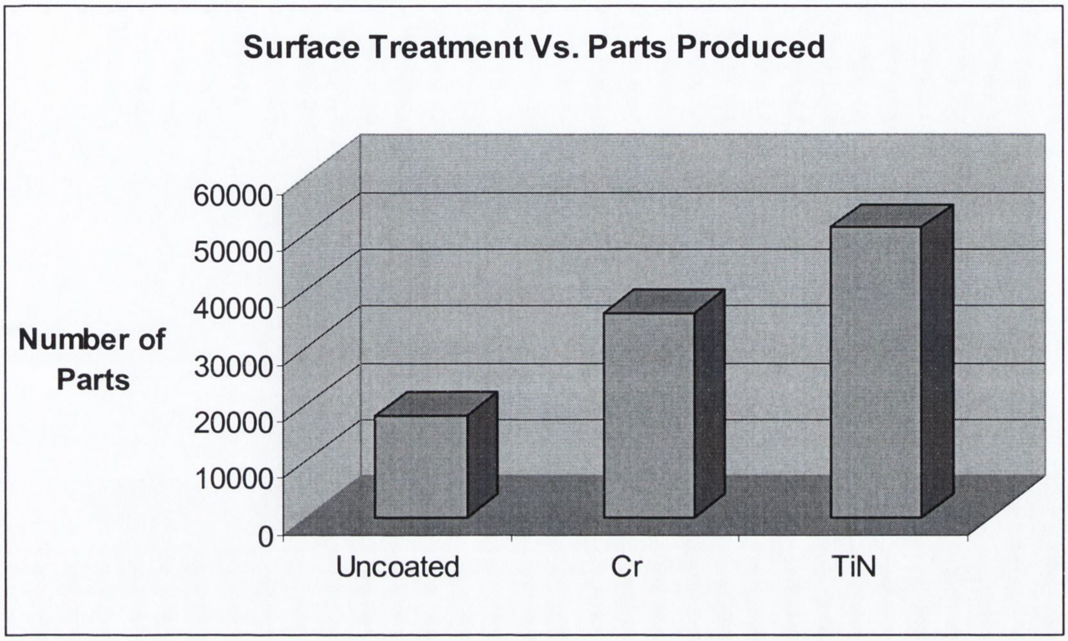

Figure 2-16: Improvements in Die Life in Press Forging by Coating Application [9]

2.4.2 Plastic Deformation

Plastic deformation, also known as overloading, mushrooming or indentation, occurs when a process exceeds the yield strength of steel, typically defined as the point where 0.2% plastic strain has taken place. Although fewer die failures can be ascribed to overloading, an overloading die wears rapidly and may break prematurely [2]. Overload fracture can be avoided by using modern techniques of stress and strain evaluations such as the Finite Element Method (FEM) [25].

2.4.3 Fracture

Fracture is defined as the complete separation of a material that occurs when a crack reaches a critical size and reduces the strength below that required to carry the service load. The final fracture is usually abrupt, but it is generally preceded by a cracking process that occurs slowly over the service life from various growth mechanisms such as fatigue, stress-corrosion cracking, creep and hydrogen-induced cracking.

Initial approaches to understand fracture involved a recognition that the toughness of a material was associated with its ability to absorb energy. The area under the stress-strain curve is taken as a measure of the energy required to rupture one unit volume of the material in question. Therefore materials, which have a good combination of strength and ductility, should therefore exhibit good toughness. For materials that do not contain flaws and are only loaded in uniaxial tension, then this approach is sufficient. However, in many engineering applications a notch is present on a component and impact loads are applied in service. The Charpy Test accounts for both of these effects and is widely used to compare the relative behaviour of materials under impact loads in the presence of a notch. The Charpy test is simple and widely used [20].

Charpy tests were conducted by the author on the trim die material M2 having the exact heat treatment as outlined in the previous Section 2.2.4, and compared with AISI 1045 which is known to exhibit a ductile fracture pattern due to its ductility. The two different fractured surfaces are shown in figure 2-17 below.

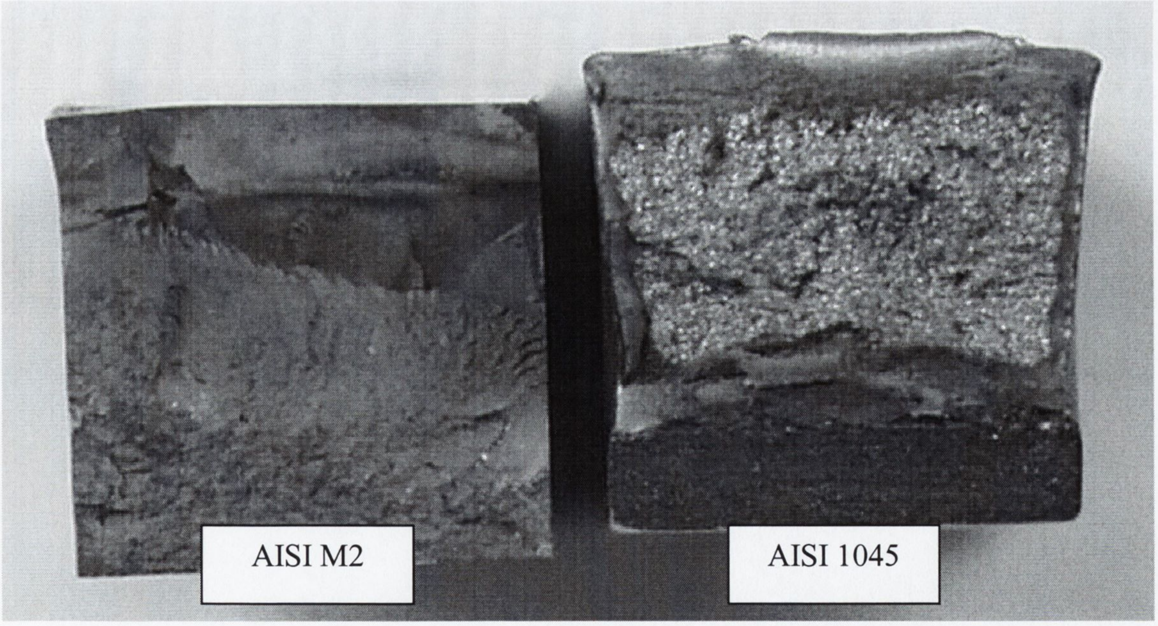

Figure 2-17: Brittle and Ductile Fracture of AISI M2 and AISI 1045

With reference to figure 2-17, the harder and less ductile AISI M2 material is shown on the left, while the fractured surface of the more ductile AISI 1045, is shown on the right. The surfaces shown above clearly indicate the plastic deformation associated with ductile fracture of the AISI 1045. From these Charpy tests, it was established that due to the high hardness of the M2 (59-62HRc) there is a reduction in the toughness. The energy absorbed in causing fracture of the AISI M2 and AISI 1045 was 32 Joules and 64 Joules respectively.

Based on the appearance of the fractured surface, fracture modes can be classified into the following three general categories:

- Ductile Fracture (Dimple Rupture)
- Brittle Fracture (Cleavage)
- Fatigue

2.4.3.1 Ductile Fracture

Ductile fracture can often be easily recognised from a macroscopic examination of the surfaces of a failed specimen due to the significant amount of contraction that occurs before failure [34]. Figure 2-18 below shows the contraction associated with the ductile fracture of AISI 1045.

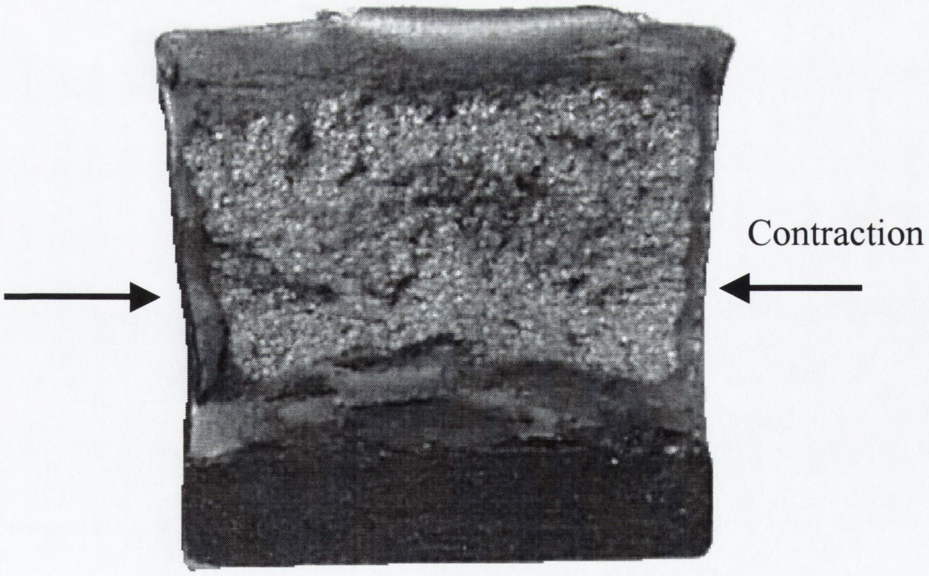

Figure 2-18: Ductile Fracture of AISI 1045

On a microscopic scale most structural materials fails by a process known as Microvoid Coalescence [20]. Another term used to describe this mode of failure is 'dimpled rupture'. While it is a ductile micromechanism, the presence of Microvoid Coalescence on a fracture surface does not guarantee that the fracture absorbed a significant amount of energy. It has been stated that there are a number of situations where dimpled rupture is observed for embrittled materials [20].

The sequence of fracture is: void initiation, void growth and finally void coalescence. Figure 2-19 below illustrates the three stages of microvoid coalescence.

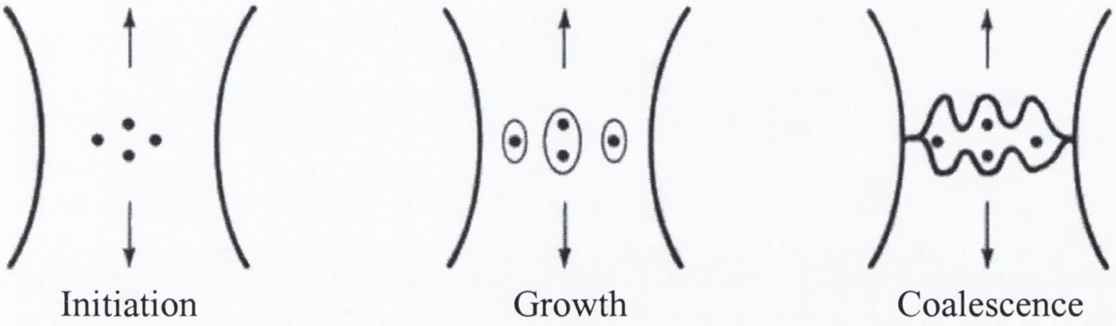

Figure 2-19: The Three Stages of Microvoid Coalescence in Ductile Fracture [2]

Void initiation occurs at second phase particles or inclusions [2]. Voids are initiated because hard particles do not deform to the same extent as the softer matrix material surrounding them. This causes the matrix material to deform more than normal, which in turn produces more strain hardening, thus creating a higher stress in the matrix near a particle. When the stress becomes sufficiently large the interface between the particle and matrix may separate, or the particle may crack [34].

The second stage of ductile fracture is void growth, which is a strain-controlled process. Voids elongate as they grow, and the ligaments of matrix material between the voids become thin. Therefore, the final stage of ductile fracture is hole coalescence through the separation of the ligaments, which links the growing voids.

2.4.3.2 Brittle Fracture

A truly brittle fracture is caused by cleavage. Cleavage takes place by the separation of atomic bonds along well-defined crystal planes [34]. Because steels are polycrystalline materials, with grains randomly orientated with respect to each other, the cleavage propagation has to change direction as it crosses a grain boundary. Most steels contain particles, precipitates, carbides or other imperfections that further complicate the fracture path.

An interesting paradox concerning brittle fracture is that cleavage fracture occurs in materials that exhibit little or no capacity for plastic deformation as well as materials that exhibit significant plastic deformation [20]. The mechanism of cleavage fracture in brittle materials has already been outlined as the separation of atomic bonds, however the separation in materials, which exhibit significant plastic deformation, has perplexed and fascinated researchers for decades [20]. It has been stated that in steels, cleavage fracture is hard to explain because the crack tip stress is below the theoretical fracture stress [20]. The most common explanation for this is that carbides fracture ahead of the crack tip, producing sharp crack stresses equal to the theoretical fracture stress.

The changes of orientation between grains and the various imperfection (carbides, particles) produce markings on the surface that are characteristically associated with cleavage. These characteristic features are shown in figures 2-20 [34].

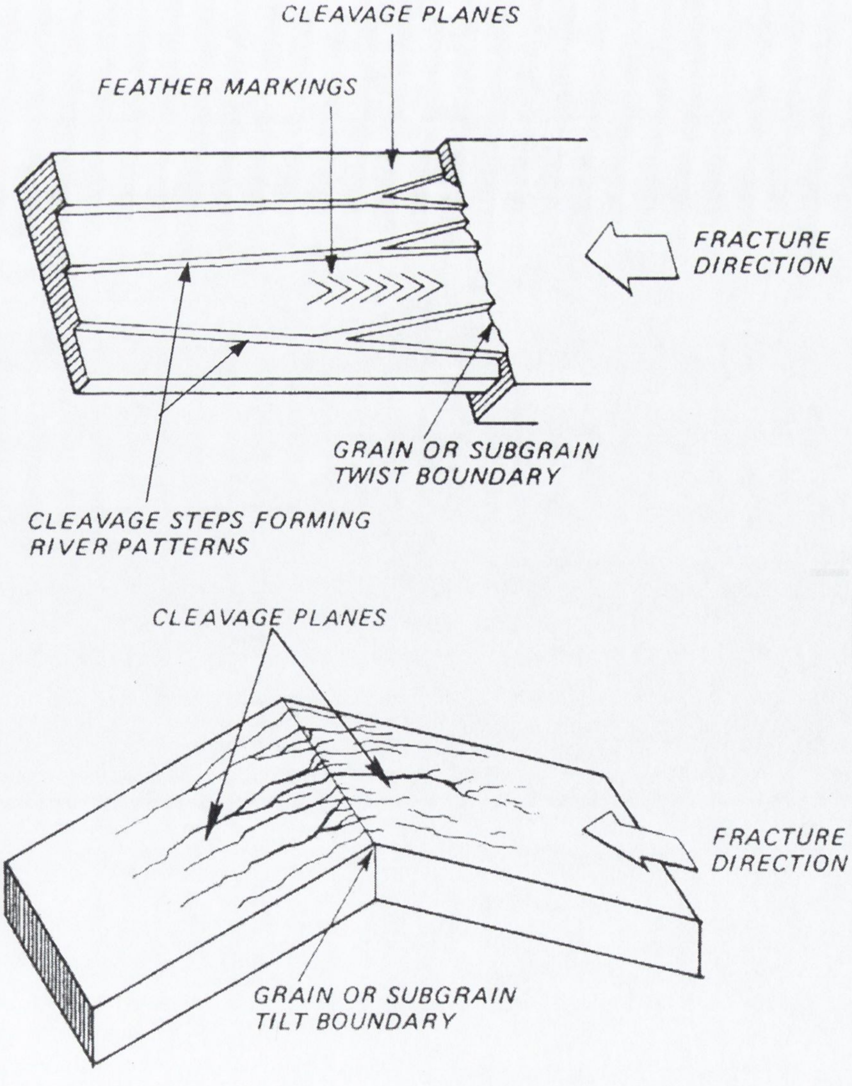

Figure 2-20: Characteristic Features Associated With Brittle Cleavage Fracture [34]

2.4.3.3 Fatigue

Engineers have long known that alternating stresses of relatively small magnitudes can cause fracture in a metallic structure that is capable of carrying a much greater static load. Fatigue cracking is the common failure mode that ends the service life of cold forging tooling [31]. It has been stated that in cold work applications fatigue might appear as fine chipping at the cutting edge [35]. Despite the huge volume of research which has been conducted in this area and the many hundreds of papers and reports published each year on the problem of fatigue life prediction, fatigue induced fracture remains the principle limitation on the life prediction of components, especially components such as aircraft, vehicles, medical devices and machine tools [36].

Sir William Fairbairn carried out some of the earliest quantitative research into metal fatigue in 1861. He found that raising and lowering a 3 tonne mass onto a wrought iron girder some 3 million times would cause it to break, while it required a static load of almost 12 tonne to cause rupture. Ten years later, August Wohler continued work in this area and developed the fatigue-testing machine, which bears his name. The testing method adopted by A. Wohler is the stress-life or safe-life philosophy and is the oldest approach to understanding fatigue [20]. The stress-life or S-N approach is in principle one of a safe-life, infinite-life regime. It is generally categorised as "high cycle fatigue" methodology, with most considerations based on maintaining elastic behaviour in the sample. The phrase "infinite-life" is related to the asymptotic behaviour of steels, many of which display a fatigue limit or "endurance" limit at a high number of cycles, typically above 1 million. Most other materials do not exhibit this response; but instead display a continuously decreasing stress-life response even at a great number of cycles (1 million to 100 million). Figure 2-21 below shows a typical S-N curve for steel and non-ferrous alloys.

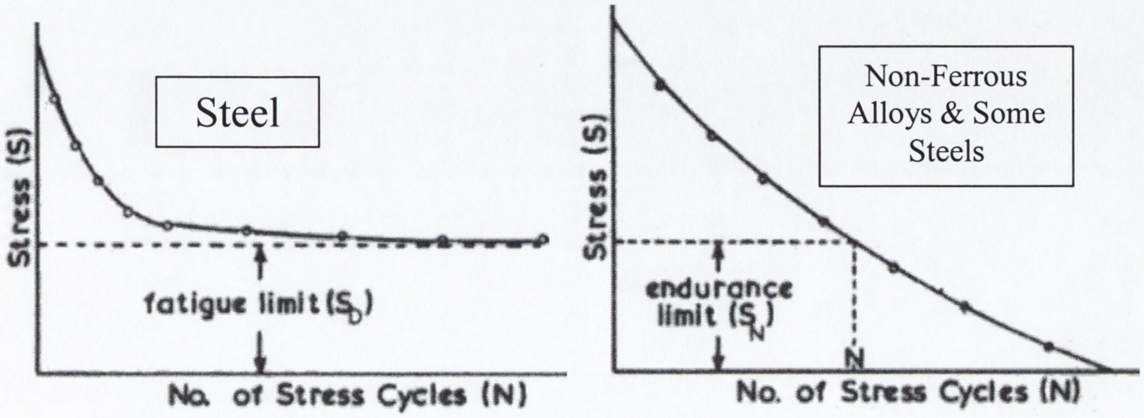

Figure 2-21: S-N Curves For Steel And Non-Ferrous Alloys [6]

In accordance with ASTM standard E 468-90 [37], the most typical formats for data presentation of S-N curves are to plot the log number of cycles to failure versus either stress amplitude, maximum stress or stress range.

Factors, which affect fatigue life, may be grouped into the following categories [18]:

- Microstructure
- Processing techniques
- Environmental factors
- Geometry

Effect of Microstructure

Grain structure, average grain size and microstructural flaws all have a strong influence on fatigue life. At ambient temperatures, a material with a large grain size will exhibit a lower fatigue limit compared to one with a smaller grain size. However, if cycled at high temperatures, the reverse in observed.

Effect of Processing Techniques

Processing techniques such as forging, rolling and extrusion produce directional properties in materials due to grain orientation. Heat treatment, case hardening, cold and hot working, surface coating, plating can all influence residual stresses [18]. As previously stated in Section 2.3.4.2 on page 19, compressive residual stresses at external surfaces generally enhance fatigue life, while tensile residual stresses are detrimental. Processes such as shot peening, cold rolling and static preloading are employed to induce compressive residual stresses.

Environmental Factors

A corrosive environment causes degradation of the material, the most common visible effect being pitting or surface roughness (etching). These notch-like regions act as stress raisers and are generally the sites of crack nucleation.

Effect of Geometry

Surface finish has a significant influence on crack initiation [18]. Geometric discontinuities in a component such as holes, notches and joints are sources of stress concentrations and are often the sites of crack initiation.

Fatigue failure is a multi-stage process. It begins with the initiation of cracks, and with continued cyclic loading the cracks propagate, finally leading to the rupture of the component [18].

There are three modes of loading generally considered in the analysis of fracture and fatigue, called:

- Mode I 'opening mode'
- Mode II 'sliding mode'
- Mode III 'tearing mode'.

Figure 2-22 below illustrates the basic differences between each mode.

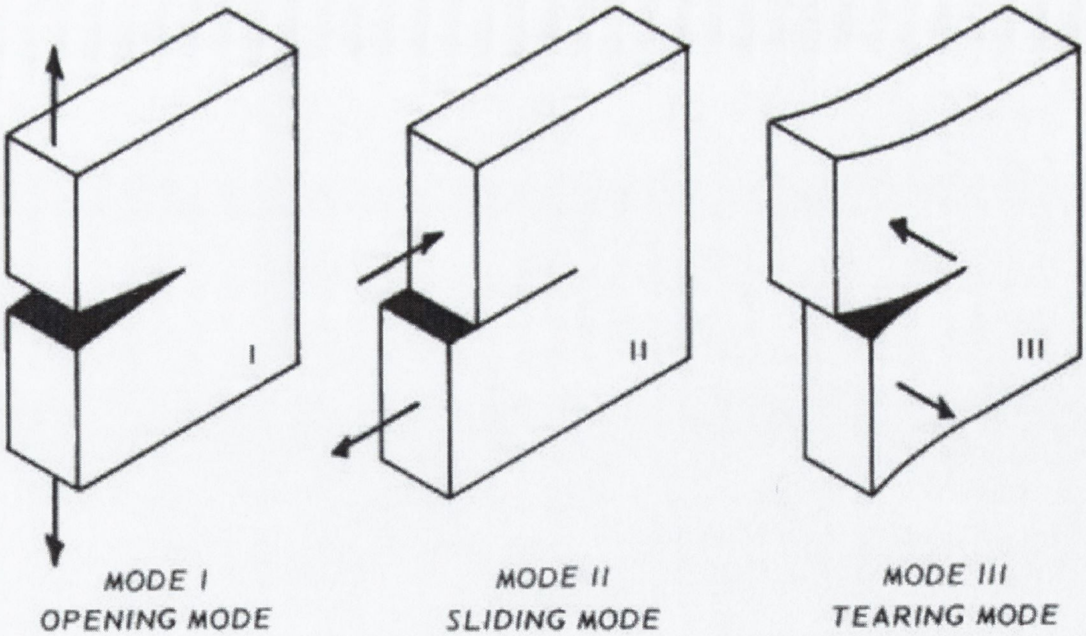

Figure 2-22: The Three Modes Of Loading [34]

Fatigue crack growth during uniaxial cyclic deformation, i.e. Mode I in figure 2-22, occurs by initiation of a microcrack that propagates on a plane close to that for the maximum shear. This is termed a 'Stage I' fatigue crack [20]. The length of the stage I crack depends on the material and the loading amplitude, but is generally of the order of 3 to 4 grain sizes [18]. As the crack extends, it rotates from the plane of maximum shear to the plane normal to the maximum principal stress and is then termed a ‘Stage II’ fatigue crack.

Fatigue of uncracked metals is traditionally divided into low-cycle and high-cycle fatigue; the transition is usually associated with about 10,000 cycles to failure.

Fatigue fractures generated during stage II fatigue may exhibit crack marks known as fatigue ‘striations’, which are a visual record of the position of the fatigue crack front during crack propagation through the material. It is unclear why sometimes fatigue striations do not appear [20], but it has attracted considerable investigation. However the absence of fatigue striations does not mean that the basic mechanism by which the crack advanced has changed. A lack of striations on a fatigue fracture surface may be due to their having been obscured by ‘crack-closure’ induced rubbing of the fractured surfaces.

2.4.4 Summary

From the confluence of aspects influencing tool life, it is clear that there is no general recipe for increasing tool life and tool quality [14]. From numerous investigations in the area of bulk forming operations, it has been established that the die life is mainly constrained by wear, plastic deformation and fracture.

Section 2.4.1 on page 23 outlined the four mechanisms of tool wear and detailed other research work which suggests that wear was the most frequent mechanism of failure in warm and hot forging. Section 2.4.2 on page 26, outlined how failure due to plastic deformation can be avoided by using finite element techniques to estimate the magnitudes of stress and strain within the tooling.

Finally, Section 2.4.3 on page 26, explained that the appearance of the fractured surface could be used to identify three modes of fracture: ductile rupture, brittle fracture and fatigue. The whole area of fracture is so vast that only a brief outline of these three modes was given.

Fatigue is a complicated process, which is affected by a number of factors. The complexity of the fatigue process is compounded by the fact that some of the factors mentioned in this Section are interrelated and cannot be easily isolated for a quantitative evaluation. This is partly why there is such a vast literature on the subject of fatigue.

2.5 Finite Element Method

2.5.1 Introduction

The history of metal forming is based on a highly empirical form of technology. In times past the trial and error methods used in industry were frequently better than the available analytical methods. This was mainly due to the fact that computers were slow, expensive, and cumbersome to use. An experienced die designer could usually solve a production problem faster, with a higher confidence level than that possible using any other available form of analysis [38].

The application of Finite Element Methods (FEM) to metal forming during the 1970's and early 1980's provided a new perspective on metal forming practices. One such computer package called DEFORM (Design Environment for FORMing) was developed at Battelle Columbus Laboratories, USA [39, 40]. The initial work that led to this development was sponsored by the US Air Force and derived from the pioneering studies on rigid-plastic FEM, conducted by Professor Shiro Kobayashi et al [41] of the university of California Berkeley. When using FEM based programs to analyse engineering problems, the complex geometry needs to be divided into a finite number of simple geometric shapes called elements. The collection of the elements is called a mesh, and the procedure of dividing the geometry into elements is known as mesh generation. Before 1989 mesh generation in DEFORM was done using a Mapping Method. In that mapping method, the user would sub-divide the geometry into four-sided patches and assign the desired density distribution of elements. This process was not only time consuming but also prone to error, as the mesh density assigned by the user usually required prior knowledge of the solution behaviour. To counteract this problem, W. T. Wu et al [42] developed, as part of his doctoral thesis, an Automated Mesh Generation (AMG) module that enabled the user to mesh geometric shapes faster, and for the novice, more accurately. Due to the large deformation that occurs in bulk forming processes, the FEM mesh would degenerate quite frequently during analysis [38]. Many manual remeshes were needed to complete a simulation.

Therefore in 1991 automatic Remeshing capabilities were added to DEFORM. With the use of automatic remeshing (or adaptive remeshing), during the simulation module when the elements become too distorted, the process is 'paused' while a new mesh is applied to the geometry. An Interpolation module was developed to interpolate the values of temperature and strain from the highly deformed "old" mesh onto the newly generated mesh. The combined, and automated, use of modules for automatic mesh generation (AMG) and interpolation, was called Automatic Remeshing, and enabled a continuous simulation of a forming process without any interface by the user, even if several remeshes were required [39, 40]. This is one of the major advantages that DEFORM has over some of its rivals.

Prior to using FE to model an engineering application, it is most important that the modelling techniques and boundary conditions used are defined as accurately as possible. The most assured method of verifying the FE results is by direct comparison with experimental results. Once the predictions from the FE results have been shown to correlate with the experimental data, the FE technique can be used to its full potential.

Extensive references on the use of the finite element method in metal forming can be found in [43, 44 – 54].

2.5.2 DEFORM

DEFORM employs 4-noded isoparametric quadrilateral elements, which were used to model the trimming process.

DEFORM essentially consists of three modules:

2.5.2.1 Pre-Processor

The following parameters are generally required in the pre-processor:

- Geometry of parts to be modelled
- Material properties
- Load conditions – magnitude – how they are applied etc.
- Boundary conditions
- Type of analysis to be performed

The geometry of each component to be modelled is usually constructed within the pre-processor, however for complex geometries external packages such as AutoCAD and Mechanical Desktop are utilised.

2.5.2.2 The Simulation Engine

The actual FEM based analysis is carried out in this portion of DEFORM. The basic equations of equilibrium, constitutive relations and boundary conditions are converted to non-linear algebraic equations by utilising the FEM discretisation procedure as outlined in [41]. The user does not have any access to this simulation module except the possibility of selecting one of the two available solution techniques for the solution of simultaneous equations, namely, the direct iteration method or the conventional Newton-Raphson method. All the input and output data are stored in binary form and are accessed by the user through the post-processor.

2.5.2.3 Post Processor

The post-processor is used to display the results of the simulation in graphical or alphanumeric form. Available graphic representations include:

- FE Mesh
- Contour plots of stress and strain, strain-rate and temperature distributions
- Velocity vectors
- Load-stroke curves

Within the FE package, the material behaviour of the components to be tested can be considered as one of the following:

- Elastic
- Elastoplastic
- Ideal Plastic

In the case of the trimming operation, analysed for this project, the workpiece material was considered as plastic whilst the trim die was considered elastoplastic. To understand and explain the difference between these three concepts, the basics of FEA will have to be discussed.

2.5.3 Mathematical Framework

In the numerical analysis, the elastic strains were calculated using the following expression [41]

$$\varepsilon_E = \frac{\sigma'_{ij}}{2G} + \left[\frac{1-2\upsilon}{E}\right]\sigma_m \qquad \text{...........(2.1)}$$

Where υ = Poisson's ratio, ε_E = Elastic strain tensor, σ'_{ij} is the deviatoric stress, G is the shear modulus, E is Young's modulus and σ_m is the hydrostatic pressure given by [41]

$$\sigma_m = \frac{\sigma_1 + \sigma_2 + \sigma_3}{3} \qquad \text{...........(2.2)}$$

For the plastic portion of the simulation, the basic formulae and conditions to be satisfied are expressed as:

Equilibrium conditions $$\frac{\delta\sigma_{ij}}{\delta x_j} = 0 \qquad \text{...........(2.3)}$$

Strain rate deformation $$\dot{\varepsilon}_{ij} = \frac{1}{2}\left[\frac{\delta v_i}{\delta x_j} + \frac{\delta v_j}{\delta x_i}\right] \qquad \text{...........(2.4)}$$

The constitution relation used by the DEFORM code for metal forming is given by [41]

$$\sigma'_{ij} = \frac{2\bar{\sigma}}{3\dot{\bar{\varepsilon}}}\dot{\varepsilon}_{ij} \qquad \text{...........(2.5)}$$

Where:

$$\bar{\sigma} = \sqrt{\frac{3}{2}\left(\sigma'_{ij}\sigma'_{ij}\right)} \qquad \text{...........(2.6)}$$

$$\dot{\bar{\varepsilon}} = \sqrt{\frac{2}{3}(\dot{\varepsilon}_{ij}\dot{\varepsilon}_{ij})} \qquad \text{...........(2.7)}$$

Boundary conditions $\sigma_{ij} n_{ij} = \overline{F_i}$ on S_F ....(2.8)

And $V_i = \overline{V}_i$ on S_F

Where σ_{ij}, $\dot{\varepsilon}_{ij}$ and V_i are the stress, strain rate and velocity components on the boundary. $\bar{F}_i$ is the force applied to the surface S_F. The deviatoric stress components, σ'_{ij}, are defined by

$$\sigma'_{ij} = \sigma_{ij} - \delta_{ij}\sigma_m \qquad \text{...........(2.9)}$$

Where δ_{ij} is the kronecker delta and is equal to 1 when $i = j$ and 0 if $i \neq j$

In the equations given above, the flow stress $\bar{\sigma}$, is the factor modified to allow the software to model various materials. The flow stress can be modelled using various functions, which relate the flow-stress to strain, strain rate and the temperature of the material $\bar{\sigma} = f(\varepsilon, \dot{\varepsilon}, T)$. However, for this project the necessary stress and strain data for the heat-treated trim die material M2 was obtained experimentally by the author and entered directly into the F.E. code, Section 3.2.1 on page 71 will outline this experimental procedure. This allowed for an accurate representation of the flow behaviour of the material during the trimming process.

The solution to the equations given above can be obtained by minimising the internal energy of the system [41]. This is obtained using a variational equation and is expressed as:

$$\delta\Phi = \int_v \bar{\sigma}\delta\dot{\varepsilon}dV + \int_V Q\,\dot{\varepsilon}_v\delta\dot{\varepsilon}_v dV + \int_{S_F} \overline{F_i}\delta v_i dS = 0 \qquad \text{...........(2.10)}$$

Where V and S_F are the volume and surface of the workpiece respectively, F_i represents the surface traction applied to the surface S_F and $\dot{\varepsilon}_v$ is the volumetric strain rate. The first term of the equation represents the potential energy of the system and contains both the elastic and plastic contribution of the deforming body. The second term represents the strain energy of the system, where Q is a large positive constant to penalise volume change. The final term represents the external work done on the system, in this case both the normal and frictional components over the surface of the body are incorporated into the model. Equation 2.10 is converted to a non-linear algebraic form by utilising the FEM discretisation procedure. DEFORM uses the Rayleight-Ritz technique to minimise the energy of the system with respect to the elemental variables

$$\delta\Phi\left[u_{i0}\right] = 0 \equiv \frac{\delta\Phi}{\delta u_{i0}} = 0 \qquad \text{...........(2.11)}$$

Or generally represented as:

$$K\left(\bar{\dot{\varepsilon}}, T\right)\{u\} = \{F\} \qquad \text{...........(2.12)}$$

Where K represents the stiffness matrix and is dependent on the strain, strain rate and temperature of the system, {u} is a vector representing the elemental velocity and {F} is a vector of the nodal forces. Equation 2.12 is solved in terms of velocity using both the Direct and Newton-Raphson techniques. The utilisation of these two techniques ensures that fast and accurate convergence is obtained. This is because the Direct method is more efficient at initially converging the solution while the Newton-Raphson method is more suitable for converging the analysis when the solution approaches the final value. Once the elemental velocities are obtained, the effective strain rate is calculated from a derivative of the velocity components or more explicitly for equation 2.2.

For a small time step, the strain can be evaluated by an explicit integral with the assumption of no internal effects. The explicit integral requires that for a small interval of time the velocity and strain rate changes are small, hence the strain at time t+Δt can be evaluated as, [41],

$$\varepsilon_{t+\Delta t} = \varepsilon_t + \dot{\varepsilon}_t \Delta t \qquad \text{...........(2.13)}$$

Where ε_t is the strain at time t, $\varepsilon_{t+\Delta t}$ is the strain at time t+Δt and $\dot{\varepsilon}_t$ is the strain rate at time t. A similar approach is used with respect to updating displacements using velocity values.

Once the strain and strain rate are obtained, the effective and deviatoric stresses can be obtained from equations 2.1 to 2.9.

2.5.4 Friction and Contact Modelling

2.5.4.1 Friction

Friction conditions at the die-material interface greatly influence metal flow, formation of surface and internal defects, stresses acting on the dies, and load and energy requirements. Numerous studies on the modelling of friction in metal forming processes have been prepared [55 - 62]. There are three basic types of lubrication governing the frictional conditions in metal forming [63, 64].

1. Dry conditions, in which no lubricant is present at the interface, however the oxide layers present on the die and workpiece materials may act as a 'separating' layer. In this case friction is high, and such a situation is desirable in only a few forming operations, such as hot rolling of plates and slabs and the nonlubricated extrusion of aluminium alloys.
2. 'Hydrodynamic' lubrication exists when a thick layer of lubricant is present between the dies and the workpiece. In this case the friction conditions are governed by the viscosity of the lubricant and by the relative velocity between the die and the workpiece. The viscosities of most lubricants decrease rapidly with increasing temperature. Consequently, in most practical high speed forming operations, such as strip rolling and wire drawing, the hydrodynamic conditions exist only within a certain regime of velocities, where the interface temperatures are relatively low [64].
3. 'Boundary' lubrication is the most widely encountered situation in metal forming. Increases in temperature at the interface and the relatively high forming pressures do not usually allow the formation of a hydrodynamic lubrication regime. However Boundary lubrication, on the other hand, does not lend itself to reliable analysis. As a result, most of the knowledge on metal forming lubrication is empirical.

In most forming applications, the lubricity of a lubricant is the single most significant factor since it directly determines the interface friction. Lack of lubrication promotes wear and shortens the life of the die [65]. In order to evaluate the performance of various lubricants, and to be able to predict forming pressures, it is necessary to express the interface friction quantitatively in terms of a friction factor or coefficient. The friction shear stress f_S, is most commonly expressed as:

$$f_S = \mu p \qquad \text{...........(2.14)}$$

Where (p) is the compressive stress normal to the interface, and (μ) is the coefficient of friction, or as:

$$f_S = mk \qquad \text{...........(2.15)}$$

Where (k) is the shear strength of the deforming material and (m) is the friction factor, having a range of $0 \le m \le 1$.

It has been recommended [41] that equation 2.15 adequately represents the friction conditions in most bulk forming processes, while equation 2.14 is more commonly used to represent friction in sheet metal forming processes. The reason for this is that the compressive normal stress at the interface in sheet metal forming is generally much smaller in magnitude compared to that in a bulk deformation processes. For various forming conditions, the values for the friction factor (m) varies as follows [66]:

- m = 0.08 – 0.1. Cold forming of steels, aluminium alloys and copper, using conventional phosphate-soap lubricants or oil.
- m = 0.2 – 0.4. Hot forming of steels, copper and aluminium alloys with graphite based lubricants.
- m = 0.1 – 0.3. Hot forming of titanium and high temperature alloys with glass lubricants.
- m = 0.7 – 1.0. When no lubricants are used. For example in hot rolling of plates or slabs in nonlubricated extrusion of aluminium alloys.

2.5.4.2 Contact Modelling

The trimming process induces complex contact conditions simultaneously between trim die, top tool and workpiece. When a node from one deformable object contacts the surface of another deformable object, a relationship between the two objects must be established to keep the objects from penetrating each other. This relationship is referred to as a master-slave or slave-master relationship. When two objects are contacting each other, the contact nodes move with the master surface as long as the two objects are in contact.

The slave nodes are considered to be in contact with the master object as long as the nodal forces indicate a compressive state. When a slave node develops a tensile force, the node is considered to have separated from the master object.

The slave object should be the softer of the two materials and should have the finer mesh. In the case of two objects consisting of the same material, either can be the slave although the object expected to elastically deform the most should be defined as the slave. Setting a No-Contact relation between two objects causes the objects to be invisible and allows them to pass through each other [66].

Figure 2-26 below shows a screen snapshot taken from the pre-processor of DEFORM highlighting the inter object interface relationships.

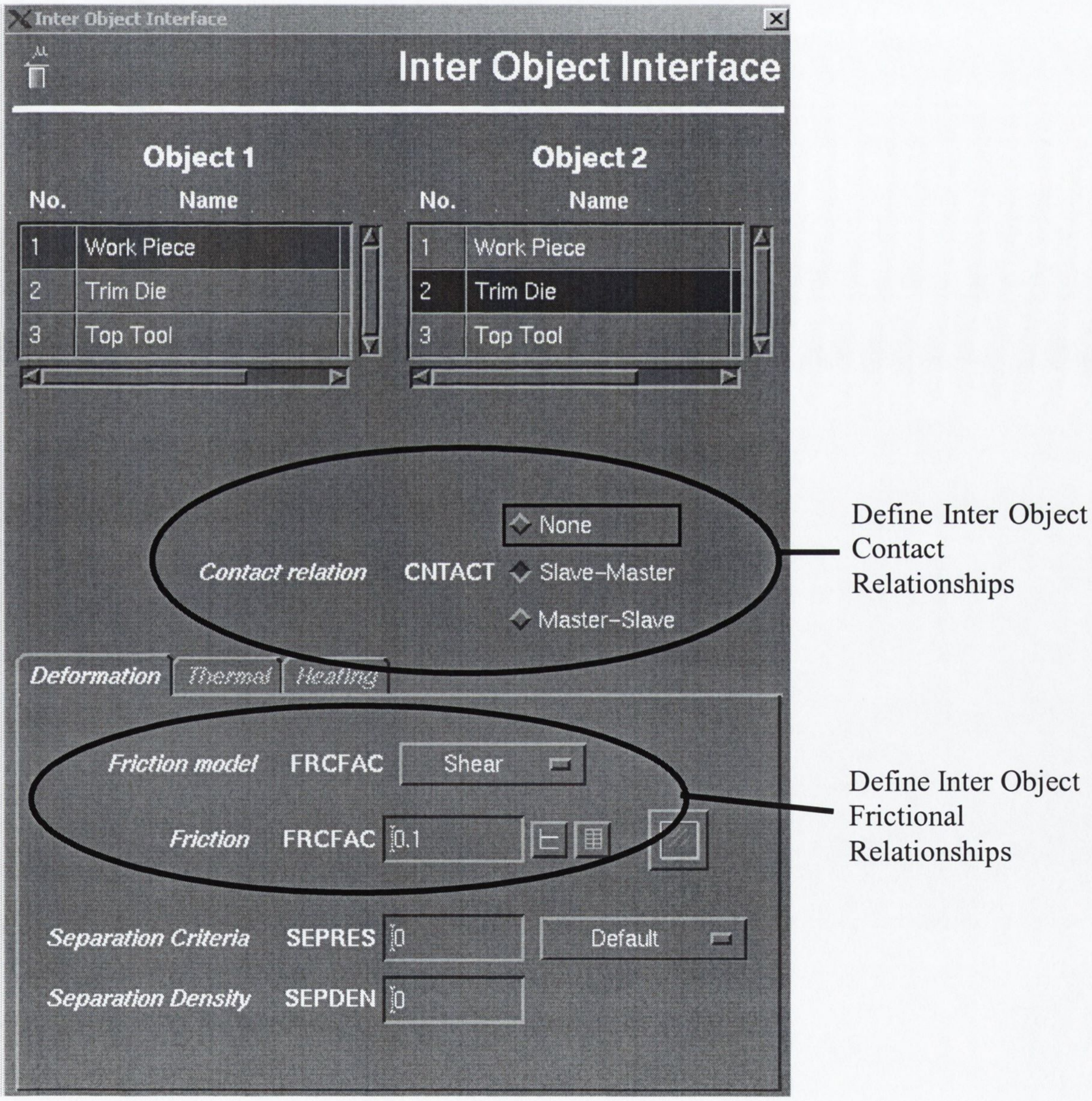

Inter Object Interface

Object 1

No.	Name
1	Work Piece
2	Trim Die
3	Top Tool

Object 2

No.	Name
1	Work Piece
2	Trim Die
3	Top Tool

Contact relation CNTACT ◇ None ◆ Slave-Master ◇ Master-Slave

Deformation | *Thermal* | *Heating*

Friction model FRCFAC Shear

Friction FRCFAC 0.1

Separation Criteria SEPRES 0 Default

Separation Density SEPDEN 0

Define Inter Object Contact Relationships

Define Inter Object Frictional Relationships

Figure 2-26: Screen Snapshot From DEFORM Showing Inter Object Interface Relationships

With reference to figure 2-26, the workpiece is selected in the 'Object 1' column, while the trim die is selected in the 'Object 2' column. By selecting the 'Slave-Master' option, the workpiece becomes the 'Slave' to the 'Master' trim die. The next step is to define the friction model and coefficient. As previously outlined in Section 2.5.4.1 on page 41, it has been recommended that the 'Shear' friction model adequately represents the friction conditions in most bulk forming processes [41]. The friction factor (m) used for all the FE models simulated in this project was 0.1 as recommended for cold forming of steels [41, 66].

2.5.5 The Yield Criteria

A yield criterion is a law that determines the stress level at which plastic deformation begins.

For isotropic materials, plastic yielding can be expressed as being dependent on the magnitude of the principal stresses. Therefore the yield stress can be expressed as:

$$f_1(I_1, I_2, I_3) = Const \qquad \text{...........(2.16)}$$

The yield stress has been shown to be strongly dependent on the deviatoric stress tensor and to a lesser degree on the hydrostatic or mean stress, as shown previously in equation 2.9. Since the principal deviatoric stress components are not independent ($\sigma_1' + \sigma_2' + \sigma_3' = 0$), then the yield criteria can be written as [41]

$$f(J_2, J_3) = Const \qquad \text{...........(2.17)}$$

Where

$$J_2 = -\left(\sigma_1'\sigma_2' + \sigma_2'\sigma_3' + \sigma_3'\sigma_1'\right) \qquad \text{...........(2.18)}$$

$$J_3 = \sigma_1'\sigma_2'\sigma_3' \qquad \text{...........(2.19)}$$

2.5.6 Two Criteria

The two simplest criteria, which have been extensively used for the analysis of metal deformation, are the Tresca criterion and the Von Mises (or Hueber-Mises) criterion.

2.5.6.1 Tresca Yield Criterion (1864)

This states that yielding begins when the maximum shear stress reaches a critical value. It states that yielding begins when [41]

$$\sigma_1 - \sigma_3 = 2k \qquad \text{...........(2.20)}$$

When $\sigma_1 \geq \sigma_2 \geq \sigma_3$

2.5.6.2 Von Mises Yield Criterion (1913)

The Von Mises criterion states that yielding will occur when the J_2 component reaches a critical value, but that the J_3 component is not critical. This flow rule is also known as the J_2 flow rule. Modifying equation 2.18 and rewriting gives

$$J_2 = \frac{1}{2}\left(\sigma_1^{'2} + \sigma_2^{'2} + \sigma_3^{'2}\right) = \frac{1}{2}\sigma_{ij}^{'}\sigma_{ij}^{'} = k^2 \qquad \text{...........(2.21)}$$

Or:

$$J_2 = (\sigma_1 - \sigma_2)^2 + (\sigma_2 - \sigma_3)^2 + (\sigma_3 - \sigma_1)^2 = 6k^2 \qquad \text{...........(2.22)}$$

Or:

$$J_2 = (\sigma_x - \sigma_y)^2 + (\sigma_y - \sigma_z)^2 + (\sigma_z - \sigma_x)^2 + 6\left(\tau_{xy}^2 + \tau_{yz}^2 + \tau_{zx}^2\right) = 6k^2 \qquad \text{...........(2.23)}$$

Where k is a parameter dependant on the material properties and is obtained from a simple tensile or compression test.

For DEFORM, the interpretation of k is given below as:

$$k = \frac{1}{\sqrt{3}}\sigma_y \text{ (Yield stress in Shear)} \qquad \text{...........(2.24)}$$

Therefore yielding occurs when the stress in the object reaches the yield stress of the material obtained from a tensile test and is expressed mathematically as

$$\sigma_y = \sqrt{(\sigma_x - \sigma_y)^2 + (\sigma_y - \sigma_z)^2 + (\sigma_z - \sigma_x)^2 + 6\left(\tau_{xy}^2 + \tau_{yz}^2 + \tau_{zx}^2\right)} \text{...........(2.25)}$$

2.5.7 Flow Rule

The material flow rule used with the Von Mises yield criteria is the Prandtl-Reuss flow equation. This equation describes how the individual stress/strain components develop after yielding has occurred. The general form of this equation is [41]

$$\dot{\varepsilon}_{ij}^{\,P} = h\frac{\delta g}{\delta \sigma_{ij}}\dot{f} \equiv \frac{\delta f}{\delta \sigma_{ij}}\dot{\lambda} \quad \text{(Assuming f = g)} \quad \text{...........(2.26)}$$

$$d\varepsilon_{ij}^{\,P} = h\frac{\delta g}{\delta \sigma_{ij}}\delta f \equiv \frac{\delta f}{\delta \sigma_{ij}}\delta\lambda \qquad \text{...........(2.27)}$$

Where h and g are scalar functions of the invariant of the deviatoric stress. $\dot{f}$ is the yield function and g(σ_{ij}) is called the plastic potential (where dλ or $\dot{\lambda}$ is a positive proportionality constant, being equal to $h\dot{f}$ or hδf), which determines the amount of plastic straining. Hence the flow equation is a function of the yield stress and when expressed in a rate form becomes:

$$\dot{\varepsilon}_{ij}^{\,P} = \sigma'_{ij}\dot{\lambda} \qquad \text{...........(2.28)}$$

Since

$$\frac{\delta f}{\delta \sigma_{ij}} = \sigma'_{ij} \qquad \text{...........(2.29)}$$

Equation 2.28 can be rewritten and expressed in terms of the plastic strain and the deviatoric stress components to give

$$\frac{\dot{\varepsilon}_x^{\,P}}{\sigma_x'} = \frac{\dot{\varepsilon}_y^{\,P}}{\sigma_y'} = \frac{\dot{\varepsilon}_z^{\,P}}{\sigma_z'} = \frac{\dot{\gamma}_{xy}^{\,P}}{2\tau_{xy}'} = \frac{\dot{\gamma}_{yz}^{\,P}}{2\tau_{yz}'} = \frac{\dot{\gamma}_{zx}^{\,P}}{2\tau_{zx}'} \qquad \text{............(2.30)}$$

Combining the elastic strain rate components and the plastic strain rate components according to $\dot{\varepsilon}_{ij} = \dot{\varepsilon}_{ij}^{\,P} + \dot{\varepsilon}_{ij}^{\,E}$, gives the Prandtl-Reuss equation for elasto-plastic solids, as:

$$\dot{\varepsilon}_{ij} = \sigma_{ij}'\dot{\lambda} + \frac{1}{2G}\dot{\sigma}_{ij}' + \delta_{ij}\left(\frac{1-2\upsilon}{E}\right)\dot{\sigma}_m \qquad \text{............(2.31)}$$

2.5.8 Hardening Rule

The hardening rule used in DEFORM is the bilinear isotropic hardening rule. This rule assumes that the yield stress expands uniformly in all directions, [41], based on the amount of plastic work done on the material. The material stress/strain data for the FE simulations consisted of six linear segments. The bilinear isotropic hardening rule implies that if the load is reversed, the material will not yield on subsequent loading until the maximum applied stress exceeds the induced stress/residual stress from the previous step and the yield stress of the material in the opposite loading direction, [41].

2.5.9 Die Profile Optimisation

Computer-optimisation of engineering designs is a powerful emerging technology. Currently, technical designs are based on the intuition and the experience of design engineers. In the future, computer optimisation will assist in the search for optimal technical solutions [29].

Established FE packages such as ANSYS have design optimisation algorithms built into the pre-processor module of the programme. Unfortunately, as will be outlined in Section 3.1.3.2 on page 60, ANSYS was unable to simulate the large-scale deformation associated with the trimming process analysed in this project. However a short description of the optimisation module within ANSYS is helpful as it shows the power of computer-optimisation techniques, provided that the process to be simulated can be simplified to a sufficient level. For example to calculate the 'optimum design', the ANSYS program performs a series of analysis-evaluation-modification cycles [67]. This basically means that an analysis of the initial design is performed, the results are calculated and evaluated against user specified design criteria, and the design is modified if necessary. This process is repeated until all specified criteria are met. The ANSYS theory manual [67] states that the term 'optimum design' is one that meets all specified requirements but with minimum expense of certain factors such as weight, surface area, volume or stress.

Design optimisation can be used to optimise dimensions such as thickness, shape fillet radii, placement of supports and natural frequency. Any ANSYS item that can be expressed in terms of a parameter known as a Design Variable (DV), can be subject to optimisation. Upper and lower limits are specified on design variables to act as 'constraints' and to prevent impractical geometries.

Design variables (DV) are usually geometric parameters such as length, thickness or diameter. They are restricted to positive numbers. Figure 2-27 below show some of the possible DV's for the optimisation of a connecting rod profile.

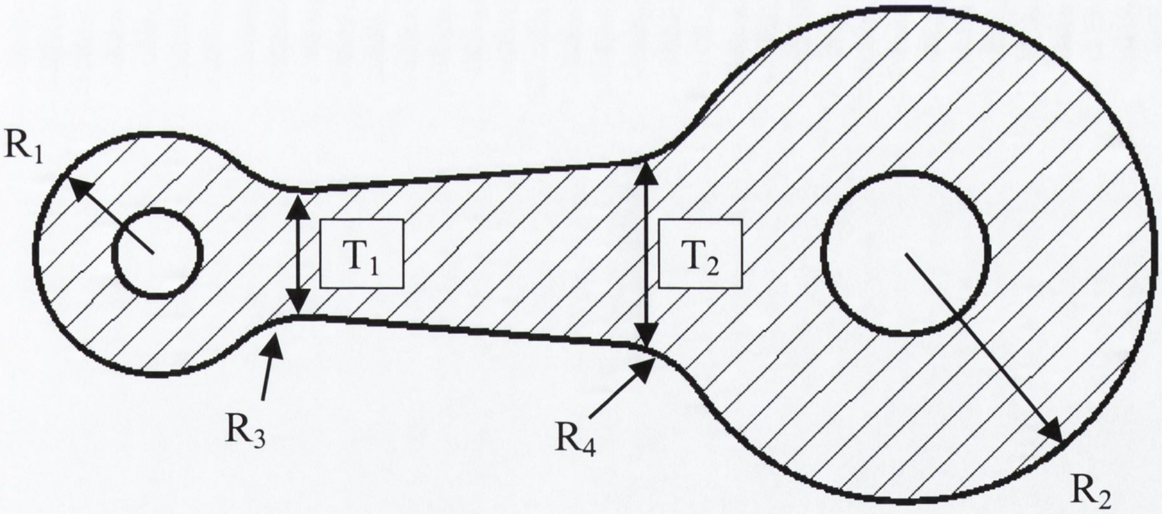

Figure 2-27: Possible Design Variables (DV) in a Connecting Rod Profile [67]

An extensive literature review into the area of die profile optimisation techniques has found numerous successful methods [22, 23, 24, 25, 27, 30 & 32]. However all the research work to date, known to the author, primarily considers the profile optimisation of extrusion dies. Due to a feature of the extrusion process, a simplification to the FE models enables optimisation procedure to be performed on the die profile. This simplification can be made because once the extrusion process is running, the problem can be considered as having steady state flow. Figure 2-28 below illustrates the concept of steady flow during the extrusion process.

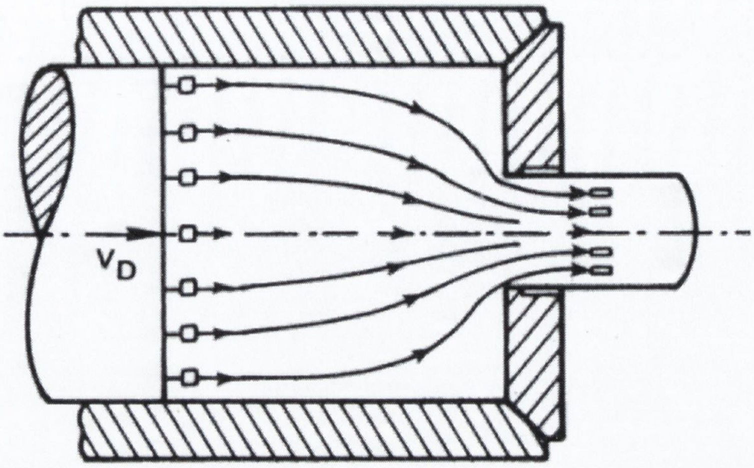

Figure 2-28: Steady State Flow of Material During Extrusion Process [41]

Because the extrusion process essentially has a steady flow of material, the velocity field remains unchanged. Therefore a major simplification can be made in the FE model, by assuming a constant internal pressure to represent the extruded material.

The trimming process investigated in this project however is an example of 'non-steady flow' meaning that the velocity field changes continuously with time as in the case of upset forging illustrated in figure 2-29 below.

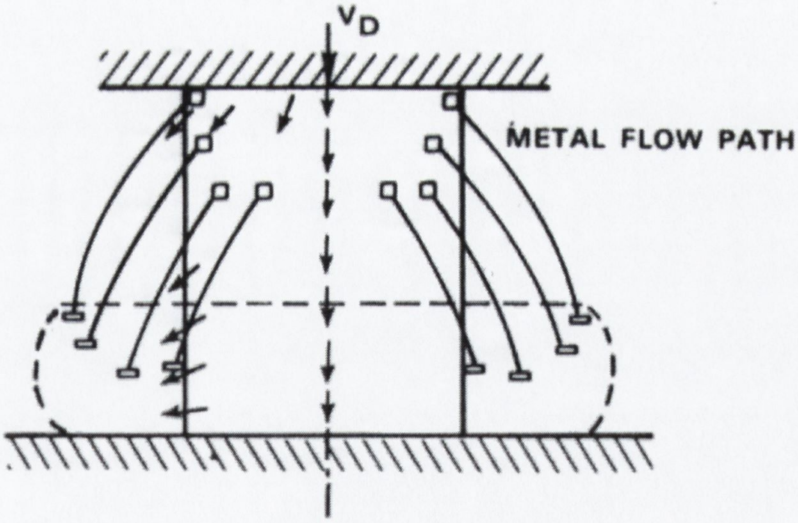

Figure 2-29: Non-Steady State Flow of Material During Upset Forging [41]

To the authors knowledge therefore, no commercial FE package, capable of simulation the large plastic deformation inherent in the trimming process, is available for die profile optimisation. For this reason, the trim die profile optimisation procedure conducted in this thesis followed a more 'manual' approach, as detailed in Section 4.1 on page 79.

2.6 Objectives of the Thesis

The objective of the work presented in this thesis is to reduce the likelihood of trim die failure by establishing an 'optimum' trim die profile, and to improve the quality of the finished product. To that end the investigation performed in this project has to determine the following:

- A better understanding of the complete trimming process and the stress distribution within the trim dies.

- The influence of the various trim die profile parameters on the stress magnitudes and distributions within the tooling.

- An optimisation of the trim die profile and investigate the possibility of interaction between parameters.

- The most likely mechanisms of trim die failure.

- The theoretical 'critical' stress component, most likely to induce failure within the trim die.

- An 'Optimum' trim die profile which would induce:

    - The lowest level of the 'critical' stress component, hence reducing the likelihood of failure.
    - The lowest level of Effective stress within the trim die geometry.

Part III.

3 Work Programme

This section highlights, in chronological order, the sequence of events, which took place during the development of the new trim die profile. An explanation of the iterative process and the main conclusions, where necessary, are discussed. The main body of results will not be presented in this section, see Part IV on page 79 for an in dept analysis.

3.1 Finite Element Models

3.1.1 Introduction

The fundamentals of the forging/trimming process were explained in Section 2.1.1. The first attempt to simulate this forging process was carried out in 1994 [3], see figure 3-1. This research in 1994 made certain assumptions relating to the trim die, workpiece and top tool profile, which will now be explained in this section. An extensive literature research into the trim die forging process concluded that no other research work had been attempted in respect of this particular manufacturing process. For that reason no theoretical structure of research was in place to guide the path for the design process to follow. Due to this fact, the design process became an iterative procedure. With the introduction of a new finite element package called DEFORM, the results from tests carried out previously in 1994 were used as a starting point, see figure 3-1. Modifications to the trim die profile and top tool configuration was the first area of investigation in this research programme and is therefore designated *Phase 1* within this thesis. The conclusions from these Phase 1 tests steered the design procedure in the next tests, and so on. Hence inducing an iterative design procedure, see the theoretical path in the flow chart illustrated in figure 3-1.

The culmination of the finite element simulations enabled the selection of a trim die profile that sustained a significantly reduced level of effective and tensile radial stresses within the trim die during the forging process. The results obtained from these simulations are detailed in Part IV.

The FEA package DEFORM allows the user to analyse various stress and strain components such as radial, axial, mean, shear, hoop and effective. At the time when the Phase 1 models were being simulated, the exact failure mechanism was not yet understood. Experimental testing and investigation was conducted in tandem with the theoretical FEA simulations, this is illustrated by the flow chart shown in figure 3-1 on the following page. The question remained however, which stress component was the dominant factor leading to the failure of the trim die. The final result was already known; cracks within the trim die causing chipping and failure, see section 1.1. During crack propagation plastic deformation is necessary, even in a material on the whole, which remains elastic, localised yielding occurs. Plastic deformation is related to slip, in the grain structure, which is dependent on shearing action. *Von-Mises* yield criterion is also based on this concept of shear. It has been shown that any complex stress system can be regarded as a combination of hydrostatic stress and a function of the difference of principle stresses, i.e. shear stress, and therefore a yield criterion such as *von-Mises*, which is based on the principle of stress difference, or shear stress would seem to be most logical.

The values DEFORM produces for effective stress are obtained using *Von-Mises* yield criterion. For this reason it was concluded that the die geometry that produced the lowest amount of effective stress, will increase the life of the trim die. Fatigue tests and surface topography of the trim die coating highlighted a more important stress component within the trim die, that of radial stress. The reason for considering radial stresses, their location and the subsequent results are discussed in part IV.

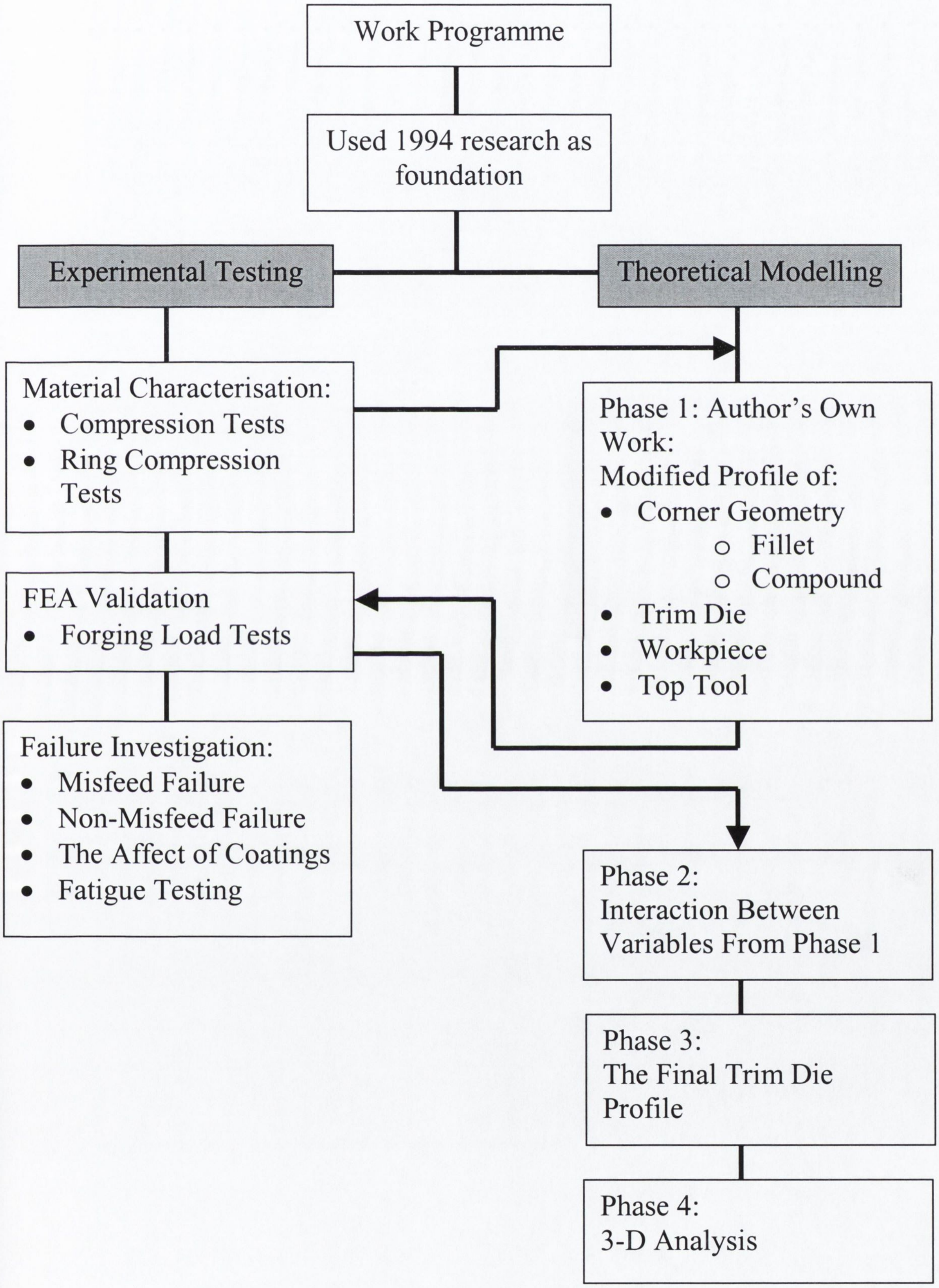

Figure 3-1: Schematic Flow Chart Representing the Work Programme

3.1.2 Basic Assumptions made in 1994

When simulating a complex operation, such as the trimming process, assumptions are necessary to simplify the problem, while maintaining good confidence in the results. The forging process investigated in this project is inherently a three-dimensional (3D) problem due to the internal hexagonal hole within the trim die, see figure 3-2. The earlier research carried out in 1994 [3] made certain assumptions. The main assumption related to the approach of representing the 'real world' three dimensional (3D) trim die to a theoretical two dimensional (2D) model. The method used to do this was classified the 'worst case scenario' and will now be discussed.

3.1.2.1 Worst Case Scenario

If using a 2D model can make a reasonably accurate representation of the 3D component, the modelling process becomes simpler, and more importantly, the solution times are reduced significantly. A 3D simulation can be one and a half orders of magnitude more demanding than a comparable 2D problem [68].

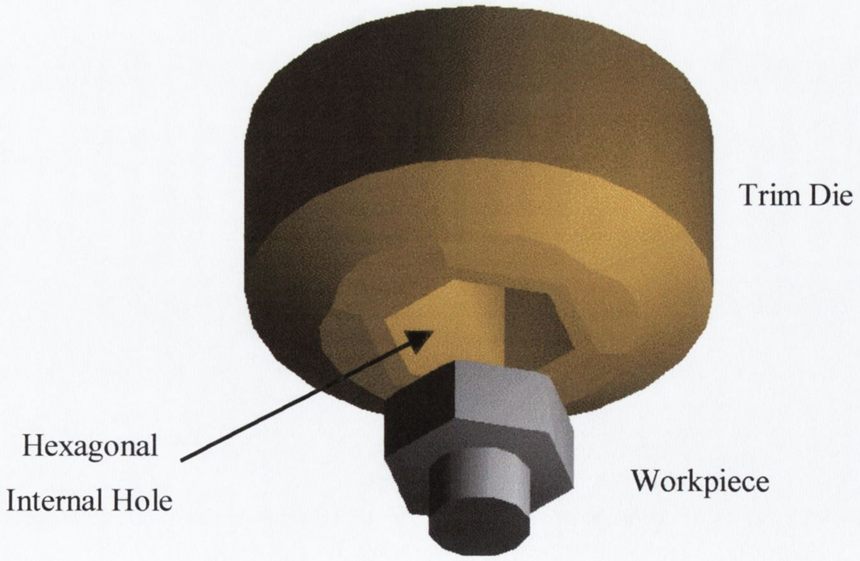

Figure 3-2: Trim Die and Workpiece showing internal hexagonal hole

Considering the 'Worst Case Scenario' enabled the construction of a 2D model, which would represent the 3D model. The 'worst case scenario' considers a plane, through the trim die, where the greatest amount of stress is experienced during the forging process. The selection of this plane was made possible by considering where the greatest amount of workpiece material would have to be trimmed. Figure 3-3, illustrates a plan view showing the outline of the trim die in green and the outline on the workpiece shown as a black dashed circle.

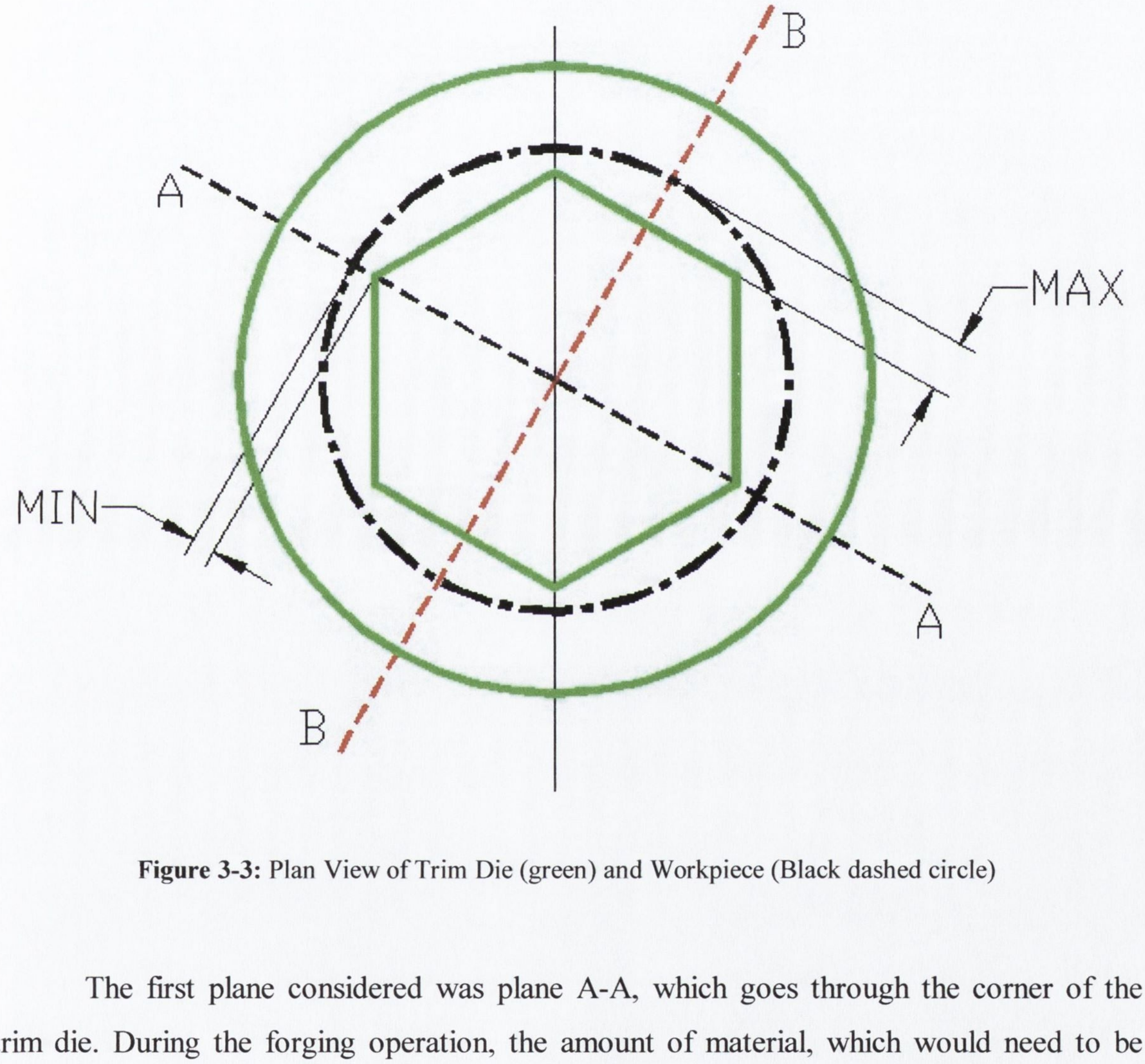

Figure 3-3: Plan View of Trim Die (green) and Workpiece (Black dashed circle)

The first plane considered was plane A-A, which goes through the corner of the trim die. During the forging operation, the amount of material, which would need to be trimmed, is at a minimum at this location, see figure 3-3. If plane B-B were considered, through the centre of the flats of the hexagon, the maximum amount of material would need to be trimmed. This plane, B-B, was deemed the 'worst case scenario' and a section taken through the workpiece, trim die and top tool along this plane represents the location where the greatest amount of stress is experienced. Both experimental and theoretical tests have verified that it is on this plane, that the greatest amount of stress arises. The location of trim die failure due to chipping, see Section 4.5.4 on page 215, and by the high stress pattern produced in the 3D modelling on the centre of the flats of the hexagon, see Section 4.4 on page 177.

Figure 3-4, shows the section through the trim die representing the 'worst case scenario' plane B-B. All the models simulated in this analysis are based on plane B-B. The trim die profile (shown by black outline in figure 3-4) is obtained from this section.

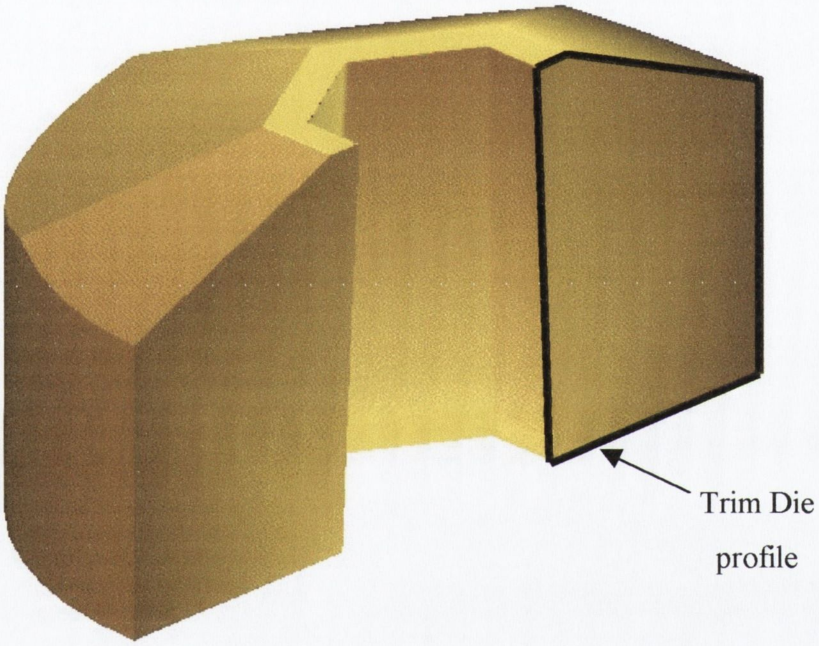

Figure 3-4: Worst Case Scenario section through the flats of the Trim Die

3.1.2.2 Axisymmetric FEA Models

The profile of the trim die, workpiece and top tool could now be entered into the FEA package. Figure 3-5, illustrates the profiles of the trim die, workpiece and top tool used in the initial tests in '94. The FEA models were considered as being axisymmetric. The centre line used as the point of rotation is shown in figure 3-5. Obviously, this assumption converts the hexagonal hole within the centre of the trim die to a circular one. The only way to overcome this is to model the entire process in 3D, but as already mentioned this is very time consuming. Figure 3-6 illustrates a 3D representation of the trim die profile, taken from figure 3-5, and rotated about the centre line. This is the shape that the FEA package assumes to be pushing into the workpiece, not one with a hexagonal hole. The experimental validation, detailed in section 3.2.4 on page 75, had to take this circular trim die into consideration.

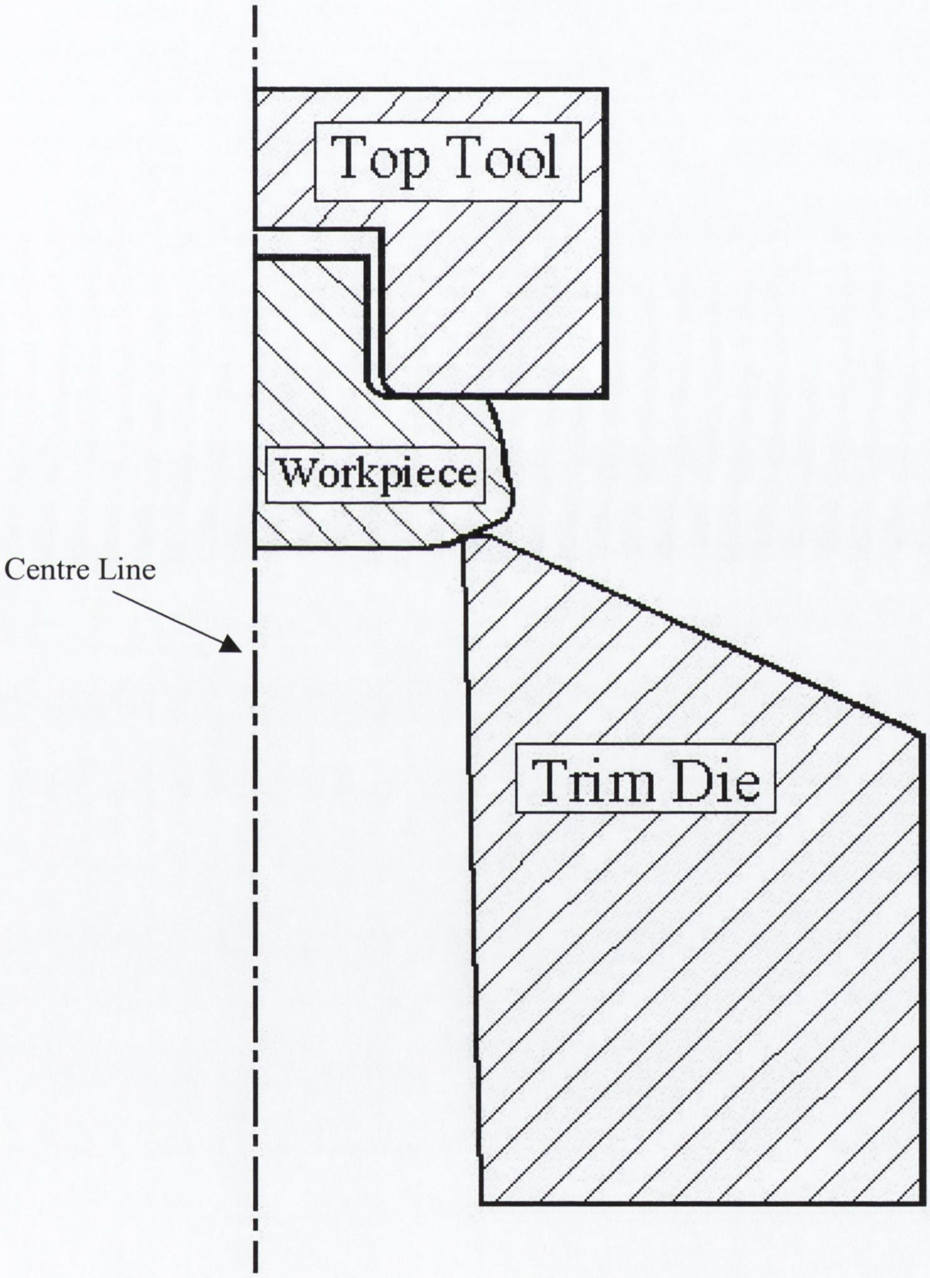

Figure 3-5: Initial Profile of Top Tool and Workpiece used in the FEA simulations

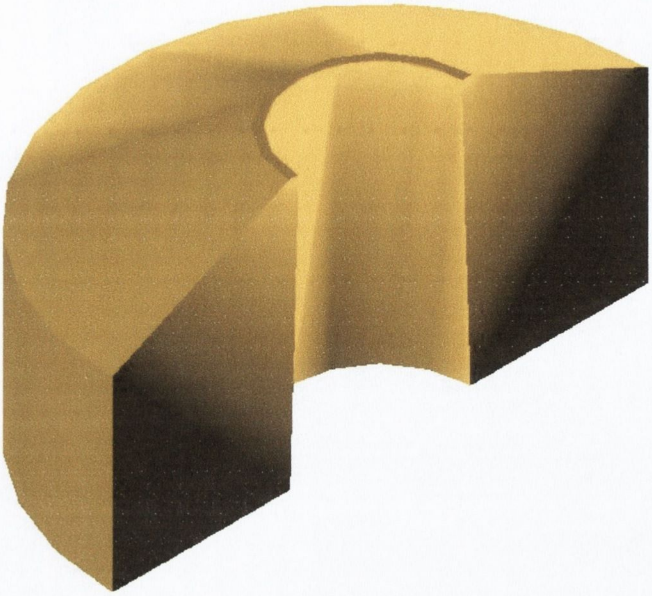

Figure 3-6: 3D representation of the 2D axisymmetric FEA model

3.1.2.3 Trim Die Profile

The trim die profile illustrated in figure 3-4 was further divided into two basic categories. These categories were called 'Fillet' and 'Compound' radii. The detail of a 0.1mm Fillet trim die profile is illustrated in figure 3-7.

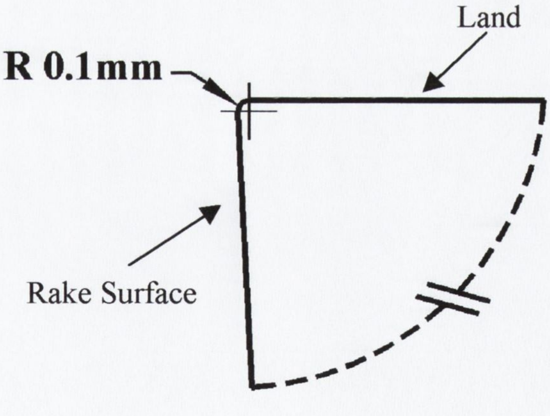

Figure 3-7: Corner Detail of a 0.1mm Fillet Trim Die Profile

The fillet radius of 0.1mm blends the top surface, known as the *Land*, and inner surface of the die, known as the rake. In the initial tests in '94 four fillet models were constructed with a blend radius ranging from 0.1mm to 0.4mm in steps of 0.1mm. The second category, Compound, is illustrated in figure 3-8, showing a 0.1mm compound trim die profile.

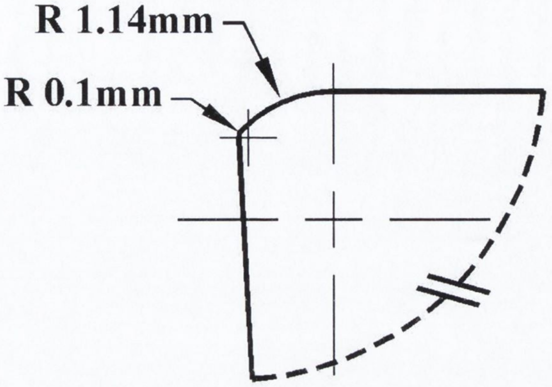

Figure 3-8: Corner Detail of a 0.1mm Compound Trim Die Profile

This category of die gets its name from the fact that the corner radius is composed of two radii, which are compounded together. The larger radius of 1.14mm, known as the Averbach Radius after its inventor, was held constant while the blend radius was varied to the following values 0.07, 0.1, 0.145, 0.2 and 0.25mm. Using these assumptions as a foundation, the initial FEA models were simulated in '94, and conclusions made as to the optimum corner profile [3]. But as seen in the next section, there were major limitations in the available software at that time to simulate such a forging process.

3.1.3 Initial Models

As explained in the introduction of the chapter, the earlier tests carried out in 1994 were used as a foundation to build upon. The flow chart in figure 3-1, illustrates this point. As mentioned previously, the investigation carried out in '94 utilised finite element analysis to study the effect corner geometry had on the induced stresses within the trim die. As mentioned in section 3.1.2.1, the 'worst case scenario' was adopted to make a two dimensional representation out of an inherently three-dimensional one. This 2D profile was further broken up into two basic categories and classified as *Fillet* and *Compound*. A total of nine models were constructed, four 'Fillet' and five 'Compound'. The finite element packages used to simulate the trimming process were FORM2D and ANSYS 5.0. Both of these packages had advantages and disadvantages.

3.1.3.1 FORM 2D v 2.1

FORM2D is a P.C. based program developed in Russia, capable of simulating the very large amount of plastic deformation that occurs during a bulk forging process. Unfortunately, FORM2D at that time was only capable of providing details of stress or strain distributions within the workpiece, but not within the tooling. Figure 3-9 shows a captured image taken from the earlier FORM2D work carried out in 1994. Effective strain contour lines within the workpiece are shown, but note no strain values within the trim die.

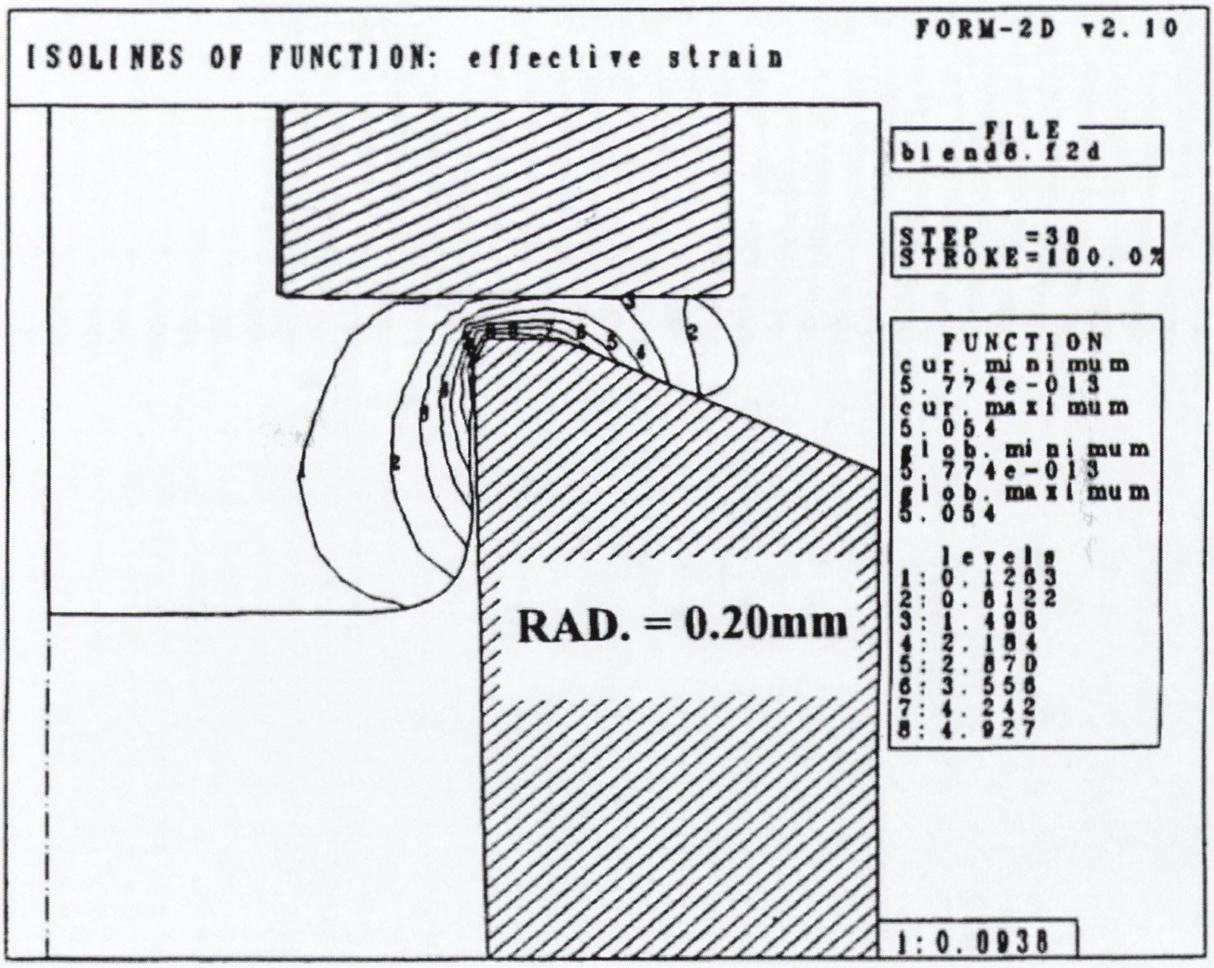

```
ISOLINES OF FUNCTION: effective strain
FORM-2D v2.10
FILE
blend6.f2d
STEP   =30
STROKE=100.0%
FUNCTION
cur.minimum
5.774e-013
cur.maximum
5.054
glob.minimum
5.774e-013
glob.maximum
5.054
levels
1:0.1263
2:0.8122
3:1.498
4:2.184
5:2.870
6:3.556
7:4.242
8:4.927
1:0.0938
```

Figure 3-9: Image taken from FORM 2D showing effective strain in the workpiece [3]

3.1.3.2 ANSYS 5.0

The FEA software ANSYS 5.0 on the other hand was capable of simultaneously calculating the stresses in both workpiece and trim die. Figure 3-10 illustrates a close-up view of the contact between the trim die and workpiece. The stress distribution within both the trim die and workpiece are displayed.

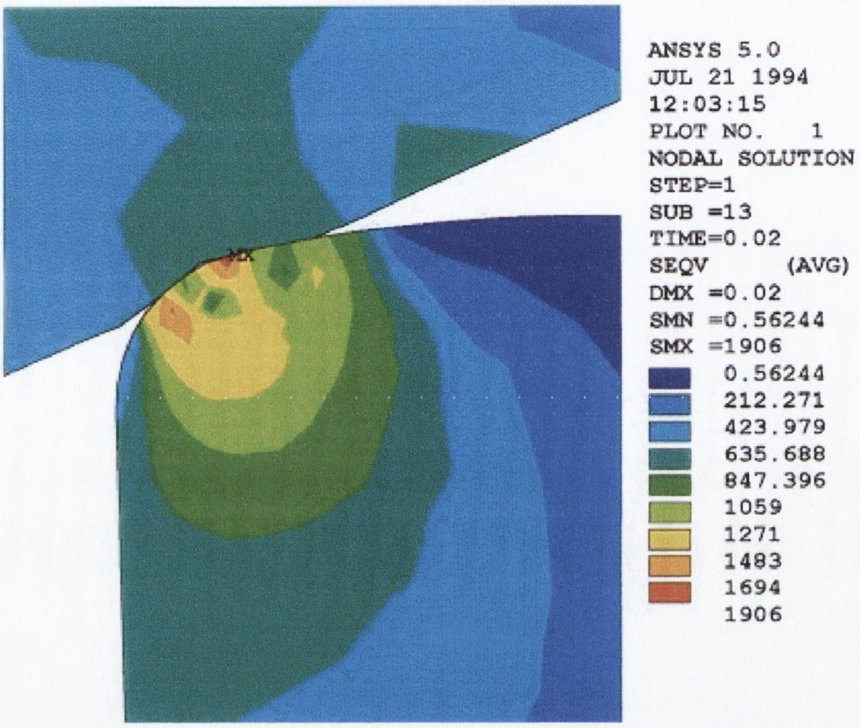

Figure 3-10: Effective Stress Contours in workpiece and trim die [3]

Unfortunately due to the large amount of plastic deformation occurring within the workpiece during the trimming, ANSYS was not capable of simulating the entire forging process. Figure 3-10 shows the maximum penetration (or stroke) of the trim into the workpiece that was possible to simulate at that time. The maximum penetration in the '94 ANSYS tests [22] was only 0.02mm when in fact the necessary penetration, or stroke of the trim die should be 3mm.

Although the amount of penetration into the workpiece was small, conclusions where made as to the optimum corner geometry [3]. It was obvious that until prediction of stresses in both the workpiece and trim die could be provided, throughout the entire forging process, a lot of unanswered questions would remain.

3.1.4 Phase 1: Updating the Initial Models

With the introduction of the elastoplastic finite element package, DEFORM, the tests carried out in 1994 were used as a foundation, from which a more advanced research programme was initiated. This was the starting point of the author's research program and hence designated *Phase 1*, see figure 3-1.

As mentioned in section 2.5.2 on page 36, DEFORM can simulate large plastic deformations due to its adaptive remeshing capabilities, while simultaneously calculating the necessary stress components in both workpiece and trim die. For this reason, all the finite element models presented in this report were simulated using DEFORM.

3.1.4.1 Modifications to the Top Tool Profile

By studying component drawings of the tooling used in industry, it became clear that the top tool used in the initial models did not accurately represent the actual configuration used in industry. Figure 3-11, illustrates the old and new top tool configuration.

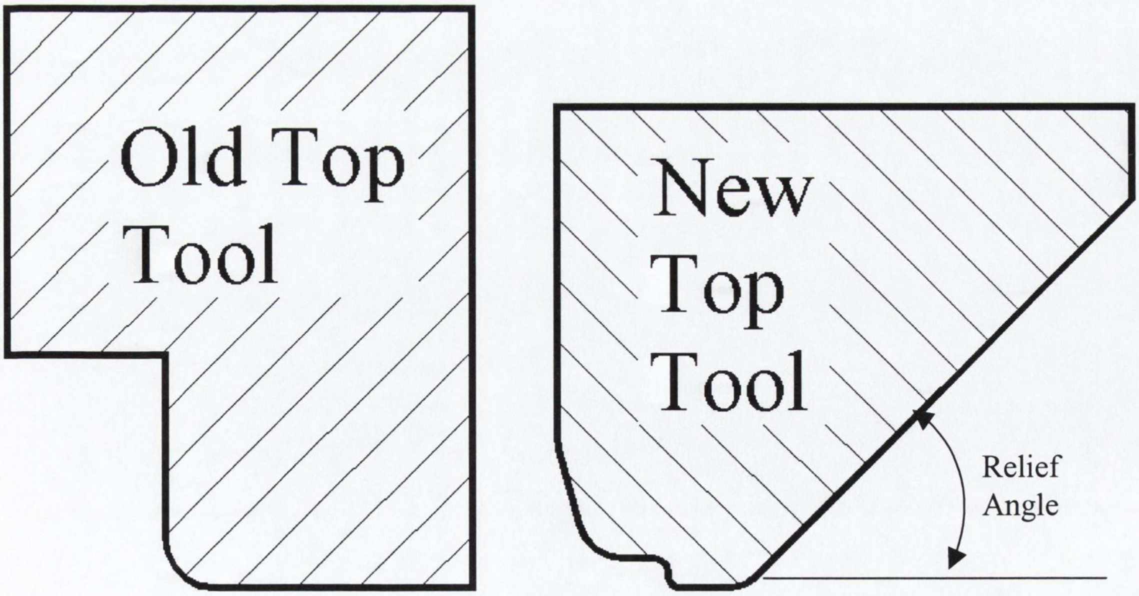

Figure 3-11: Old and New Top Tool Configurations

With reference to figure 3-11, the main difference between the old and new top tool configuration was the addition of a relief angle. The initial models did not have this relief angle and as a consequence, at the end of the trim die stroke, it caused a considerable amount of the workpiece material to become trapped, between the trim die and top tool, see figure 3-12.

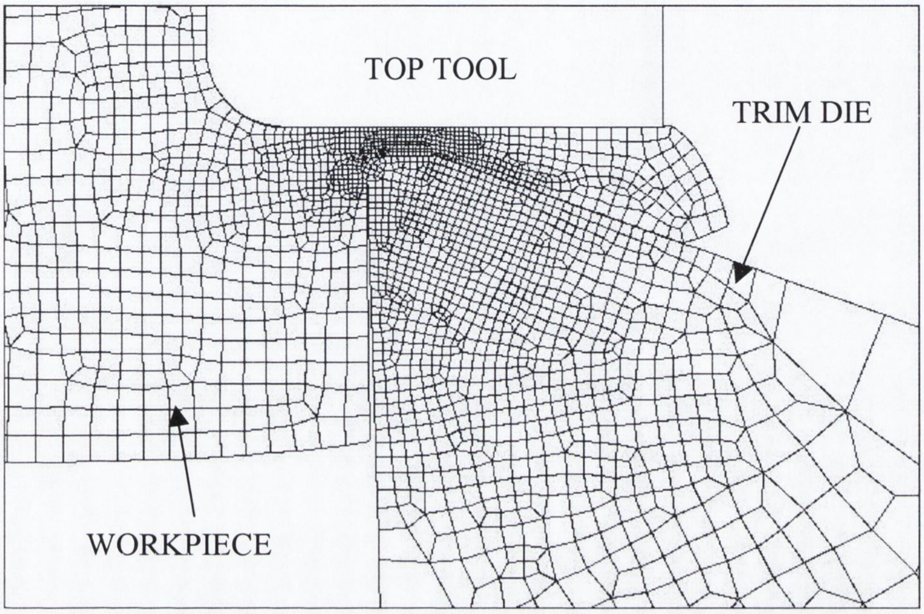

Figure 3-12: Trapped workpiece material at the end of the trim die stroke with the old top tool.

The new top tool allows the trimmed workpiece material to flow into the relief angle. Figure 3-13 illustrates this point.

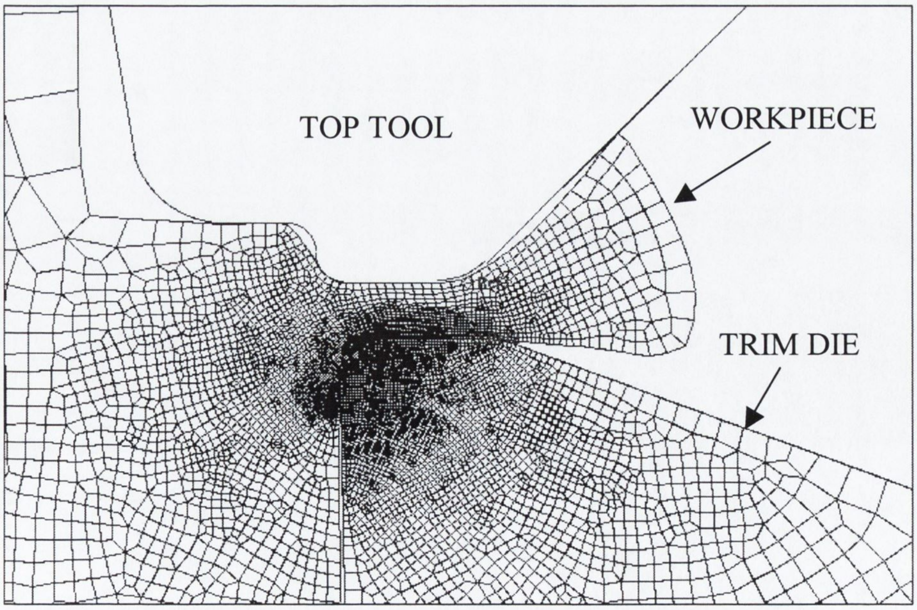

Figure 3-13: New Top Tool Configuration allowing the trimmed material to flow into the relief angle

3.1.4.2 Modifications to the workpiece Profile

To model the trimming process effectively, it was necessary to obtain an accurate measurement of the workpiece profile. To do this a series TM 300 Mitutoyo toolmakers microscope was used, see figure 3-14. To increase the edge definition when taking the measurements, the workpiece was machined in half using a Bridgeport milling machine, see figure 3-15.

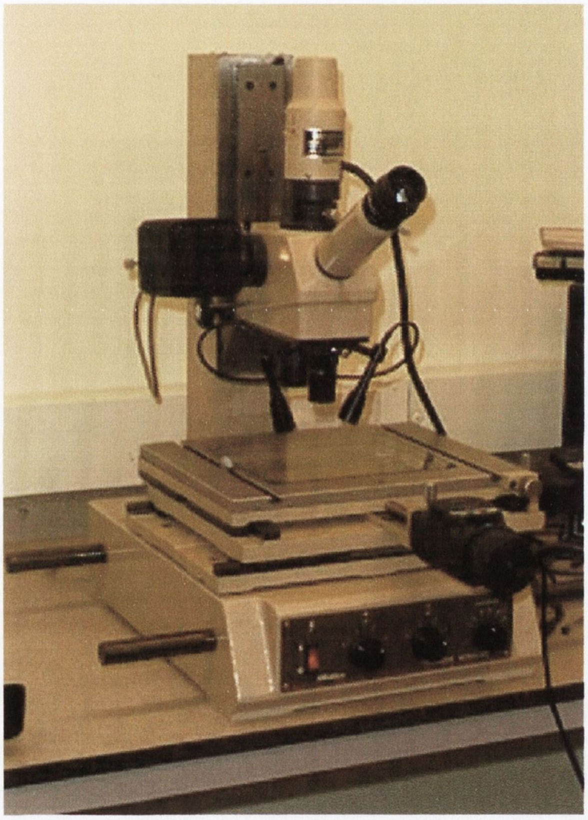

Figure 3-14: Mitutoyo Tool Makers Microscope

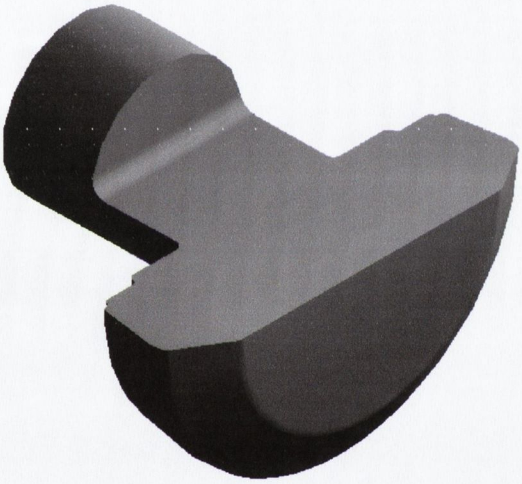

Figure 3-15: Milled Workpiece for edge definition

The old and new workpiece configurations are shown in figure 3-16.

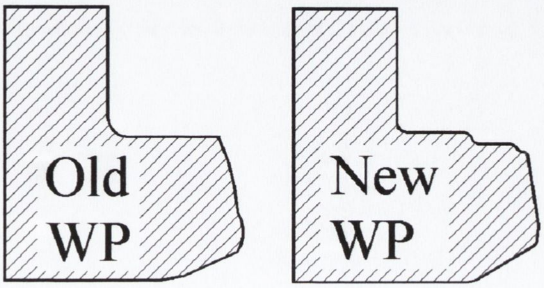

Figure 3-16: Old and New Workpiece (WP) Profiles

3.1.4.3 Modifications to the Trim Die Profile

The initial tests performed in '94 only considered the variation of the corner radius [3]. However the corner radius on the trim die is only one of a number of profile features whose influence was not yet known, therefore it was decided to increase the scope of the investigation to study the influence of modifying additional parameters of the trim die profile.

The trim die profile was divided into four main features, *corner radius*, *land width*, *petal and rake angle*, see figure 3-17.

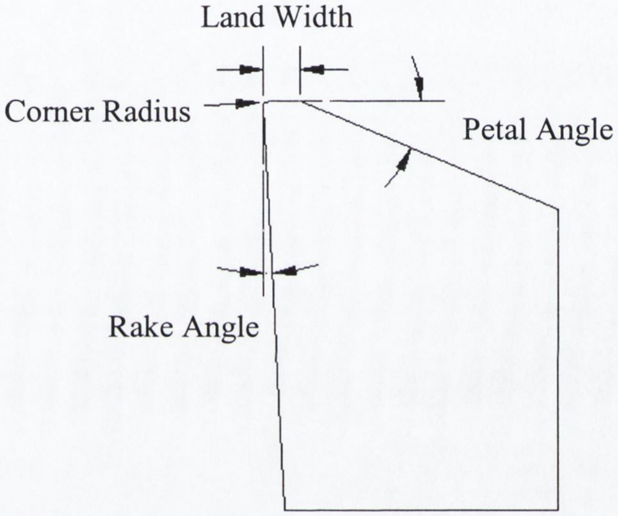

Figure 3-17: The Four main Features Of a Trim Die Profile

At this stage of the project, the role each feature played during the forging process was unclear. Each feature of the trim die profile had a range of possible values, see table 3-1.

FEATURE		VARIATION
CORNER RADIUS	FILLET	0.1, 0.2, 0.3 and 0.4mm
	COMPOUND	0.1, 0.15, 0.2 and 0.25mm
LAND WIDTH		0.2, 0.4, 0.6, 0.8, 1.0 and 1.5 mm
PETAL ANGLE		20°, 25°, 30°, 35°, 40° and 45°
RAKE ANGLE		1°, 1.5°, 2°, 2.5° and 3°

Table 3-1: Range of Variation for each Profile Feature

The addition of these new variables caused a problem because the possible number of trim die combinations then rose from 9 to 1620, see figure 3-18.

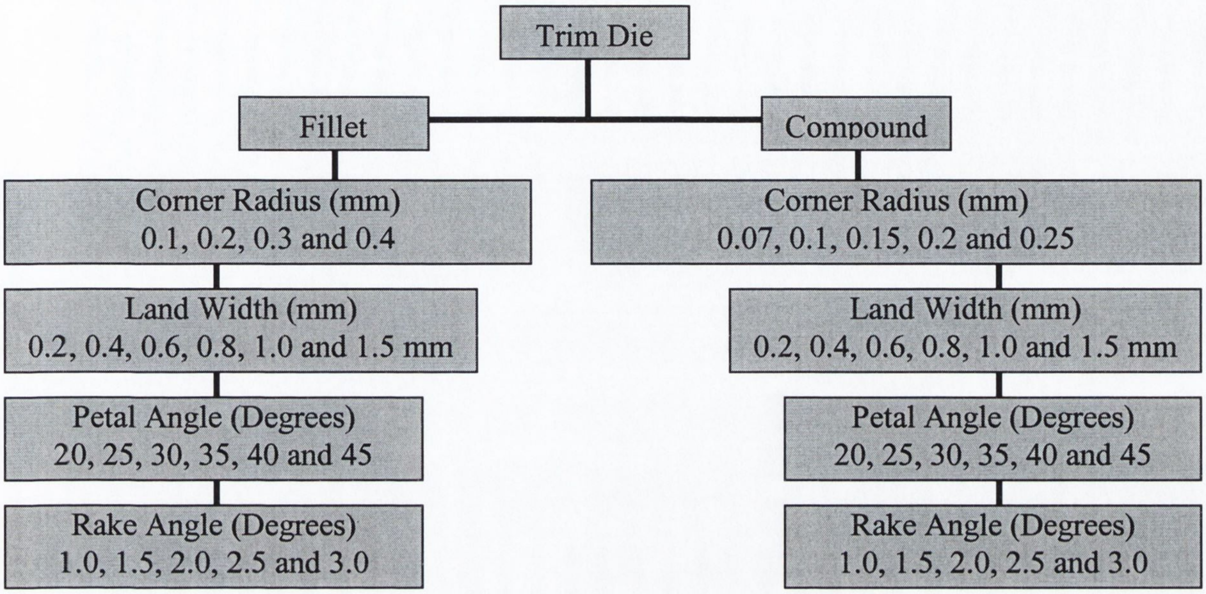

Figure 3-18: Flow Chart Showing All Possible 1080 Trim Die variations

Obviously running 1620 FEA simulations would not be practical due to computational constraints. Therefore in an attempt to reduce this large number of simulations a new approach called '*one-factor-at-a-time* ' was implemented.

This method consists of selecting a starting point for each factor, then successively varying each factor over its range while the other factors were held constant. With this one-factor-at-a-time method, twenty four trim die profile combinations were constructed. Graphs of effective stress versus stroke enabled the prediction of the 'near' optimum values for the land width, petal and rake angle.

Phase 1 provided a more in depth understanding of the forging process and gave an insight as to the influence each feature of the trim die profile had on the induced stresses.

Unfortunately there is a major disadvantage of the "one-factor-at-a-time" strategy and this is that it fails to consider any possible interaction between factors [69]. This issue of *interaction* needed further investigation and is discussed in Phase 2.

3.1.4.4 Material Input Data

Before an accurate model could be constructed, various material input data was necessary. To obtain this data compression tests where carried out on the M2 trim die material, to ascertain its flow stress properties, see Section 4.5.1 on page 184 for the results from these tests. The use of compression tests to obtain stress / strain data is the preferred method in FEA, and is favoured over tensile testing because it enables a greater level of strain to be subjected onto the test piece. Ring compression tests where also conducted to determine a coefficient of friction between the workpiece and trim die, see section 4.5.2 on page 185 for the results.

3.1.4.5 Boundary Conditions

Once the material data had been collected, and the geometric profiles of the workpiece, trim die and top tool had been entered into the FEA package DEFORM, boundary conditions needed closer examination.

As with all finite element simulations, the correct boundary conditions are essential in order to obtain accurate results. For all the models simulated within this thesis, the parameters listed in table 3-2 were maintained:

Object Name	Material	Object Type	Element No.	Remeshing Criteria	Velocity
Trim	M2	Elastoplastic	5,000	--	3 mm/second
Workpiece	SPS 0.9	Plastic	3,000	Every 5 Steps	--
Top Tool	--	Rigid	--	--	--

Table 3-2: Input parameters Held During All FEA Simulations

Rigid objects are modelled as non-deformable bodies. No boundary conditions are necessary for rigid objects. The workpiece was considered as a plastic object. The boundary conditions are illustrated in figure 3-19. The left hand boundary of the workpiece profile, see figure 3-19, was constrained to have zero velocity in the direction of the x-axis. This boundary lies on the centre line of the axisymmetric model. The boundary conditions for the trim die are shown in figure 3-20.

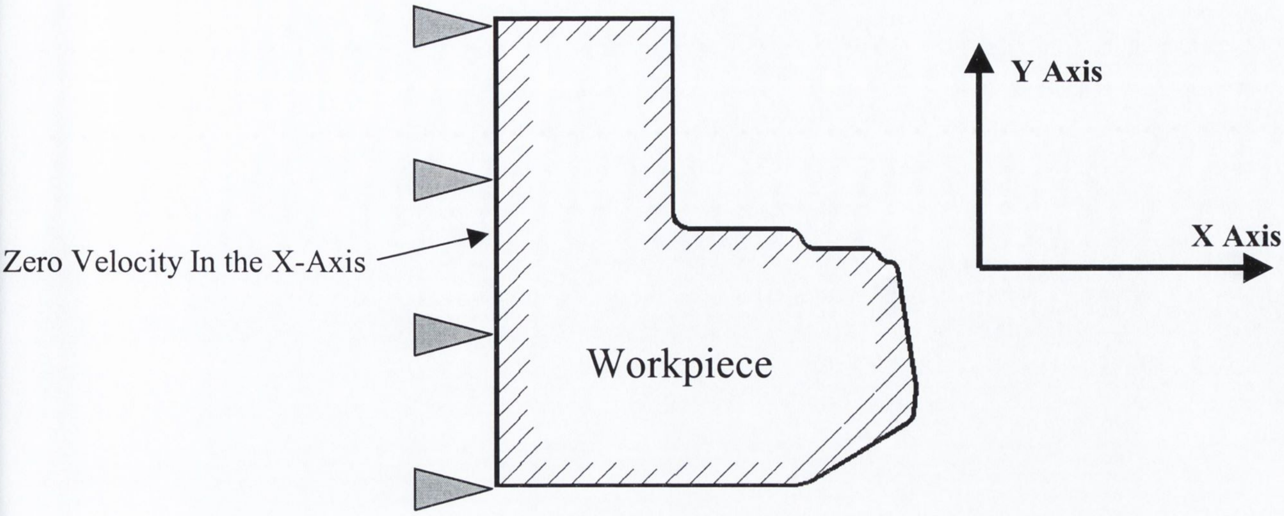

Figure 3-19: Workpiece Boundary Conditions

With Reference to figure 3-20, the right hand side of the trim die is constrained to have zero velocity in the direction of the x-axis.

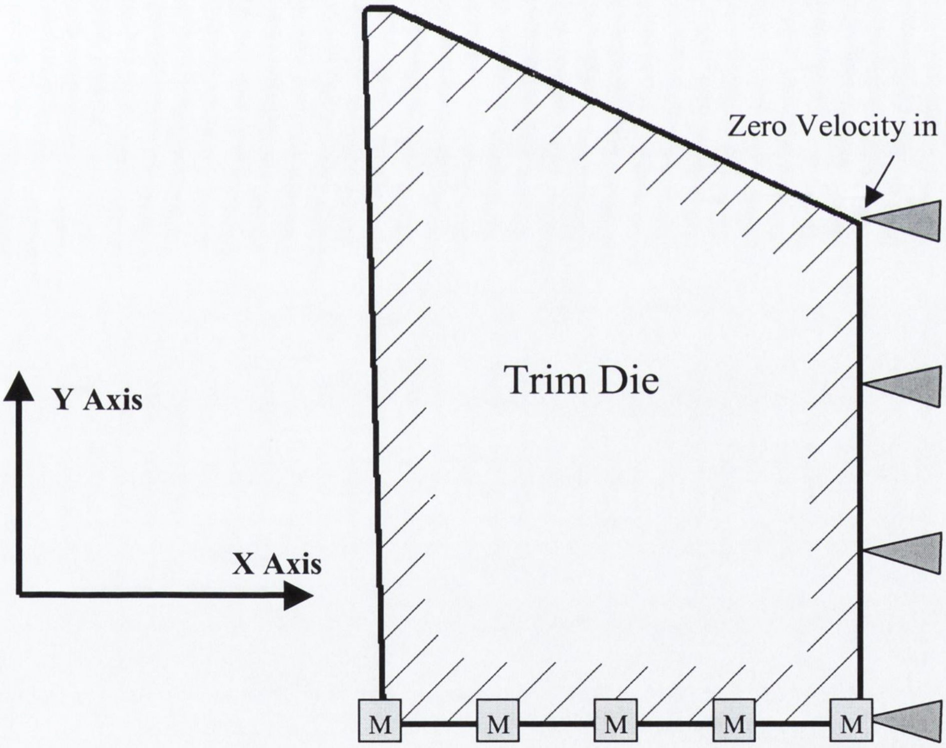

Figure 3-20: Trim Die Boundary Conditions

In DEFORM, in order to move a non-rigid object, it is necessary to specify movement boundary condition. These boundary conditions were applied to the base of the trim die, as shown in figure 3-20, and caused the trim die to move in the positive direction of the y-axis at a velocity of 3mm/sec to simulate the tool movement during the trimming operation.

3.1.5 Phase 2: Interaction

As mentioned in Section 3.1.4.3 on page 65, a 'one-factor-at-a-time' analysis does not account for interaction between parameters. The correct approach to dealing with several potentially interactive parameters is to conduct a factorial analysis [69]. Factorial analysis is an analytical strategy in which parameters are varied together instead of one at a time. A 'two by two' (2^2) factorial analysis was conducted, where two parameters are varied at two levels to analyse their influence. The two levels chosen were the extreme of those values listed in table 3-1,and are shown in table 3-3 below.

Parameter	VARIATION
FILLET CORNER RADIUS	0.1 and 0.4mm
LAND WIDTH	0.2 and 1.5mm
PETAL ANGLE	20° and 45°
RAKE ANGLE	1° and 3°

Table 3-3: Levels taken for two by two Factorial Analysis

A total of 24 models where constructed which enabled the corner radius to be compared against land width, petal and rake angle. The land width against petal and rake angle. And finally the petal angle against rake angle. These variations are listed in table 3-4 below.

Parameter	AGAINST
CORNER RADIUS	LAND WIDTH PETAL ANGLE RAKE ANGLE
LAND WIDTH	PETAL ANGLE RAKE ANGLE
PETAL ANGLE	RAKE ANGLE

Table 3-4 Comparisons for Two by Two Factorial Analysis

Once the models had been simulated, the maximum effective stress values occurring at the end of the trim die stroke were recorded and used to plot graphs comparing parameters as listed in table 3-4. From these graphs the effect of interaction between each feature was evident. By combining the conclusions from phase 1 and 2, the possible number of trim die profile combinations was reduced from 1620 to 9. Now that the optimum values for land width, petal and rake angle had been developed, these conclusions were combined to construct new models, which were simulated in phase 3.

3.1.6 Phase 3: The Final Trim Die Profile

To recall, Phase 1 was the author's first attempt to completely simulate the trimming process. The corner radius was altered between two categories, fillet and compound. The values of land width, petal and rake angle were varied one at a time. Phase 1 provided conclusions as to the effect of corner radius, land width, petal and rake angle. Phase 2 considered what interaction, if any, existed between the parameters analysed in phase 1.

In the Phase 3 analysis, two trim die profiles were modelled and compared. The first trim die profile, designated 'Optimum', was based on the conclusions deduced from Phase 1 and 2. During the course of the analysis in the Phase 1 and 2 tests, it was obvious that the land width had a large influence on the induced effective stress and tensile radial stresses within the trim die. For this reason, the second trim die analysed in Phase 3 was a new and previously unconsidered trim die profile, designated a 'Reverse Compound'. This new Reverse Compound trim die profile had the land width region replaced by a generous blend radius. The Phase 3 tests compared the 'Optimum' and 'Reverse Compound' trim die profiles. In conclusion, both models induced very low tensile radial stresses along the top surface of the trim die, hence improving its failure resistance. Also the new, and previously unconsidered, Reverse Compound trim die induced an effective stress approximately 15% lower than the 'Optimum' trim die.

3.1.7 Phase 4: 3D Analysis

The FE models simulated in Phases 1, 2 and 3, were considered as axisymmetric by utilising the 'worst case scenario' as outlined in Section 3.1.2.1 on page 53. This assumption assumes that the trim die has a circular internal hole as illustrated in figure 3-6 on page 57. Obviously, the only way to represent the hexagonal internal hole is by using 3D analysis. Phase 4, outlines the 3D models, the difficulties with running such a complex forging sequence, and the initial results.

3.2 Experimental Tests

3.2.1 Compression Tests

The accuracy of FEA simulations of metal flow, and of forming process in general, is largely governed by the accuracy with which the actual material flow stress under forming conditions can be modelled. A major problem encountered in the use of finite element analysis of metal forming processes is the determination of correct values for the material flow stress. In Part 3 of this thesis, relating to the work programme, table 3-2 on page 66, explains that the trim die was modelled as elastoplastic. Considering the trim die as elastoplastic allows for plastic deformation within the tooling if the stress levels are sufficiently high. Obviously, if the trim die deforms plastically, failure would have occurred in the real component. DEFORM requires stress/strain data for any material in order to simulate its elastoplastic properties. With this in mind compression tests where conducted to ascertain the stress/strain data for the trim die material, AISI M2.

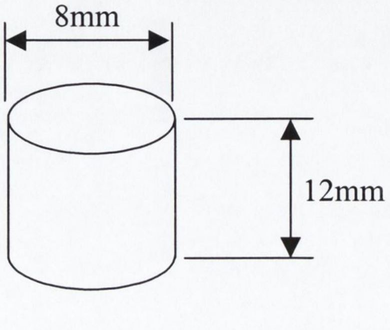

Figure 3-21: Dimensions of the M2 specimen for the compression tests

The tests where conducted in accordance with the ASTM standard E 9 – 89a$^{\varepsilon 1}$ “compression testing of metallic materials at room temperature” [70]. A L/D ratio (length/diameter) of 1.5 was employed for the test samples, see figure 3-21 on the previous page. The compression tests were conducted on an INSTRON 1196 universal testing machine. The specimens were compressed between two hardened anvils with PTFE tape attached between the test specimen and the hardened anvils to ensure homogeneous deformation. The movement of the crosshead and the subsequent increase in load on the Instron was controlled with the aid of Instron series 9 software. A micrometer, accurate to 0.01mm, was used to measure the reduction in height of the specimen. The reduction in height and subsequent load are used to calculate the stress/strain data, see Section 4.5.1 on page 184 for compression test results.

3.2.2 Ring Compression Tests

Lubricity, as defined by the friction factor (m), is most commonly measured using the Ring Compression Test [41]. However due to an unforeseen difficulty in conducting the ring compression tests, spurious results were obtained. The ring compression test procedure is detailed in Appendix C on page 234, while an explanation of the spurious results obtained are outlined in Section 4.5.2 on page 185.

3.2.3 Fatigue Tests

Four point bending tests where conducted to ascertain the fatigue limit of the trim die material. As detailed earlier in Section 2.3.4 on page 18, coatings can have a detrimental effect in relation to the fatigue properties of dies. A standard trim die leaves the factory with a three-layer coating consisting of titanium carbide, titanium carbonitride and titanium nitride, see Section 2.3.3 on page 17, it was therefore necessary to conduct fatigue tests on coated and uncoated specimens to study the effect that coatings had on the fatigue properties of AISI M2. The fatigue specimens where machined from round stock using a

Bridgeport milling machine. The finished dimensions of the fatigue specimen had a rectangular cross section of 10 x 20mm and a length of 135mm.

The dimensions of the fatigue test pieces following milling were oversize by 0.5mm on each surface and the finished dimensions were obtained by grinding. Due to the thermal loading on the specimen during the machining process, stress relieving was necessary. The grinding parameters applied to the specimen were identical to those used on the trim die surface. The coating, heat treatment and tempering cycle as detailed in Section 2.2 on page 6, was then applied to the specimens so that they matched as closely as possible the actual trim dies. As mentioned in Section 2.4.3.3 on page 31, fatigue results can be presented using the stress-life or S-N approach.

Figure 3-22 shows the four-point bending test rig, with a coated M2 specimen in position. The four-point bending test rig was then placed into a series 8801 INSTRON Universal Testing Machine, which is rated to ± 100KN. With respect to figure 3-22 below, it can be seen that the test rig is comprised of two parts. The top part of the rig is connected to the load cell of the INSTRON, while the bottom part is attached to the hydraulic ram, which induces the cyclic displacement.

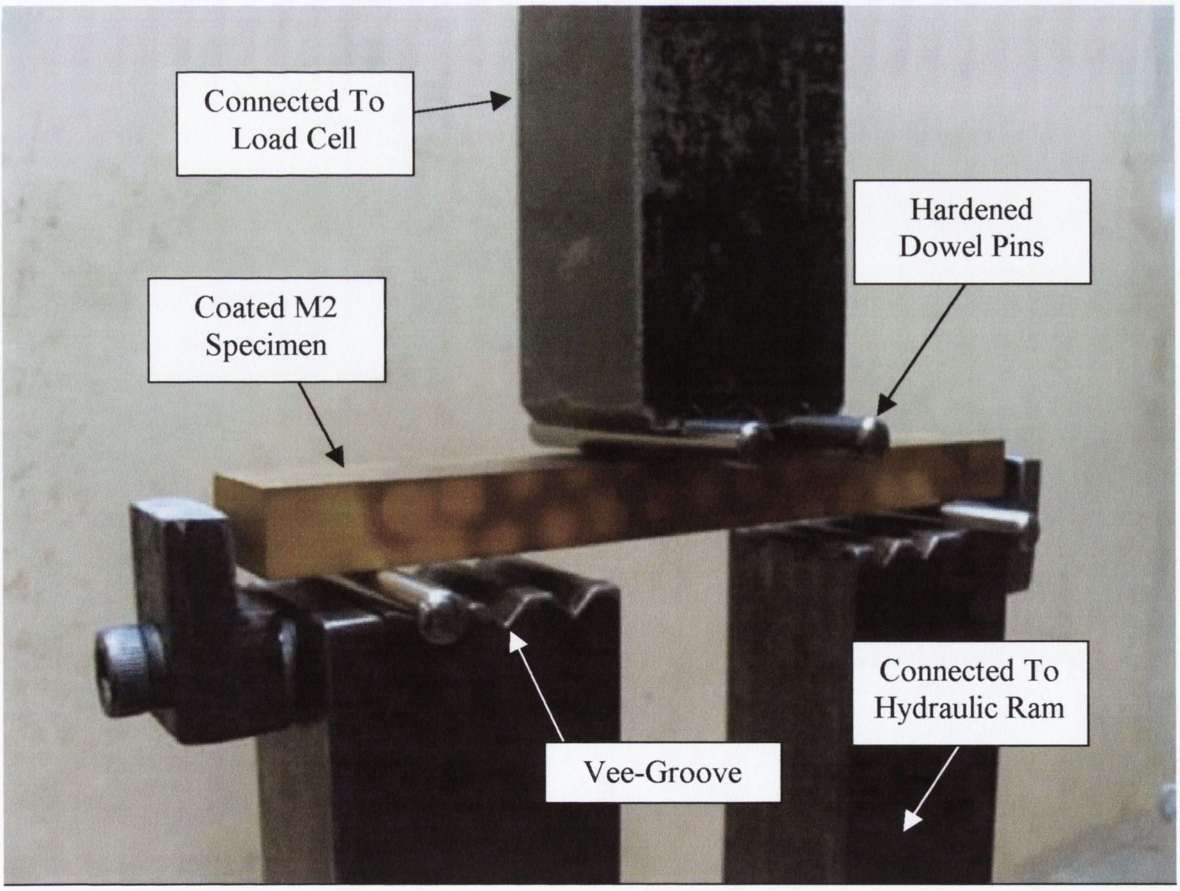

Figure 3-22: Initial Four Point Fatigue Bending Rig

The hardened dowel pins were glued into the vee-grooves to prevent sliding during the test. However after numerous fatigue tests the cleaning off of the excess glue caused the dimensions of the machined vee-grooves to change. The change in the vee-groove dimensions resulted in a misalignment of the dowel pins and caused the top and bottom halves of the test rig to rotate independently. This independent rotation caused multiaxial stress states within the test sample and rendered the results useless

To counteract this problem a new fatigue testing rig was designed. Figure 3-23 below shows the new test rig in operation. Figure 3-23 illustrates that due to the addition of two guide rods on either side of the specimen, no rotation between the top and bottom part of the test rig can take place. Now that the rig had been produced, the fatigue testing began. For all the tests conducted in this project, the frequency of loading was held constant at 10 hertz, while the stress ratio (R), which is given by the ratio of the minimum stress to the maximum stress, was held at 0.1. The results from these fatigue tests are detailed in Section 4.5.4.4 on page 215.

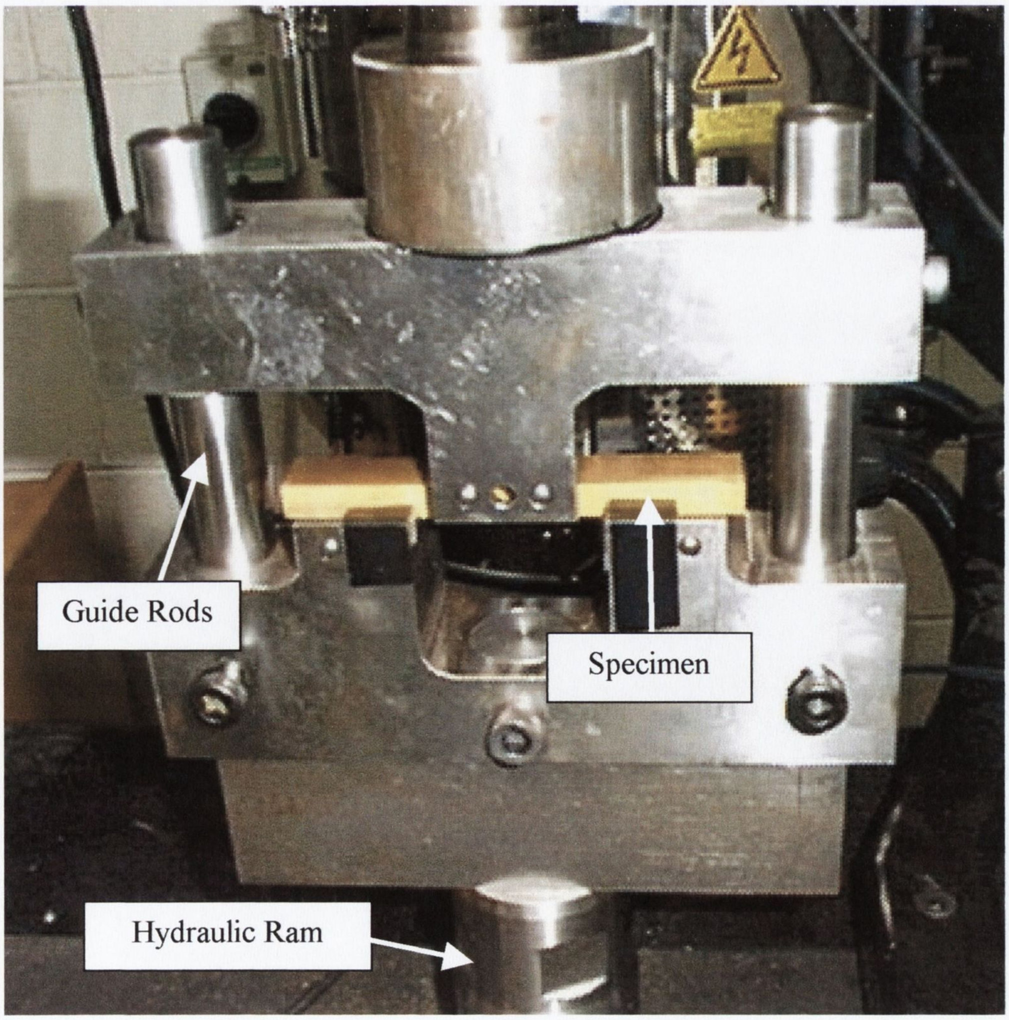

Figure 3-23: New Four Point Fatigue Bending Rig

3.2.4 Experimental Validation

3.2.4.1 Forging Load Tests

As with all finite element analysis, experimental validation is useful if not essential. The trimming process is of no exception. Due to difficulties of obtaining access to the trimming machines on the factory floor, it was decided to reproduce the forging operation within the college laboratory.

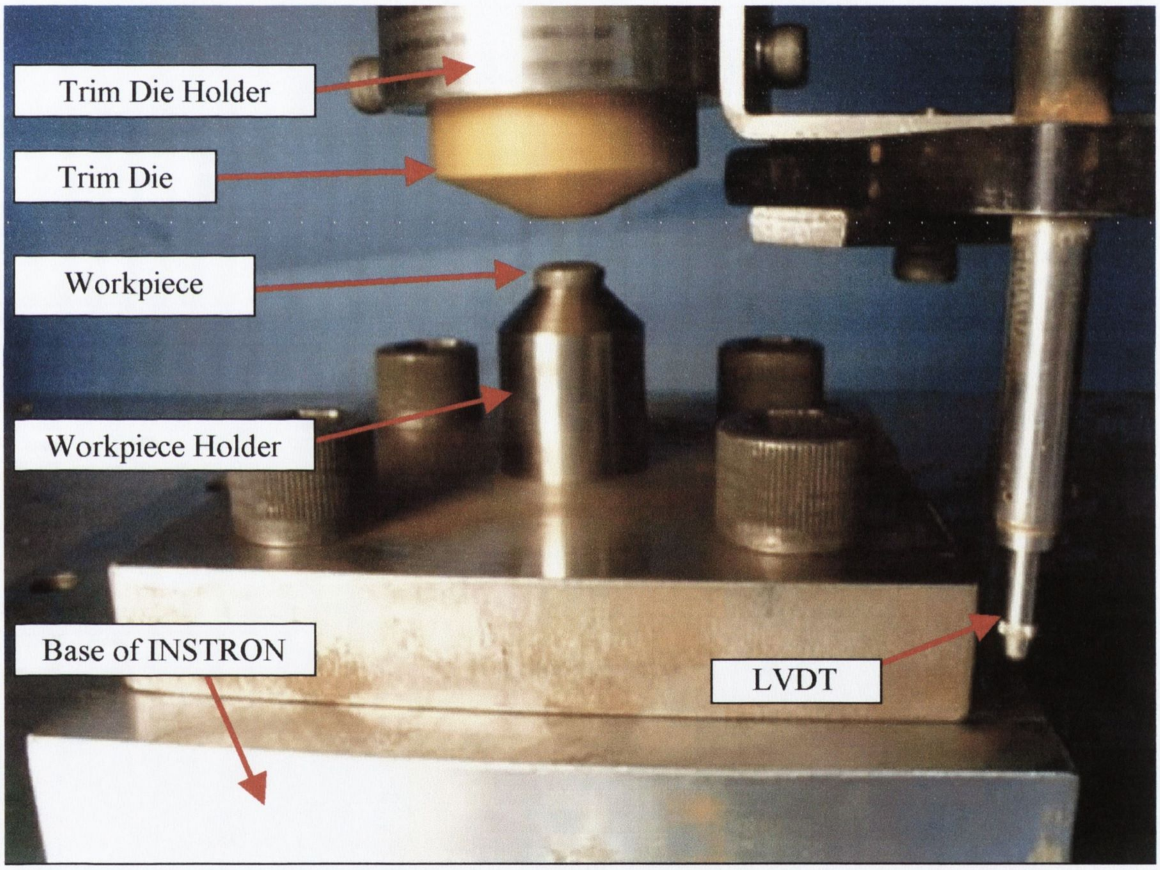

Figure 3-24: Test rig for the experimental measurement of load and stroke

Figure 3-24 shows the main features of the test rig, constructed by the author for these tests. The test rig was designed to fit into a series 1196 INSTRON universal testing machine. The workpiece holder was bolted to the base of the Instron while the trim die holder screwed into the moveable crosshead. The workpiece, known as the 'cheese head', due to its shape (see figure 3-25) was positioned into the workpiece holder. The crosshead of the Instron was instructed to move downwards at constant velocity for a predetermined stroke, at which point a limit switch was triggered, which stopped the machine. The Instron was capable of measuring the necessary load to forge the head on the fastener, along with the displacement of the crosshead.

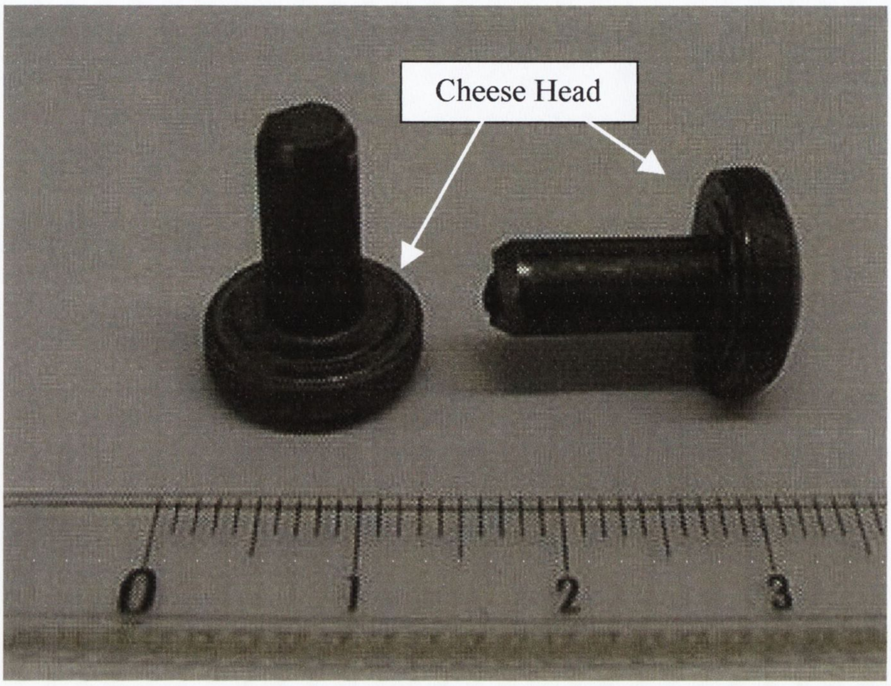

Figure 3-25: Workpiece (Cheese Head) dimensions (mm)

The initial load versus displacement (or stroke) graphs did not replicate the theoretical curves obtained from FEA very well. These graphs are displayed in Section 4.5.3 on page 187. After much deliberation, it was discovered that the discrepancy between the experimental and the FEA/theoretical load/stroke curves was caused by deflection of the crosshead. The Instron did not account for this deflection. To overcome this, a Linear-Variable Differential Transformer (LVDT) was utilised. The principal operation of an LVDT is essentially two small transformers sharing the same magnetic core. As the core moves the output of one increases while the other decreases. The 'out of balance' current is a measure of the core position and therefore displacement. This device was then mounted directly onto the trim die holder.

Once the displacement/stroke had been corrected, a very good correlation was obtained between experimental and theoretical forging loads. This knowledge was used as a ‘foundation’ to anchor the FEA stress results.

3.2.5 Failure Investigation

As mentioned in the objectives of this thesis, the main reason for discarding a trim die on the factory floor is cracking or chipping. For this reason, a failure investigation was carried out in an effort to understand the main factors influencing die failure.

Firstly the M2 trim die material was sectioned and mounted for analysis using both Light and Scanning Electron microscopy. Due to the high hardness of the trim die material, 60-62HRc, a Metaserv cut-off machine, with an abrasive wheel attached, was used to cut the trim die into more manageable pieces. Unfortunately this process induces high temperatures within the material. These high temperatures could alter the configuration of the cut surface, therefore an additional cutting process was necessary to remove this possible heat affected zone. A Labcut, series 1010, mounted with a diamond coated cutting wheel was used to remove the heat-affected zone. Once the specimen was cut to a suitable size it was mounted. The mounting material was 'EPO-Mount' and it is basically a hot mounting epoxy resin. The epoxy resin was used in preference to a conductive phenolic mounting resin as the epoxy gives better edge retention. This edge retention becomes more important when high magnification images are required of the coating along the edge of the specimen. Finally, the mounted M2 was polished using a 'Jean Wirtz' Phoenix 4000 polishing machine. The recommended abrasive paper, rotational speed, pressure and direction of rotation where specified in the Buehler dialog reference manual [71]. Some of the mounted samples were etched to expose the carbides within the M2 microstructure. The etchant most widely used for tool steel is 2 to 5% nital. High-speed steels require a 5% concentration [72]. The etching is performed by immersion. Etching times are difficult to generalise, because of the wide range of tool steel compositions and because heat treatment can markedly alter etch response [72]. For this reason, the final etching time of one minute was obtained by trial and error.

The failed trim dies could be divided up into two categories. The first category was a collection of trim dies, that had failed due to a 'misfeed'. When the bolt making machine is running at full speed, if a situation arises where there is no workpiece present, the momentum of the ram which drives the trim die, causes the trim die and top tool to make contact. The footprint of the top tool is hexagonal, therefore when the two collide, a hexagonal impression (called a witness mark) remains on the land surface of the trim die. Failed trim dies, which had this witness mark, were sectioned, mounted, polished and etched as previously detailed. With the use of a scanning electron microscope (SEM) and a light microscope, the crack detail was clearly visible. The cracks obtained from these dies are detailed in Section 4.5.4.1 on page 191. A finite element model, which simulated the occurrence of a misfeed, highlighted the mechanism for the formation of the cracks observed in the trim dies, see page 193.

The second category of failed trim dies had failed due to the occurrence of severe chipping on the centre of the flats of the hexagon within the trim die, but no witness mark was evident. Again these failed trim dies were prepared in the same manner as the trim dies in the first category, and the crack patterns obtained using the same microscopy techniques outlined previously. The crack patterns produced from this second category were very different from the first. It was from these crack patterns in the second category, that led to the conclusion that fatigue loading was having an effect on the life of the trim die. See Section 4.5.4.2 on page 194, for details from the failure investigation.

3.2.6 Surface Topography

As outlined in Section 2.2.4 on page 12, the heat treatment cycle is applied to the trim dies after the coating is applied. To investigate any possible effect that the heat treatment cycle might have on the surface topography of the coatings, a trim die was coated and sectioned in half. One half of the trim die received the heat treatment cycle, while the other half did not. Using an SEM, large differences in the surface composition were recorded along with severe surface cracking on the post heat treatment trim die. Details of the images taken are listed in Section 4.5.4.3 on page 208. Both halves of the trim die were then placed into a series 100 Zygo white light profilometer. The Zygo machine uses phase shift interferometer to measure surface roughness. This machine is capable of accurately measuring surface profiles. The results from these tests provided evidence of the severe changes within the coating after the heat treatment cycle. These changes can be attributed to either the effects of residual stress that arise due to a thermal mismatch between the substrate and the coating or by the rapid quenching, see Section 4.5.4.3 page 208.

The investigation into the adverse effects of the use of coatings, indicated that it is possible to have cracks present along the surface of the coating before the trim die forges its first fastener. These cracks have been seen to propagate through the coating and into the substrate, see Section 4.5.4.3 on page 208. If these coating cracks are present, they tend to remain 'dormant' unless subjected to a threshold level of tensile stress. It is for this reason that the maximum tensile radial stress component is also considered within FEA results, Section 4 on page 79.

Part IV.

4 Finite Element and Experimental results

This chapter will explain in detail the results obtained from the various 'Phases' of the work programme outlined in the previous chapter. A flow chart of this work programme was given in section 3.1.1 on page 51.

4.1 Phase 1: Updating The Initial Models

The research carried out in 1994 [3] was used as a foundation to build upon. The profile of the workpiece and top tool, for the current work presented in this thesis were modified to accurately represent the actual profiles used in industry, see Sections 3.1.4.1 and 3.1.4.2 on pages 62 and 64 respectively.

In Phase 1, FEA models were constructed and analysed to study what effect of:

- Fillet corner geometry
- Compound corner geometry
- Land Width
- Petal Angle
- Rake Angle

For each set of FEA models listed above, a strategy called 'one-factor-at-a-time' was implemented [69]. As the name suggests, only one factor or parameter, was varied at any one time, while the others remained constant. In the case of the first set of FEA models, used to study the effect of 'Fillet' corner geometry, only the corner radius was altered while the land width, petal and rake angle remained constant. Table 4-1, lists the values of the fillet corner radii used along with those for the fixed parameters.

All the FEA models simulated for this thesis were triggered to stop once a critical distance between the trim die and top tool had been reached. Figure 4-1 shows the configuration of the trim die, workpiece and top tool at the start of the simulation. 'Ref 1' refers to a user defined location on the trim die profile, while 'Ref 2' corresponds to a point on the top tool profile. Once the material properties, boundary and movement conditions were applied to the objects as outlined in section 3.1.4, DEFORM was instructed to end the simulation when the distance between Ref 1 and Ref 2 reached a value of 0.25mm in the y-axis. Due to a feature of the trim die profile, varying the corner radius had an effect on how far the trim die travelled. As a result, trim dies with smaller corner radii needed to travel further than the trim dies with larger corner radii to achieve a final stopping distance of 0.25mm. This can be seen in the following Sections 4.1.1 and 4.1.2 when the effective stress results are plotted against the trim die stroke. This effect is explained in greater detail in Appendix D on page 238.

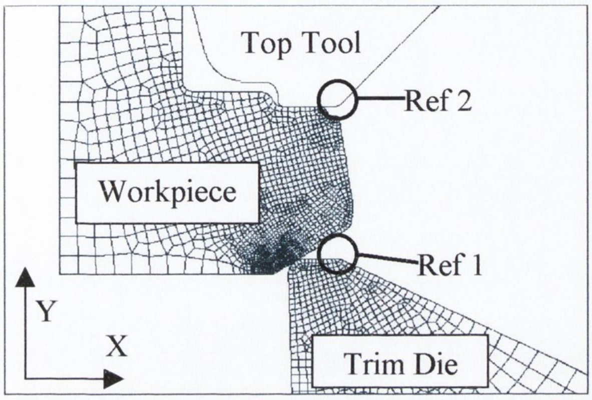

Figure 4-1: FEA Model showing Ref 2 and Ref 3

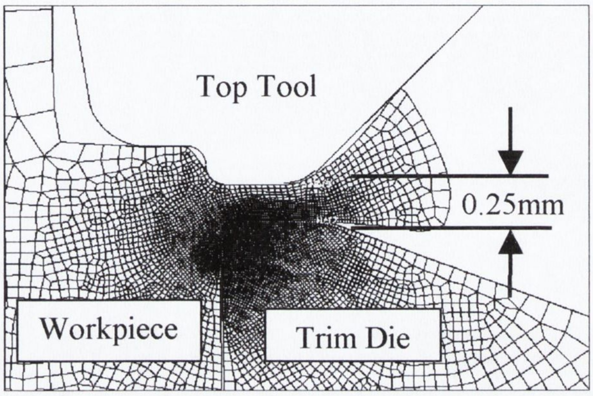

Figure 4-2: Final Stopping Distance = 0.25mm

From an analysis of the graphs of effective stress versus trim die stroke, it became apparent that there were three distinct areas to the curve. Figure 4-3 illustrates a typical max effective stress versus trim die stroke graph, showing the three areas of interest. The stresses highlighted in figure 4-3 are induced within the trim die during the trimming operation.

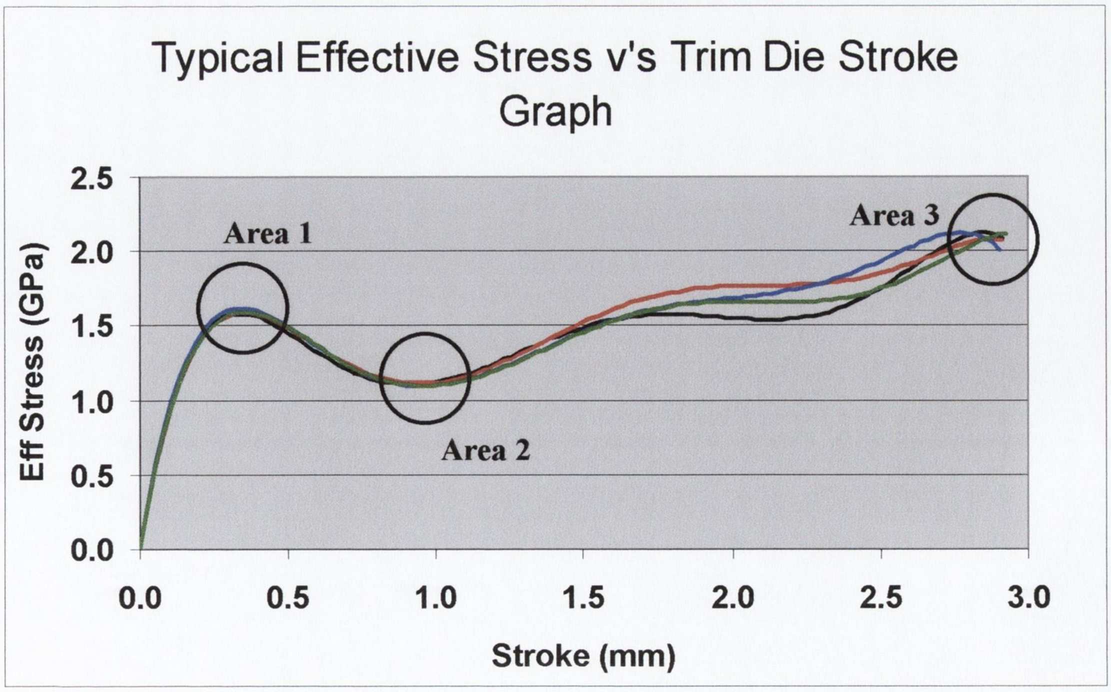

Figure 4-3: Three Main Areas Of Interest Within The Trim Die Stroke

Area 1, 2 and 3 relate to trim die strokes of 0.3, 1.0 and 3.0 mm respectively. The maximum effective stress and maximum tensile radial stress at each of these three trim die strokes will now be presented.

4.1.1 The Effect of Fillet Corner Geometry

As mentioned in section 3.1.2.3, the corner region of the trim die profile was divided into two categories 'Fillet' and 'Compound'. This section will now detail the FEA results obtained from trim dies having a 'Fillet' corner geometry.

Table 4-1, lists the variation in fillet corner radii simulated along with the fixed values of land width, petal and rake angles.

Parameter	Value
Corner Radius ('Fillet')	0.1, 0.2, 0.3, 0.4mm
Land Width	1.5mm (Fixed)
Petal Angle	45° (Fixed)
Rake Angle	3° (Fixed)

Table 4-1: Variation in 'Fillet' Corner Radii for the Phase 1 analysis

4.1.1.1 Effective Stress Within The Trim Die

Area 1: Trim Die Stroke = 0.3mm

Figure 4-4 illustrates a graph of effective stress, measured in Giga Pascals (GPa), versus trim die stroke, measured in millimetres. The range of trim die stroke is displayed on the x-axis of the graph, which has been modified to 'zoom-in' on the first area of interest, Area 1 see figure 4-3. The trim die with the smallest 'Fillet' corner radius of 0.1mm, shown in black, induced the greatest level of effective stress at this point.

The results presented in table 4-2 show the effect of increasing the fillet corner radius on the induced effective stress at Area 1. At this stroke of 0.3mm, increasing the radius from 0.1mm to 0.4mm causes a decrease in the level of effective stress from 1.996 GPa to 1.634GPa, which is a reduction of 17%. Because there is a linear relationship between the induced effective stresses and the value of the corner radius, only the 0.1mm and 0.4mm 'Fillet' FEA models are shown in figures 4-5 and 4-6 respectively. The maximum effective stress induced within the trim die is highlighted at the bottom of each figure.

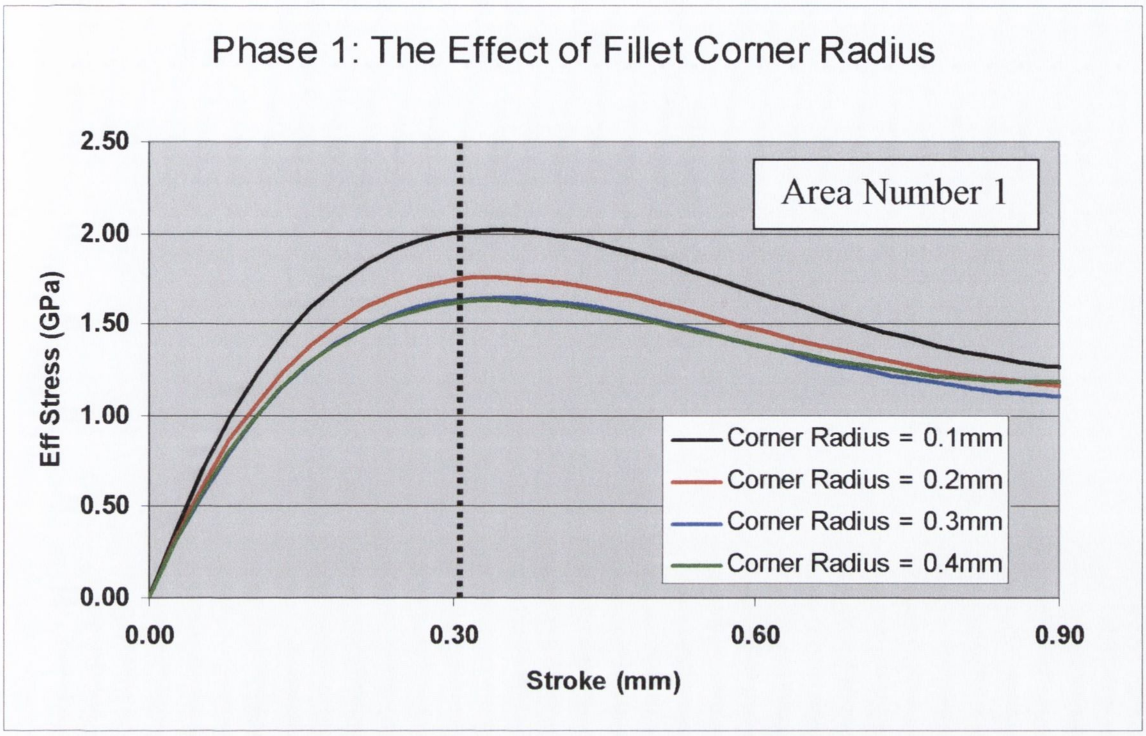

Figure 4-4: Effective Stress vs. Stroke for all 4 Fillet models, stroke range 0-0.9 mm

'Fillet' Corner Radii (mm)	Induced Effective Stress (GPa)
0.1	1.996
0.2	1.754
0.3	1.652
0.4	1.634

Table 4-2: The Effect of Increasing the 'Fillet' Corner Radius at a Stroke of 0.3mm

The area in contact between the workpiece and trim die is illustrated in figures 4.5-4.6 by a yellow line around the die corner. Comparing figure 4-5 with figures 4.6, which corresponds to a 0.1mm and the 0.4mm fillet corner radius, the change in contact area between the trim die and workpiece is observed. At the onset of yielding of the workpiece material, the amount of contact between the trim die and workpiece is directly proportional to the corner radius. When the corner radius is small, so too is the area of contact. For this reason, reducing the corner radius, reduces the contact area thereby causing an increase in the induced stress within the trim die, hence producing the results displayed in table 4-2. Once this stroke of 0.3mm is passed, all four models show a reduction in the level of stress.

This initial high level of stress at a stroke of 0.3mm corresponds to the workpiece material yielding and starting to flow plastically.

Figure 4-4 and table 4-2 plot the maximum effective stress values. Where these stresses act and how they are distributed is important. With reference to figures 4-5 to 4-6, the locations of the maximum values listed in table 4-2 are highlighted by the small square symbol. In all four models at this stroke, the location of the maximum effective stress is within the body of the trim die and not along the contact surface between the trim die and workpiece.

Figure 4-4 and table 4-2 show that the 0.1mm trim die (black line) induced the highest level of effective stress at this stroke of 0.3mm. With reference to figures 4-5 to 4-6, the areas over which the high stresses are distributed are highlighted. Figure 4-5 illustrates that these high stress levels are distributed over a smaller area than the 0.4mm corner radius model, figure 4-6.

While having a small corner radius makes the trim die more efficient in shearing the workpiece material compared to the larger radius, there is a smaller area of contact between the workpiece and trim die, and subsequently higher stresses are induced within the trim die. Reducing the corner radius also weakens the trim die, just as in the case of a cutting tool.

By considering figure 4-4 and table 4-2 it could be concluded that increasing the corner radius to 0.5mm or 0.6mm might further reduce the induced effective stresses within the trim die. However, when the corner radius is increased to a value greater than 0.4mm the finished quality of the bolt head is reduced, as it tends to produce a bur under the shoulder of the bolt. For some applications the addition of a bur would not have any real consequences, however in high precision applications, tight quality control prevents this type of defect and therefore limits the maximum possible corner radius to 0.4mm.

The yield stress of the trim die material M2 is 2.5GPa. Figure 4-4 clearly shows that the smaller the corner radius, the closer the induced stresses approach this yield stress value. On this basis the 0.4mm corner radius trim die was considered as being the optimum, for Area 1, because it induced the lowest maximum effective stress and it distributed these stresses over the greatest area in comparison to the other three models.

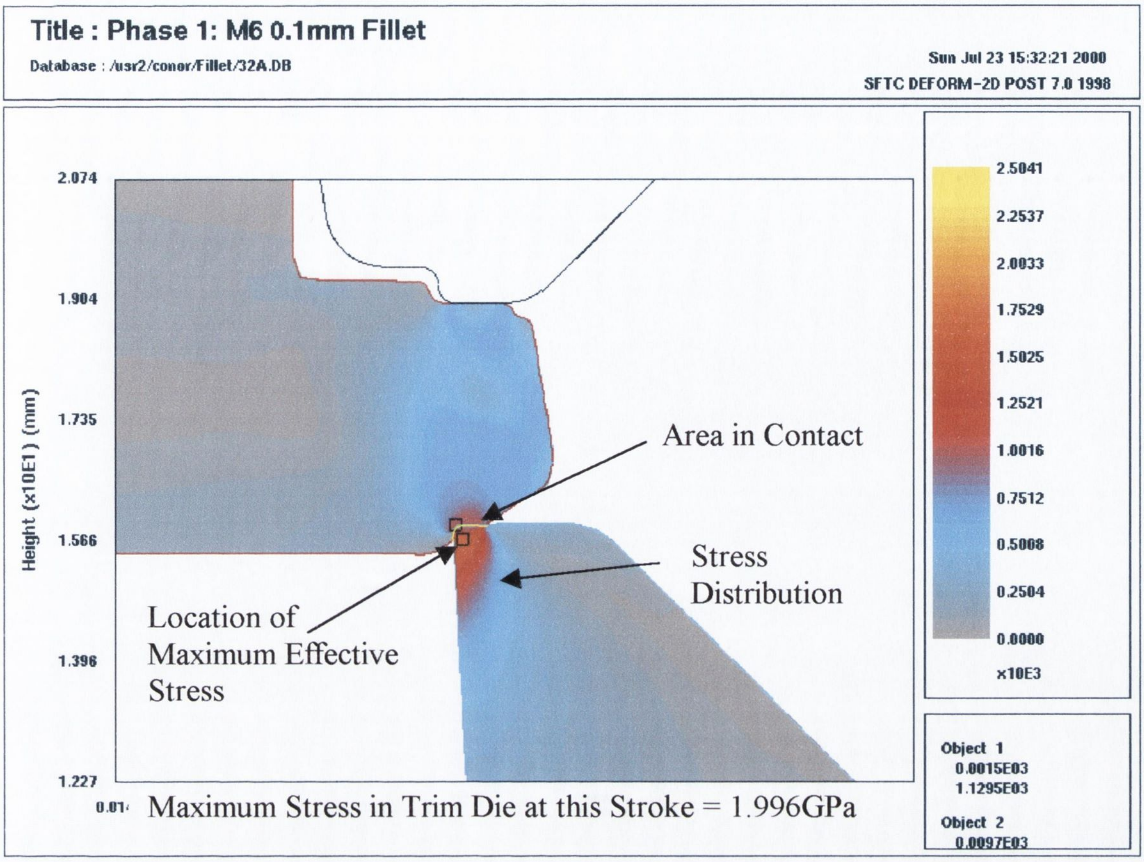

Figure 4-5: Effective Stress in the 0.1 mm 'Fillet' Trim Die at 0.3 mm Stroke

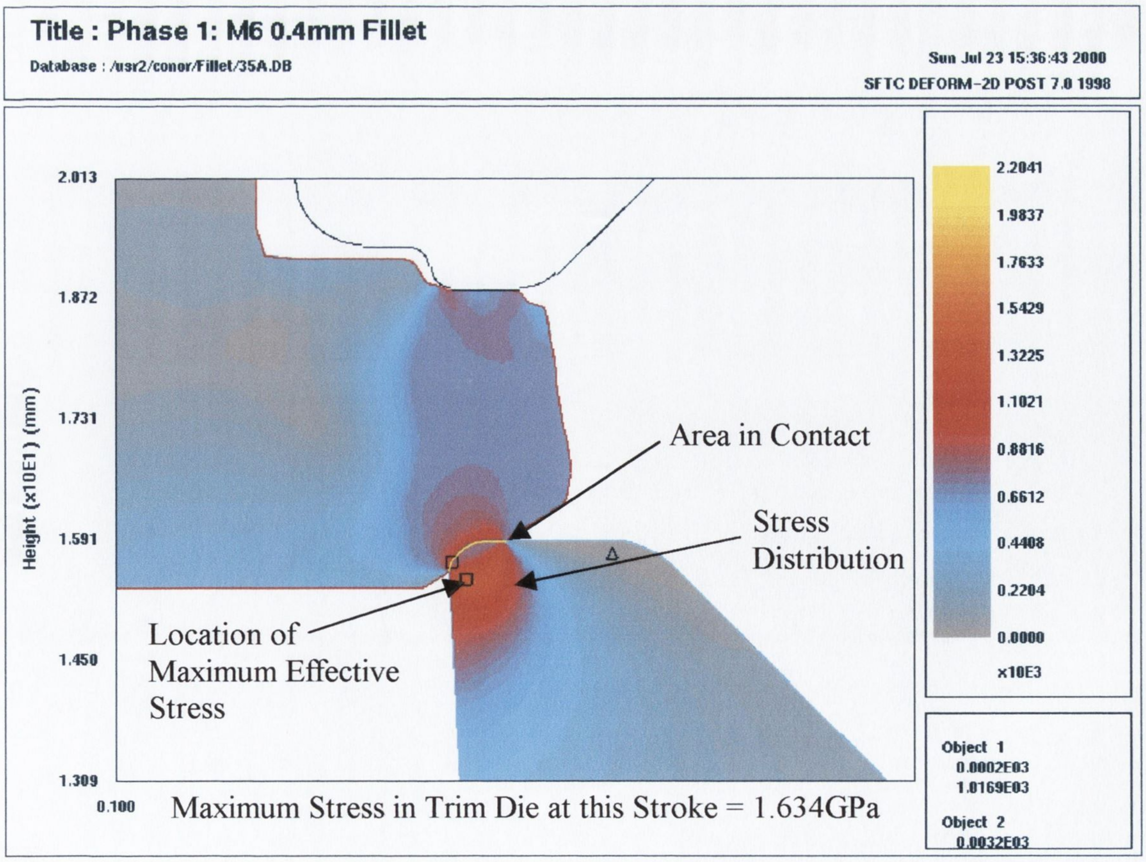

Figure 4-6: Effective Stress in the 0.4 mm 'Fillet' Trim Die at 0.3 mm Stroke

Area 2: Trim Die Stroke = 1.0mm

Figure 4-7 shows the effective stress results for the four models at a stroke of 1.0mm. The range of stroke displayed on the x-axis of 0.5 to 1.5mm allows the trends leading up to, and following the 1.0mm mark to be visualised.

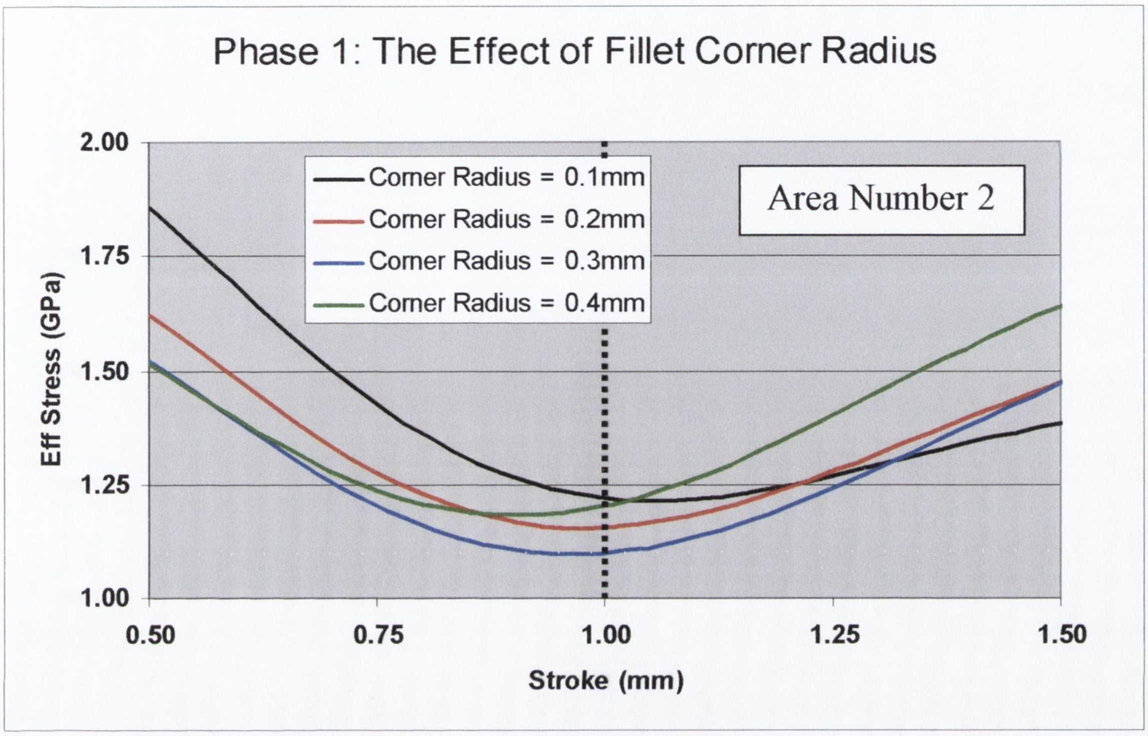

Figure 4-7: Effective Stress vs. Stroke for all 4 Fillet models. Stroke Range 0.5 to 1.5mm

Figures 4-9 to 4-12 show the four models at a stroke of 1.0mm. As previously mentioned, once the workpiece material yields, the stress levels in all four models reduce. With reference to figure 4-7, when the stroke reaches Area 2 (a value of 1.0mm), the stress levels start to rise again. This rise in the level of induced effective stress can be explained by considering the velocity of the workpiece material during the deformation process. Figure 4-8 illustrates the velocity plot of the workpiece material at a trim die stroke of 0.3mm. During the deformation process, the workpiece material has two possible paths to follow. The yellow arrow in figure 4-8 defines the first path. The material, which follows this path, becomes the 'flash' or trimmed material. The blue vertical arrow in figure 4-8 defines the second path. Eventually the workpiece material following the path of the blue arrow makes contact with the top tool see figure 4-8. Figure 4-9 to 4-12 show that this contact of workpiece and top tool has taken place at a stroke of 1.0mm. The induced stresses start to increase from this point onwards because the workpiece material following the blue arrow is restricted from flowing upwards, and this causes greater resistance to the deformation within the workpiece.

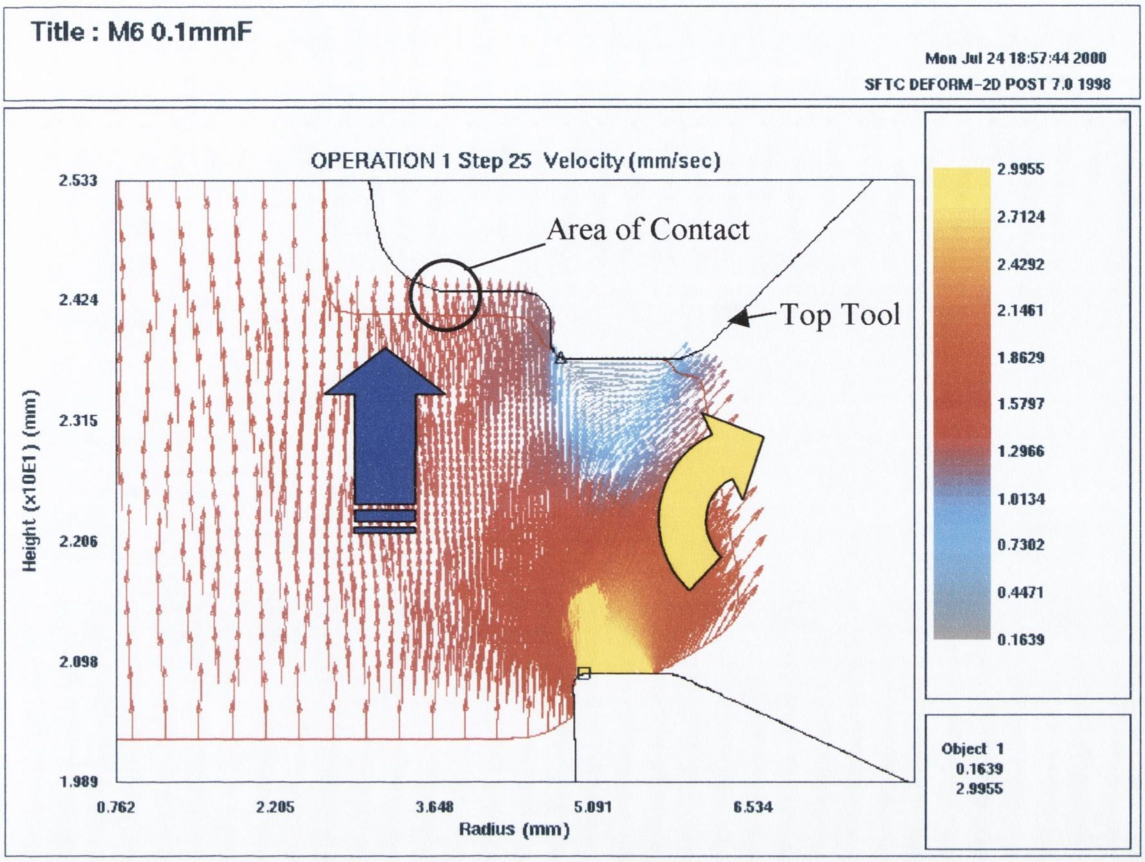

Figure 4-8: Workpiece Material Velocity Plot, showing the two Possible Paths.

With reference to figure 4-7 and table 4-3 below is it evident that altering the corner radius at Area 2, has a small effect on the induced stresses. Table 4-2, indicated that altering the corner radius at Area 1 caused a decrease in the stress level of over 17 %, table 4-3 below shows that this change in effective stress is down to approximately 9%.

‘Fillet’ Corner Radii (mm)	Induced Effective Stress (GPa)
0.1	1.22
0.2	1.16
0.3	1.11
0.4	1.21

Table 4-3: The Effect of Increasing the ‘Fillet’ Corner Radius at a Stroke of 1.0 mm

The black, red and blue lines displayed in figure 4-7, corresponding to fillet corner radii of 0.1, 0.2 and 0.3mm all show a drop in the level of stress as the corner radius is increased. The green line, representing a corner radius of 0.4mm, does not follow this trend. With reference to table 4-3, the model having a 0.4mm corner radius induced the second highest level of effective stress at this stroke of 1.0mm. This increase in stress can be explained by considering the effects of friction between the workpiece and trim die.

The area of contact between the workpiece and trim die for the 0.1 and 0.4mm fillet corner radii models are shown in figures 4-9 and 4-12 by a yellow line. The 0.4mm fillet radius model has a greater area of contact, compare figures 4-9 and 4-12, which causes the load to be distributed over a greater area and should therefore induce a lower value of stress within the trim die. However, due to the very large forging loads required in this process, the frictional effects over this larger area of contact cause an increase in forging load.

At this stage of the forging process, increasing the corner radius, which increases the area of contact, has two main effects. On one hand, increasing the area of contact reduces the level of induced stress as the loads are distributed over a greater area. However, increasing the area of contact increases the influence of the frictional effects, which causes an increase in the stress level within the trim die.

Furthermore, altering the 'fillet' corner radius changes the distribution of the stresses within the trim die. Figure 4-9 illustrates the relatively small area over which the highest stress levels are distributed for this stroke. Again the location of the maximum stress occurs within the body of the trim die. As the corner radius increases, the area over which the stresses act also increases. Figure 4-12 shows the stress pattern when the corner radius of 0.4mm is simulated. Comparing figure 4-12 and 4-9 illustrate this change in the stress distribution area.

With reference to figure 4-7 and table 4-3, the trim die which induced the lowest level of effective stress, at a stroke of 1.0mm, had a 0.3mm corner radius.

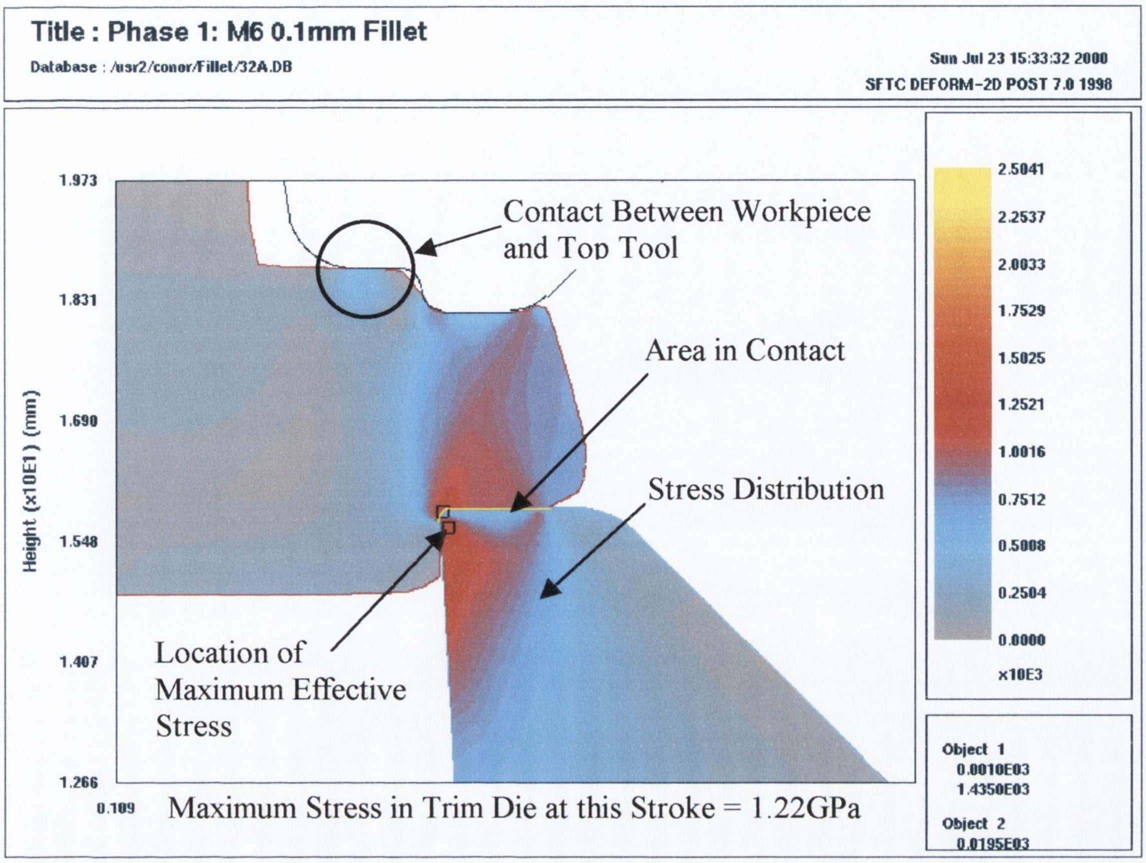

Figure 4-9: Effective Stress in the 0.1 mm 'Fillet' Trim Die at 1.0 mm Stroke

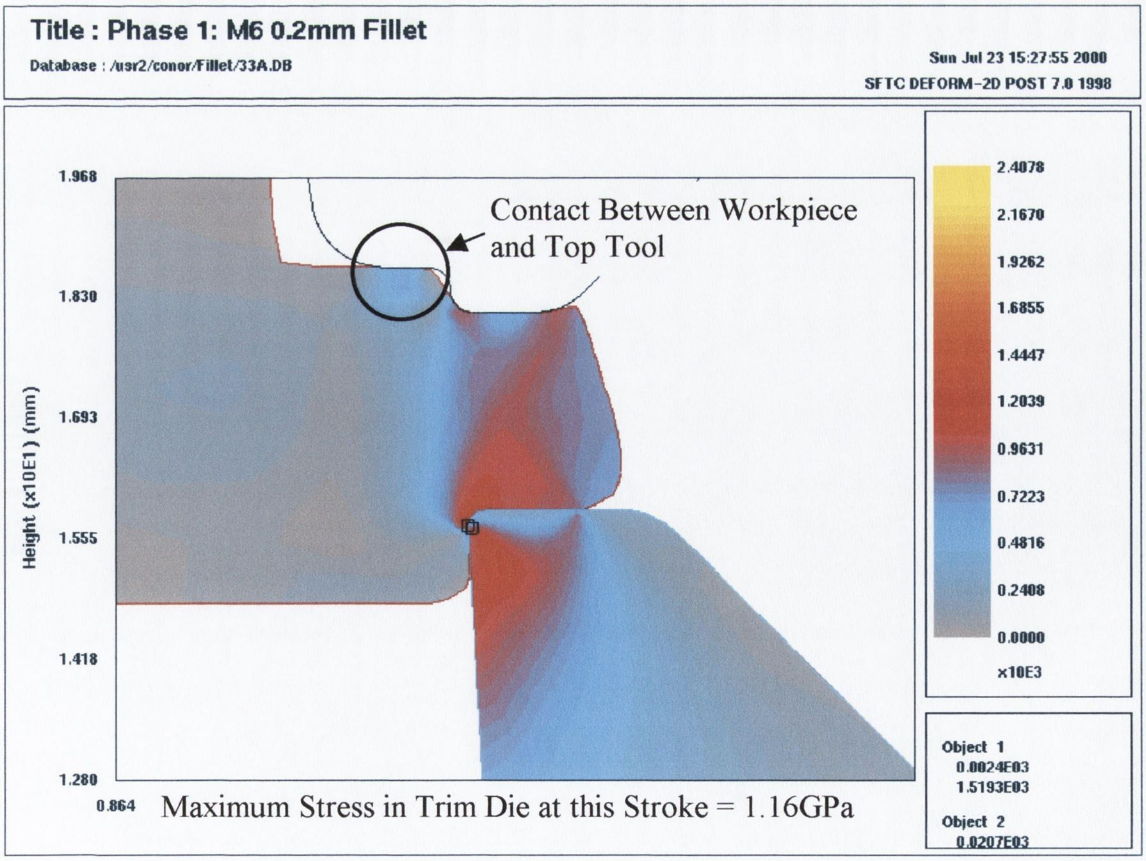

Figure 4-10: Effective Stress in the 0.2 mm 'Fillet' Trim Die at 1.0 mm Stroke

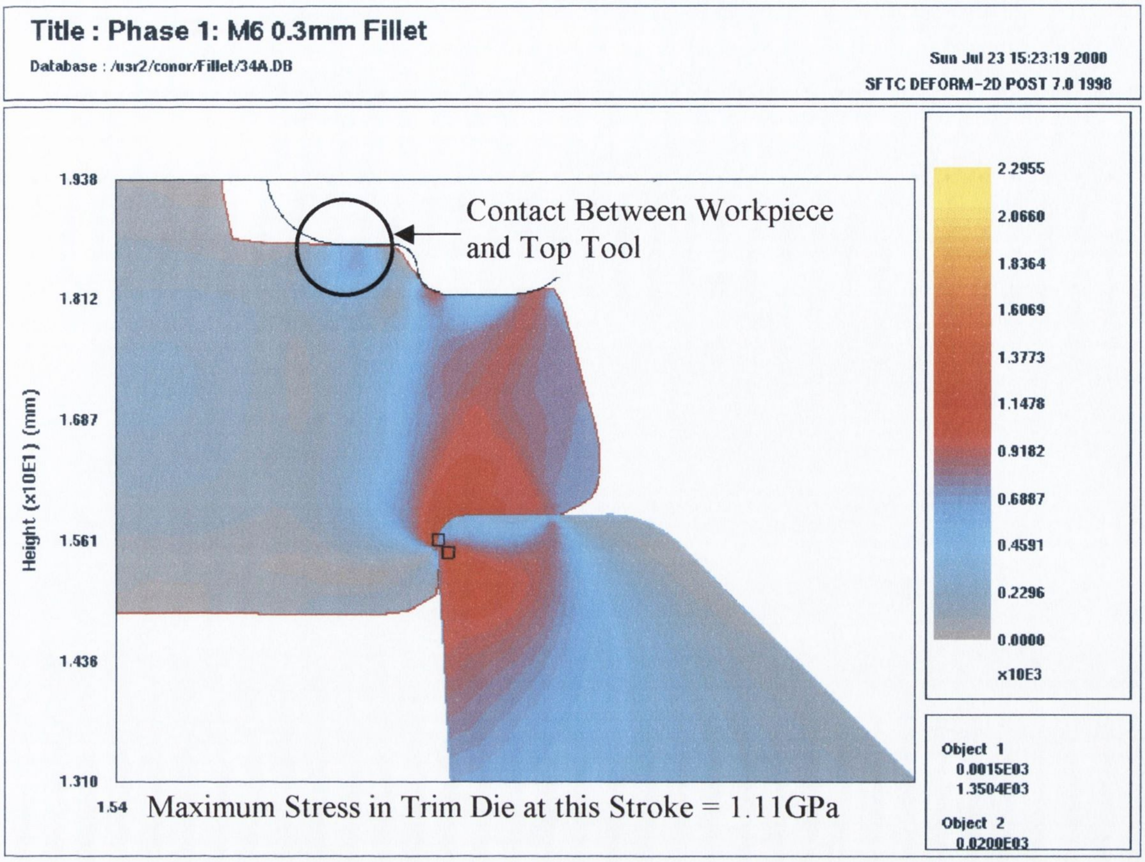

Figure 4-11: Effective Stress in the 0.3 mm 'Fillet' Trim Die at 1.0 mm Stroke

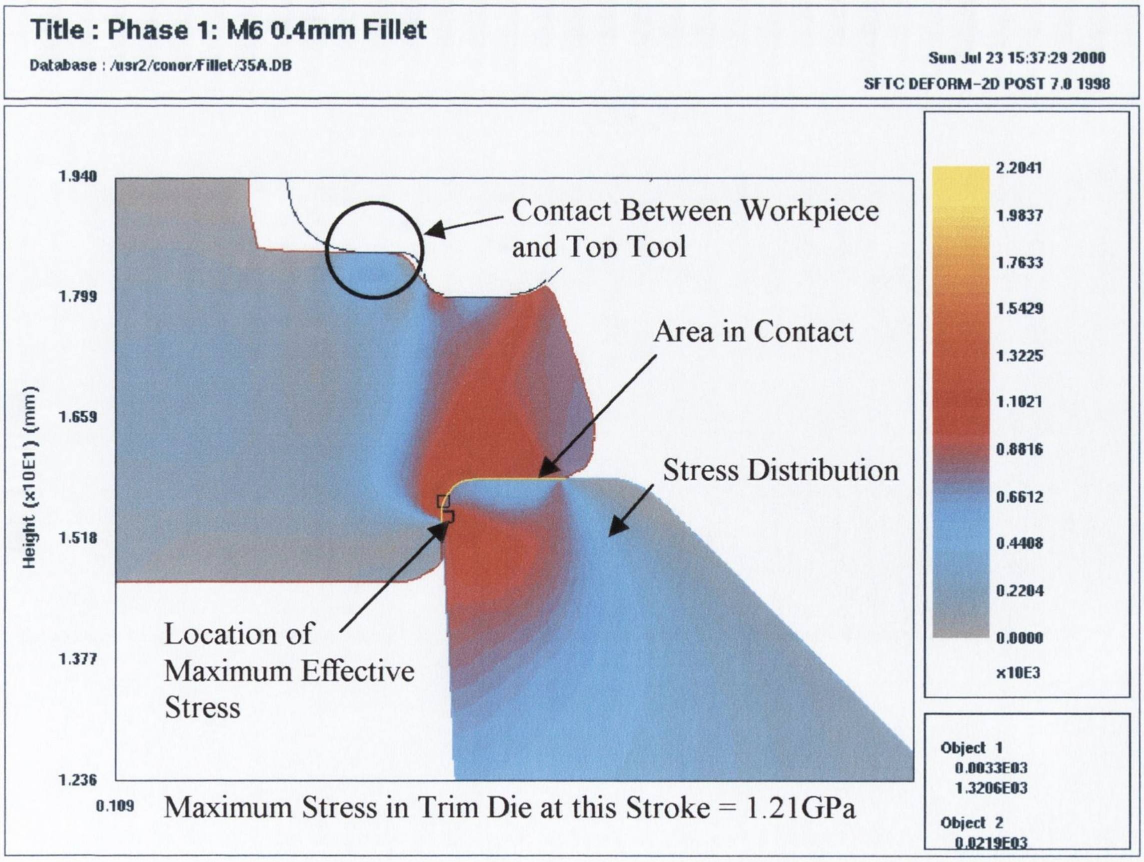

Figure 4-12: Effective Stress in the 0.4 mm 'Fillet' Trim Die at 1.0 mm Stroke

Area 3: Trim Die Stroke = 3.0mm

Figure 4-13 shows the effective stress versus stroke for the four 'Fillet' corner radii trim dies.

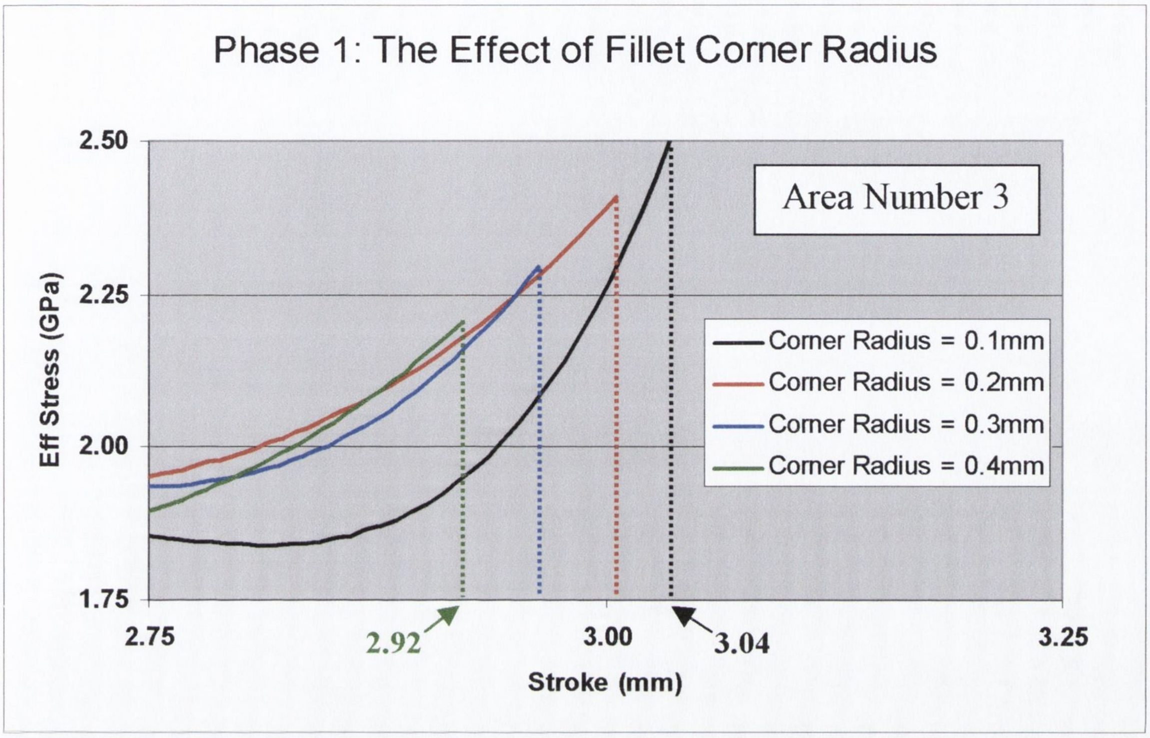

Figure 4-13: Effective Stress vs. Stroke for all 4 Fillet models. Stroke Range 2.75 to 3.25 mm

As mentioned at the start of this chapter in section 4.1, page 79, due to a feature of the trim die profile, varying the corner radius had an effect on how far the trim die travelled during the process. This effect is explained in greater detail in Appendix D on page 238, but its consequences can be seen in figure 4-13. The black line, which represents the 0.1mm corner radius, recorded the greatest amount of trim die stroke of 3.04mm, while the largest corner radius of 0.4mm recorded a stroke of 2.92mm this represents a change of almost 4%. The variations in the induced effective stress at the end of the trim die stroke for each of the four models displayed in figure 4-13 are listed in table 4-4 below

'Fillet' Corner Radii (mm)	Induced Effective Stress (GPa)
0.1	2.5041
0.2	2.4078
0.3	2.2953
0.4	2.2041

Table 4-4: The Effect of Increasing the 'Fillet' Corner Radius at the Final Stroke

With reference to table 4-4, increasing the corner radius from 0.1mm to 0.4mm at the end of the stroke, causes a decrease of 12% from 2.5041GPa to 2.2041GPa in the level of effective stress within the trim die. The yield stress for the trim die material, M2, is 2.5GPa. Referring to table 4-4, the 0.1mm fillet radius model has surpassed the yield stress of M2, while the 0.2mm fillet model is dangerously close. The stress level within the trim die cannot exceed the yield stress of the material during the forging operation, therefore the use of a trim die with a 0.1mm fillet radius would be unacceptable. The decrease in effective stress, at the end of the trim die stroke, can be attributed to a change in the aspect ratio.

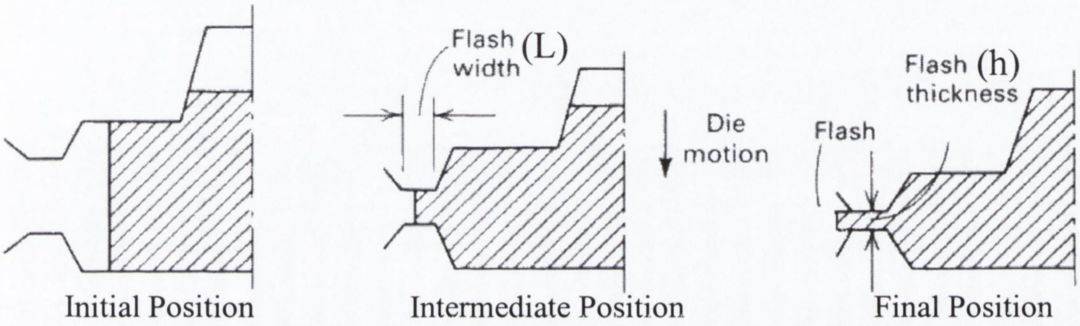

Figure 4-14: Aspect Ratio Between Flash Width and Flash Thickness

The influences of flash thickness and flash width on forging pressure are reasonably well understood from a qualitative viewpoint [2]. Figure 4-14 shows a typical forging operation with a stationary bottom die, moveable top die and workpiece material shown hatched in between. The initial position is shown on the left and final position on right. The direction of the moveable top die is illustrated in the intermediate position. As the die moves downwards, the excess material is forced into the 'Flash' area. With reference to figure 4-14, it has been documented that the forging pressure increases with decreasing flash thickness (h) and with increasing flash land width (L). This increase in forging pressure is caused by a combination of reducing the gap, increasing the frictional forces, and decreasing the metal temperatures at the flash gap [2]. The forging operation depicted in figure 4-14 is very similar to the trimming process simulated in this thesis. In relation to figure 4-16, the flash thickness (h) and the flash land (L) are illustrated. As previously mentioned, the stopping criterion for all the FEA models was a critical distance between the top of the trim die surface and the top tool. Therefore the final stopping distance of 0.25mm was used as the (h) value. The only variable is the flash land, or in the case of this thesis, the length of the flat surface on the top of the trim die, known as the land width, see figure 3-17, page 65 for additional details. This land width value was held constant at 1.5 mm for all the models used to investigate the effect of 'Fillet' corner geometry, see table 4-1. However, as the corner radius increases from 0.1mm to 0.4mm, this effectively reduces the land width from 'X' to 'Y'. This is illustrated in figure 4-15.

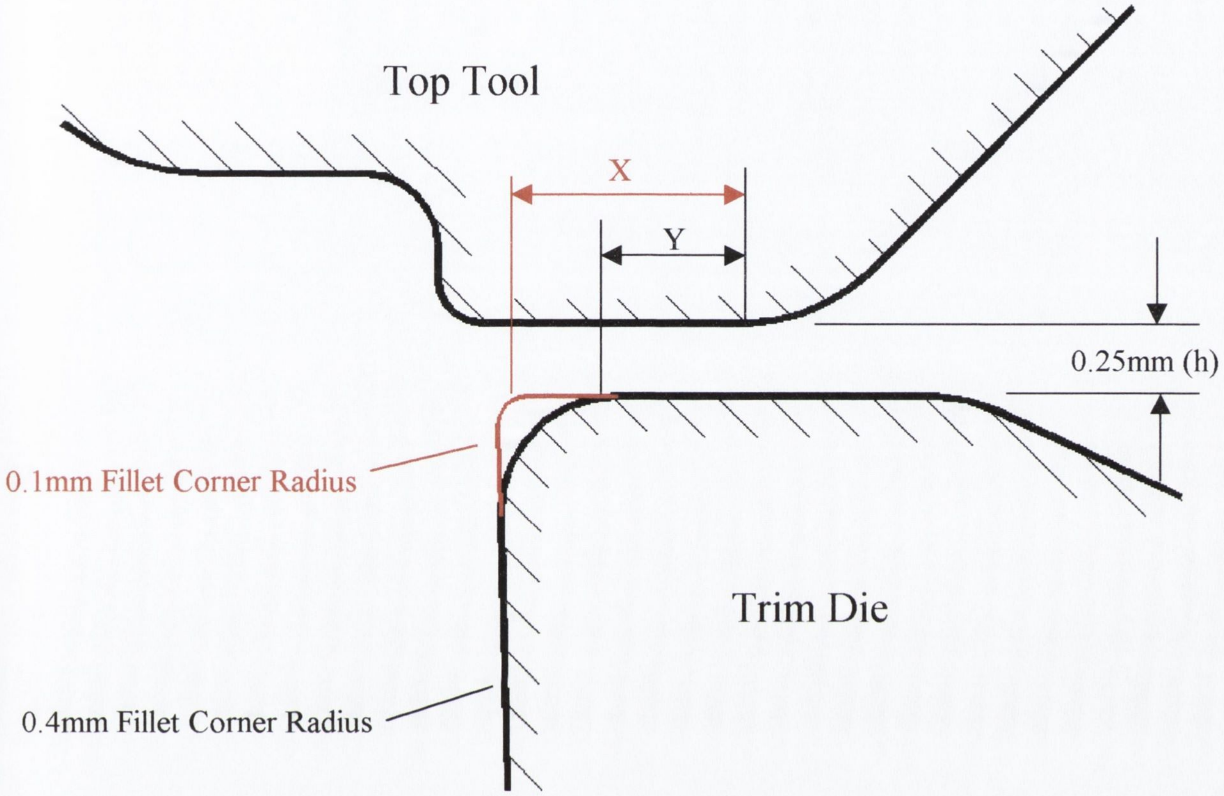

Figure 4-15: Close-up Detail of Trim Die and Top Tool at the Final Stopping Distance of 0.25mm

Figure 4-15 depicts the location of the trim die and top tool at the end of the stroke are illustrated in figure 4-15. The black line represents the trim die having a 0.4mm fillet corner profile, while the red line represents the 0.1mm fillet corner profile. The dimensions of the top tool remain unchanged in all the models simulated in this thesis. As already mentioned, the final stopping distance of 0.25mm also remained constant for all the models. For these models the aspect ratio is defined as a ratio of the land width (L) to the flash thickness (h). Therefore with respect to figure 4-14, the aspect ratio is the value of (L) divided by the value of (h). The larger this aspect ratio, the higher the forging pressure required.

The aspect ratio for the 0.1mm fillet radius trim die shown in figure 4-15 is given as the land width (X) divided by the flash thickness (h). With reference to figure 4-15, the 0.4mm fillet trim die model is going have a smaller aspect ratio than the 0.1mm fillet trim die model. The 0.1mm fillet model has a greater length, (X), for the parallel surfaces between the trim die and top tool, while the 0.4mm fillet model has a value of (Y). Hence the 0.4mm 'Fillet' trim die produces a smaller aspect ratio at the end of the trim die stroke and because of this, the forging load required to cause this level of deformation, and therefore stress, is reduced.

Table 4-5 below plots corner radii against the corresponding aspect ratios and induced effective stresses.

Fillet Corner Radius	Aspect Ratio = L / h	Induced Effective Stress (GPa)
0.1	0.7438 / 0.25 = 2.9752	2.5041
0.2	0.6412 / 0.25 = 2.5648	2.4078
0.3	0.5385 / 0.25 = 2.154	2.2953
0.4	0.4359 / 0.25 = 1.7436	2.2041

Table 4-5: Change in Aspect Ratio With Corner Radius and Subsequent Change in Effective Stres

For all the FEA models simulated within this thesis, the final stopping distance (or flash thickness) was held constant at the industrial norm of 0.25mm. An investigation into the possibility of altering this flash thickness is detailed in Appendix E on page 240. With regard to table 4-5 above, the flash thickness (h) is held at 0.25mm while the land width (L) reduces as the corner radius is increased. As previously explained, increasing the corner radius effectively reduces the land width. Reducing the land width reduces the aspect ratio, which causes a reduction in the magnitude of the effective stresses within the trim die.

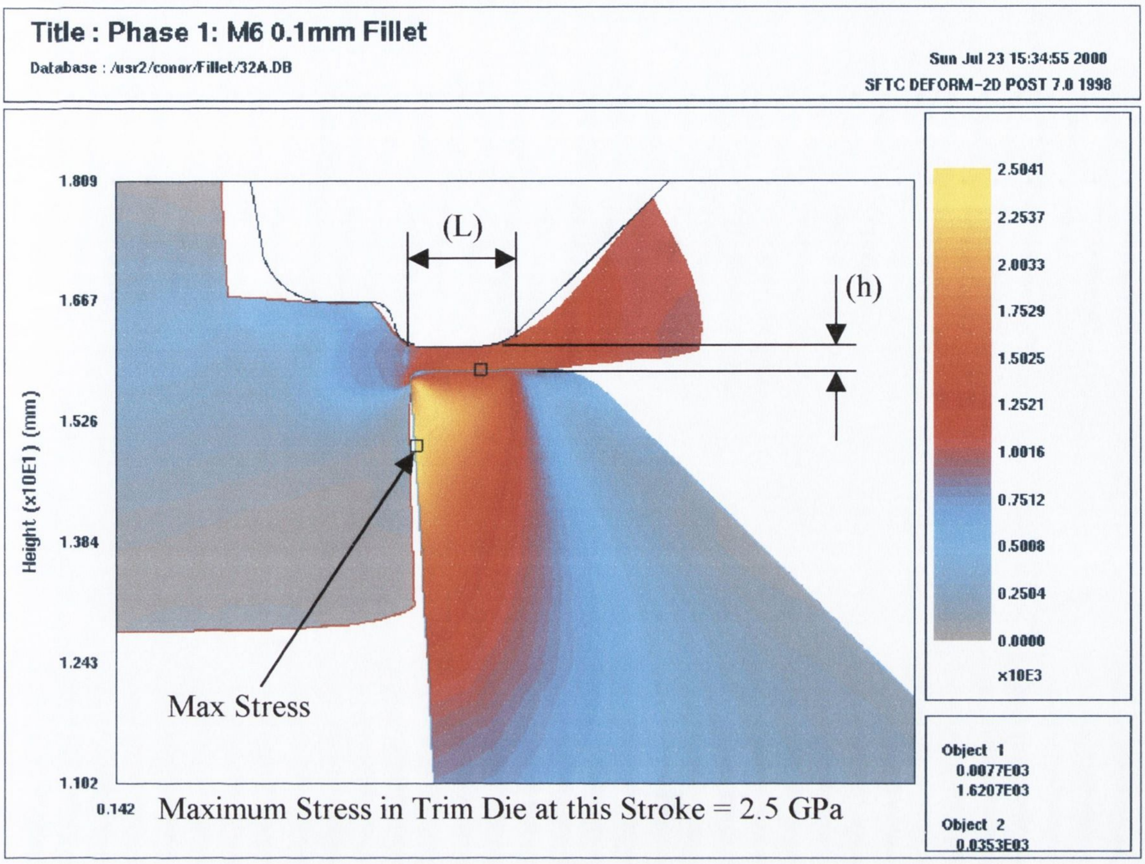

Maximum Stress in Trim Die at this Stroke = 2.5 GPa

Figure 4-16: Effective Stress in the 0.1 mm 'Fillet' Trim Die at the Final Stroke

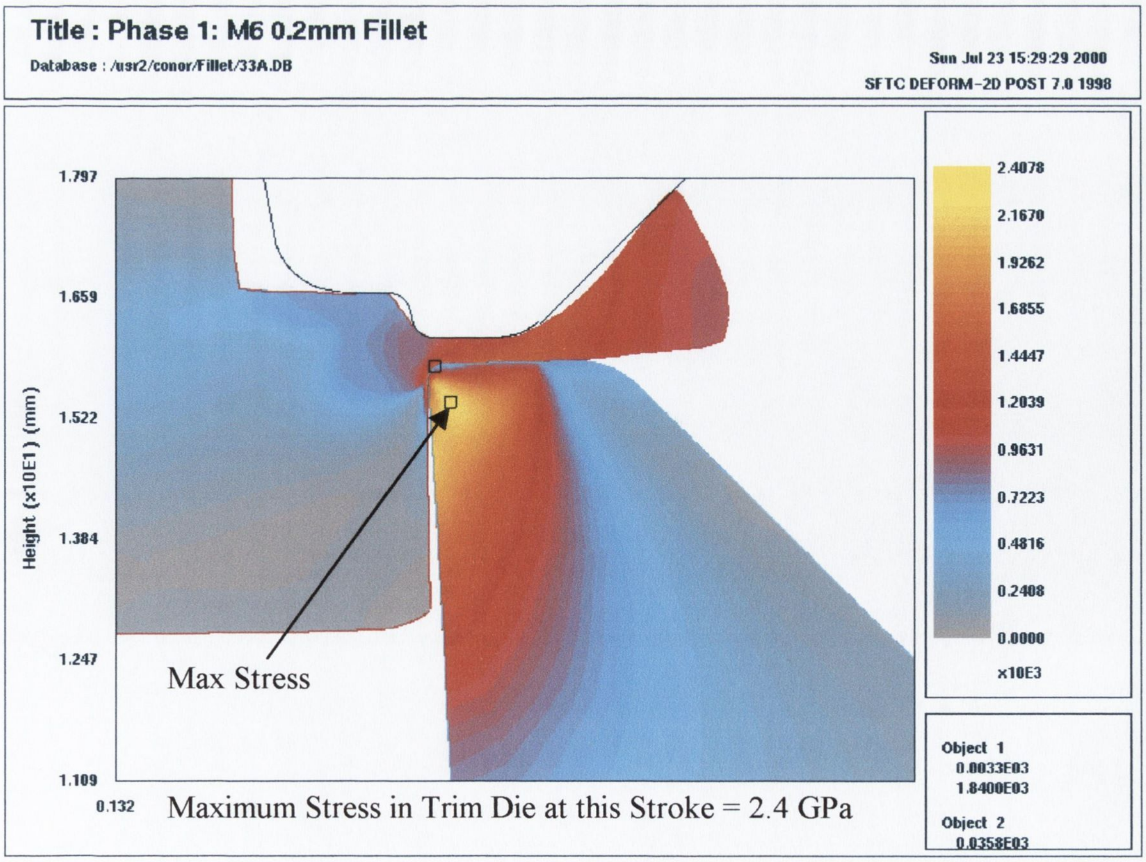

Maximum Stress in Trim Die at this Stroke = 2.4 GPa

Figure 4-17: Effective Stress in the 0.2 mm 'Fillet' Trim Die at the Final Stroke

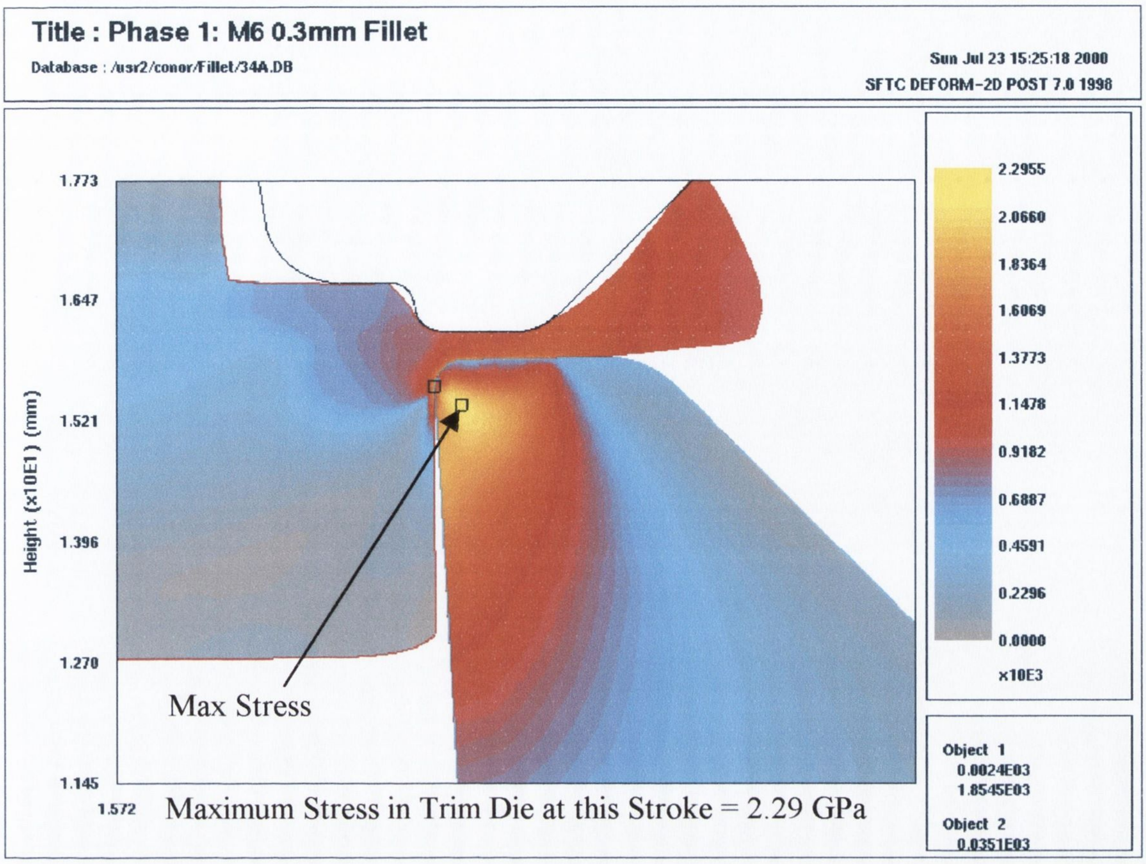

Max Stress

Maximum Stress in Trim Die at this Stroke = 2.29 GPa

Figure 4-18: Effective Stress in the 0.3 mm 'Fillet' Trim Die at the Final Stroke

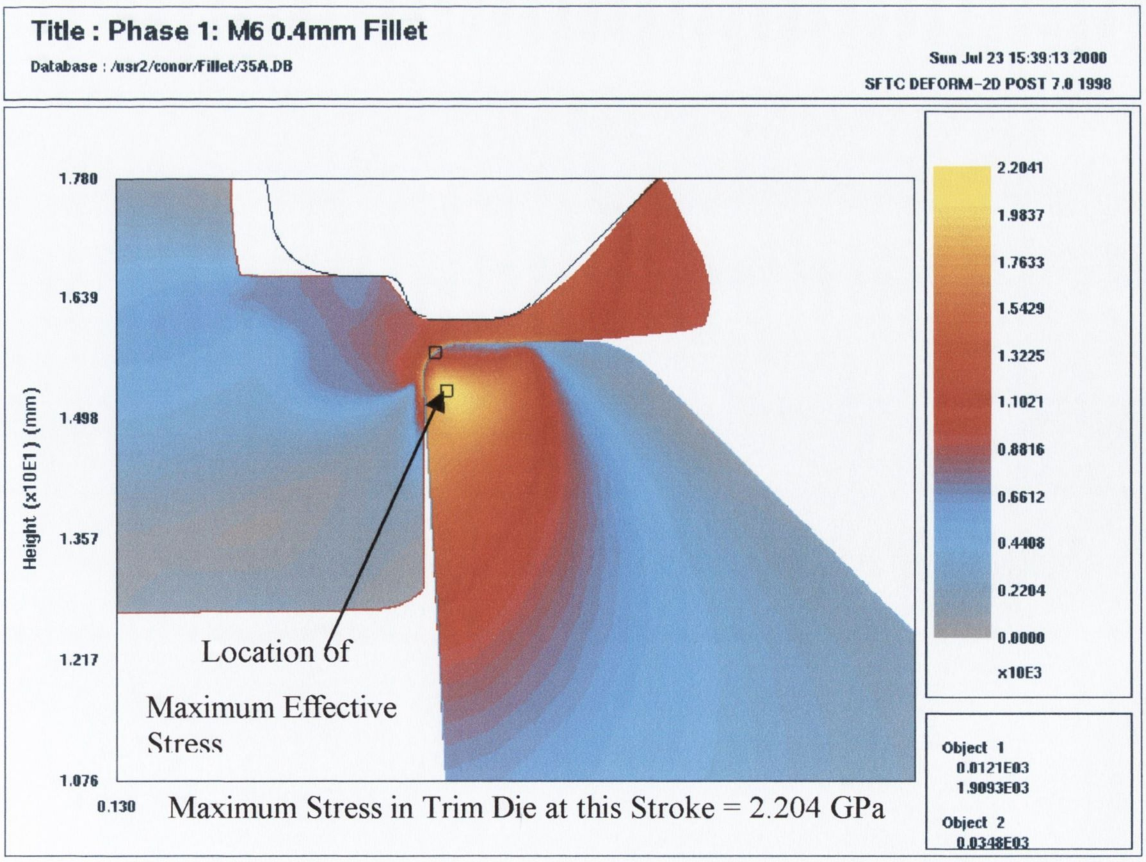

Location of Maximum Effective Stress

Maximum Stress in Trim Die at this Stroke = 2.204 GPa

Figure 4-19: Effective Stress in the 0.4 mm 'Fillet' Trim Die at the Final Stroke

4.1.1.2 Maximum Tensile Radial Stresses:

The investigation into the adverse effects of the use of coatings, indicated that it is possible to have cracks present along the surface of the coating before the trim die forges its first fastener. These cracks have been seen to propagate through the coating and into the substrate and will be discussed in greater detail in Section 4.5.4 on page 190. If these coating cracks are present, they tend to remain 'dormant' unless subjected to a threshold level of tensile stress. It is for this reason that the maximum tensile radial stress component is now considered. Section 4.5.4 on page 190 details the analysis carried out on failed trim dies.

The location of crack initiation was along the top surface of the trim die, known as the 'Land Surface'. Figures 4-20 to 4-23 illustrate the radial stresses within the trim die at strokes of 0.125, 0.25, 0.5 and 0.75 mm respectively. In each of these graphs, a triangle and square symbol are visible. The triangle represents the location of the maximum compressive radial stress, while the square locates the maximum tensile radial stress. As the trim die progresses into the workpiece, the location of this maximum tensile radial stress moves out along the land surface until it reaches the petal surface, see figure 4-23.

It was found that for each of the 'Fillet' corner geometry models simulated in this section, once the trim die stroke exceeded 0.75mm, the location of the maximum tensile radial stress moved onto the petal surface. None of the failed trim dies analysed in section 4.10 indicated failure on this petal surface, only on the land surface. The maximum tensile radial stress in each of the models simulated, up to a stroke of 0.75mm, was recorded. This confirmed that the location of the maximum tensile radial stress was always along the land surface. These maximum tensile radial stress values are plotted against the 'Fillet' corner radius as shown in figure 4-24. The effect of altering the corner radius from 0.1mm to 0.4mm is tabulated in table 4-6 below.

'Fillet' Corner Radii (mm)	Maximum Tensile Radial Stress (MPa)
0.1	530.3
0.2	295
0.3	157
0.4	86

Table 4-6: Fillet Corner Radius Versus the Max Tensile Radial Stress

With reference to table 4-6, increasing the corner radius from 0.1mm to 0.4mm reduces the maximum tensile radial stress from 530.3 MPa to 86 MPa, which is approximately a six-fold reduction.

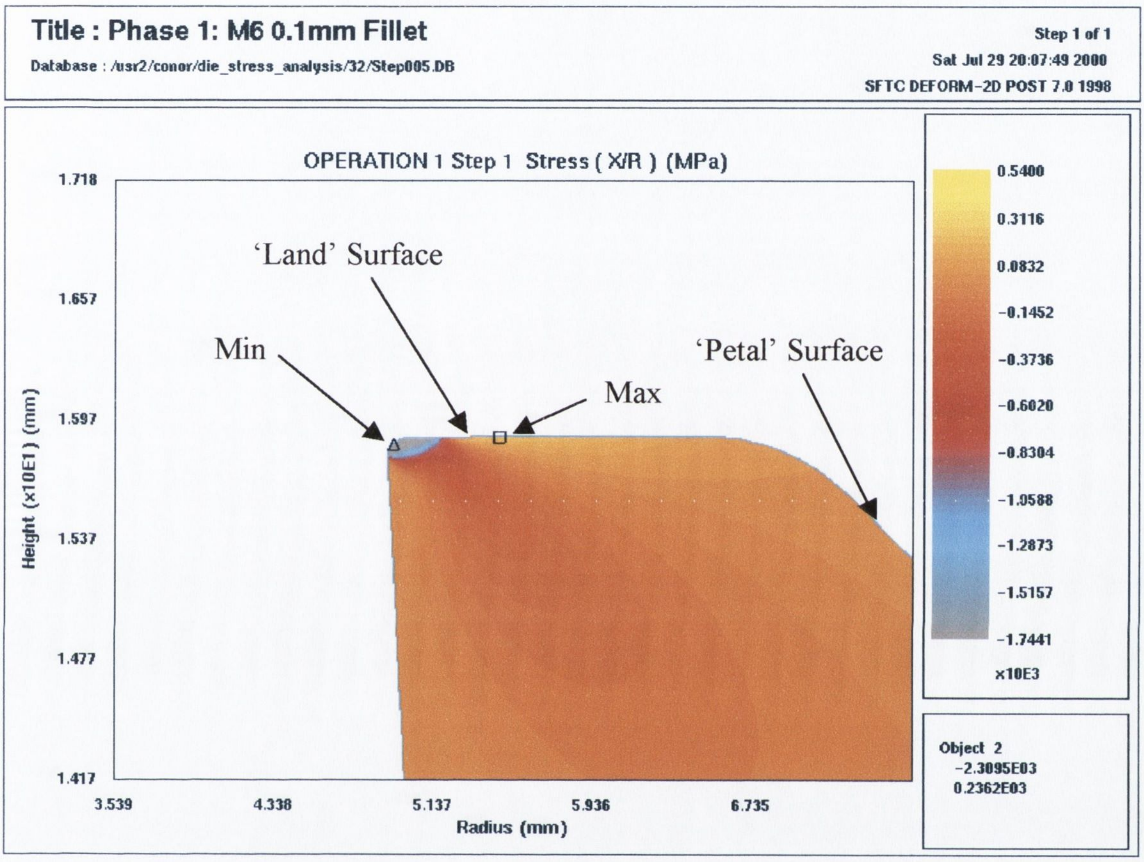

Figure 4-20: Location of Max Tensile Radial Stress at a Stroke of 0.1 mm

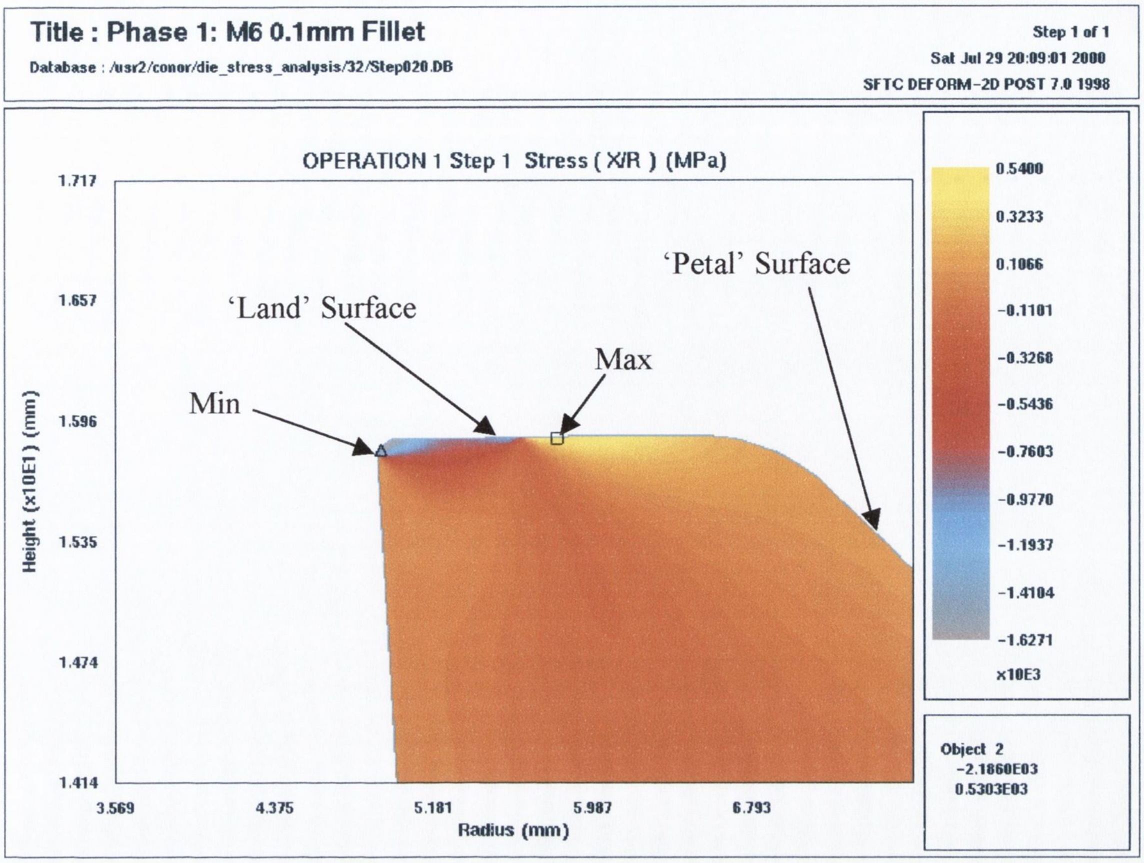

Figure 4-21: Location of Max Tensile Radial Stress at a Stroke of 0.25 mm

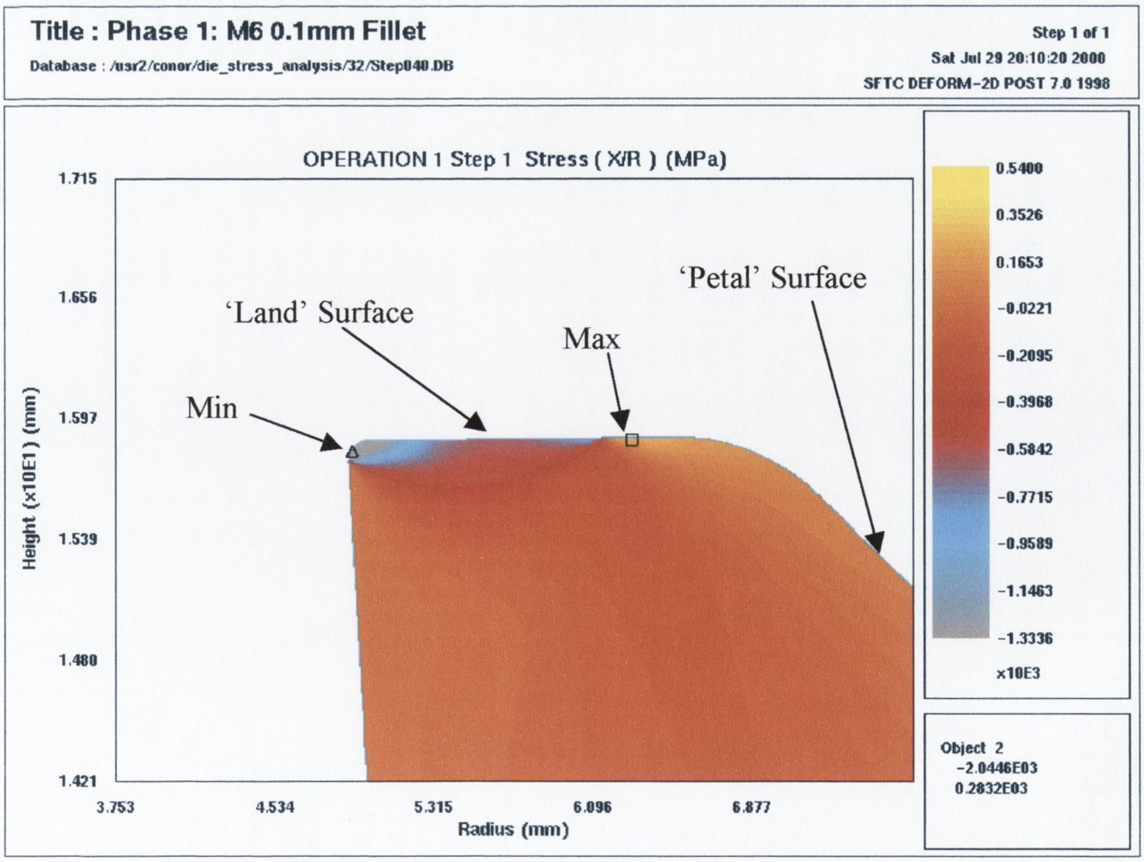

Figure 4-22: Location of Max Tensile Radial Stress at a Stroke of 1.0 mm

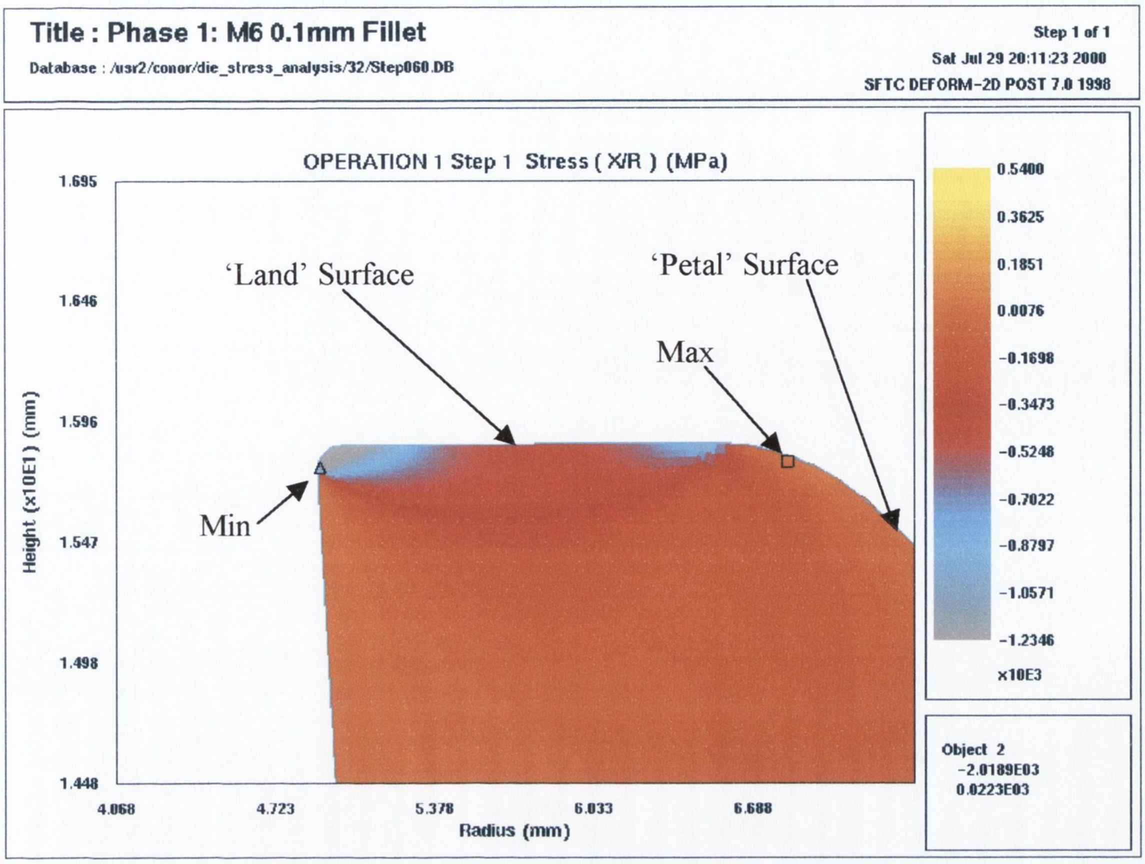

Figure 4-23: Location of Max Tensile Radial Stress at a Stroke of 1.5 mm

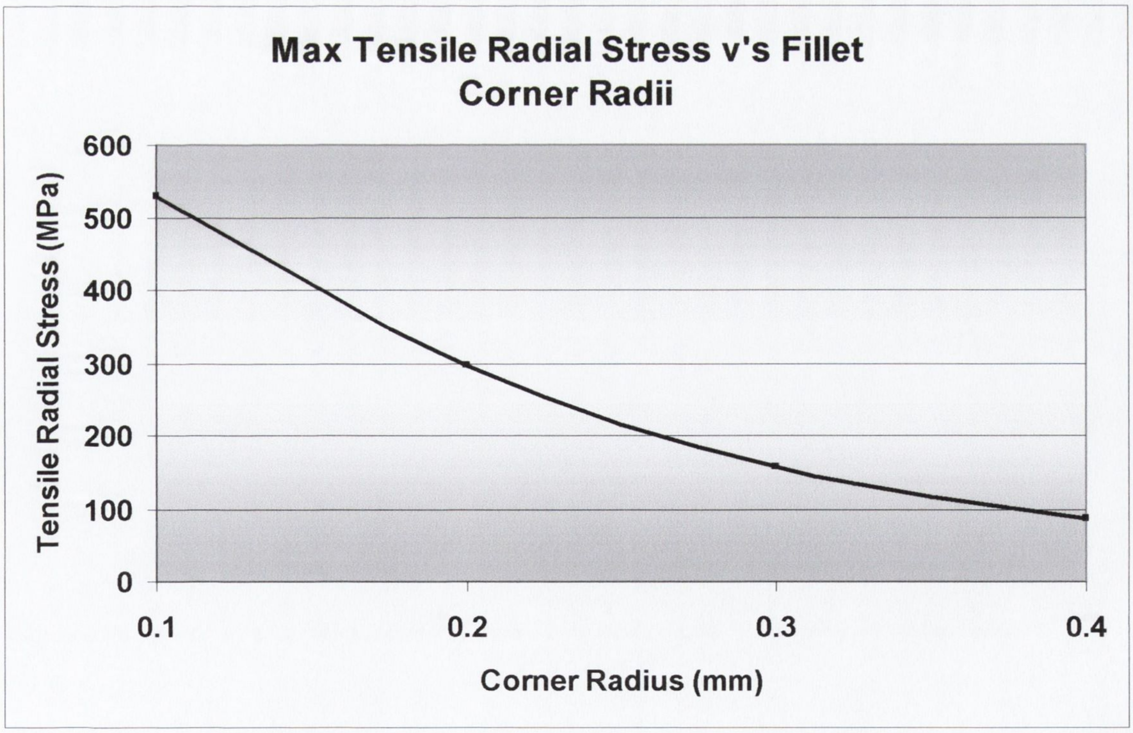

Figure 4-24: Maximum Tensile Radial Stress Versus 'Fillet' Corner Radius

4.1.1.3 Summary

In section 4.1.1, four FEA models were constructed having a 'Fillet' corner geometry. The remaining parts of the trim die profile, i.e. the 'Land Width', 'Petal' and 'Rake Angle' were held constant at the values listed in table 4-1 on page 81. The trim die stroke was divided into three areas to enable closer examination. These three areas corresponded to a trim die stroke of 0.3, 1.0 and 3.0mm. At each of these areas 1, 2 and 3, the effective stress results were plotted against trim die stroke, and the distribution of these stresses within the trim die were analysed.

Area Number	Trim Die Stroke (mm)	Optimum Fillet Corner Radius (mm)	Lowest Induced Effective Stress (GPa)
1	0.3	0.4	1.634
2	1.0	0.3	1.11
3	3.0	0.4	2.204

Table 4-7: Optimum Fillet Corner Radius

Table 4-7 illustrates that at Area 1, which relates to a trim die stroke of 0.3mm, the optimum fillet corner radius was 0.4mm. This 'fillet' corner radius induced an effective stress value of 1.634 GPa within the trim die. At Area 2 (1.0mm stroke) the optimum fillet radius was 0.3mm, while at Area 3 (3.0mm stroke) the 0.4mm fillet radius model again induced the lowest effective stress value.

The effective stress values listed in table 4-7 are the lowest levels between all four 'fillet' models at areas 1, 2 and 3. At Area 3, which relates to a stroke of 3.0mm, the 0.4mm corner radius model caused the lowest induced stress level of 2.204 GPa. The levels of stress at Area 3 are of a higher magnitude than Areas 1 or 2. This high level of stress at Area 3 is due to the workpiece material becoming trapped between the trim die and top tool. Obviously the model, which induces the lowest level of stress at this Area 3, is very important in the selection of the optimum geometry. But selection of an optimum trim die geometry based on the maximum values induced is not sufficient. The 'fillet' trim die, which satisfied the following three criteria, was deemed 'optimum'.

1. The FEA model which induced the lowest level of effective stress within the trim die throughout the forging process.

2. The FEA model which distributed these stresses over a larger area, hence reducing the severity on the trim die.
3. The 'fillet' corner radius, which induced the lowest level of tensile radial stress during the forging process.

Therefore in this Section 4.1.1, the 'fillet' trim die model, which fulfilled the above criteria, had a corner radius of 0.4mm.

The above statement as to the 0.4mm 'fillet' corner radius being 'optimum' is only relevant to this Phase 1 analysis, as will be shown later, the other parameters of the trim die profile such as 'Land Width', 'Petal' and ' Rake Angle' all have an influence on the selection of the 'optimum' profile.

4.1.2 The Effect of Compound Corner Geometry

As previously mentioned in section 3.1.2.3 page 58, the trim die corner geometry was divided into two categories, 'Fillet' and 'Compound'. This section will now detail the FEA results obtained from the trim dies having a 'Compound' corner geometry. Table 4-8 below, lists the variation in compound radii simulated along with the fixed values of land width, petal and rake angle. the largest possible Compound corner radius was limited to 0.25mm due to a feature of the compound geometry. Figure 4-69 on page 150 clearly highlights that a corner radius greater than 0.25mm effectively removes the 'Averbach' radius to produce a simple 'Fillet' trim die geometry.

Parameter	Value
Corner Radius (Compound)	0.07, 0.1, 0.15, 0.2 and 0.25 mm
Land Width	1.5mm (Fixed)
Petal Angle	45° (Fixed)
Rake Angle	3° (Fixed)

Table 4-8: Variation in 'Compound' Corner Radii for the Phase 1 analysis

The compound trim die models closely replicated the results from the fillet trim dies analysed in the previous Section 4.1.1. At area 3, the largest compound corner radius of 0.25mm induced the lowest level of effective stress within the trim die and was therefore deemed 'optimum'.

Table 4-9 on the following page compares the maximum induced effective stresses, at area 3, for the fillet and compound models. The simulations which induced yielding within the trim die material are highlighted in yellow. Table 4-9 shows that using a fillet, or compound, corner radii lower than 0.2mm will cause yielding. The 0.2mm radius fillet and compound trim dies, shown in table 4-9, induced an effective stress level of 2.4078GPa and 2.441GPa respectively. This corresponds to a difference of approximately 1.3%. This suggests that the larger fixed radius in all the compound trim dies of 1.14mm (known as the Averbach Radius, see Section 3.1.2.3 on page 58 for greater detail), has no effect on magnitude of effective stresses and might actually cause an increase. This is discussed further in the Phase 1 conclusions in Section 4.1.6 on page 148.

Corner Profile (mm)		Induced Effective Stress (GPa)
Fillet	Compound	
0.1		2.5041
0.2		2.4078
0.3		2.2953
0.4		2.2041
	0.07	2.758
	0.1	2.610
	0.15	2.558
	0.2	2.441
	0.25	2.381

Table 4-9: Comparison of Effective Stresses for the Fillet and Compound Radii Models at Area 3

4.1.2.1 Maximum Tensile Radial Stresses

The maximum tensile radial stresses along the top, or 'Land' surface of all five 'Compound' trim dies, modelled in this section, are listed in table 4-10 below.

'Compound' Corner Radii (mm)	Maximum Tensile Radial Stress (MPa)
0.07	545.3
0.1	435.5
0.15	323
0.2	252
0.25	170

Table 4-10: Compound Corner Radius Versus the Max Tensile Radial Stress

With reference to table 4-10, increasing the corner radius from 0.07mm to 0.25mm reduced the maximum tensile radial stress from 545.3 MPa to 170 MPa, which is approximately a 3-fold reduction. These results are plotted in figure 4-25 and clearly indicate the large drop in tensile radius stresses achieved by increasing the compound corner radius.

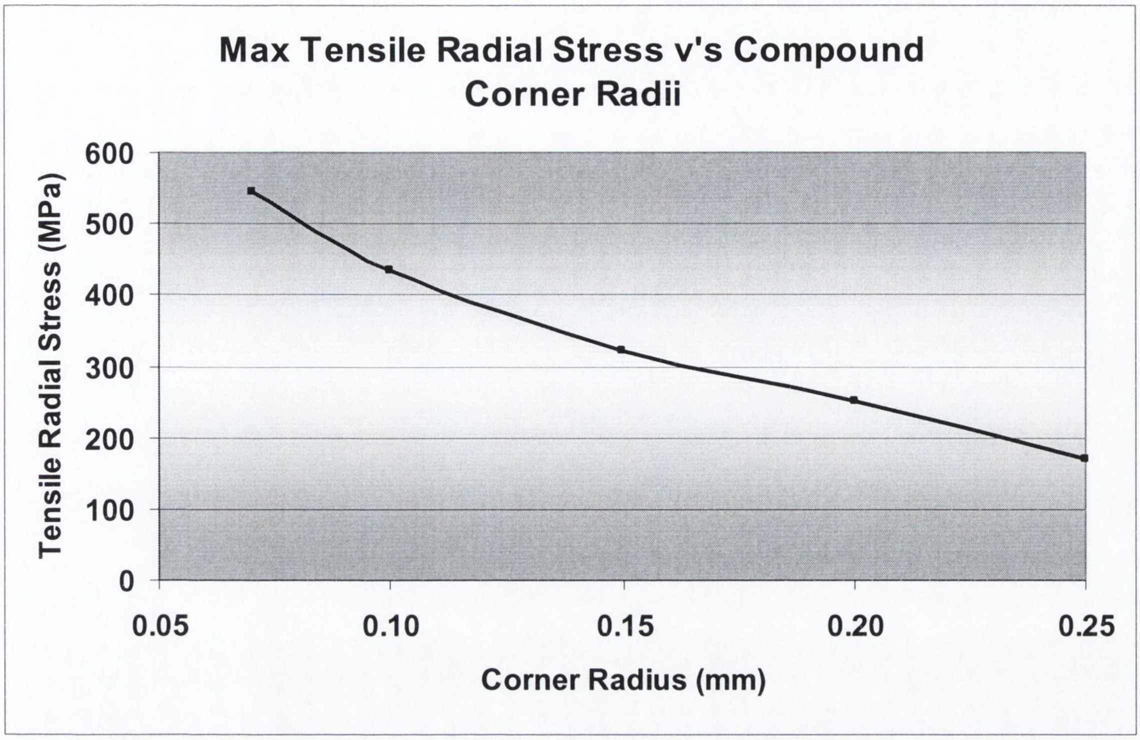

Figure 4-25: Maximum Tensile Radial Stress versus 'Compound' Corner Radius

4.1.2.2 Summary

In this Section 4.1.2, five FEA models were constructed having a 'Compound' corner geometry. The remaining parts of the trim die profile, i.e. the 'Land Width', 'Petal' and 'Rake Angle' were held at the values listed in table 4-8 on page 102. As in the previous section relating to the 'Fillet' corner geometry models, to enable closer examination, the trim die stroke was divided into three areas. At each of these areas the effective stress results were plotted against the trim die stroke, and the distribution of these stresses within the trim die was analysed. The 'optimum' models at each of the three areas are listed in table 4-11 below.

Area Number	Trim Die Stroke (mm)	Optimum Compound Corner Radius (mm)	Lowest Induced Effective Stress (GPa)
1	0.3	0.25	1.671
2	1.0	0.25	1.11
3	3.0	0.25	2.381

Table 4-11: 'Optimum' Compound Corner Radii

With reference to table 4-11, the compound corner radius of 0.25mm induced the lowest levels of effective stress in all three areas of the trim die stroke. The selection of the 'optimum' compound corner geometry based on the maximum effective stress alone is not sufficient. The 'compound' trim die, which satisfied the following three criteria, was deemed 'optimum':

1. The FEA model which induced the lowest level of effective stress within the trim die throughout the forging process.
2. The FEA model which distributed these stresses over a larger area, hence reducing the severity on the trim die
3. The 'Compound' corner radius, which induced the lowest level of tensile radial stress during the forging process.

The 'compound' trim die, which met the above criteria for this phase 1 analysis had a corner radius of 0.25mm.

4.1.3 The Effect of Land Width

Figure 4-26, illustrates the location, on the trim die profile, of the 'Land Width'. The models used to investigate the effect of 'Fillet' and 'Compound' corner radius, discussed in the previous section, all had a fixed land width value of 1.5mm, see Section 4.1.1, table 4-1 and table 4-8. The effect of altering the 'land width' value was, as yet, unknown. For this reason FEA models were constructed where only the land width was altered. Altering only 'one-factor-at-a-time' is a good method for reducing a possible large number of analytical combinations, but it does fail however to consider 'interaction' between the various profile parameters. This issue of 'interaction' is detailed in Section 4.2.

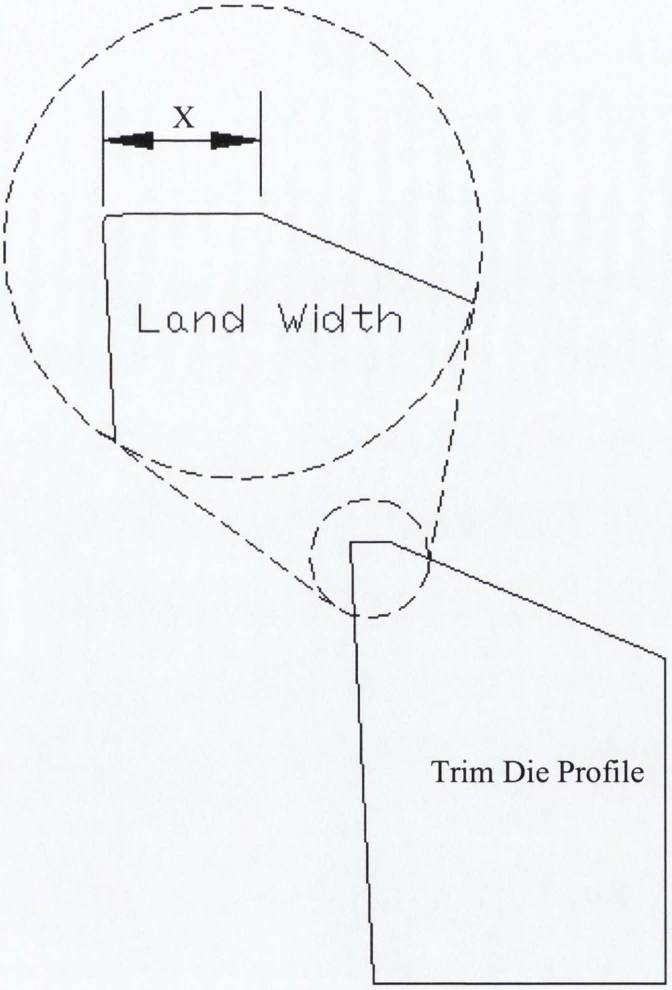

Figure 4-26: Trim Die Profile showing Location Of the Land Width Parameter.

The values for the 'land width' modelled are listed in table 4-12 and refer to the dimension 'X' shown in figure 4-26 above. Therefore for this Section, a total of 6 FEA models were simulated.

Parameter	Value
Land Width	0.2, 0.4, 0.6, 0.8, 1.0 and 1.5mm
Corner Radius ('Fillet')	0.2mm (Fixed)
Petal Angle	20° (Fixed)
Rake Angle	1° (Fixed)

Table 4-12: Trim Die Profile parameters and their corresponding values

The effective stress results along with the tensile radial stresses within the trim die are now presented. As in the earlier sections, the trim die stroke is divided into 3 areas. Area 1, 2, and 3 relate to a trim die stroke of 0.3, 1.0 and 3.0mm stroke.

4.1.3.1 Effective Stress Results

Area 1: Trim Die Stroke = 0.3mm

Figure 4-27 illustrates the effective stress plotted against trim die stroke. A total of six models were simulated with the 'land width' values specified in table 4-12 above. Table 4-13 below illustrates that altering the land width value, in Area 1, causes a negligible change in the level of induced effective stress within the trim die. The largest difference is between the land width values of 0.2 and 0.8mm, which induced an effective stress value of 1.737GPa and 1.677GPa respectively. This variation corresponds to a percentage drop of only 3.45%.

'Land Width' Value (mm)	Induced Effective Stress (GPa)
0.2	1.737
0.4	1.71
0.6	1.692
0.8	1.677
1.0	1.707
1.5	1.708

Table 4-13: The Effect of Increasing the 'Land Width' at Area 1: Stroke = 0.3mm

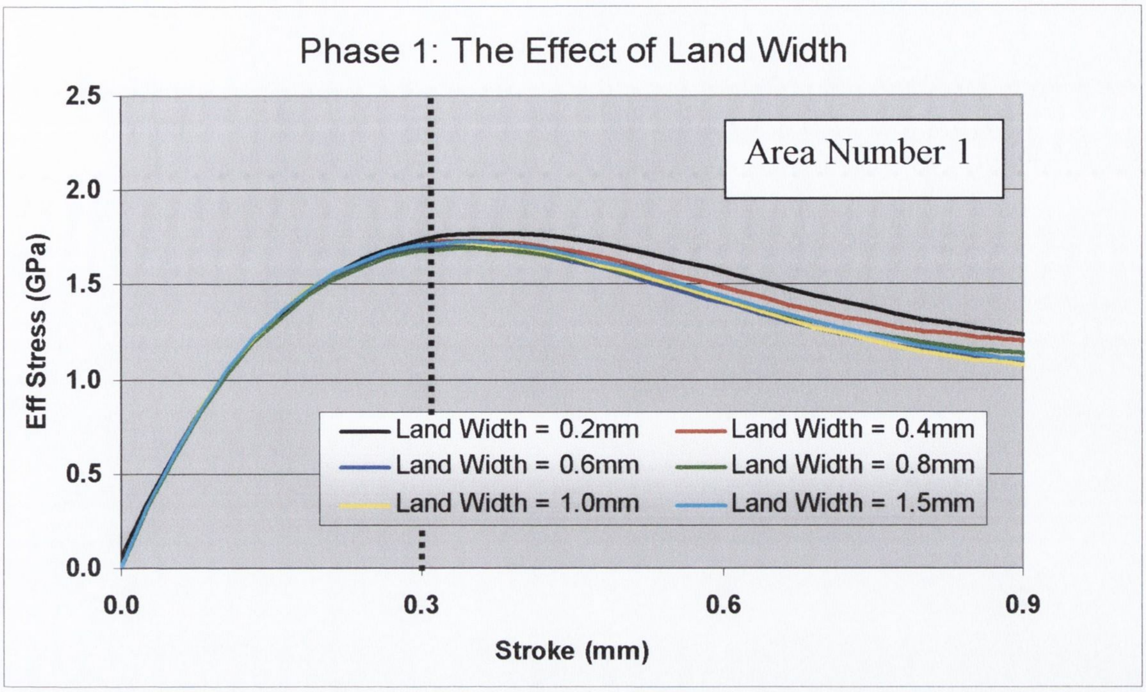

Figure 4-27: Effective Stress vs. Stroke for all 6 Land Width Models, Stroke range 0-0.9mm

The reason for this very small change in the magnitude of the effective stresses is explained due to the fact that all six models simulated had a fixed corner radius of 0.2mm, therefore the area in contact between the trim die and workpiece is approximately the same. Basically at this stroke of 0.3mm the trim die has penetrated into the workpiece by the same amount for all six models, and all have the same contact area, hence the similarity of results listed in table 4-13.

In Area 1, relating to a trim die stroke of 0.3mm, all six models induced similar effective stress values. For this reason, it is not necessary to show the shaded effective stress plots. Because of the similarity of the results it is not possible to determine the influence of the land width on the tool stresses at this level of deformation.

Area 2: Trim Die Stroke = 1.0mm

Figure 4-28 on the next page illustrates the effective stress results for all six models at Area 2. The range of stroke displayed on the x-axis allows the trends leading up to and following the 1.0mm mark to be visualised.

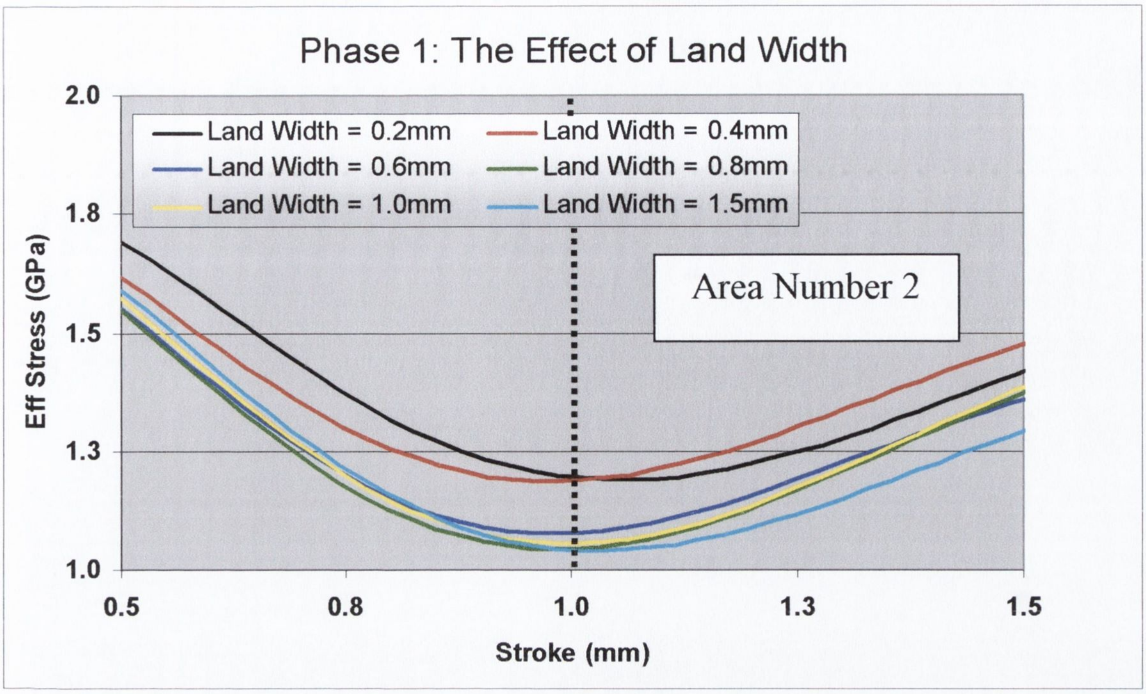

Figure 4-28: Effective Stress vs. Stroke for all 6 Land Width Models. Stroke Range 0.5 to 1.5mm

The maximum effective stress results at this stroke of 1.0mm are listed in table 4-14 below. With reference to figure 4-28 above and table 4-14 below, two distinct groups are visible. The black and red lines representing land widths of 0.2 and 0.4mm respectively, both induce very similar high stress levels, while the remaining 4 models induce similar, but lower, levels of stress.

'Land Width' Value (mm)	Induced Effective Stress (GPa)
0.2	1.195
0.4	1.186
0.6	1.076
0.8	1.042
1.0	1.055
1.5	1.041

Table 4-14: The Effect of Increasing the 'Land Width' at Area 2: Stroke = 1.0mm

Figures 4-29 to 4-34, illustrate why there are two distinct groups at this level of stroke at Area 2. The point on the trim die profile where the land width meets the petal surface is highlighted in figure 4-55, and is designated the 'land and petal corner'.

In figures 4-29 and 4-30, the workpiece material is forced to flow over the sharp land and petal corner. While in figure 4-31, the workpiece material has just started to flow over this corner and hence gives the next largest induced stress, indicated by the blue line in figure 4-28. The other three models do not experience this problem due to the larger land width values, see figures 4-31 to 4-34, and hence induce lower values of effective stress at Area 2.

With reference to figure 4-28, once the trim die has passed this stroke of 1.0mm, all six models show an increase in the effective stress levels. This occurs because from this point onwards the workpiece material makes contact with the top tool thereby introducing an additional resistance to material flow.

The 0.2 and 0.4mm land width models distribute the effective stresses over a smaller area compared to the other four models. The workpiece material flowing over the land and petal corner causes this concentration in the stress distribution.

With reference to figure 4-28 and table 4-14, the trim dies having land widths of 0.6 to 1.5mm all induced a similar level of effective stress. Changing the land width value from 0.6mm to 1.5mm caused a drop in the effective stress of 3.25%. With reference to table 4-14, the 1.5mm land width model induced the lowest value of effective stress of 1.041 GPa, and for that reason was deemed ‘optimum’ at this stage of the deformation process.

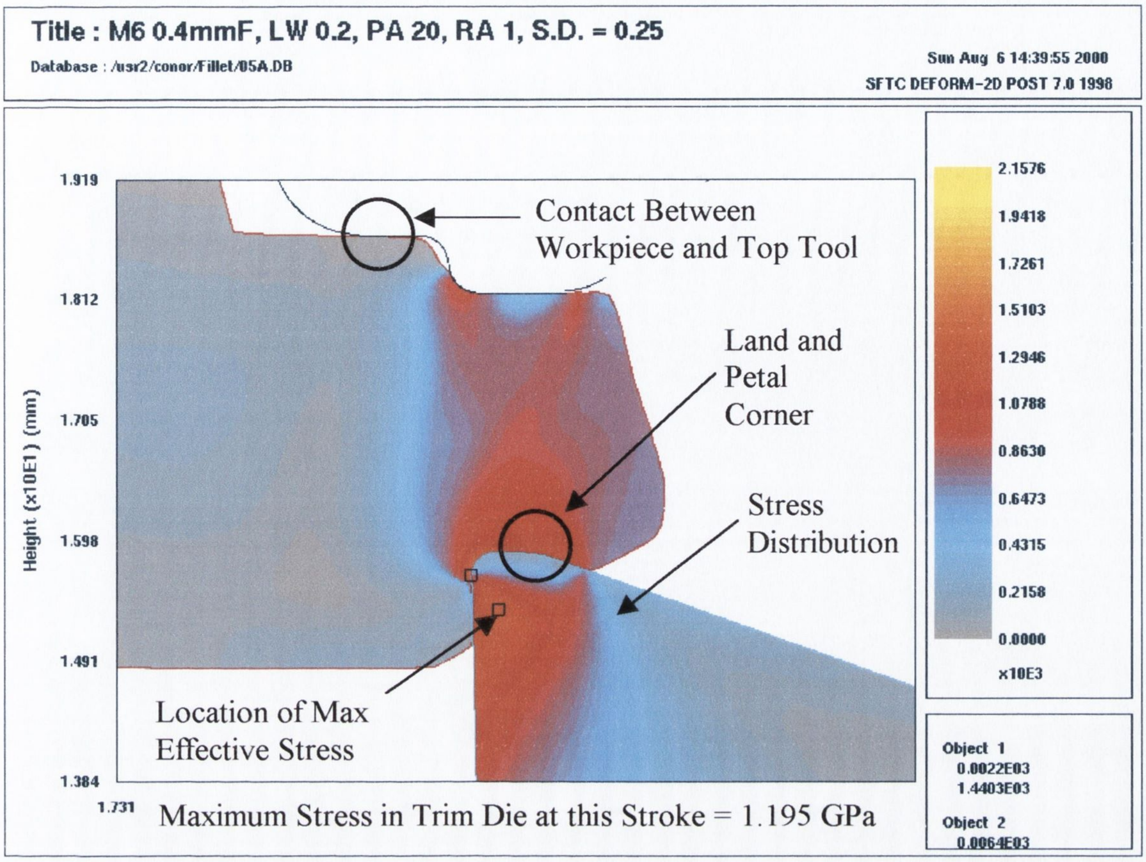

Figure 4-29: Effective Stress in the 0.2mm Land Width Trim Die at 1.0mm Stroke

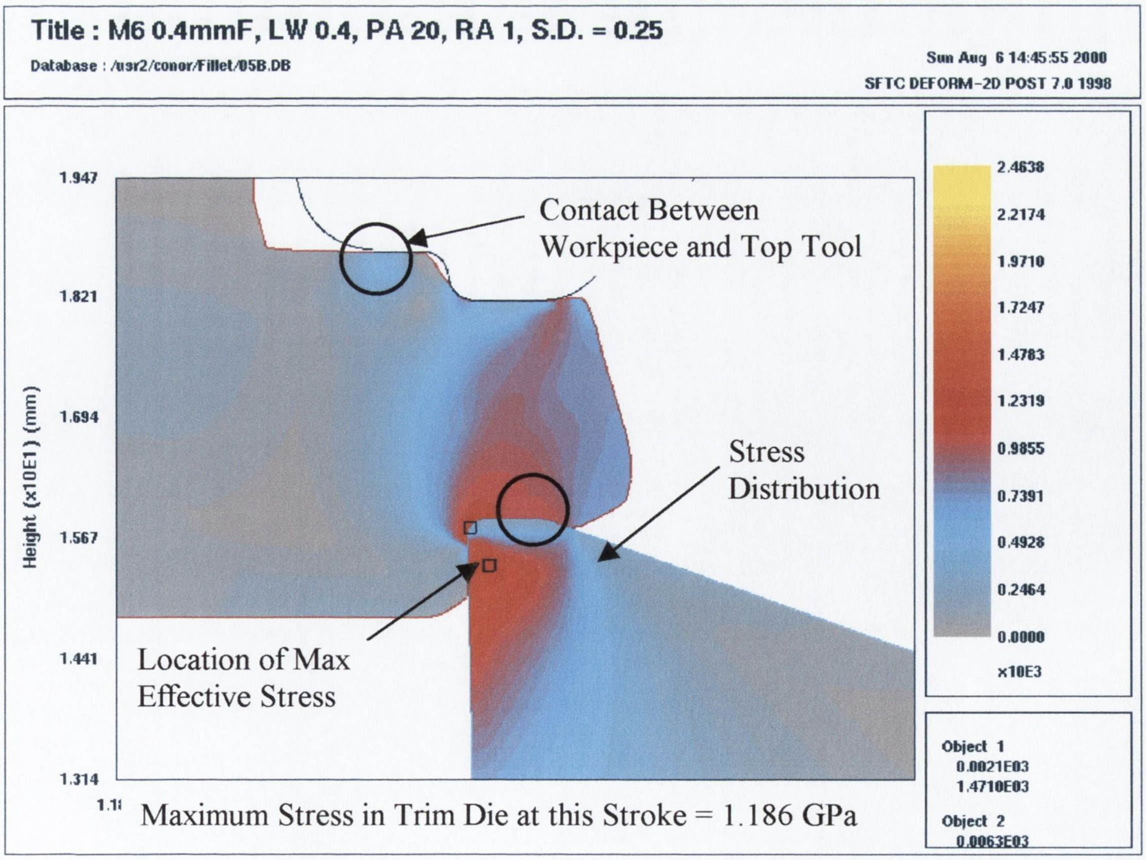

Figure 4-30: Effective Stress in the 0.4mm Land Width Trim Die at 1.0mm Stroke

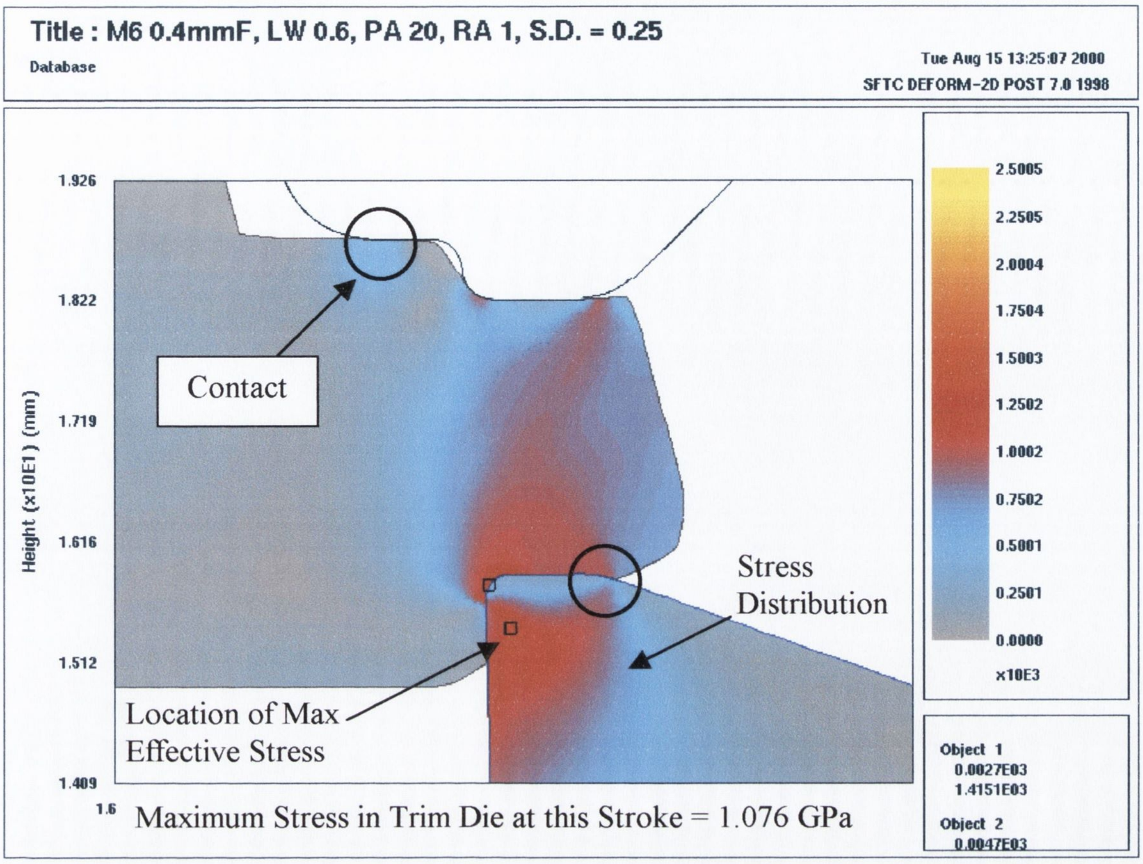

Figure 4-31: Effective Stress in the 0.6mm Land Width Trim Die at 1.0mm Stroke

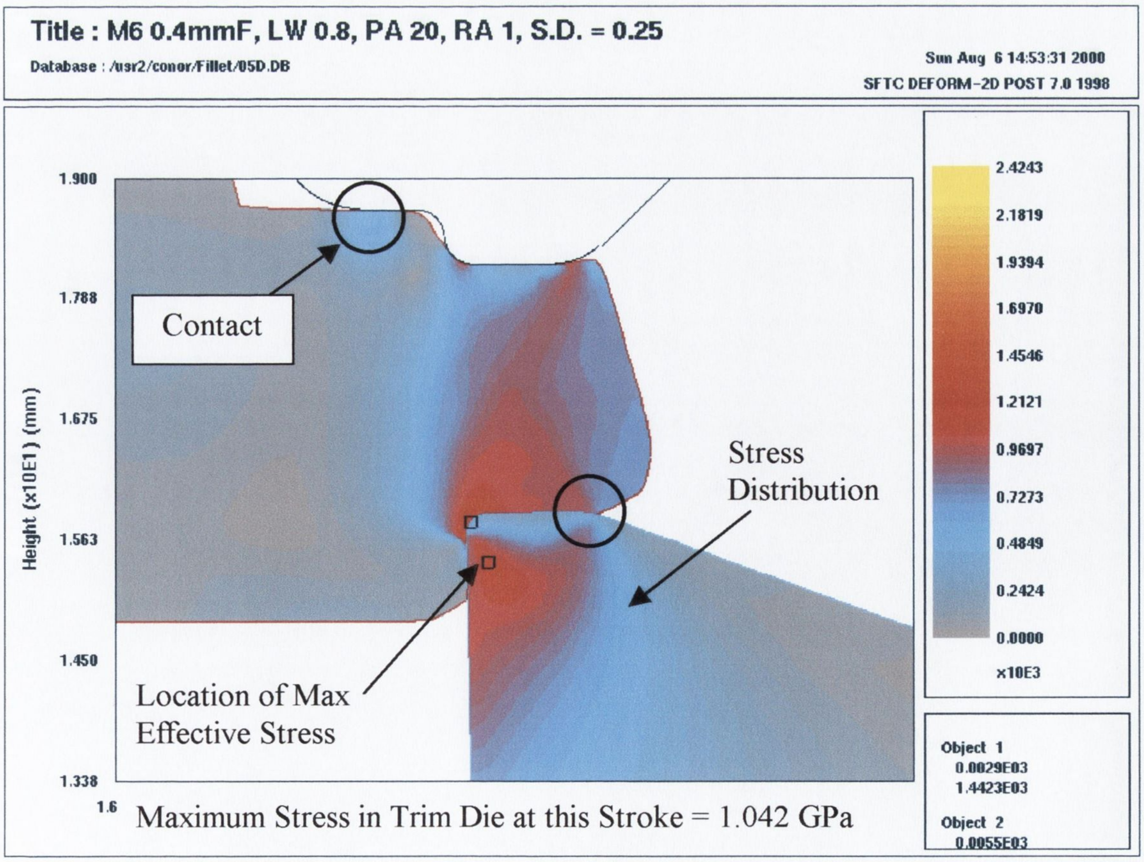

Figure 4-32: Effective Stress in the 0.8mm Land Width Trim Die at 1.0mm Stroke

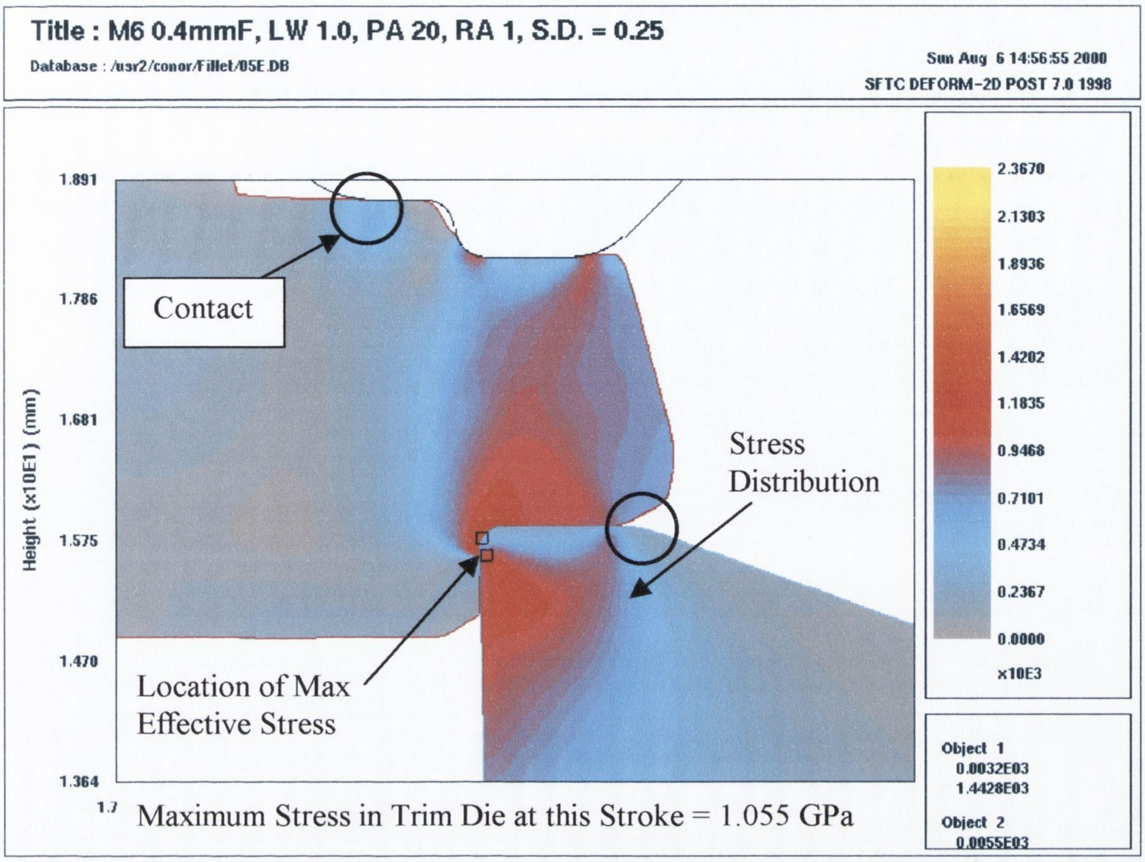

Figure 4-33: Effective Stress in the 1.0mm Land Width Trim Die at 1.0mm Stroke

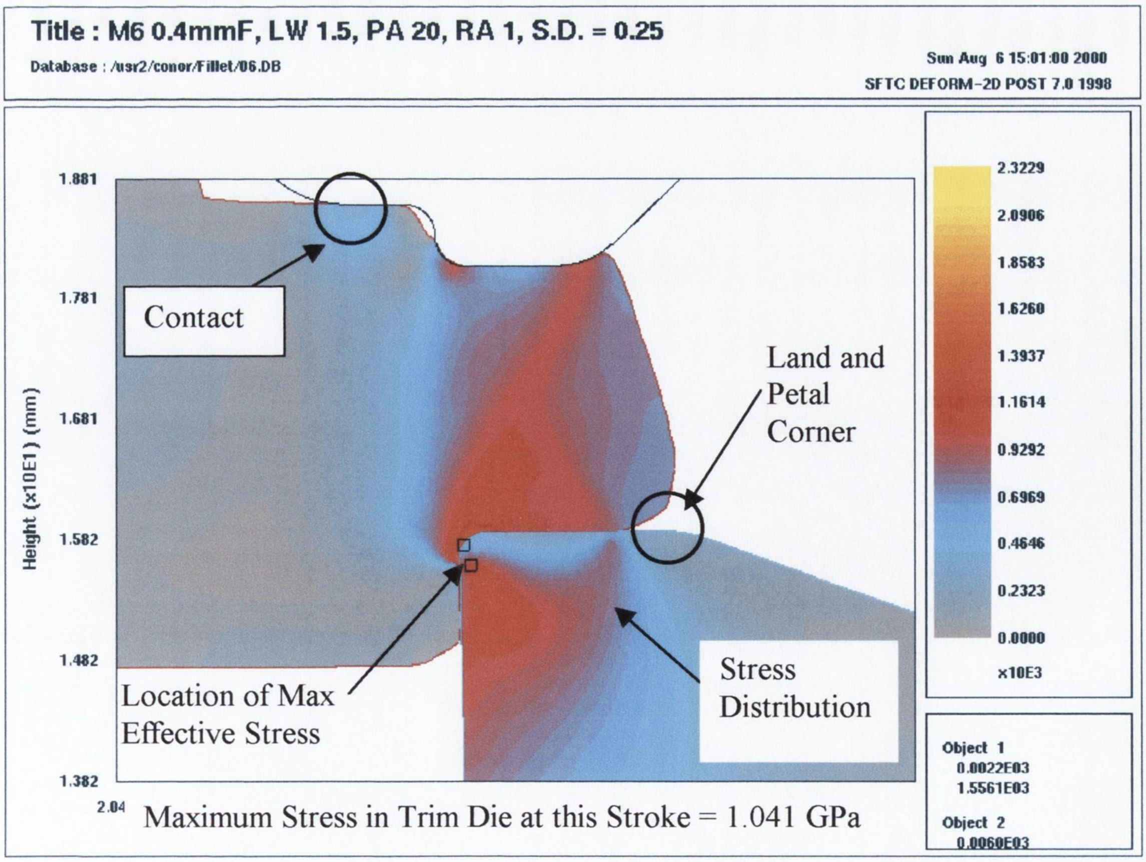

Figure 4-34: Effective Stress in the 1.5mm Land Width Trim Die at 1.0mm Stroke

Area 3: Trim Die Stroke = 3.0mm

Figure 4-35 below shows the effective stress versus stroke for all six 'Land Width' FEA models. All six models have travelled exactly the same amount of trim die stroke, 3.01mm. The two previous sections which analysed the 'fillet' and 'compound' corner geometries illustrated that in Area 3 there was a variation in the distance travelled by each trim die. The reason why all models simulated in this section travelled the same stroke is due to the corner geometry of 0.2mm, being held constant for all six models. Appendix D on page 238 provides a detailed explanation for variation in trim die stroke for models with varying corner radii.

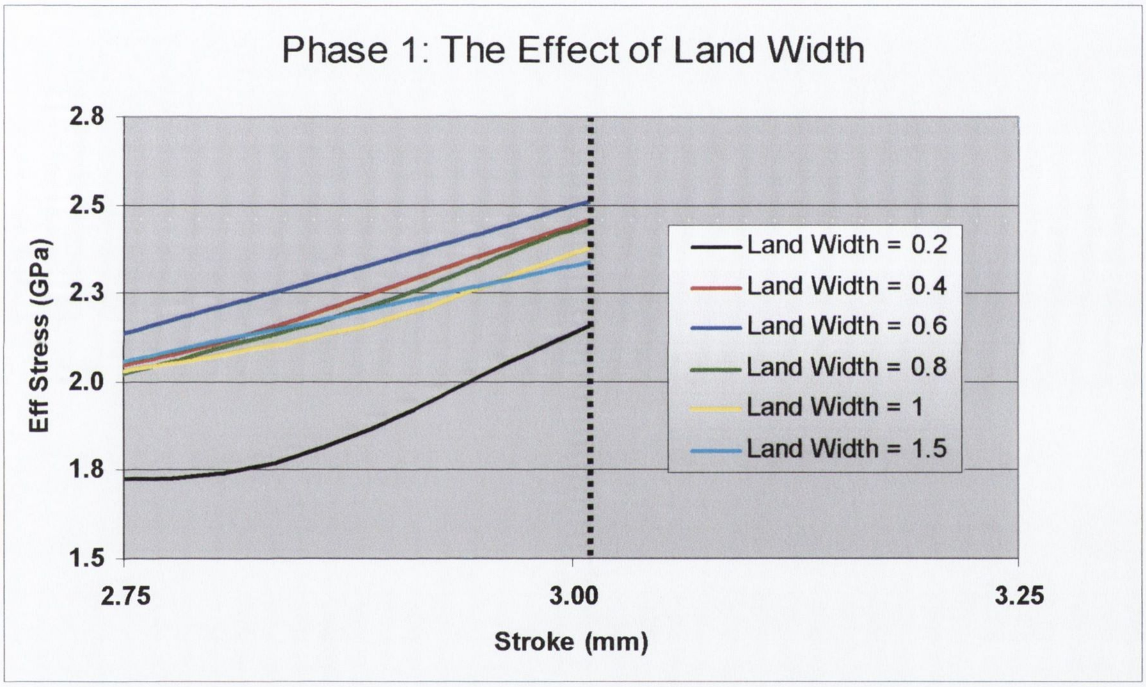

Figure 4-35: Effective stress vs. Stroke for all 6 Land Width models. Stroke range 2.75 to 3.25

The variations in the level of induced effective stress at the end of the trim die stroke are listed in table 4-15. As the land width is increased from 0.2mm to 0.6mm, the level of effective stress induced increases from 2.158 to 2.501GPa. This increase is caused, in part, by the change in the aspect ratio (L/h). The location of the trim die and top tool at the end of the stroke is illustrated in figure 4-36. A trim die profile with a land width of 0.2mm is shown in red, while the profile having a land width of 1.5mm is shown in black. As the 'Land Width' is increased from 0.2 to 0.6mm, the aspect ratio increases causing more material to become trapped and hence tending to increase the forging load and subsequent stress within the trim die.

'Land Width' Value (mm)	Induced Effective Stress (GPa)
0.2	2.158
0.4	2.464
0.6	2.501
0.8	2.424
1.0	2.367
1.5	2.323

Table 4-15: The Effect of Increasing the Land Width at the Final Value of Stroke.

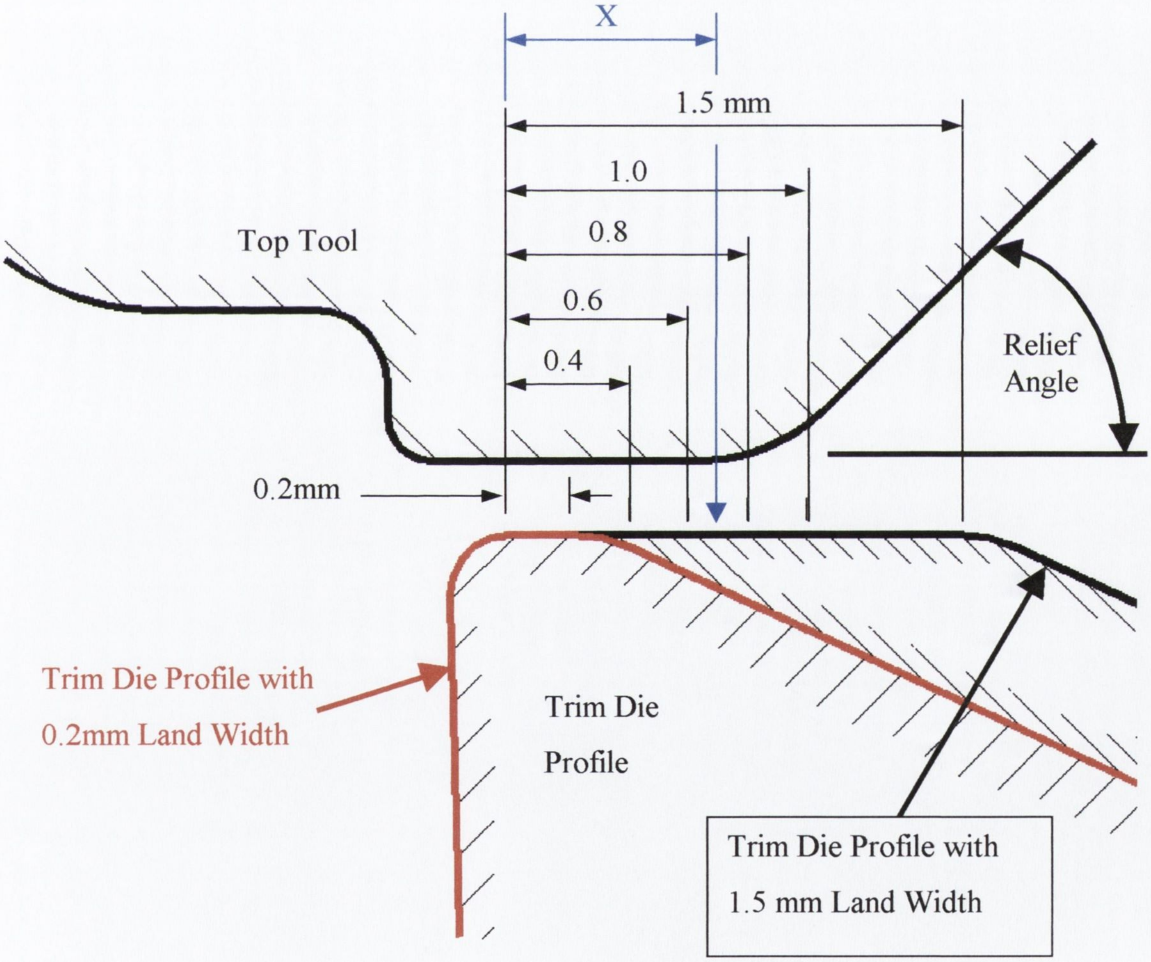

Figure 4-36: Close-up Detail of Trim Die and Top Tool Showing the Variation in Land Width Values

A further increase in the land width from 0.6 to 1.5mm should increase the induced stresses within the trim die, but they actually reduce. The reason why the stress levels drop from 2.501 to 2.323GPa is due to the shape of the top tool. A top tool with no relief angle, as in the models simulated in 1994, would cause more material to become trapped when the land width was increased from 0.6mm to 1.5mm. The blue dimension 'X' in figure 4-36 relates to a 'critical' value of the land width. The dimension 'X' relates to a value of 0.64mm, which is the length of the horizontal surface on the top tool. A trim die profile having a land width value equal to 'X', will trap the maximum amount of workpiece material between the trim die and top tool. Increasing the land width beyond this 'critical' value forces the excess workpiece material into the relief angle region provided by the geometry of the top tool. Therefore the aspect ratio reaches a maximum at the 'critical' value for the land width of 0.64mm. The flow of the workpiece material into the relief angle of the top tool is illustrated by comparing figures 4-37 and 4-42. In figure 4-42 a white arrow illustrates the upward movement of the trimmed material, caused by the large Land Width value of 1.5mm. The stress levels start to drop within the trim die once a land width of 0.8mm has been reached because of a strengthening effect produced by the increased load bearing area on the trim die. Increasing the land width, increases the amount of trim die material, and hence strengthens the tool.

A conclusion based on the levels of induced effective stress would be that the 0.2mm land width model is 'optimum' in this Area number 3.

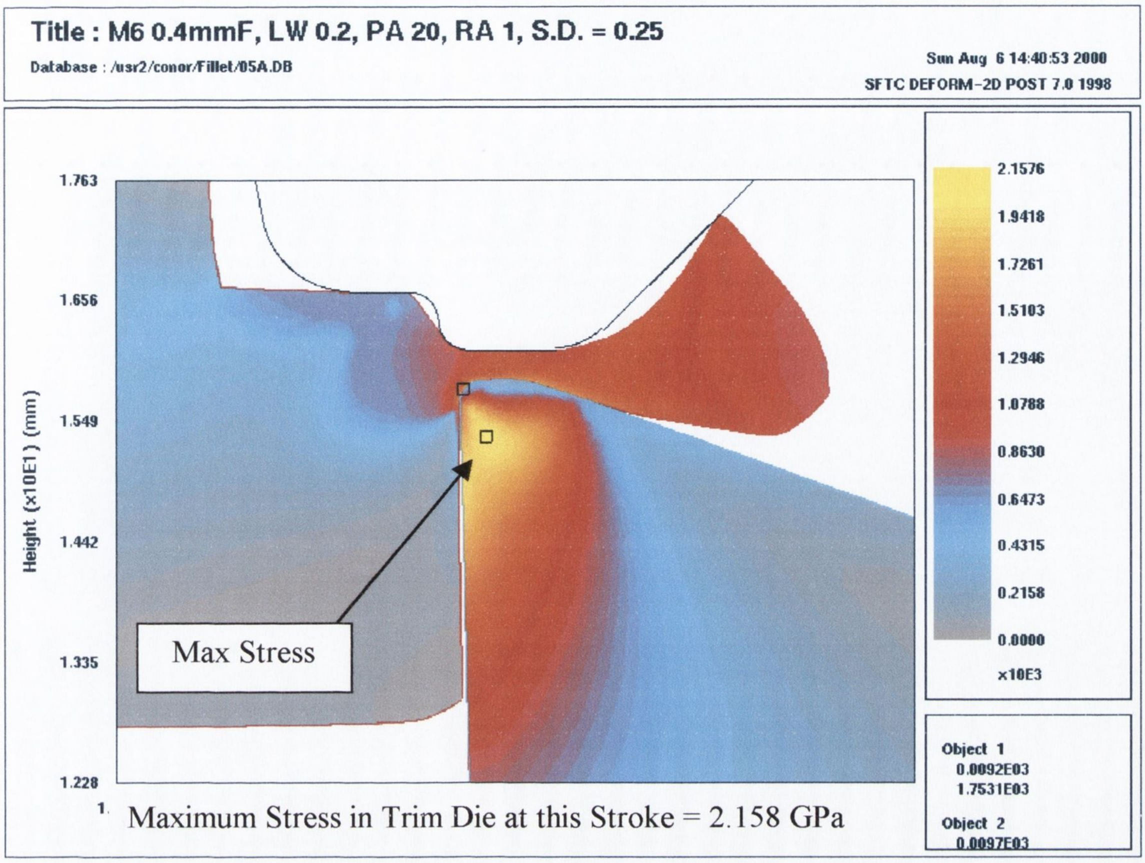

1. Maximum Stress in Trim Die at this Stroke = 2.158 GPa

Figure 4-37: Effective Stress in the 0.2mm Land Width Trim Die at the Final Stroke

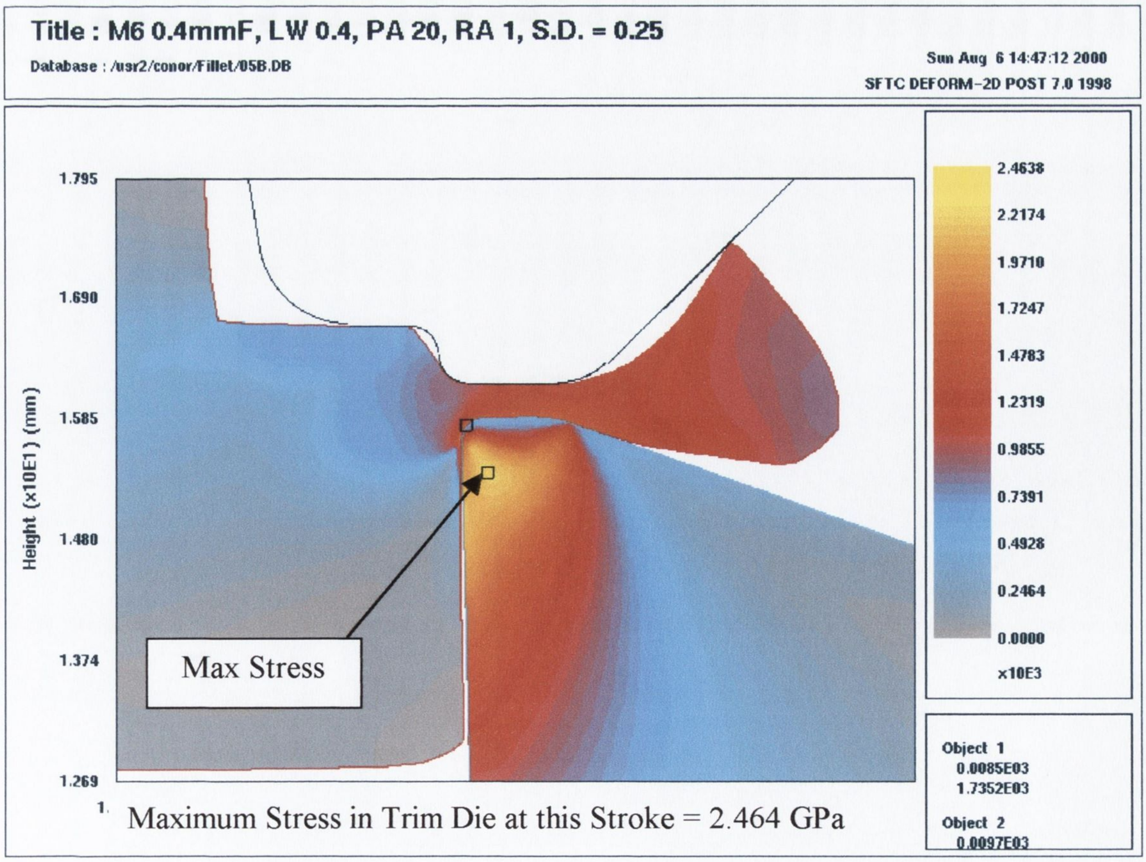

1. Maximum Stress in Trim Die at this Stroke = 2.464 GPa

Figure 4-38: Effective Stress in the 0.4mm Land Width Trim Die at the Final Stroke

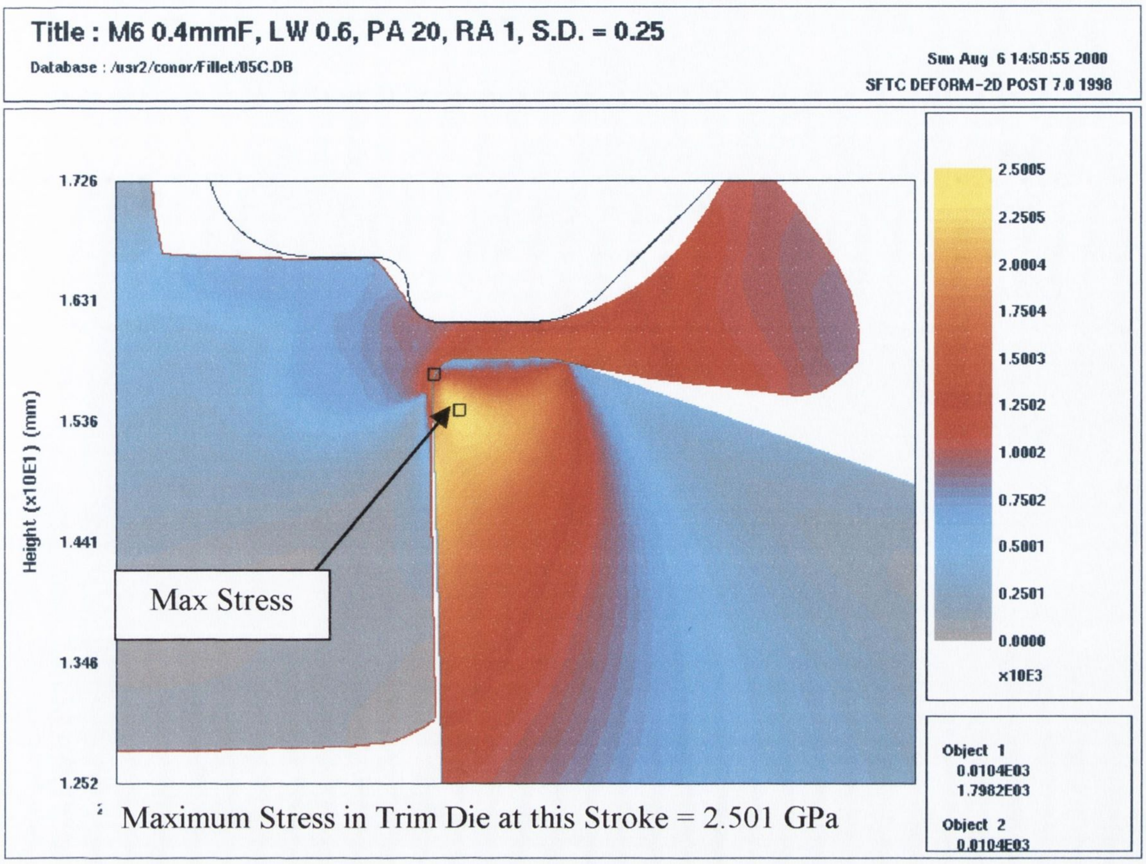

Figure 4-39: Effective Stress in the 0.6mm Land Width Trim Die at the Final Stroke

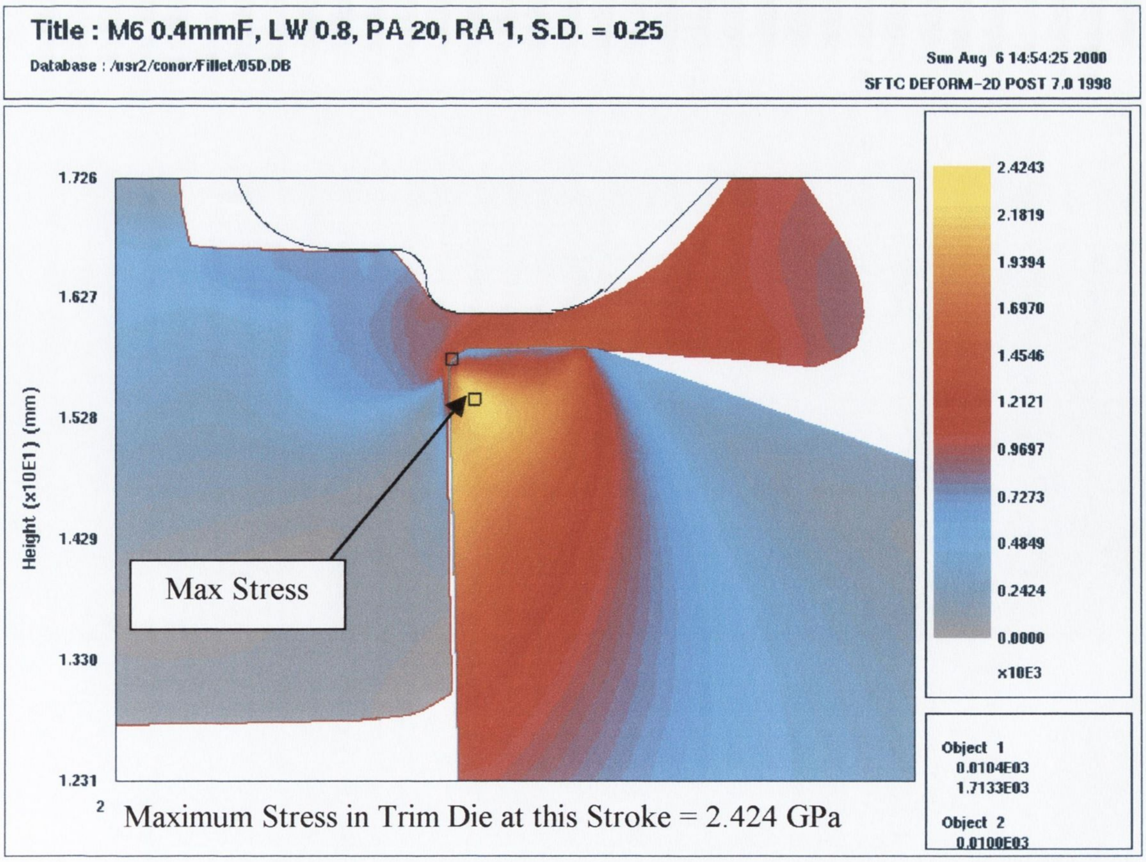

Figure 4-40: Effective Stress in the 0.8mm Land Width Trim Die at the Final Stroke

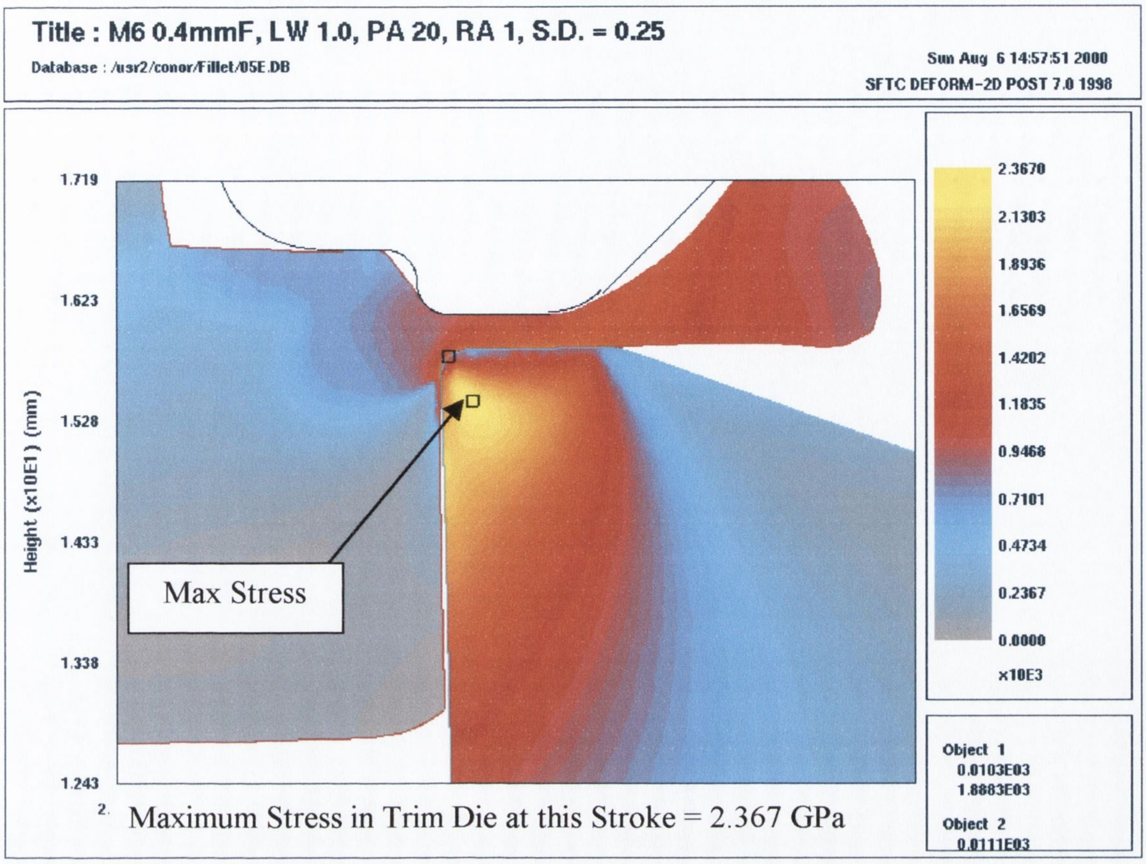

Figure 4-41: Effective Stress in the 1.0mm Land Width Trim Die at the Final Stroke

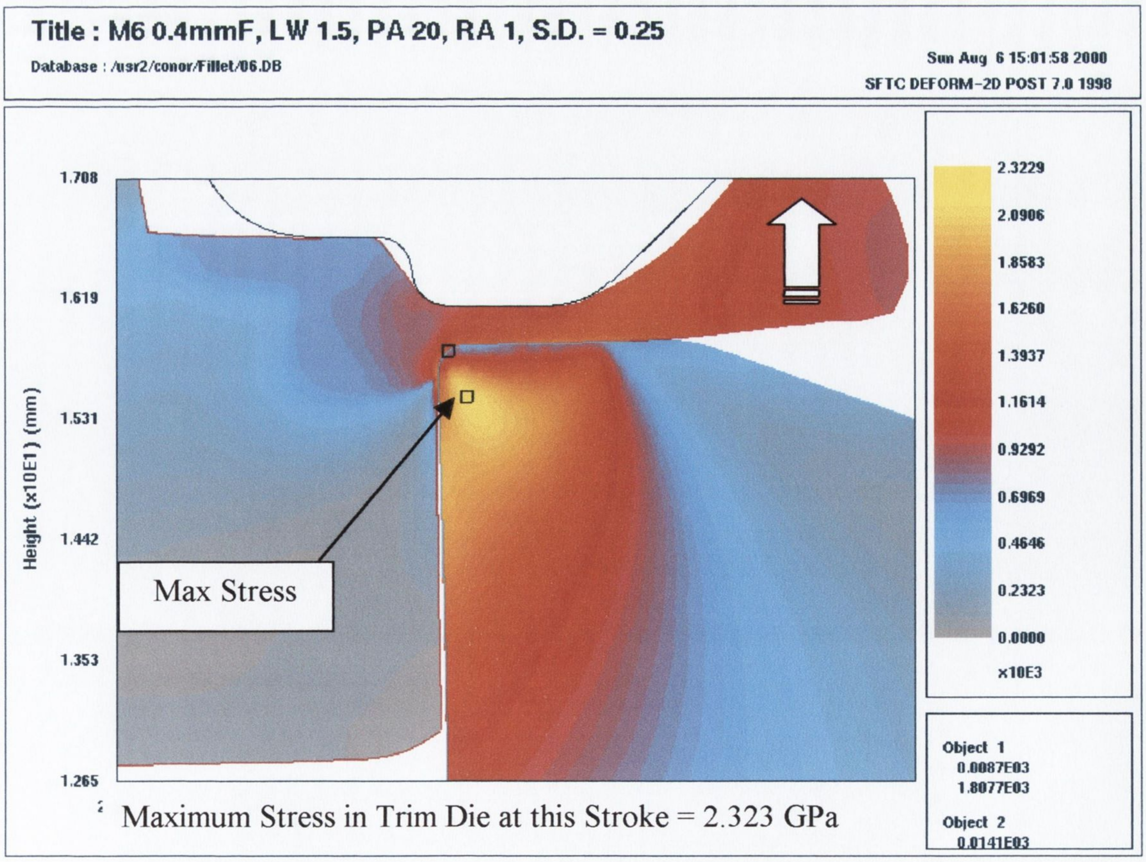

Figure 4-42: Effective Stress in the 1.5mm Land Width Trim Die at the Final Stroke

4.1.3.2 Maximum Tensile Radial Stresses:

The maximum tensile radial stresses acting along the top, or 'Land' surface of all six trim dies modelled in this section are listed in table 4-16 below.

Land Width (mm)	Maximum Tensile Radial Stress (MPa)
0.2	37.6
0.4	45.2
0.6	97.7
0.8	156.7
1.0	197.7
1.5	239.3

Table 4-16: Land Width Versus the Max Tensile Radial Stress

With reference to table 4-16, increasing the land width from 0.2 to 1.5mm caused the maximum tensile radial stress to rise from 37.6 MPa to 239.3 MPa respectively, an increase of 636%. These results are plotted in figure 4-43, and clearly indicate the large increase in the tensile radial stress when the land width is increased.

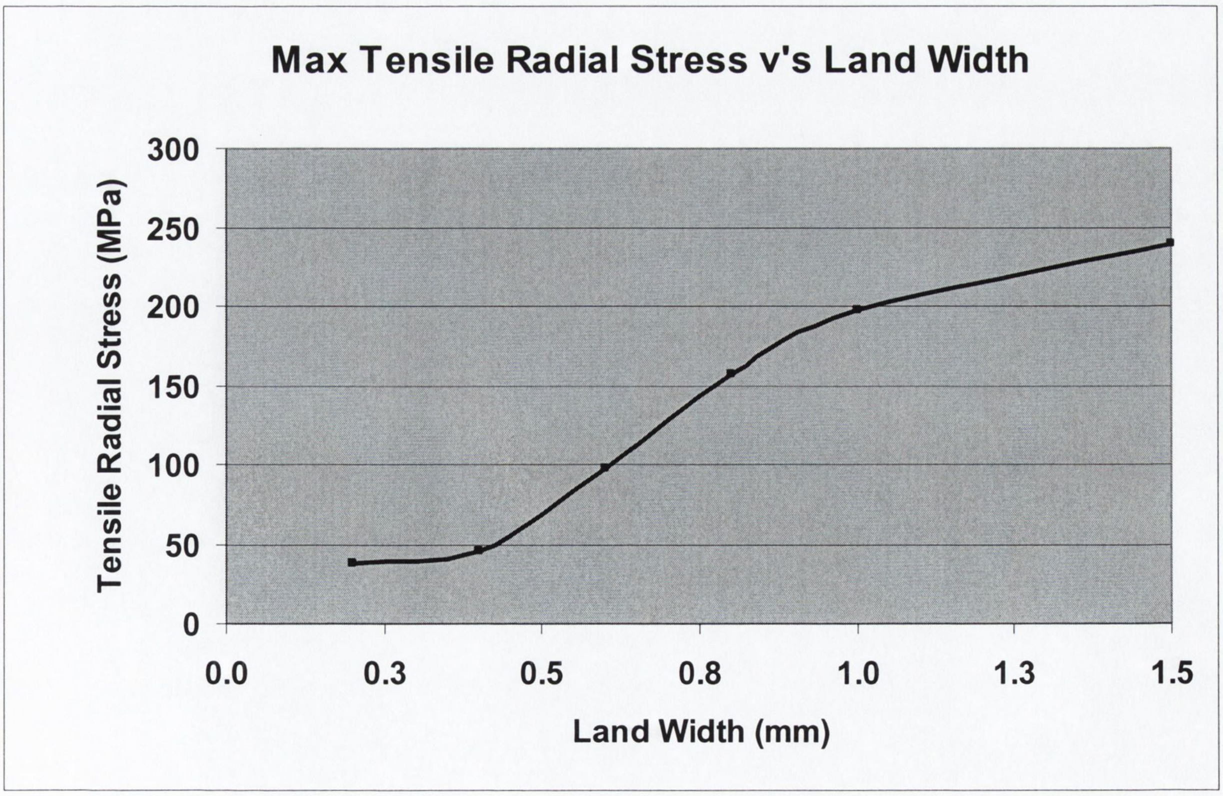

Figure 4-43: Phase 1: Maximum Tensile Radial Stress versus Land Width

4.1.3.3 Summary

In this Section 4.1.3, six FEA models were constructed where the 'Land Width' was varied, while the corner radius, petal and rake angles were held constant. The values for each of these parameters are listed in table 4-12 on page 107. The trim die stroke was divided into three areas and at each area the effective stress results were plotted against trim die stroke. The 'optimum' models at each area are listed in table 4-20 below.

Area Number	Trim Die Stroke (mm)	Optimum Land Width (mm)	Lowest Induced Effective Stress (GPa)
1	0.3	NA	1.677
2	1.0	0.6 to 1.5	1.041
3	3.0	0.2	2.158

Table 4-17: Phase 1: 'Optimum' Land Width Values

From tables 4-16, 4-17 and figure 4-43, the value of the land width, which was deemed 'optimum', was 0.2mm because:

1. This model induced the lowest effective stress at Area 3, where the stress levels are of a higher magnitude than Area 1 or 2.
2. This model induced the lowest tensile radial stress of 37.6 MPa

4.1.4 The Effect of Petal Angle

Figure 4-44 below shows the location on the trim die profile of the 'Petal Angle'. At this stage of the Phase 1 analysis, the effect of altering the petal angle was unknown. In an effort to determine the influence of this tool feature, six FEA models were constructed where only the petal angle was altered.

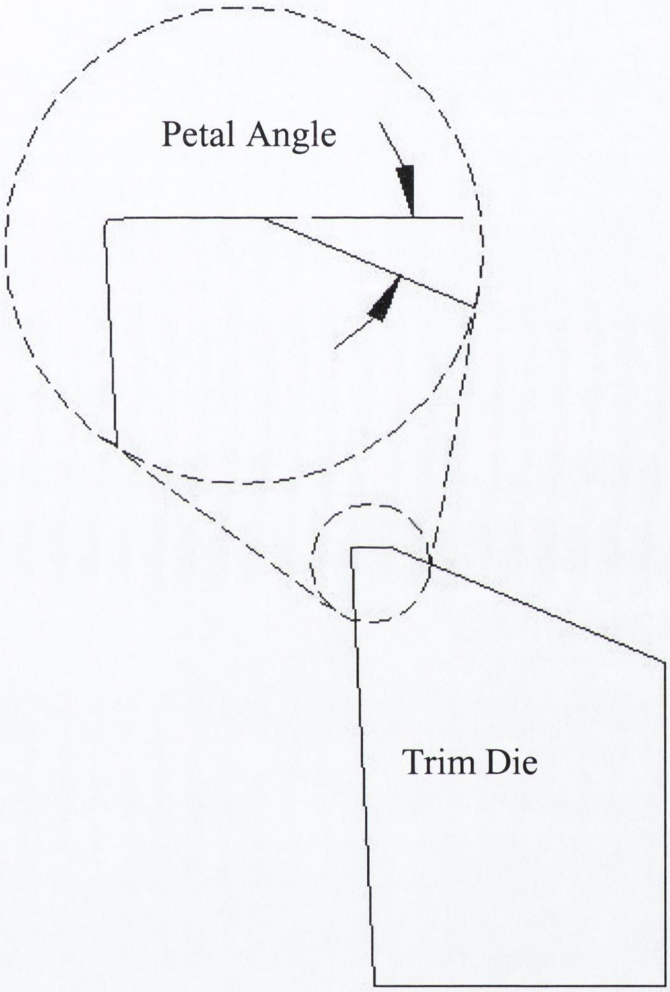

Figure 4-44: Trim Die Profile showing Location of the 'Petal Angle' Parameter

The values of the petal angle used along with the fixed values of corner radius, land width and rake angle are listed in table 4-18. As with the previous sections analysed, the trim die stroke is divided into three areas. Area1, 2 and 3 correspond to a trim die stroke of 0.3, 1.0 and 3.0mm respectively.

Parameter	Value
Petal Angle	20°, 25°, 30°, 35°, 40° and 45°
Corner Radius (Fillet)	0.4mm (Fixed)
Land Width	0.8mm (Fixed)
Rake Angle	1° (Fixed)

Table 4-18: Section 4.1.4. Trim Die Profile parameters and their corresponding Values

4.1.4.1 Effective Stress Results

Area 1: Trim Die Stroke = 0.3mm

Figure 4-45 illustrates the effective stress plotted against trim die stroke. At the stroke of 0.3mm, all the stress induced in all six models peak and then fall off towards a stroke of 1.0mm. This peak of stresses corresponds to the workpiece material yielding and then starting to flow plastically.

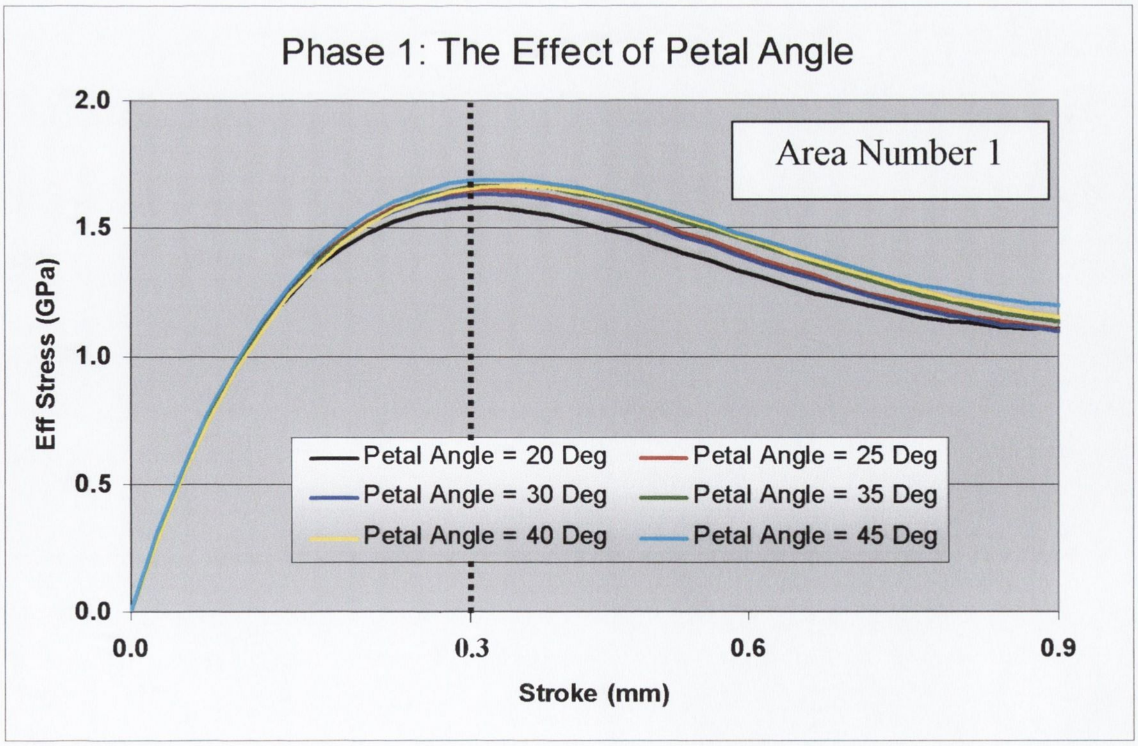

Figure 4-45: Effective Stress vs. Stroke for all 6 Petal Angle Models, Stroke Range 0-0.9mm

Table 4-19 below illustrates that increasing the petal angle in Area 1, causes a increase in the level of effective stress within the trim die.

'Petal Angle'	Induced Effective Stress (GPa)
20°	1.569
25°	1.629
30°	1.618
35°	1.637
40°	1.638
45°	1.664

Table 4-19: The Effect of Increasing the 'Petal Angle' at Area 1: Stroke = 0.3mm

Increasing the petal angle from 20° to 45° causes the effective stress to increase from 1.539 GPA to 1.664 GPa, which is an increase of approximately 8%. Figure 4-45 and table 4-19 illustrate that the level of induced effective stress, at Area 1, is directionally proportional to the petal angle, increasing the petal angle, increases the effective stress. Figures 4-46 & 4-47 show the effective shaded plots of the 20° and 45° models with a stroke equal to Area 1. From these figures it is clear that in Area 1, the workpiece material has not yet made contact with the petal surface. The area in contact at this level of stroke, is constant, therefore the rise in effective stress cannot be attributed to frictional considerations. The volume of the trim die is greatly affected by the petal angle, increasing the petal angle reduces the volume, which increases the load concentration and hence causes higher induced stresses within the trim die.

With reference to figure 4-45 and table 4-19, the trim die which induced the lowest level of effective stress at this area 1, had a petal angle of 20°.

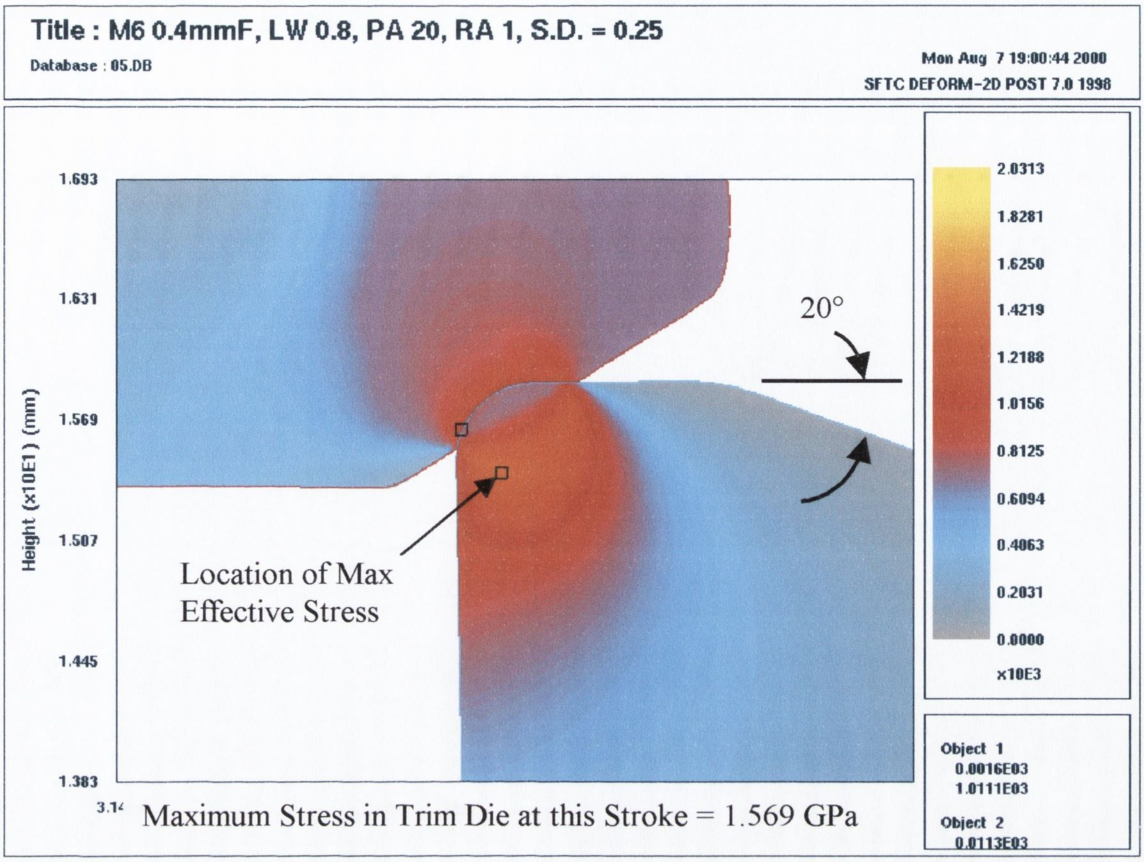

Figure 4-46: Effective Stress in the 20° Petal Angle Trim Die at 0.3mm Stroke

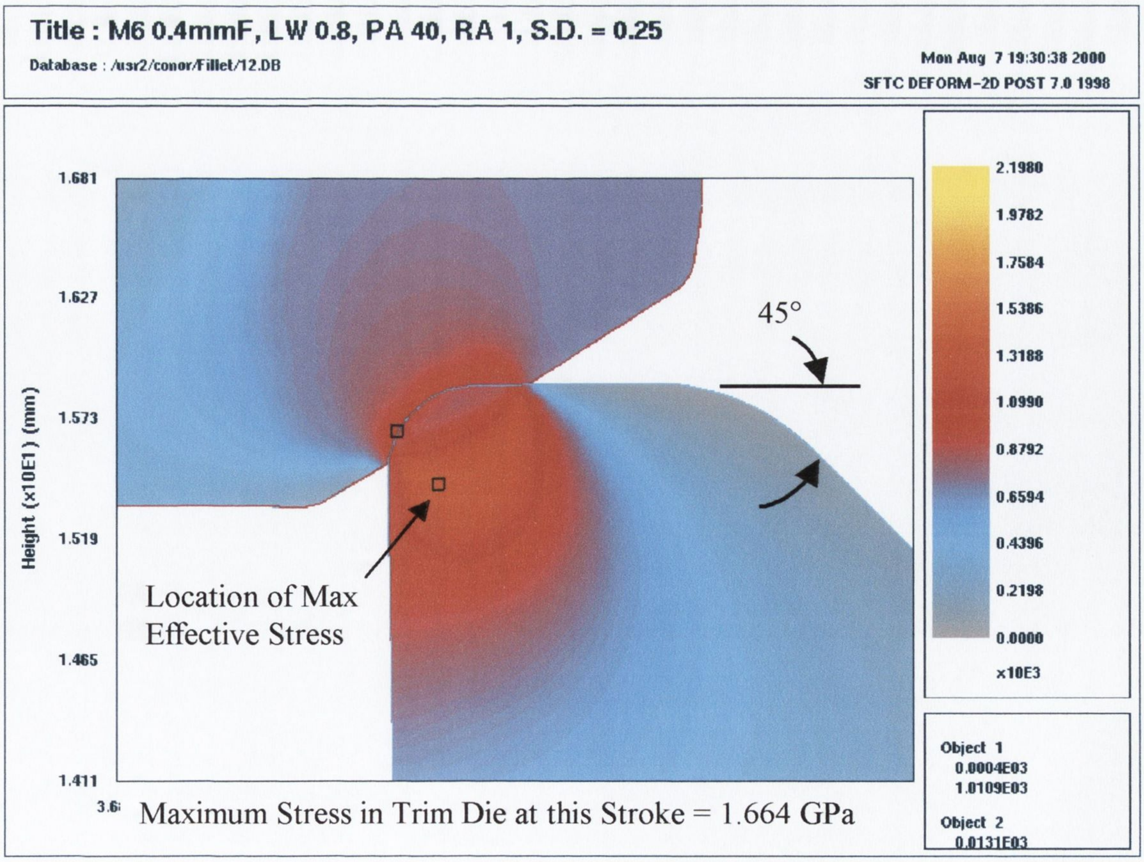

Figure 4-47: Effective Stress in the 45° Petal Angle Trim Die at 0.3mm Stroke

Area 2: Trim Die Stroke = 1.0mm

Figure 4-48 below illustrates the effective stress results against trim die stroke for all six petal angle FEA models.

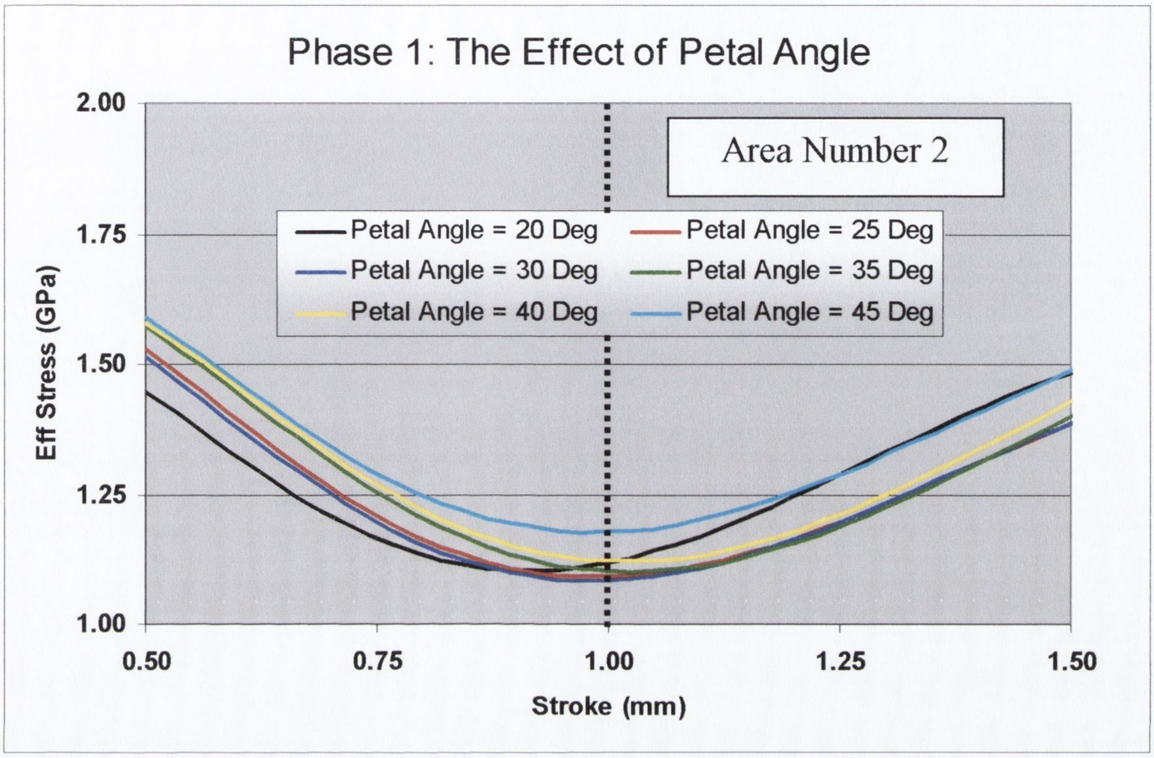

Figure 4-48: Effective Stress vs. Stroke for all 6 Petal Angle Models, Stroke Range 0.5 – 1.5mm

The maximum stress results at this stroke of 1.0mm are listed in table 4-20 below. A trim die having a petal angle of 45° induced the highest induced stress of 1.118 GPa°. After a stroke of 1.0mm, the stresses start to rise in all six models due to the workpiece material now making contact with the top tool.

‘Petal Angle’	Induced Effective Stress (GPa)
20°	1.118
25°	1.09
30°	1.087
35°	1.101
40°	1.121
45°	1.178

Table 4-20: The Effect of Increasing the ‘Petal Angle’ at Area 2: Stroke = 1.0mm

Figures 4-49 & 4-50 illustrate the distribution of effective stress for the 20° & 45° models at this level of stroke for Area 2. The location of the maximum effective stress within the trim die is in a similar position in both figures. Each trim die has the same general distribution of stress, at this level of stroke, which explains the small deviation in the induced stresses listed in table 4-20. The trim die with the largest petal angle of 45° sustained the greatest level of stress due to weakening of the trim die. As with all the models analysed to date, once the stroke of 1.0mm has been passed, all models show a rise in the level of induced effective stress. This rise is explained by the fact that the workpiece material now makes contact with the top tool and hence restricts the flow of the workpiece material. This contact between the workpiece and top tool is highlighted in figures 4-49 and 4-50, which represents the 20° and 45° petal angle models respectively.

With reference to figure 4-48, the black line, representing the 20° petal angle model, rises at a faster rate than the other five models. This faster rise in the effective stresses is caused by the smaller petal angle because it offers more resistance to the flow of the trimmed workpiece material. The increased resistance forces the workpiece material upwards into the relief angle of the top tool. The amount of penetration, at this stroke in Area 2, is insufficient to illustrate the increased resistance to flow of the workpiece material due to the smaller petal angle of 20°. For this reason, two images of the forging process at a stroke of 2.0mm are presented in figures 4-51 and 4-52. Each figure shows the shaded plot of the normal pressure during the forging process. Figure 4-51 shows the area in contact with the 20° petal angle model. The yellow region highlights the areas of the workpiece that are making contact with the trim die and top tool. There is a greater area in contact, between the workpiece and trim die in figure 4-51, than in figure 4-52 which represents a 45° petal angle model. With reference to these two graphs, it is clear that at this stage of the deformation process, having a smaller petal angle restricts the flow of the trimmed material and increases the normal pressure acting on the petal surface. This increased normal pressure causes a higher level of tangential shear stress, and friction at the interface between the workpiece and top tool. Because of this restriction, and the fact that the tangential shear stress has increased, the 20° petal angle model induced a higher rate of change in the level of effective stress in Area 2.

A conclusion based on the lowest level of effective stress induced at this stroke of 1.0mm in Area 2, is that the 30° petal angle FEA model was 'optimum'.

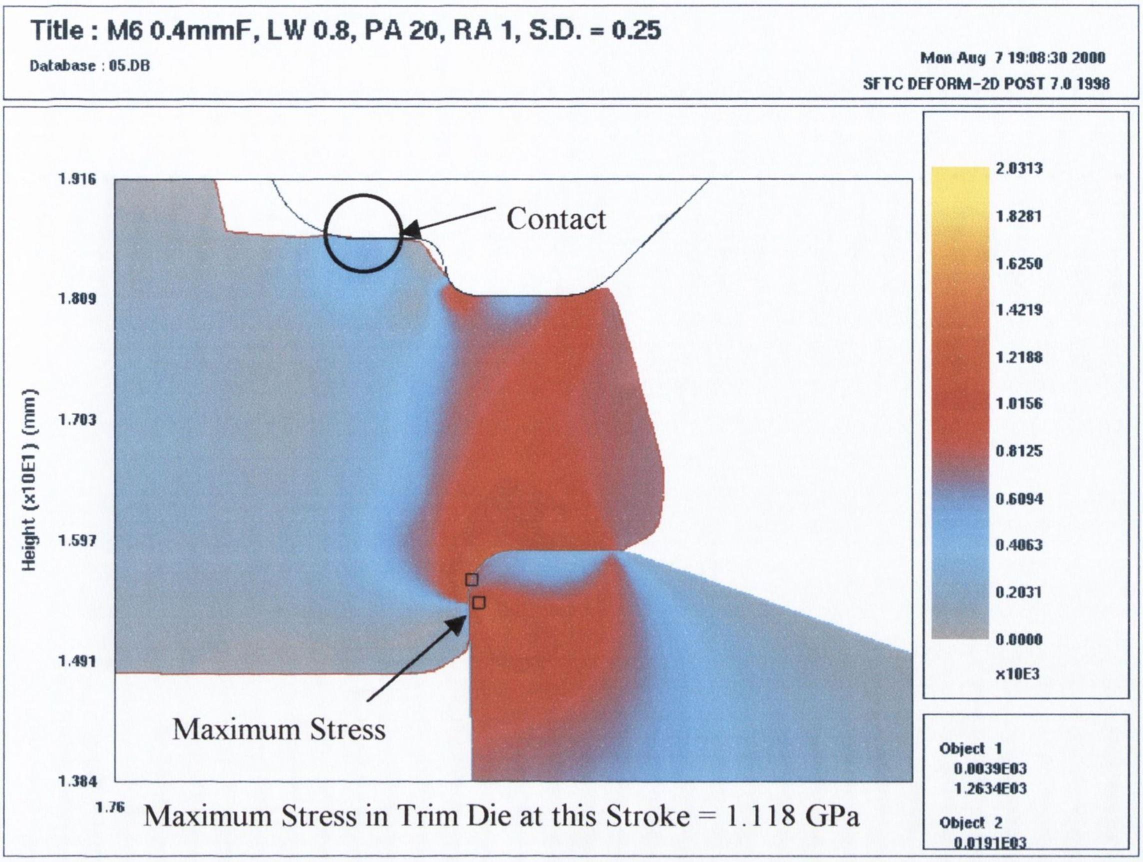

Figure 4-49: Effective Stress in the 20° Petal Angle Trim Die at 1.0mm Stroke

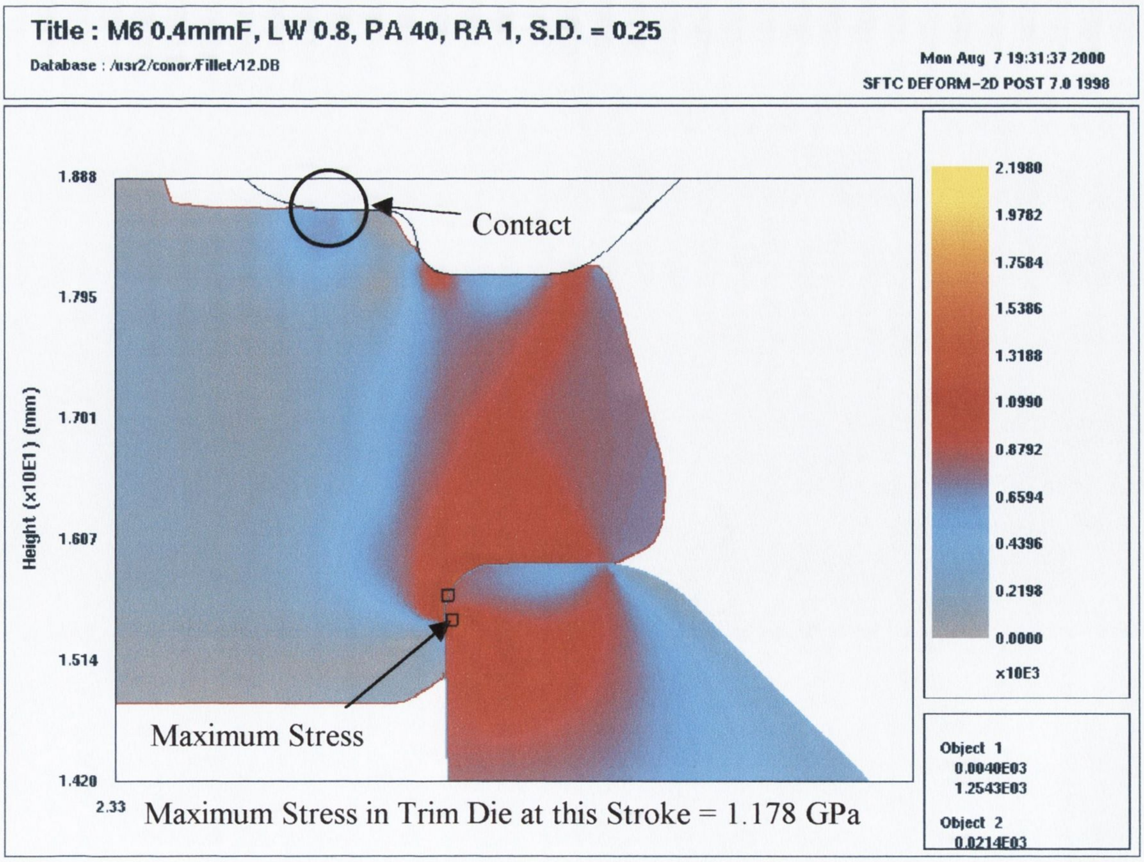

Figure 4-50 Effective Stress in the 45° Petal Angle Trim Die at 1.0mm Stroke

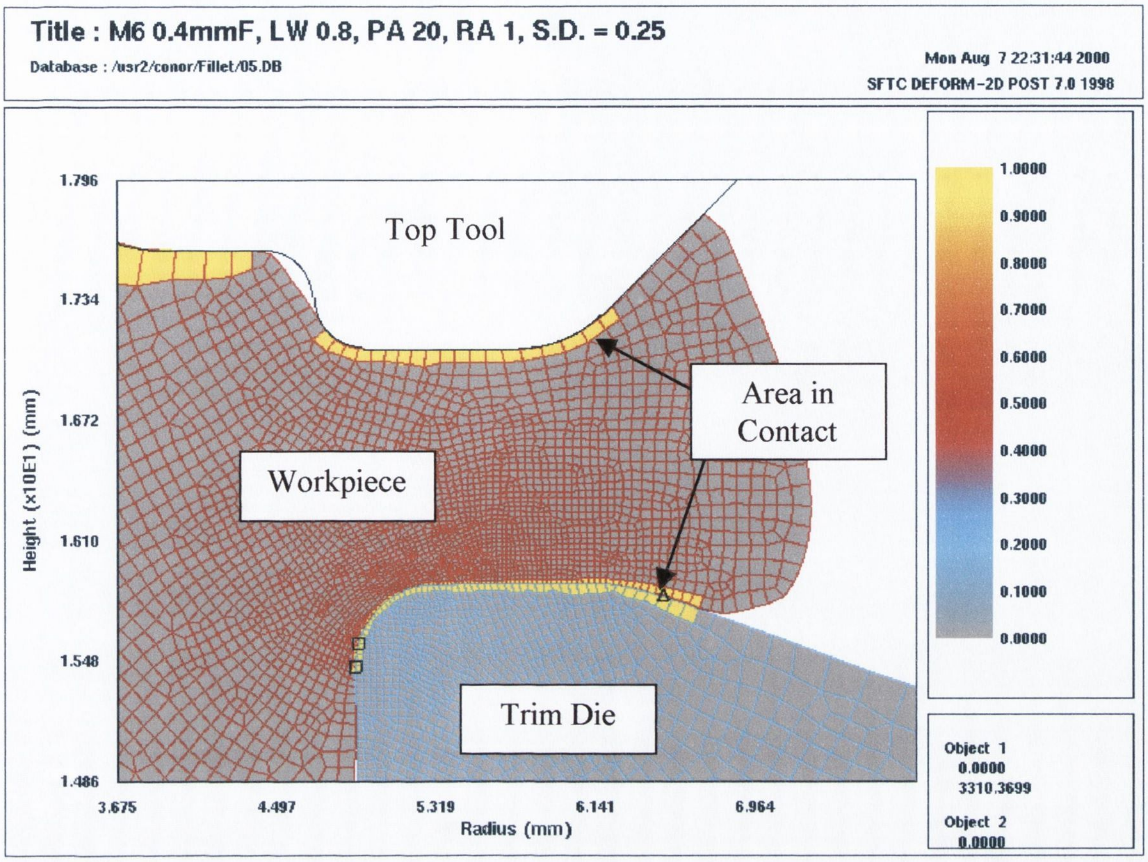

Figure 4-51: Normal Pressure at 2.0mm Stroke for the 20° Petal Angle Model

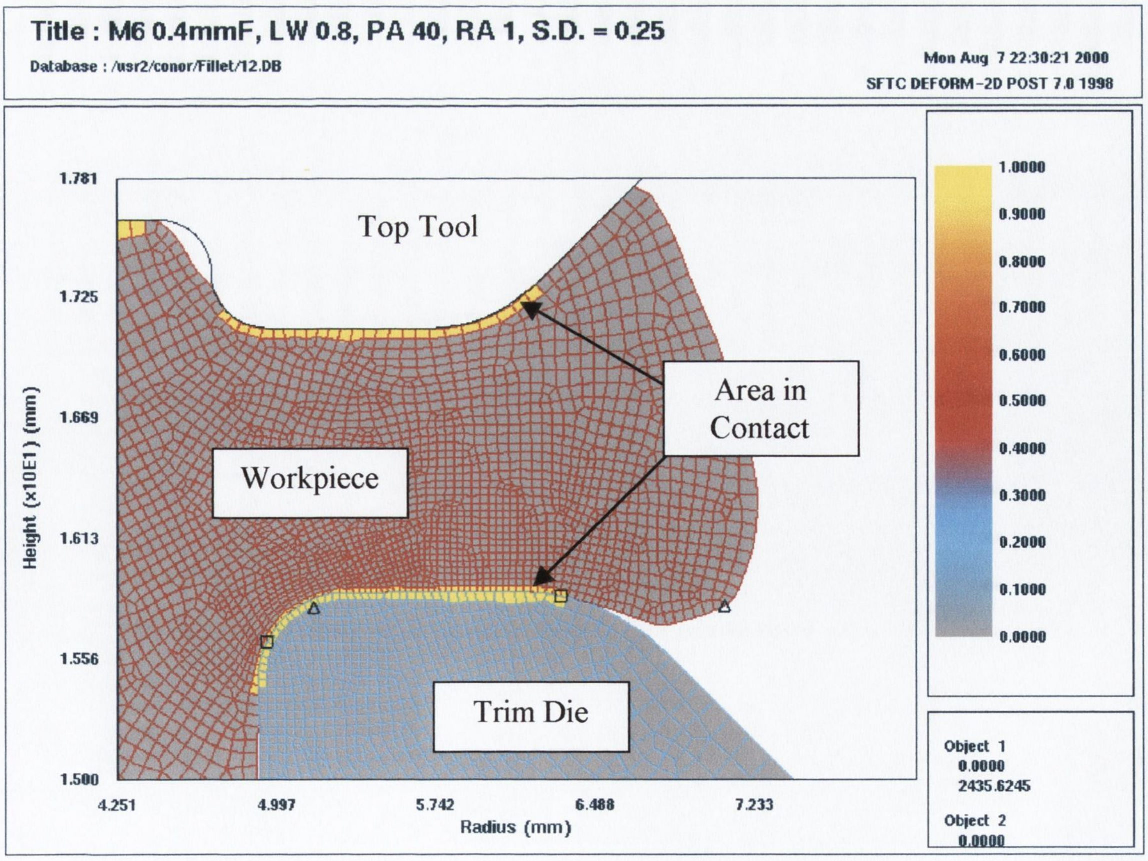

Figure 4-52: Normal Pressure at 2.0mm Stroke for the 45° Petal Angel Model

Area 3: Trim die Stroke = 3.0mm

Figure 4-53 below illustrates the effective stresses versus stroke for all six FEA models at the final stroke relating to Area 3. The total stroke of all six models was 2.92mm. This value for the final stroke is dictated by a feature of the trim die profile, mentioned earlier and which is explained in detail in Appendix D on page 238. All six models show a sharp increase in the induced stresses at the final stage of the forging process. As mentioned previously these large stresses at the final stroke of the trim die are typical for a forging operation involving trimmed or 'flash' material [41,2].

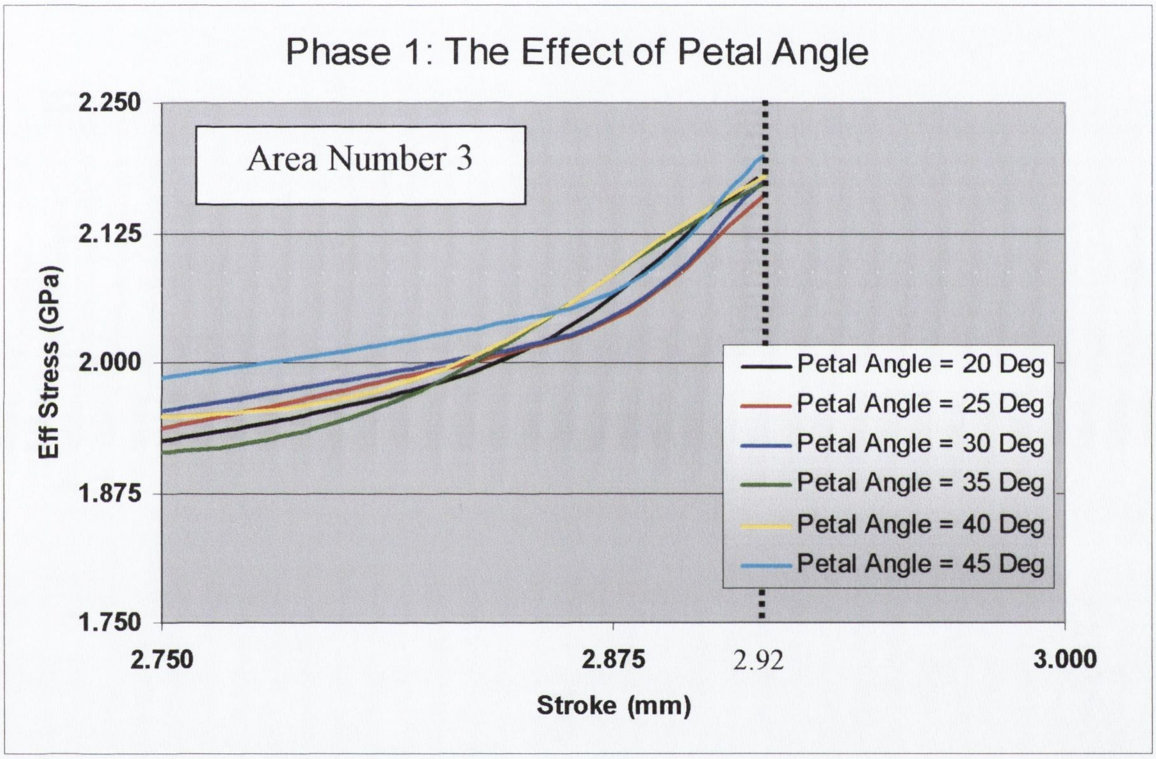

Figure 4-53: Effective stress vs. Stroke for all 6 Petal Angle Models. Stroke Range 2.75 to 3.0mm

The variations in the levels of induced effective stress at the end of the trim die stroke are listed in table 4-21. Figure 4-53 and table 4-21 indicate that the lowest effective stress value, induced in the trim die, occurred while using the 25° petal angle model, while the greatest induced effective stress occurred using the 45° petal angle model. Figure 4-54 plots the results listed in table 4-21. From this graph, the optimum petal angle of 25° is visible, however at this stage of the process, the petal angle is having little effect and the values for the effective stresses only differ by at most 1.7%.

'Petal Angle'	Induced Effective Stress (GPa)
20°	2.177
25°	2.161
30°	2.174
35°	2.172
40°	2.18
45°	2.198

Table 4-21: Phase 1: The Effect of Increasing the 'Petal Angle' at the Final Value of Stroke

As the trim die stroke increased from Area 2 to Area 3, the influence of the petal angle becomes more apparent.

As highlighted in Area 2, having a smaller petal angle causes:

1) A greater resistance to the flow of the workpiece material
2) A higher level of tangential shear stress between the workpiece and trim die due to an increase in the normal pressure

Increasing the petal angle would seem to be advantageous, but as the petal angle gets larger, the amount of trim die material available to support the forging load decreases and effectively the trim die is weakened. Therefore there is a balancing act between reducing tangential shear stress on one hand and increasing the strength of the trim die on the other. This results in a 'critical' value for the petal angle. This critical value offers a balance between the tangential shear stress at the interface between the workpiece and trim die, and the strength of the trim die. As the trim die reaches its final stroke, the influence of the tangential shear stress reduces, as the trimmed material is squeezed out in the radial direction causing separation between the workpiece, trim die and top tool. This separation is evident in figures 4-55 and 4-56 which represent the 20° and 45° petal angle models. The lowest level of induced effective stress of 2.161 GPa occurred while using the 25° petal angle model and is clearly highlighted in figure 4-54.

A conclusion based on the levels of induced effective stress would be that the 25° petal angle model is 'optimum' in this Area number 3.

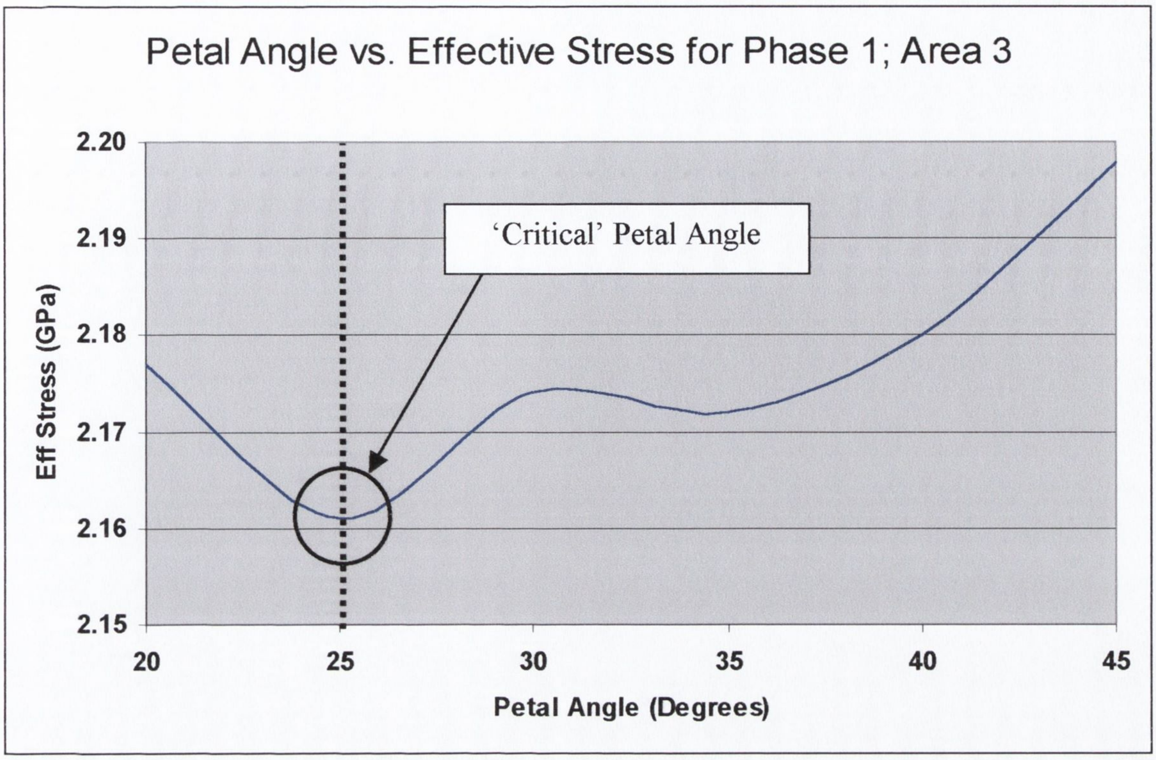

Figure 4-54: Phase 1: Effective Stress vs. Petal Angle at the final Stroke, Area 3

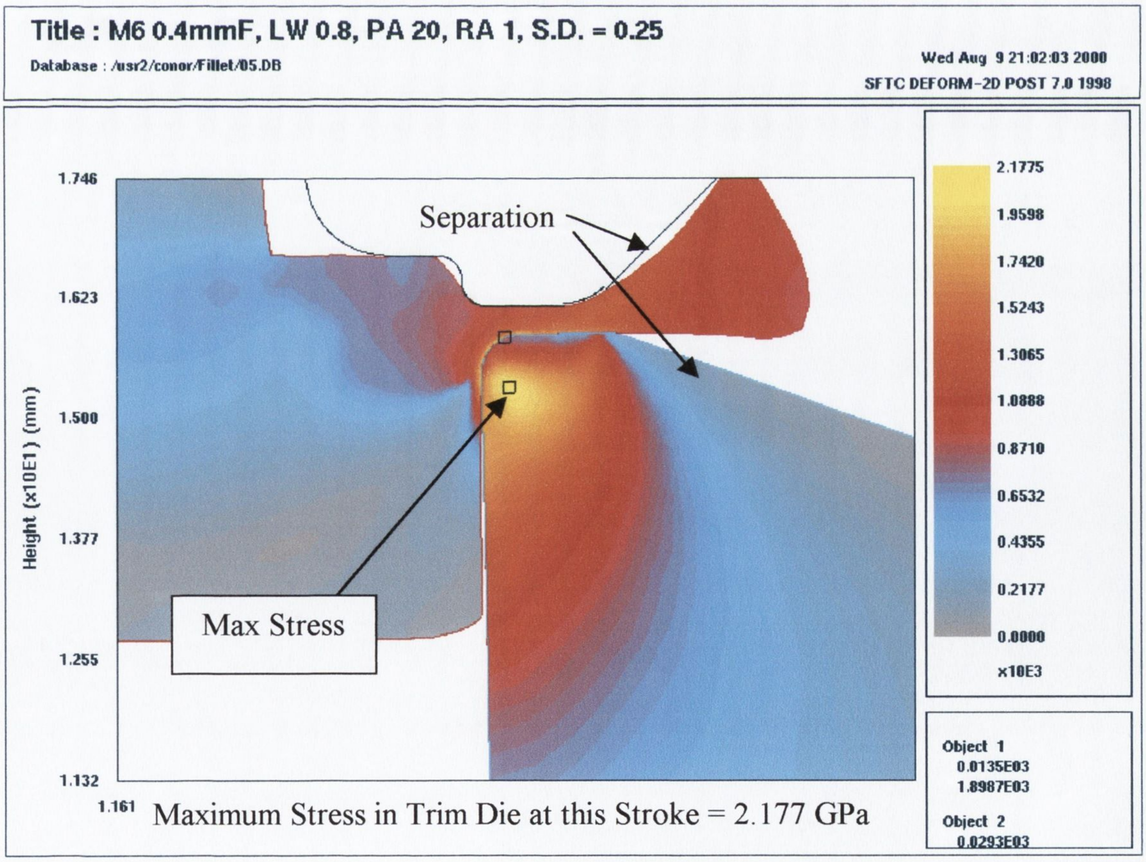

Maximum Stress in Trim Die at this Stroke = 2.177 GPa

Figure 4-55: Effective Stress in the 20° Petal Angle Trim Die at Final Stroke

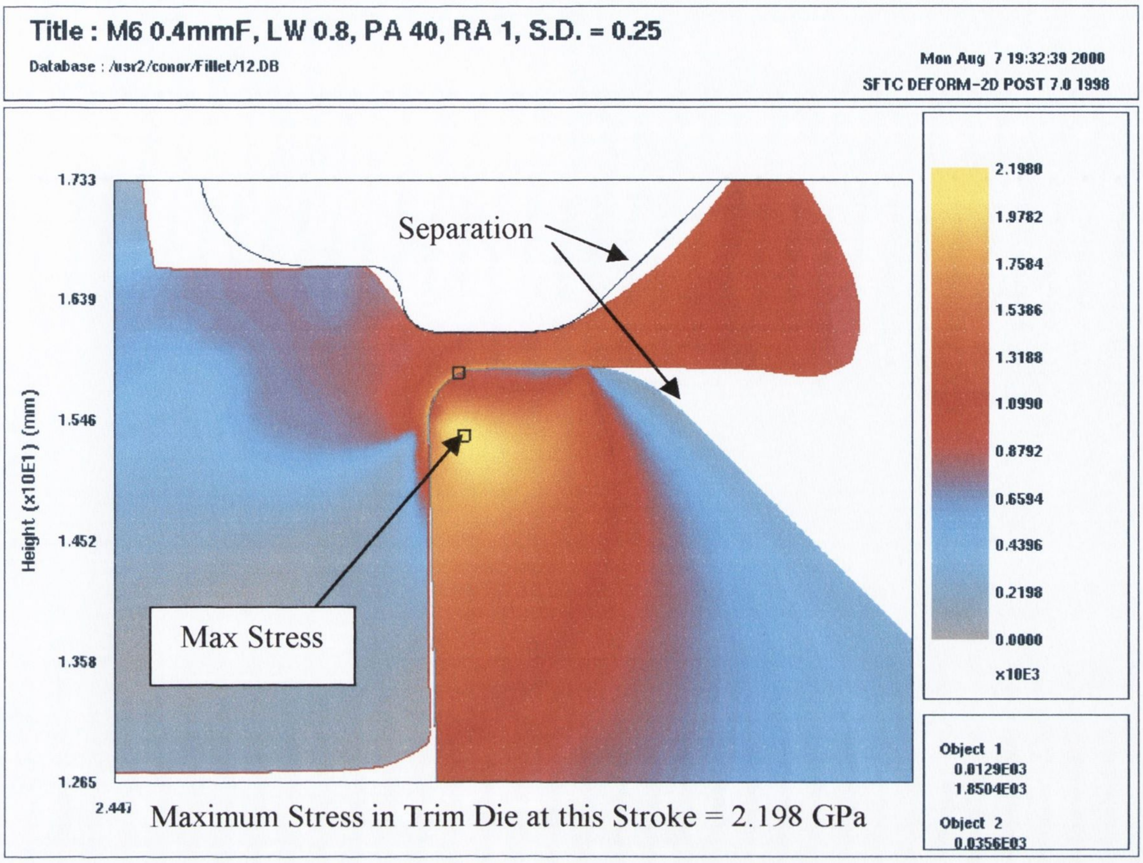

Figure 4-56: Effective Stress in the 45° Petal Angle Trim Die at Final Stroke

4.1.4.2 Maximum Tensile Radial Stresses:

The maximum tensile radial stresses acting along the top surface of all six trim dies modelled in this section are listed in table 4-22 below.

Petal Angle	Maximum Tensile Radial Stress (MPa)
20°	37.98
25°	38.49
30°	39.73
35°	39.78
40°	41.56
45°	42.35

Table 4-22: Petal Angle versus the Maximum Tensile Radial Stress

With reference to table 4-22 above, it can be seen that increasing the petal angle from 20° to 45° causes an increase in the tensile radial stresses from 37.98 MPa to 42.35 MPa which in an increase of 10.3%. These results are plotted in figure 4-57 below. Although the percentage change is small in comparison to those presented in the previous sections dealing with the 'fillet', 'compound' and 'Land Width' models, the trend is evident. Increasing the petal angle increases the tensile radial stresses along the top surface of the trim die.

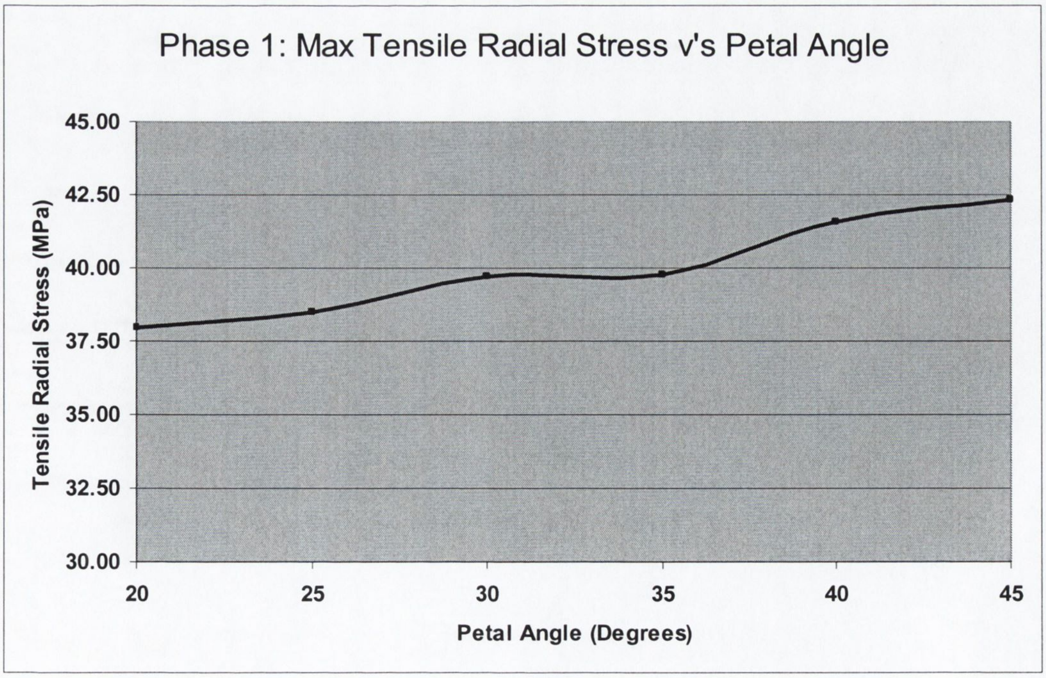

Figure 4-57: Phase 1: Maximum Tensile Radial Stress Versus Petal Angle

4.1.4.3 Summary

In this Section 4.1.4, six models were constructed and modelled where the 'Petal Angle' was varied, while the corner radius, land width and rake angle were held constant at the values listed in table 4-17 on page 123. Dividing the stroke of the trim die into three stages enabled greater detail of results. The 'optimum' petal angles for each of the stages analysed are listed in table 4-23 below.

Area Number	Trim Die Stroke (mm)	Optimum Petal Angle	Lowest Induced Effective Stress (GPa)
1	0.3	20°	1.569
2	1.0	30°	1.087
3	3.0	25°	2.161

Table 4-23: Phase 1: 'Optimum' Petal Angle Values

With reference to table 4-23, the 'optimum' petal angle varied in areas 1, 2 and 3. It is unclear as to which value of the petal angle is 'optimum'. The tensile radial stresses, shown in figure 4-57, indicated that the smaller petal angle induced the lowest tensile stress. Therefore based on the tensile radial stresses, the 20° petal angle is best. However, the maximum effective stresses listed in table 4-20, show that in the region of the highest magnitudes of stress i.e. Area 3, the 25° petal angle model induced the lowest value. The variation in tensile radial stresses between the 20° and 25° models is only 1.3%. Because of this reason, the 'optimum' petal angle for this phase 1 analyses was assumed to be 25°.

4.1.5 The Effect of Rake Angle

Figure 4-58 below shows the location, on the trim die profile, of the 'Rake Angle'. As with many of the features of the trim die profile discussed in the previous sections, the effect of altering the rake angle on tool stresses has not been considered previously. Five FEA models were constructed where only the rake angle was altered.

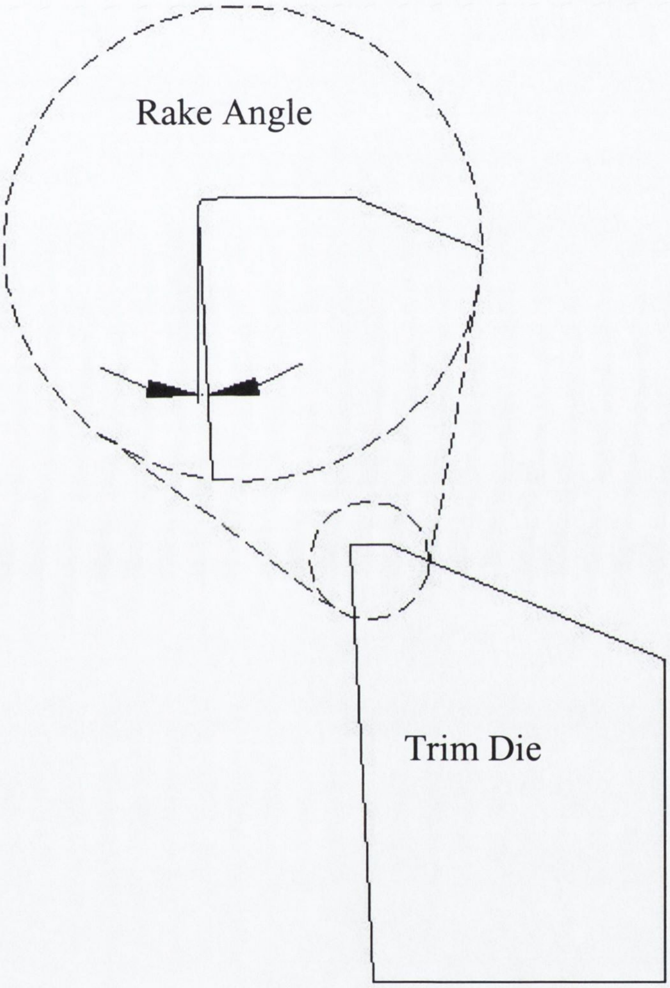

Figure 4-58: Trim Die Profile showing the Location of the 'Rake Angle' Parameter

As with all the FEA models simulated in Phase 1, only one parameter was altered at any one time. The values of the rake angle used, along with the fixed values of corner radius, land width and petal angle are listed in table 4-24. The trim die stroke was divided into stages 1, 2 and 3. For each of these stages the corresponding effective and tensile radial stresses are analysed and discussed.

Parameter	Value
Rake Angle	1°, 1.5°, 2°, 2.5° and 3°
Corner Radius (Fillet)	0.4m (Fixed)
Land Width	0.8mm (fixed)
Petal Angle	20° (Fixed)

Table 4-24: Section 4.1.5. Trim Die Profile Parameters and their Corresponding Values

4.1.5.1 Effective Stress Results

Area 1: Trim Die Stroke = 0.3mm

Figure 4-59 below illustrates the effective stress plotted against the trim die stroke. In Area 1, which relates to a stroke of 0.3mm, all the stresses induced in the five models peak and then fall off towards a stoke of 1.0mm.

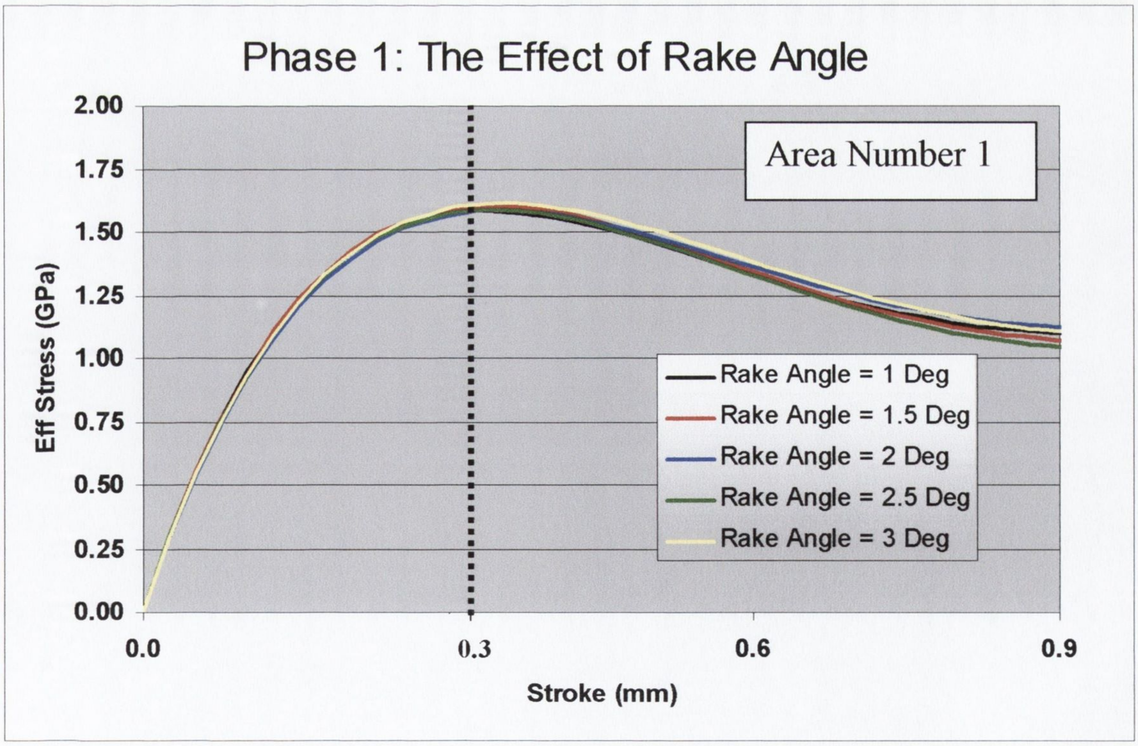

Figure 4-59: Effective Stress vs. Stroke for all 6 Rake Angle Models, Stroke Range 0-0.9mm

Table 4-25 below illustrates that increasing the rake angle from 1° to 3° causes a negligible change in the level of induced effective stress.

Rake Angle	Induced Effective Stress (GPa)
1°	1.57
1.5°	1.588
2°	1.566
2.5°	1.573
3°	1.59

Table 4-25: The Effect of Increasing the 'Rake Angle' at Area 1: Stroke = 0.3mm

The greatest difference in the magnitude of the effective stress occurred between the 1.5° and 2° petal angle models producing a maximum deviation of approximately 1.3%. All five models induced very similar levels of stress in Area 1 because each model had the same corner radius of 0.4mm and land width of 0.8mm. Due to the similarity of results for each model simulated in Area 1, only two shaded plots of the induced effective stress are shown in figures 4-60 and 4-61. Figure 4-60 and 4-61 relate to the extremes of the rake angles simulated i.e. 1° and 3° respectively.

Comparing the 1° and 3° rake angle models shown in figures 4-60 and 4-61 respectively, indicate the following:

1. The location of the maximum effective stresses within the trim is identical.
2. The distribution of these effective stresses are very similar

With reference to figures 4-59,60 and 61 and table 4-25, all five FEA models induced similar levels of effective stress and distributed these stresses over the same area. Therefore in Area 1, altering the rake angle from 1° to 3° had no significant effect on the effective stresses within the trim die but the 2° model induced a marginally lower level of effective stress. Therefore in Area 1, the 2° rake angle trim die model was marginally 'optimum'.

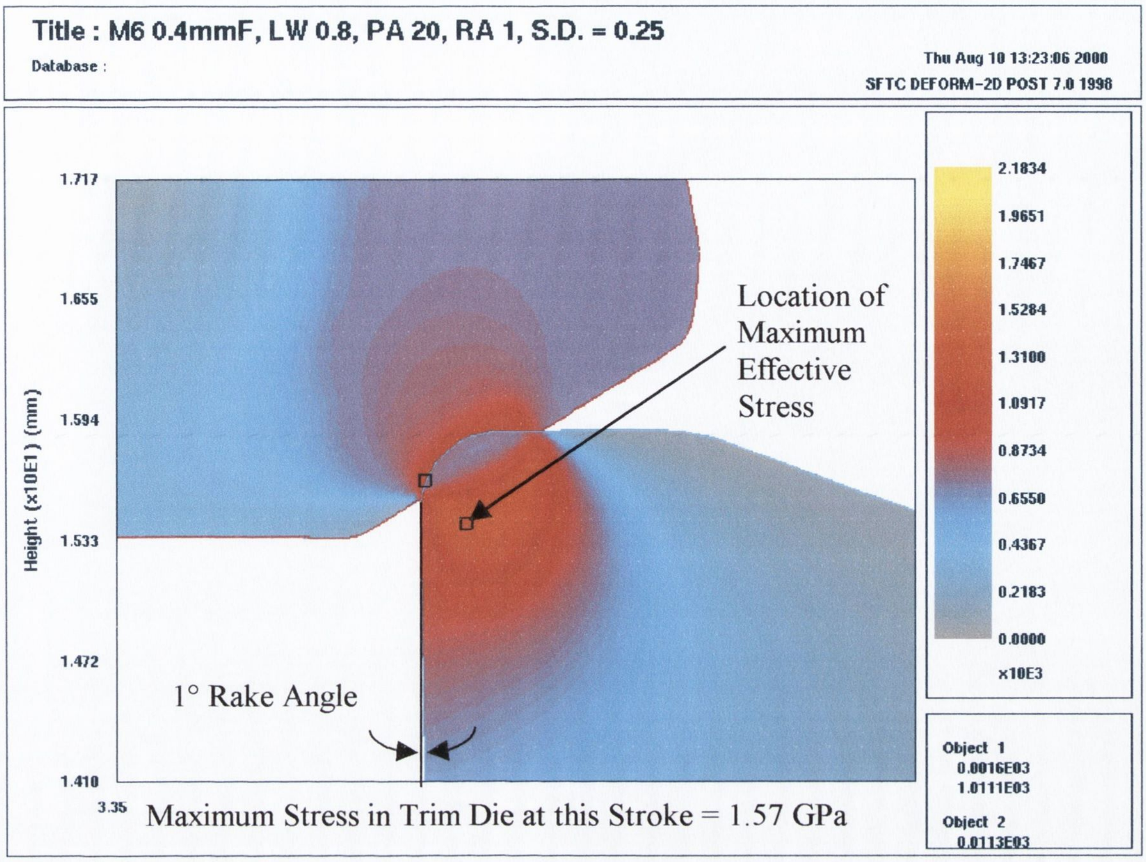

Location of Maximum Effective Stress

1° Rake Angle

Maximum Stress in Trim Die at this Stroke = 1.57 GPa

Figure 4-60: Effective Stress in the 1° Rake Angle Model at 0.3mm Stroke

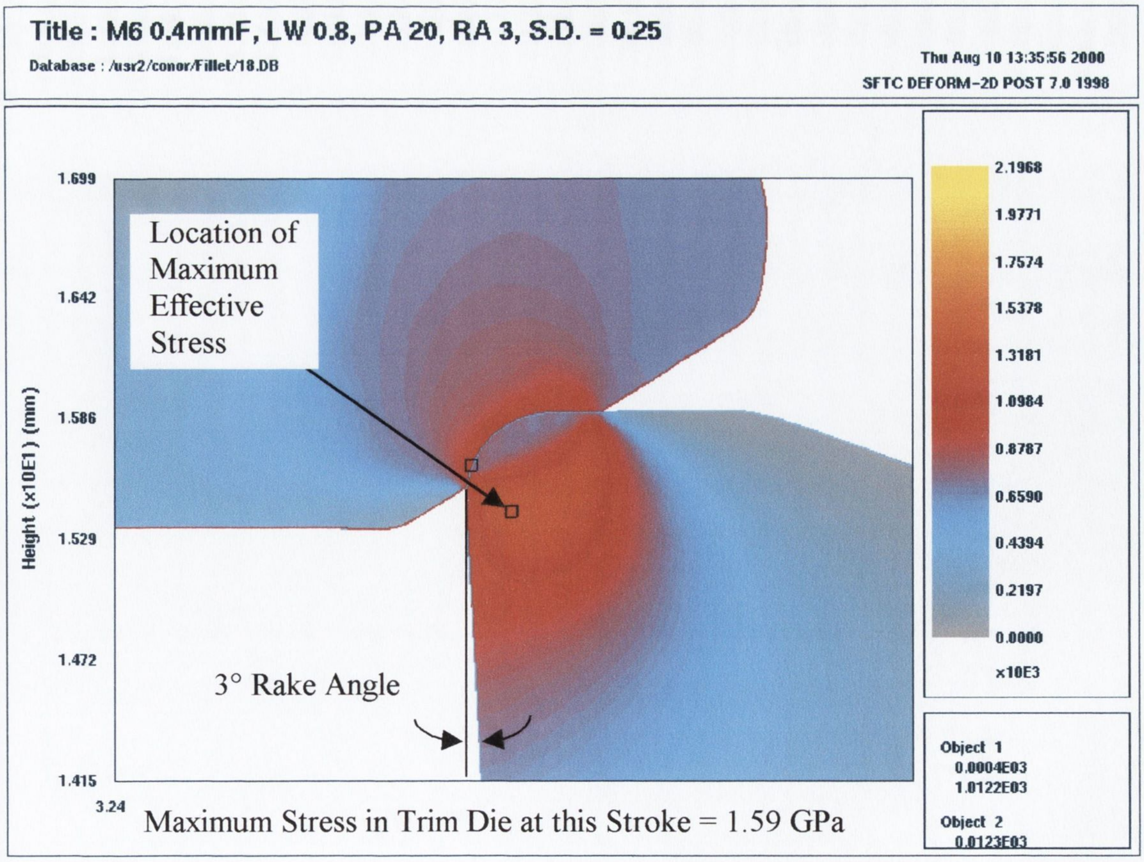

Location of Maximum Effective Stress

3° Rake Angle

Maximum Stress in Trim Die at this Stroke = 1.59 GPa

Figure 4-61: Effective Stress in the 3° Rake Angle Model at 0.3mm Stroke

Area 2: Trim Die Stroke = 1.0mm

Figure 4-62 below illustrates the effective stress results against trim die stroke for all five rake angle models.

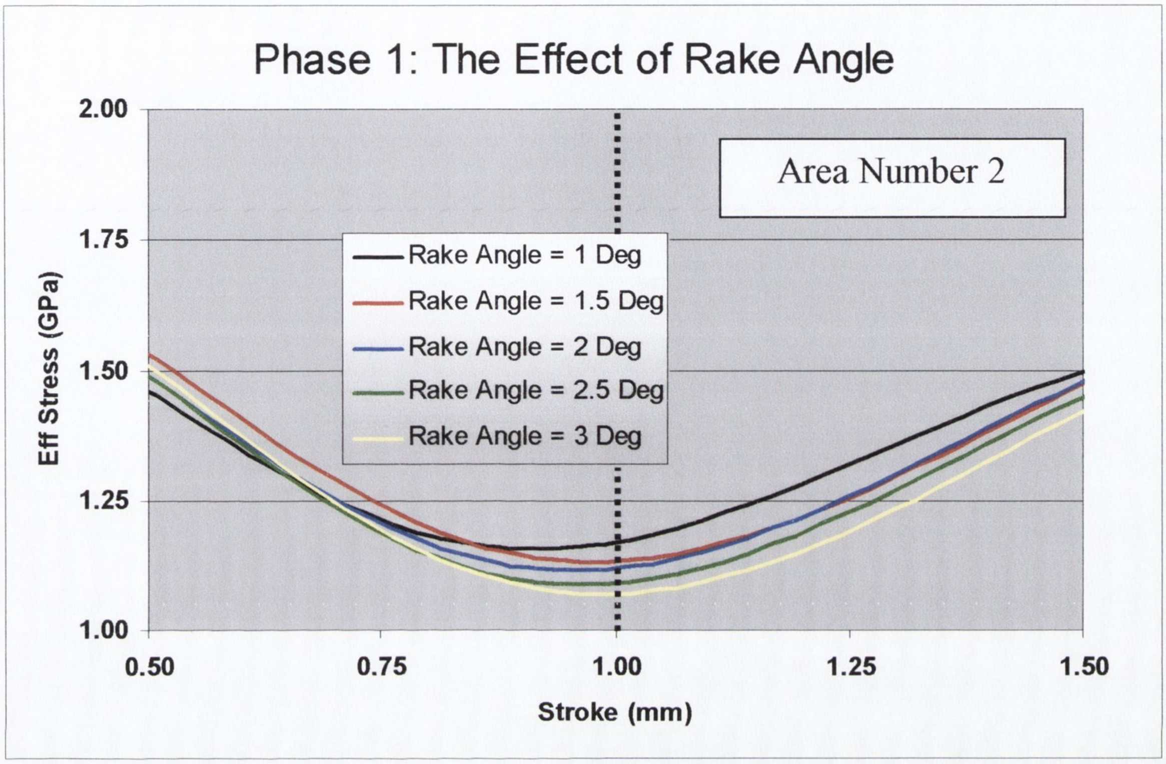

Figure 4-62: Effective Stress vs. Stroke for all 5 Rake Angle Models, Stroke Range 0.5 – 1.5mm

The maximum stress results induced within each trim die, at 1.0mm stroke, are listed in table 4-26 below.

'Rake Angle'	Induced Effective Stress (GPa)
1°	1.161
1.5°	1.132
2°	1.119
2.5°	1.089
3°	1.069

Figure 4-26: The Effect of Increasing the 'Rake Angle' at Area 2: Stroke = 1.0mm

Increasing the rake angle from 1° to 3° causes the level of induced effective stresses to drop from 1.161 Gpa to 1.069 Gpa, which is a drop of 7.95%. Therefore there is a linear relationship between the rake angle and the induced effective stresses. For this reason, only two shaded effective stress plots are highlighted in figures 4-63 and 4-64, which represents the 1° and 3° models at Area 1.

The location of the maximum effective stress within the trim die with a 1° rake angle, figure 4-63, is further down the rake face compared to the 3° rake angle model, figure 4-64. As the rake angle is increased from 1° to 3° the clearance between the workpiece and the inner surface of the trim die also increases. This greater clearance is highlighted in figure 4-64. During the forging process, a trim die having a rake angle of 1° induces higher stresses within the trim die due to rubbing between the workpiece and the inner surface of the trim die. Increasing this rake angle to 3° increases the clearance between the workpiece and inner surface of the trim die therefore reducing the level of induced stress. With reference to figure 4-64, the location of the maximum effective stress within the 3° rake angle model is at a higher point on the corner of the trim die because of the increased clearance.

Once the trim die stroke of 1.0mm has been passed, the effective stresses for all five models start to rise. As previously stated, this rise in the level of effective stress, after Area 2, is caused by the workpiece material making contact with the top tool and restricting the flow of material.

A conclusion based on the lowest level of induced effective stress in Area 2 would be that the 3° rake angle model was 'optimum'.

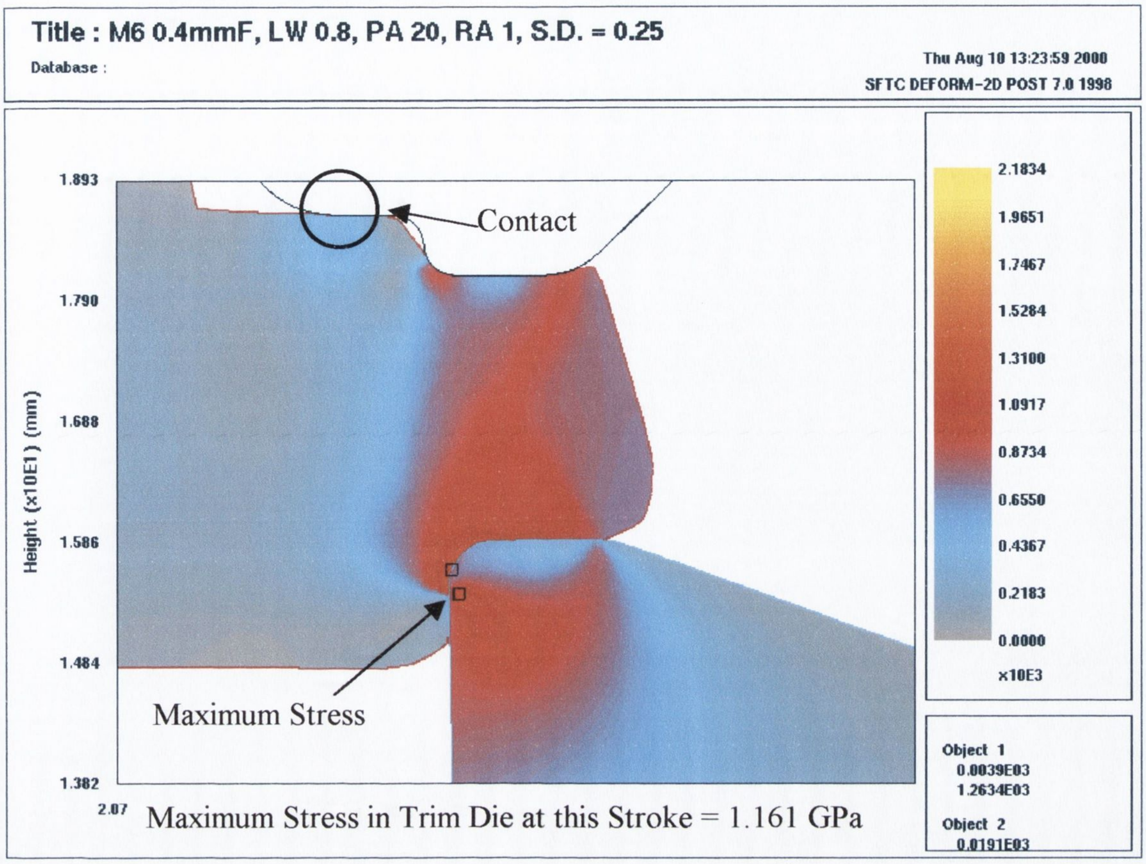

Maximum Stress in Trim Die at this Stroke = 1.161 GPa

Figure 4-63: Effective Stress in the 1° Rake Angle Model at 1.0mm Stroke

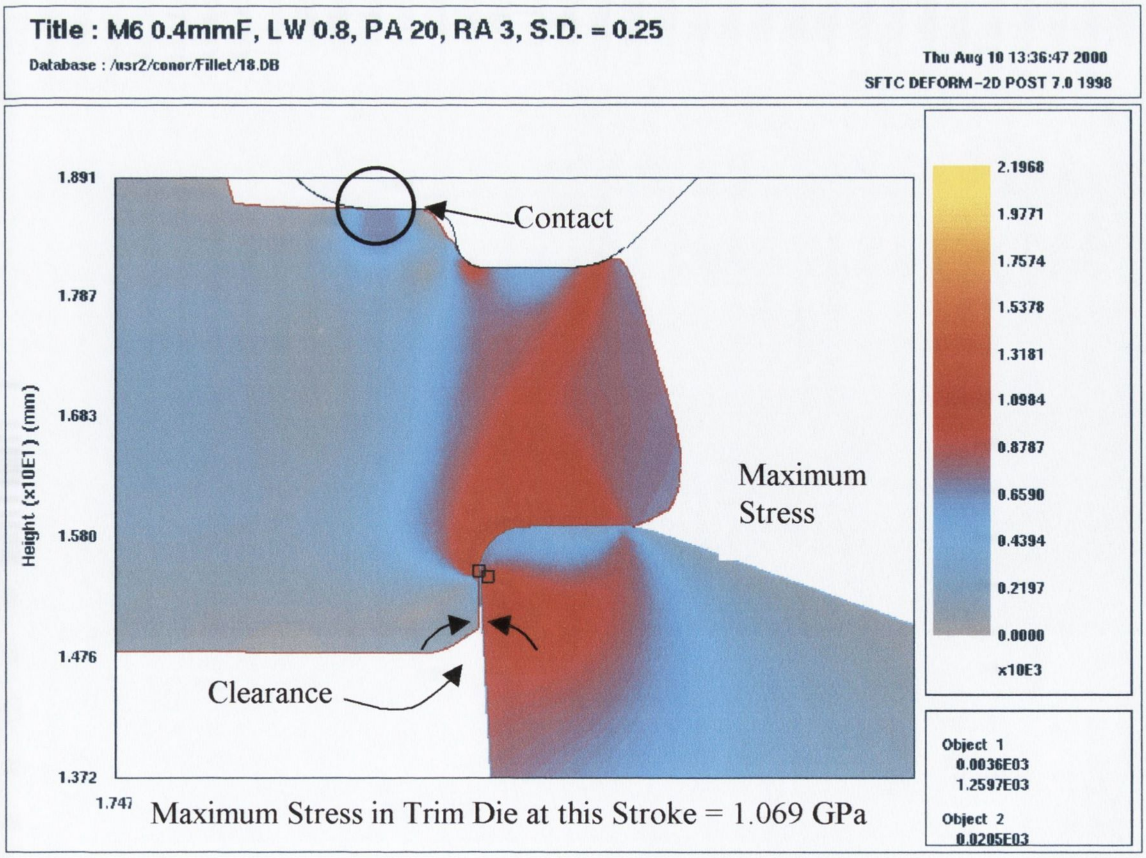

Maximum Stress in Trim Die at this Stroke = 1.069 GPa

Figure 4-64: Effective Stress in the 3° Rake Angle Model at 1.0mm Stroke

Area 3: Trim Die Stroke = 3.0mm

Figure 4-65 below illustrates the change in effective stresses versus stroke for all five FEA models at the final stroke relating to Area 3. The total stroke of all five models was 2.92mm. As mentioned in the previous sections, the final stroke of the trim die is dictated by a feature of the trim die profile, which is explained in detail in Appendix D on page 238. All five models show a sharp increase in the level of induced effective stress within the trim die at the final stroke.

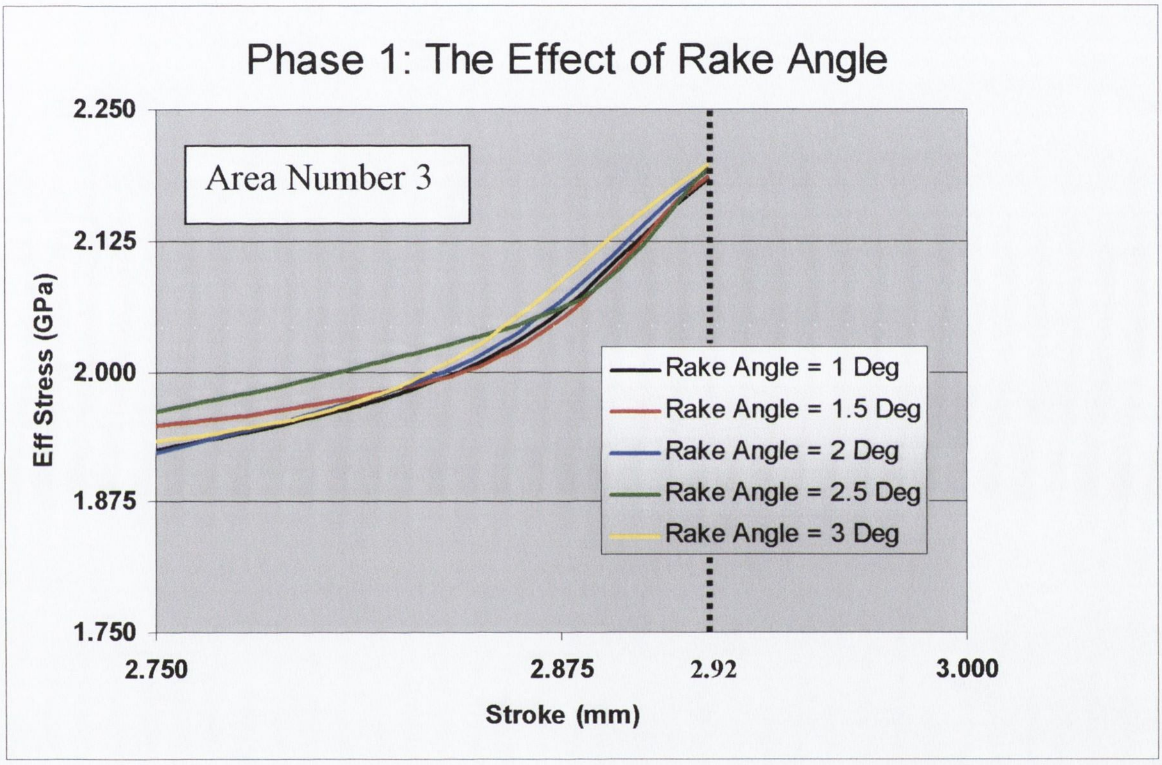

Figure 4-65: Effective Stress vs. Stroke for all 5 Rake Angle Models. Stroke Range 2.75 to 3mm

The variations in the levels of induced effective stress at the end of the trim die stroke are listed in table 4-27. With reference to figure 4-65 and table 4-27, the lowest level of induced effective stress occurred while running the 1° rake angle model. Altering the rake angle from 1° to 3° causes the effective stress to increase from 2.183 GPa to 2.1968 GPa, which is a percentage change of only 0.63%. Therefore, although increasing the rake angle increases the effective stresses, the effect is very small. However increasing the rake angle effectively weakens the trim die, similar to that of increasing the rake angle on a cutting tool.

‘Rake Angle’	Induced Effective Stress (GPa)
1°	2.183
1.5°	2.1863
2°	2.1902
2.5°	2.1935
3°	2.1968

Figure 4-27: Phase 1: The Effect of Increasing the ‘Rake Angle’ at the Final Stroke

With reference to figure 4-65 and table 4-27, due to the similarity in the final effective stresses induced in all five models, only the 1° and 3° models are plotted in figures 4-66 and 4-67. Comparing the 1° and 3° rake angle models shown in figures 4-66 and 4-67 respectively indicate the similar stress distributions and location of maximum stress.

A conclusions based on the levels of induced effective stress would be that there is very little difference between all five models but that the 1° rake angle model was marginally ‘optimum’.

It has been found in industry, through trial and error, that a standard value for the rake angle is 1° to 1.5°

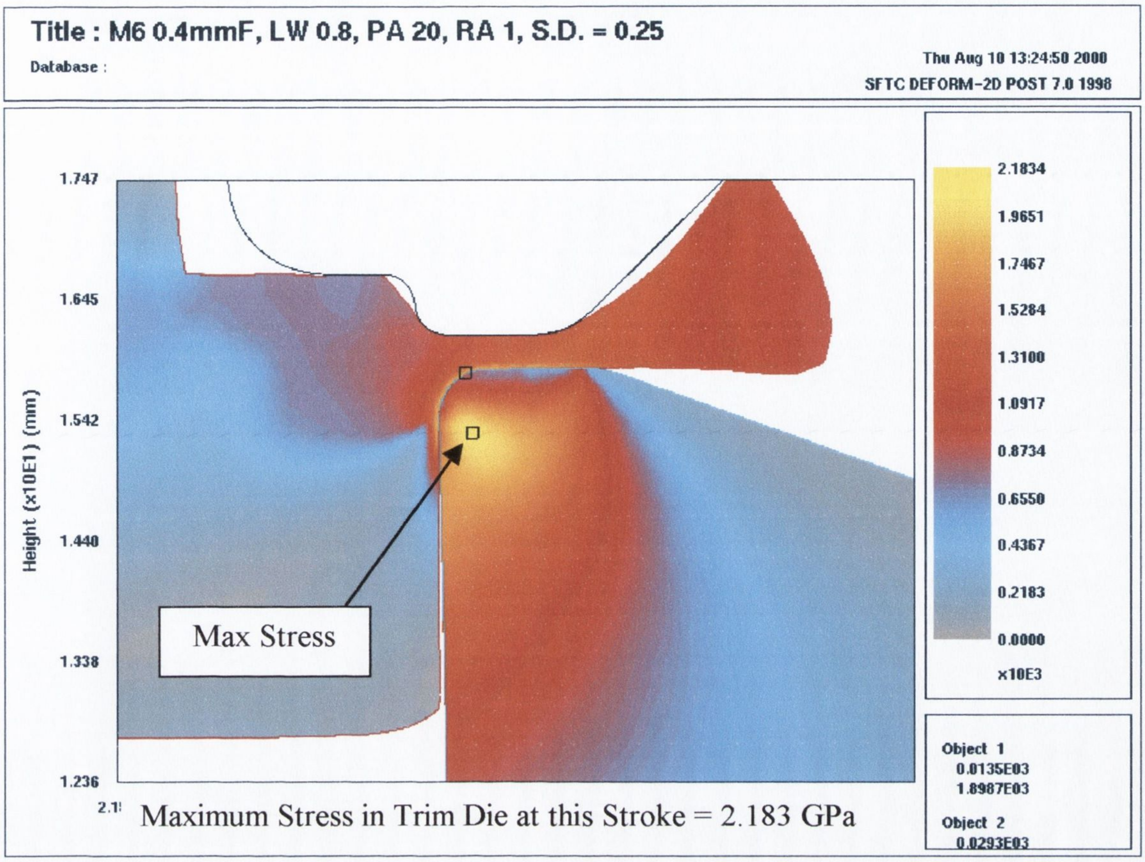

Figure 4-66: Effective Stress in the 1° Rake Angle Trim Die at the Final Stroke

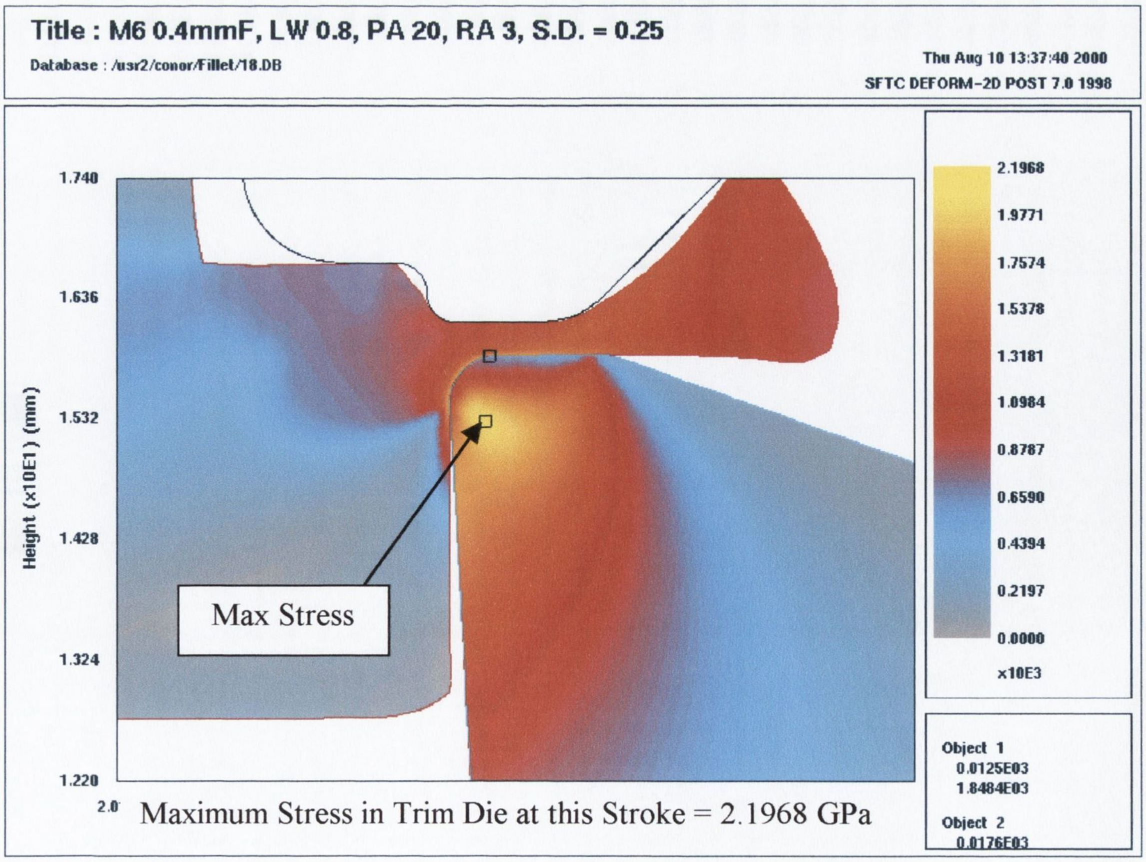

Figure 4-67: Effective Stress in the 3° Rake Angle Trim Die at the Final Stroke

4.1.5.2 Maximum Tensile Radial Stresses:

The maximum tensile radial stresses action along the top surface of all five trim dies modelled in this section are listed in table 4-28 below.

Rake Angle	Maximum Tensile Radial Stress (MPa)
1°	41.213
1.5°	41.325
2°	41.527
2.5°	41.612
3°	41.934

Table 4-28: Rake Angle versus the Maximum Tensile Radial Stress

With reference to table 4-28 above, increasing the rake angle from 1° to 3° caused the maximum tensile radial stress to increase from 41.213 MPa to 41.934 MPa, which is an increase of 1.7%. These results are plotted in figure 4-68 below. As in the previous section relating to the 'Petal Angle', although the percentage change is small, the trend is evident. Increasing the rake angle increases the tensile radial stresses along the top surface of the trim die.

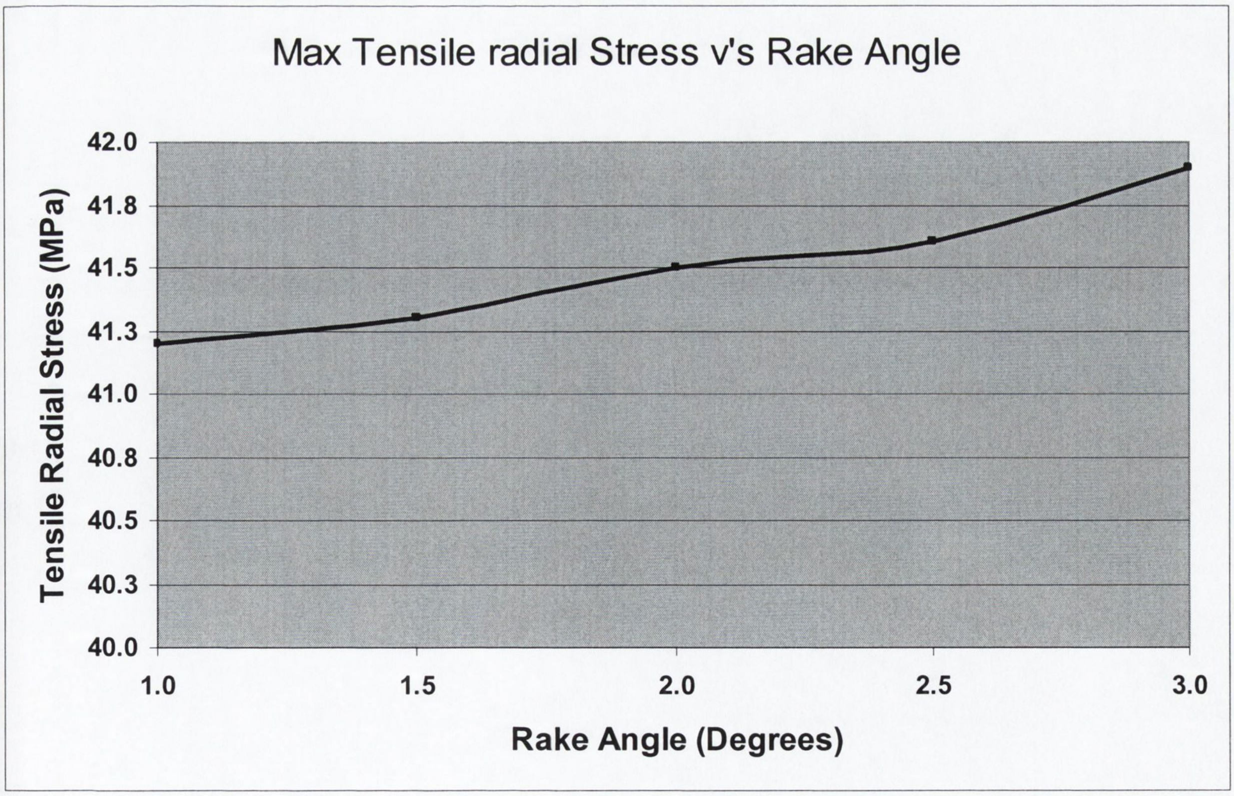

Figure 4-68: Phase 1: Maximum Tensile Radial Stress vs. Rake Angle

4.1.5.3 Summary

In this Section 4.1.5, five FEA models were constructed and modelled where the 'Rake Angle' was varied while the corner radius, land width and petal angle were held constant at the values listed in table 4-24 on page 137. Dividing the stroke of the trim die into the three areas enabled greater detail in the results. The 'optimum' rake angle for each of the areas investigated are listed in table 4-29 below.

Area Number	Trim Die Stroke (mm)	Optimum Rake Angle	Lowest Induced Effective Stress (GPa)
1	0.3	2°	1.566
2	1.0	3°	1.069
3	3.0	1°	2.183

Table 4-29: Phase 1: 'Optimum' Rake Angle Values

With reference to table 4-29 above, at Area 1 and Area 3, all five models induced very similar levels of effective stress. At Area 2, the 3° model was 'optimum' as it offered the greatest amount of clearance between the workpiece and the inner surface of the trim die. In Area 3, due to the higher magnitude of stresses in comparison to Areas 1 and 2, increasing the rake angle weakened the trim die hence causing the 1° rake angle model to become 'optimum'.

An analysis of the maximum tensile radial stresses concluded that the greater the rake angle, the higher the tensile radial stresses.

In conclusion, by combining table 4-28 and figure 4-68, it can be stated that changing the rake angle has little effect on the magnitude of the induced stresses within the trim die but that the 1° rake angle model was marginally 'optimum'.

4.1.6 Phase 1 Conclusions

In phase 1, the following five sets of finite element simulations were conducted to investigate what influence altering the five geometrical features, listed below, would have on the induced effective stress and tensile radial stress within the trim die:

1. Altering the Fillet corner radius models
2. Altering the Compound corner radius models
3. Altering the Land width
4. Altering the Petal angle
5. Altering the Rake angle

For each set of FEA models listed above a strategy called ‘one-factor-at-a-time’ was implemented. As the name suggests only one factor or parameter of the trim die profile was altered while the remaining parameters were held fixed. The selection of values chosen for these fixed parameters was purely random. For example in the land width simulations in Section 4.1.3 on page 106, the fixed value for the fillet corner radius was held at 0.2mm and not at the ‘Optimum’ value calculated in the previous Section 4.1.1 of 0.4mm. The reason for not using the optimum values previously stated was based on the fact that the possible interaction between the parameters was not yet known. It was thought, at that time, that the fixed values had no influence on the effective stresses, only the variable parameter.

The results from the five simulations listed above are detailed in table 4-33. It is important to note that the accuracy of the finite element results presented here were established by comparing the theoretical and experimental forging loads. Figure 4-101 on page 189 shows that the greatest error obtained was just over 7%. However this error is based on the experimental rig and not the ‘real-world’ trimming process. The ‘optimum’ values for each parameter simulated are highlighted in yellow, while the light grey colour highlights the models that caused yielding within the trim die material.

With reference to table 4-30, a corner radius smaller than 0.2mm, whether of ‘Fillet’ or ‘Compound’ configuration, will cause yielding within the trim die during the trimming process. Figure 4-69 illustrates that the largest possible ‘Compound’ corner radius is 0.25mm. If the compound radius is increased above this value of 0.25mm, the Averbach radius (shown in red) will be removed and the corner geometry effectively becomes that of a ‘Fillet’ trim die.

Parameter	Value	Induced Effective Stress At Area 3 (GPa)	Tensile Radial Stress (MPa)
Fillet Corner Radius	0.1mm	2.5041	530.3
	0.2 mm	2.4078	295
	0.3 mm	2.2953	157
	0.4 mm	2.2041	86
Compound Corner Radius	0.07 mm	2.758	545.3
	0.1 mm	2.610	435.5
	0.15 mm	2.558	323
	0.2 mm	2.441	252
	0.25 mm	2.381	170
Land Width	0.2 mm	2.158	37.6
	0.4 mm	2.464	45.2
	0.6 mm	2.501	97.7
	0.8 mm	2.424	156.7
	1.0 mm	2.367	197.7
	1.5 mm	2.323	239.3
Petal Angle	20°	2.177	37.98
	25°	2.161	38.49
	30°	2.174	39.73
	35°	2.172	39.78
	40°	2.18	41.56
	45°	2.198	42.35
Rake Angle	1°	2.183	42.213
	1.5°	2.1863	41.325
	2°	2.1902	41.527
	2.5°	2.1935	41.612
	3°	2.1968	41.934

Table 4-30: The Effective and Tensile Radial Stress Results from the Phase 1 FEA simulations

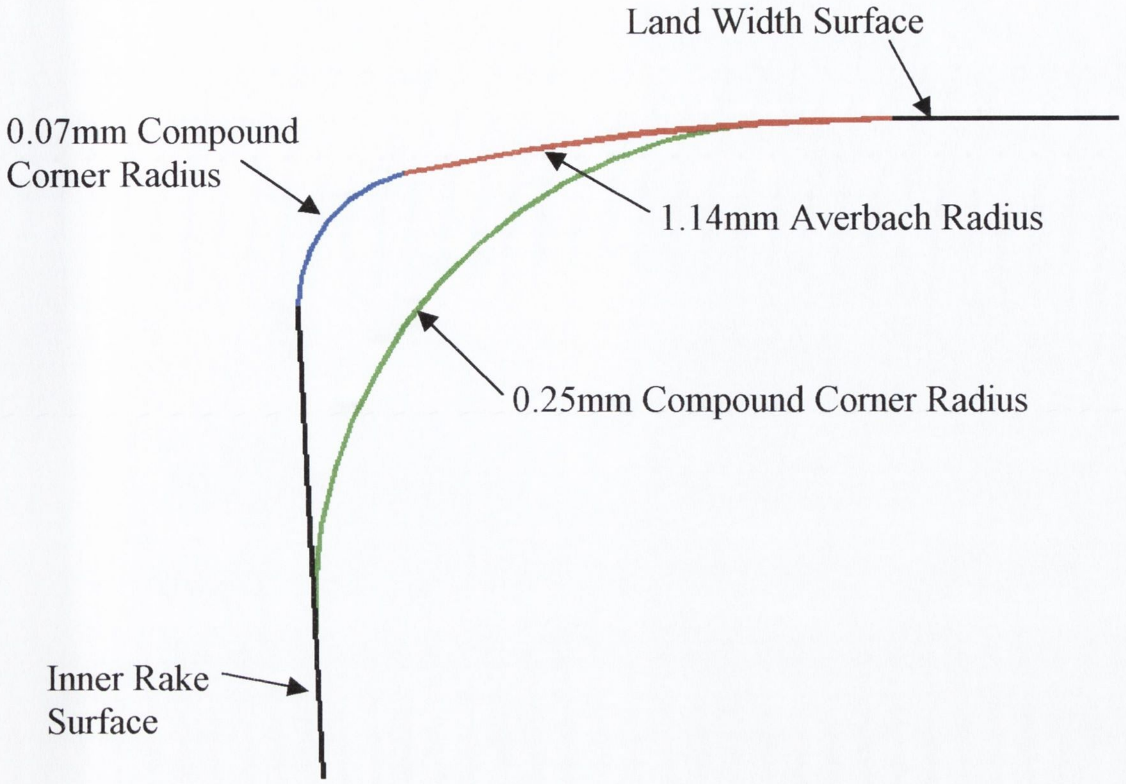

Figure 4-69: The Effect of Increasing The Corner Radius IN a Compound Trim Die

With reference to table 4-30, the 'optimum' compound geometry had a radius of 0.25mm. If this radius were increased beyond 0.25mm, the geometry would become that of a fillet trim die. The lowest induced effective stress of 2.2041GPa was obtained while using a 0.4mm fillet corner geometry trim die. Figure 4-70 plots the compound and fillet corner radii models against the induced effective stresses at area 3. The compound corner radii models, shown in red, induced a higher level of effective stress in comparison to the corresponding fillet corner radius. For example, using a 0.1mm corner radius, the compound trim die induces an effective stress of 2.610GPa while the fillet trim die induced 2.5041GPa, this represents a percentage drop of approximately 4%. Notice that both models caused yielding within the trim die material M2. The 0.1mm fillet trim die induces a lower magnitude of effective stress because the load bearing area is greater. Figure 4-71 shows the 0.1mm fillet corner profile in red with the 0.1mm compound corner profile is in black. Both have a corner radius of 0.1mm, but the length of the arc for the 0.1mm fillet trim die, designated 'Y', is greater than the length of the arc for the 0.1mm compound, designated 'X'. Therefore during the forging process, greater stresses are induced while using the compound trim die corner geometry rather than the fillet corner geometry because the loads are distributed over a smaller area.

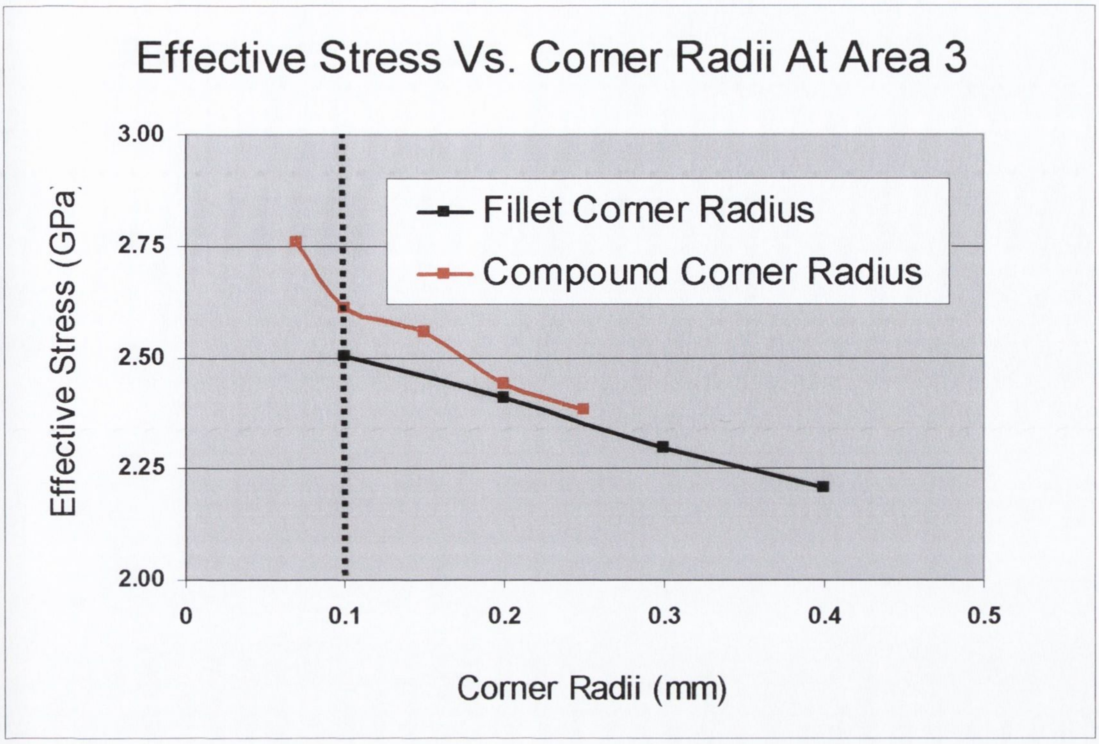

Figure 4-70: Compound and Fillet Corner Radii Plotted Against Effective Stress

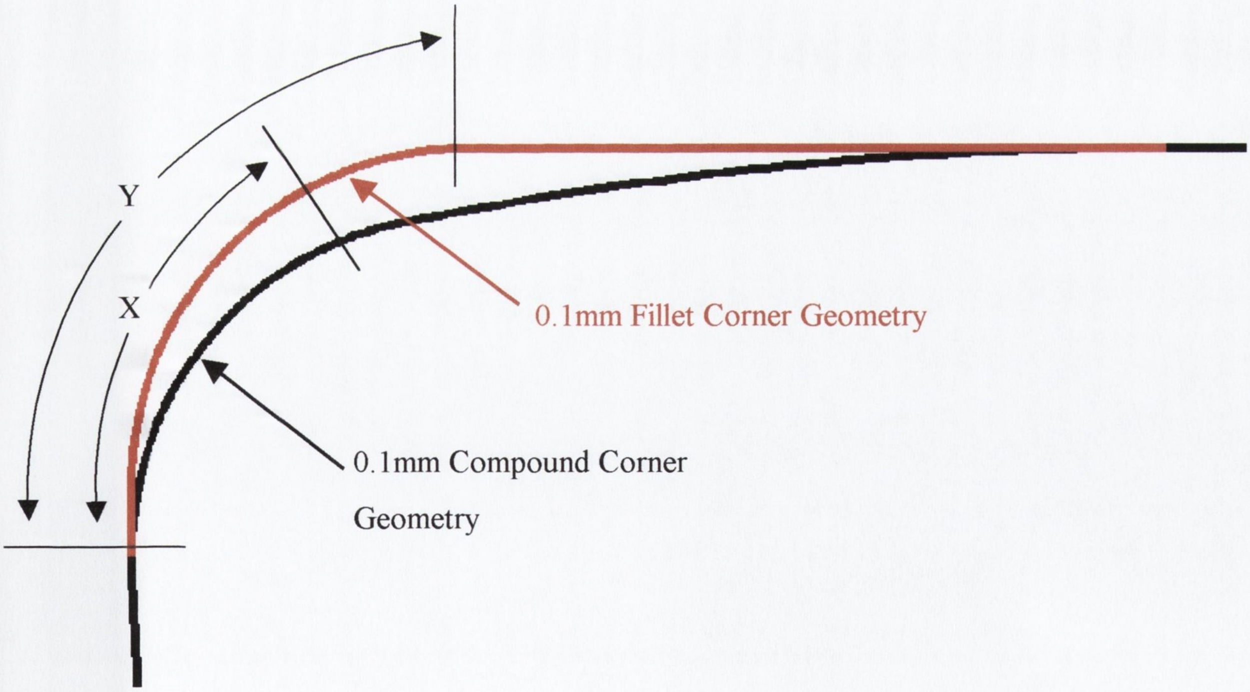

Figure 4-71: A Comparison Between the 0.1mm Fillet and 0.1mm Compound Corner Geometry

With reference to figure 4-70, as the corner radii reach 0.25mm the difference between the fillet and compound trim dies has almost diminished. As previously mentioned, for a corner radius greater than 0.25mm, the compound corner geometry effectively becomes that of a fillet trim die, hence the similarity in results.

Table 4-31 groups the highlighted values from table 4-30 and therefore, for the phase 1 analysis, the 'optimum' values for the trim die profile parameters are list in table 4-31 below.

Parameter	'Optimum' Value
Fillet Corner Radius	0.4mm
Land Width	0.2mm
Petal Angle	25°
Rake Angle	1°

Table 4-31: The 'Optimum' Values from the Phase 1 Analysis

4.2 Phase 2: Interaction

In Phase 1, models were simulated to determine the influence of the following parameters on the induced effective and tensile radial stresses:

1) Corner Radius
2) Land Width
3) Petal Angle
4) Rake Angle

Figure 4-72 below illustrates the location on the trim die profile of each of the tool features (or parameters) listed above. Each parameter had a range of values, which caused a problem by increasing the number of possible trim die combinations to 1620. Due to practical computational constraints, running this number of models was not possible. Therefore in an attempt to reduce this large number of simulations a strategy called 'one-factor-at-a-time' was implemented in Phase 1. For each sets of models simulated in Phase 1, only one parameter was altered while the other three remained constant.

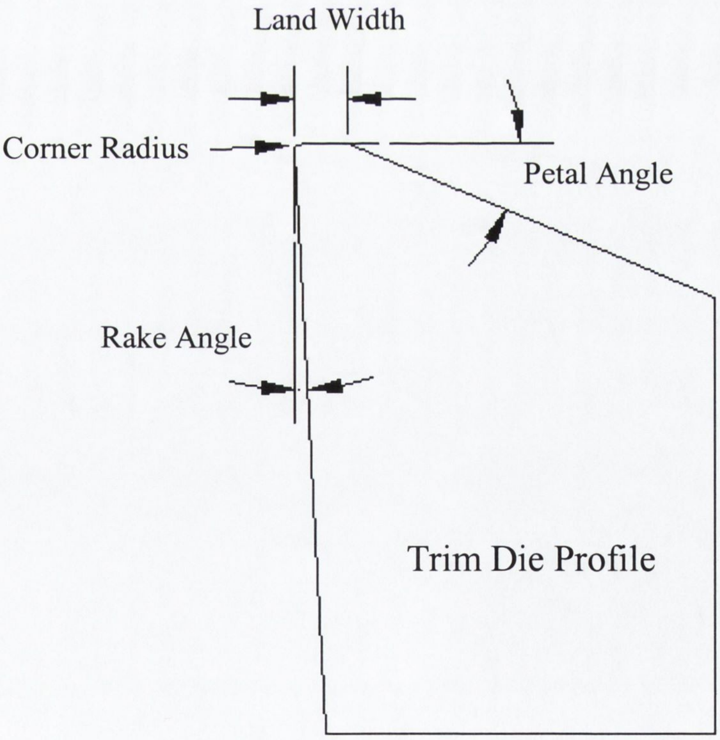

Figure 4-72: The four main trim die profile features analysed in Phase 1

Unfortunately there is a major disadvantage of the 'one-factor-at-a-time' strategy in that it fails to consider any possible interaction between parameters. The definition of

'Interaction' is as follows: when two variables interact the effect of one variable changes for different values of the second variable. Interactions are very common, and if they occur, then analysis based on a 'one-factor-at-a-time' strategy will usually produce poor results. Consequently one-factor-at-a-time experiments are always less efficient than other methods based on a statistical approach to design [69].

The correct approach in dealing with several factors is to conduct a 'Factorial Analysis' whereby factors are varied simultaneously instead of one at a time.

4.2.1 Factorial Analysis

The various parameters of the trim die profile illustrated in figure 4-72 had a range of possible values. Table 4-32 below shows the parameters and their possible values.

PARAMETER		VARIATION
CORNER RADIUS	FILLET	0.1, 0.2, 0.3 and 0.4mm
	COMPOUND	0.1, 0.15, 0.2 and 0.25mm
LAND WIDTH		0.2, 0.4, 0.6, 0.8, 1.0 and 1.5 mm
PETAL ANGLE		20°, 25°, 30°, 35°, 40° and 45°
RAKE ANGLE		1°, 1.5°, 2°, 2.5° and 3°

Table 4-32: Trim Die Profile Parameters and their corresponding Values

A factorial analysis using all the above variables was not practical, therefore a 'two by two' factorial analysis was conducted. Two by two factorial analysis (or 2^2) consists of varying two parameters at two levels to analyse their influence. The two levels chosen were the extremes of the values listed in table 4-32 above. Table 4-33 below shows the values used for each of the parameters.

Parameter	Value
CORNER RADIUS (FILLET)	0.1 and 0.4mm
LAND WIDTH	0.2 and 1.5mm
PETAL ANGLE	20° and 45°
RAKE ANGLE	1° and 3°

Table 4-33: Values used for Phase 2 Factorial Analysis

A total of twenty four FEA models were simulated, in this section, to enable six comparisons. Table 4-34 below illustrates the six comparisons.

Comparison Number	Parameter		Parameter
1	Corner Radius	Vs.	Land Width
2	Corner Radius	Vs.	Petal Angle
3	Corner Radius	Vs.	Rake Angle
4	Land Width	Vs.	Petal Angle
5	Land Width	Vs.	Rake Angle
6	Petal Angle	Vs.	Rake Angle

Table 4-34: Comparisons for the Factorial Analysis

Because the method used to calculate the interaction effect in all six comparisons listed above was identical, only two comparisons will now highlighted, the largest and smallest interaction effects.

4.2.2 Comparison No 1: Corner Radius and Land Width

The first factorial analysis considered the comparison of corner radius against land width. The values used for the corner radius and land width are listed in table 4-33. A total of four models were simulated in this section, the results of which are plotted in figure 4-73.

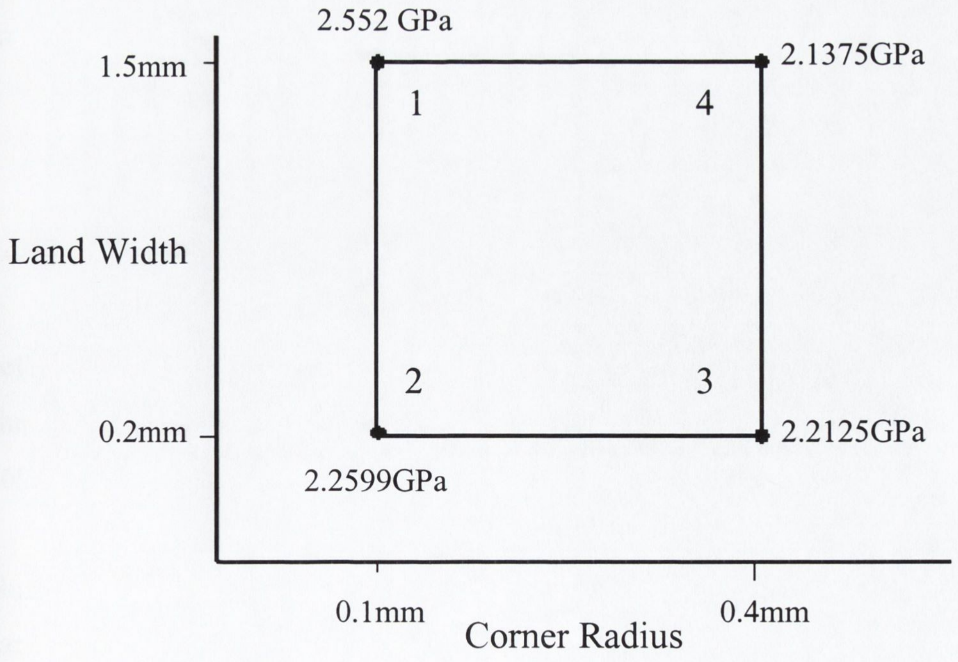

Figure 4-114: The factorial analysis of Corner Radius & Land Width with Effective Stress shown at corners

With reference to figure 4-73, the corner radius is plotted on the x-axis, while the land width on the y-axis. When the land width was held constant at 1.5mm and the corner radius varied from 0.1 to 0.4mm points one and four, in figure 4-73, were established. The values displayed at the corners of the square are the maximum effective stresses at the end of the trim die stroke.

When the land width is held at 0.2mm, the effect of altering the corner radius on the induced effective stresses is calculated by simply subtracting the stress value at corner number 2, of the square, from corner number 3. Therefore when the land width is held at 0.2mm, the effect of changing the corner radius is:

$$2.2599 - 2.2125 = 0.0474\text{GPa} \qquad \ldots\ldots\ldots\ldots\ldots (4.1)$$

The effect of corner radius at 1.5mm land width is:

$$2.552 - 2.1375 = 0.4145\text{GPa} \qquad \ldots\ldots\ldots\ldots\ldots (4.2)$$

From the above calculations it is clear that the effect of the corner radius depends of the value of the land width. When this occurs, there is an 'Interaction' between the parameters. The 'Interaction Effect' (in this case) is defined as the average difference between the effects of the corner radius at low values of land width i.e. 0.2mm, and the effects of the corner radius at high values of land width i.e. 1.5mm [69]. Therefore the magnitude of the interaction effect is the average difference between the effects calculated in equations 4.1 and 4.2 above.

Therefore the interaction effect is:

$$(0.4145 - 0.0474)/2 = 0.18355\text{GPa} \qquad \ldots\ldots\ldots\ldots\ldots (4.3)$$

Figure 4-74 plots the two variable parameters against the effective stress. With reference to figure 4-74, when the parameters are plotted against their response, in this case the effective stress, if the lines produced are not parallel then 'Interaction' has occurred [69].

From the two lines displayed in figure 4-74 a 3D surface, known as a Response Surface Plot (RSP) can be established. The RSP for the interaction of the corner radius and land width is illustrated in figure 4-75. The black and the red lines in figure 4-115 are highlighted in the RSP illustrated in figure 4-75.

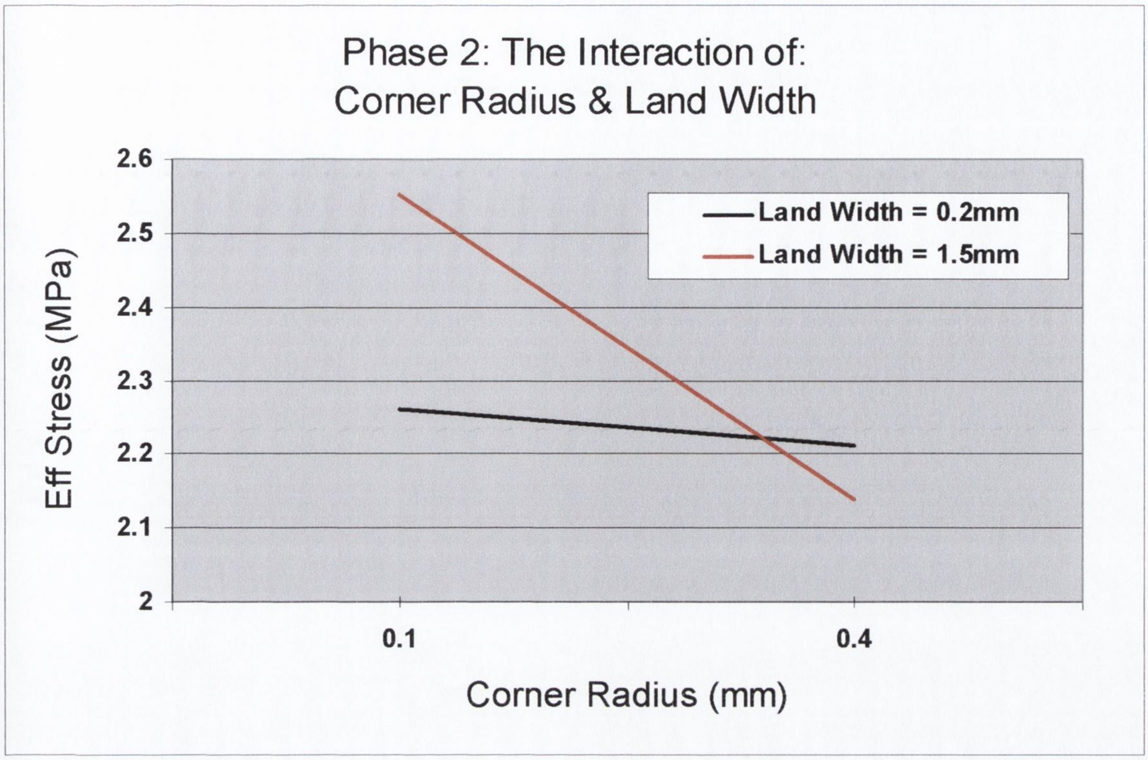

Figure 4-74: Phase 2: Corner Radius and Land Width Plotted Against Effective Stress

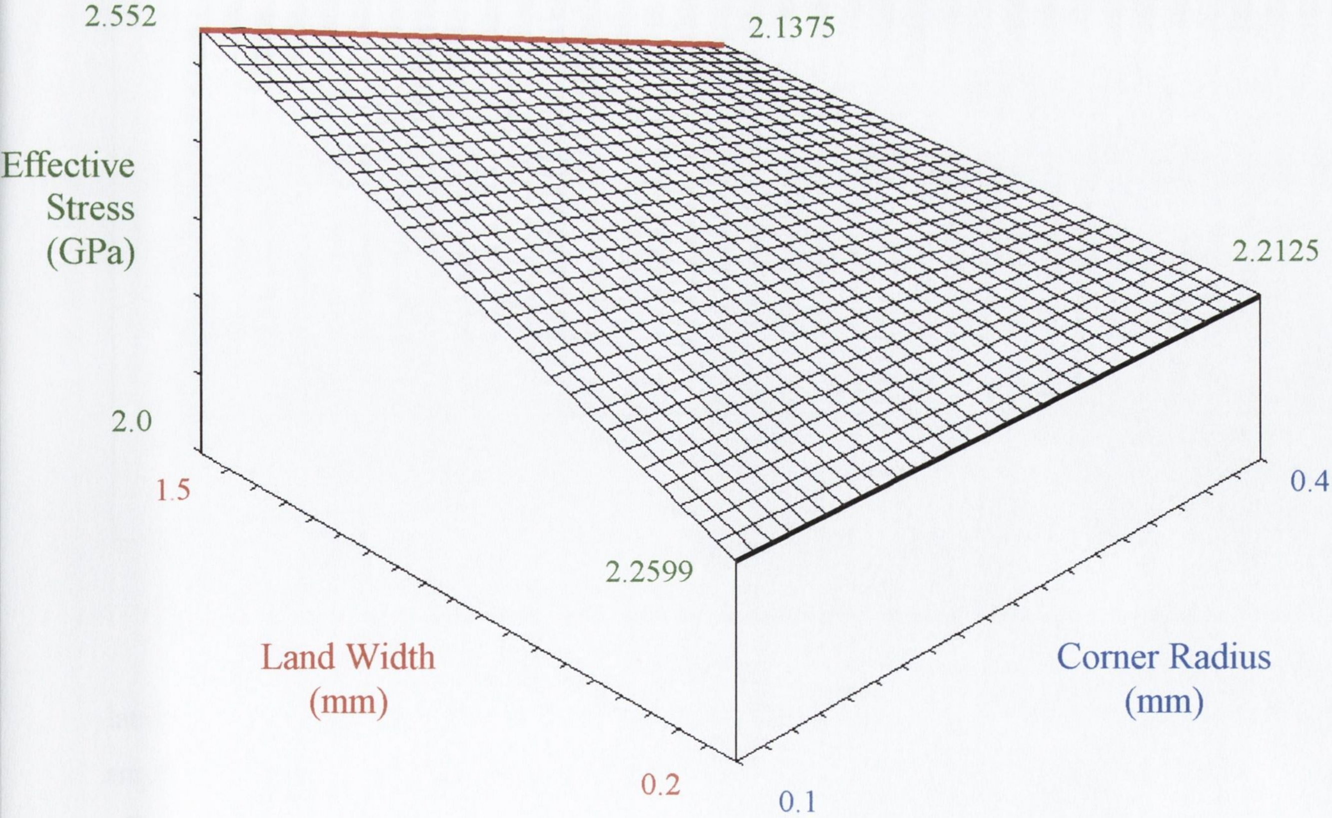

Figure 4-75: The Response Surface Plot For the Corner Radius vs. Land Width Interaction

The interaction effect causes the surface in figure 4-75 to 'twist'. This form of twisting, or curvature of the response surface, indicates Interaction.

Figure 4-76 and 4-77 illustrate the 0.1mm and 0.4mm corner radius models, both with a land width of 1.5mm. In figure 4-76, the length of the parallel top surface of the trim die and the bottom of the top tool has a value 'X'. In figure 4-77, the length of the parallel surfaces has reduced to 'Y'. As discussed in Phase 1, Section 4.1.1 on page 81, increasing the corner radius reduces the aspect ratio. Reducing the aspect ratio reduces the forging load required, hence reducing the level of stress induced within the trim die. Changing the land width while the corner radius is small will cause the greatest change in the aspect ratio and therefore the greatest change in stress.

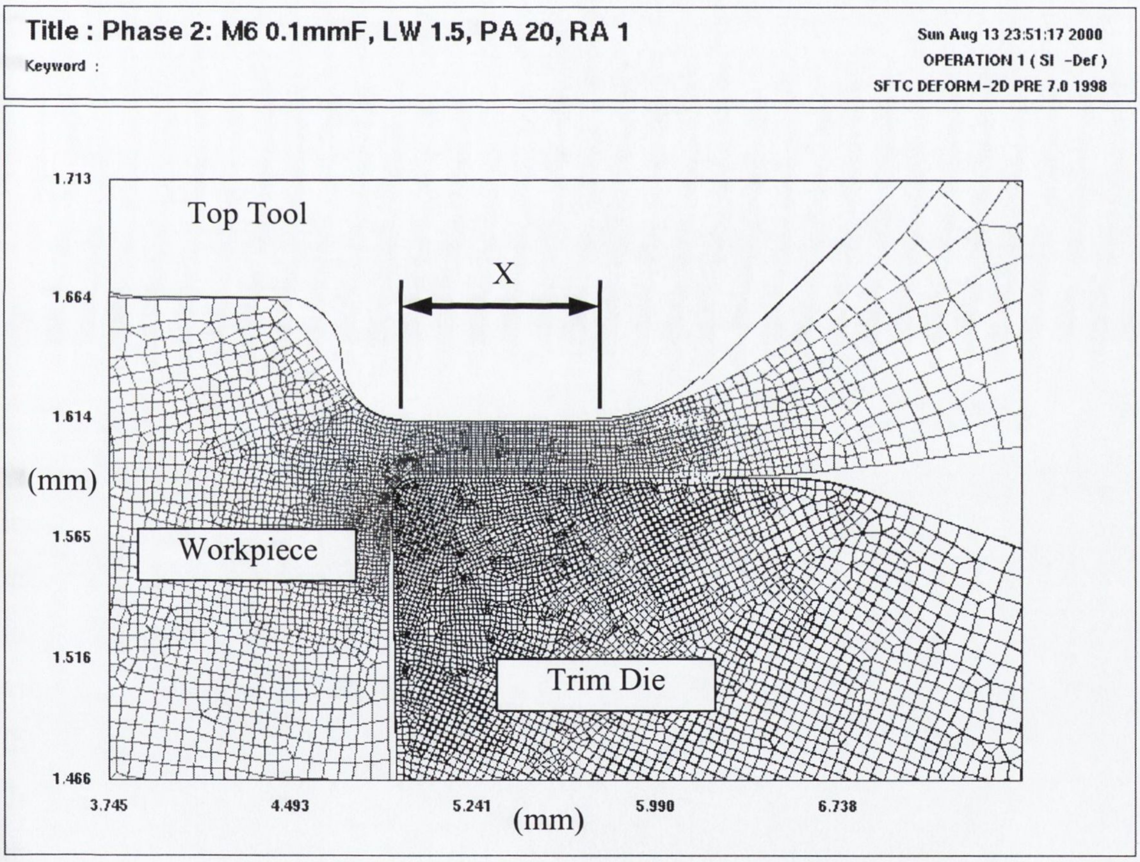

Figure 4-76: Close up of the Trim Die with 0.1mm Corner radius and 1.5mm Land Width

In conclusion, there is a large interaction effect between the corner radius and the land width. This interaction is greatest at the smaller values of corner radius. Therefore if a small corner radius is used the land width has a large influence on the level of the induced effective stresses. Whereas if a larger corner radius is used the influence off changing the land width is reduced.

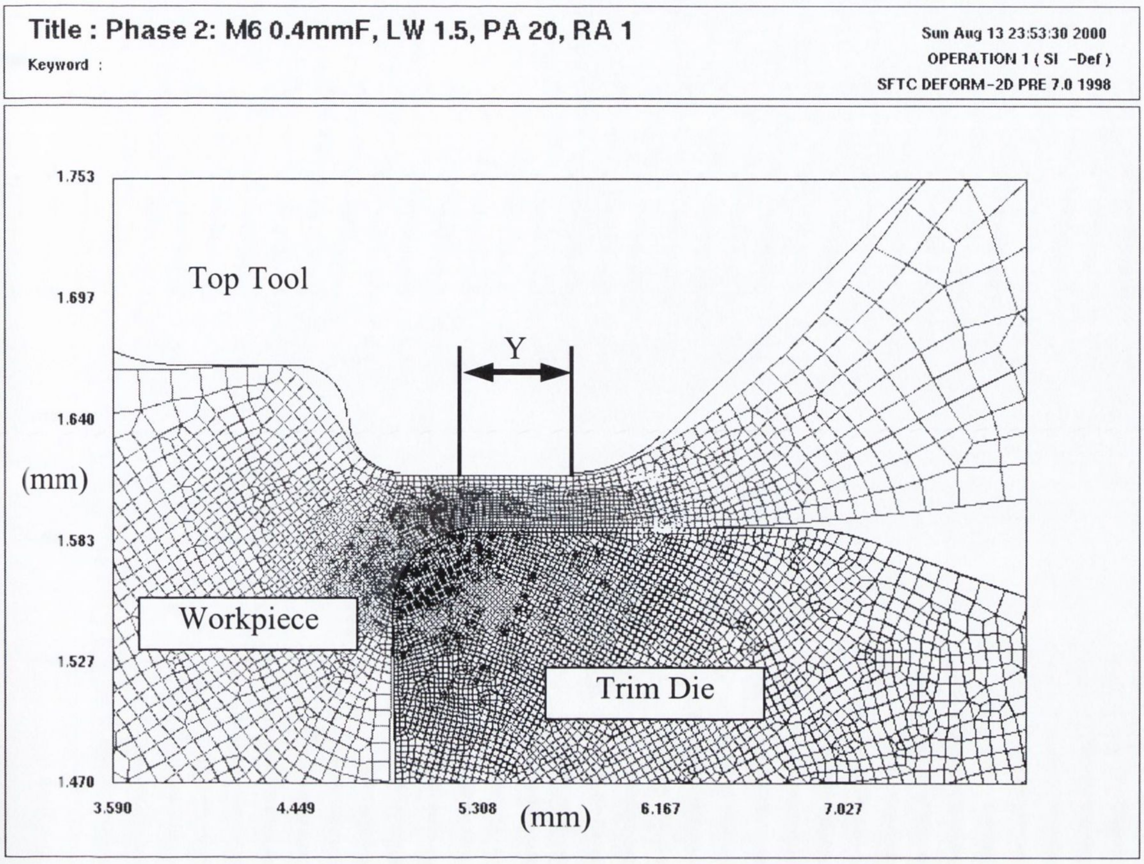

Figure 4-77: Close up of the Trim Die with 0.4mm Corner radius and 1.5mm Land Width

4.2.2.4 Summary

In this section 4.2.1.1 four FEA models were simulated to investigate the possibility of 'Interaction' between the corner radius and the land width parameters. Plotting the induced effective stresses from the end of the trim die stroke enabled the construction of three graphs. The first graph, figure 4-73 plotted the corner radius against land width. From this graph it was shown that the effect altering the corner radius was dependant on the value of the land width, i.e. Interaction was present between these two parameters. Plotting the effective stress results against the corner radius and land width on one graph, figure 4-74, illustrated this interaction effect, as the lines produced were not parallel. Finally, with the use of a Response Surface Plot, a 3D surface of the induced effective stress results was produced, see figure 4-75. This surface was 'twisted' which further indicated 'Interaction'. With reference to figure 4-74, changing the land width, while the corner radius is small, causes the greatest interaction effect. Changing the corner radius effectively changes the length of the parallel surface in contact with the workpiece and the top tool.

4.2.3 Comparison No 3: Corner Radius and Rake Angle

Figure 4-78 below illustrates the corner radius plotted against the rake angle.

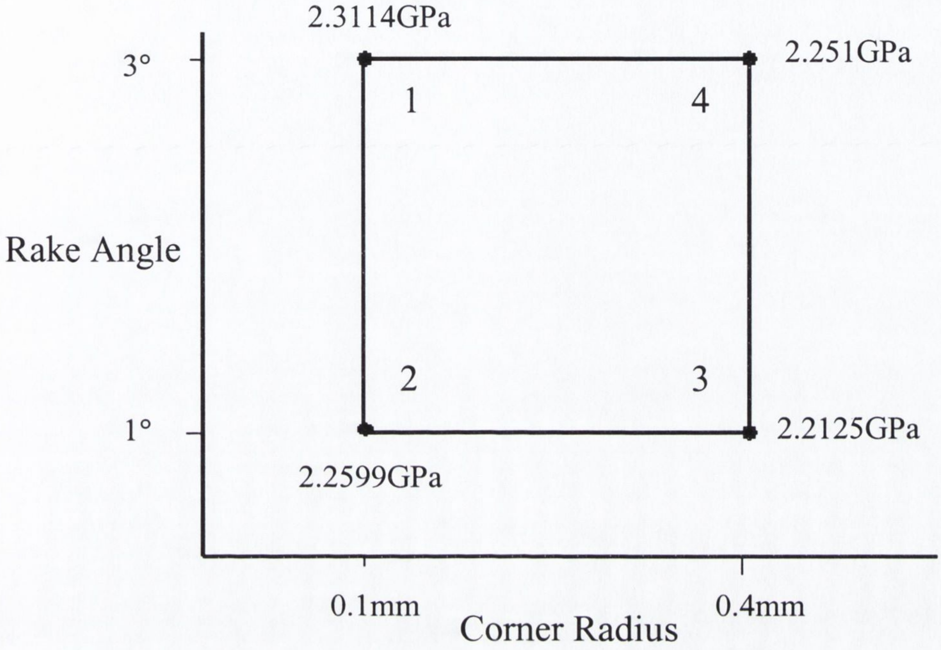

Figure 4-78: The Factorial Analysis of Corner Radius and Rake Angle with Effective Stress shown at corners

With reference to figure 4-78 above, when the rake angle is held constant at 1°, the effect of altering the corner radius is:

$$2.2599 - 2.2125 = 0.0474\text{GPa} \qquad \ldots\ldots\ldots\ldots\ldots (4.4)$$

The effect of altering the corner radius when the rake angle is held at 3° is:

$$2.3114 - 2.251 = 0.0604\text{GPa} \qquad \ldots\ldots\ldots\ldots\ldots (4.5)$$

The differences in the stresses calculated in equation 4.7 and 4.8 are very small. Using these two results the interaction effect can be calculated.

Interaction Effect: $(0.0604 - 0.0474)/2 = 0.0065\text{GPa}$ ……………. (4.6)

The interaction effect calculated in equation 4.6 of 0.0065GPa is less than 4% of the interaction effect calculated in Comparison Number 1 on page 156.

Figure 4-79 below plots the corner radius and rake angle against the induced effective stress within the trim die.

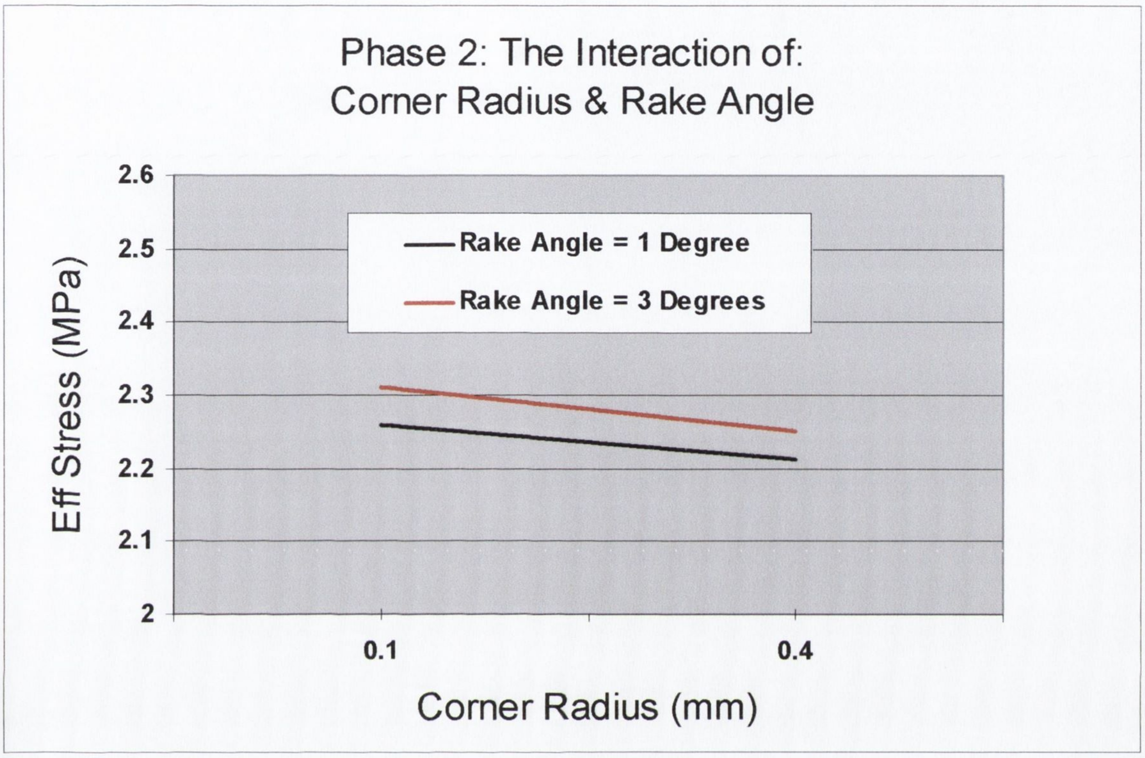

Figure 4-79: Phase 2: Corner Radius and Petal Angle Plotted against Effective Stress

Figure 4-79 above clearly indicates that there is little or no interaction between the corner radius and rake angle as both lines plotted are almost parallel.

4.2.3.1 Summary

Four models were simulated to investigate the possible interaction between the corner radius and rake angle. The effective stresses induced in the trim die, at the end of the stroke, were plotted in figure 4-78. From this graph, the interaction effect was calculated to be 0.0065GPa. Table 4-34 on page 162 illustrates that this interaction effect was the lowest in the six comparisons conducted in Phase 2. This interaction effect was the lowest value of interaction between the corner radius and the other two parameters (land width and petal angle) analysed to date. When the corner radius and rake angle were plotted against the induced effective stress, two parallel lines were produced. This confirmed that there was no interaction between the two parameters.

4.2.4 Phase 2 Conclusions

In Phase 2 a total of twenty four FEA models were simulated to investigate the possible interaction between the parameters analysed in Phase 1. Table 4-35 below illustrates the six comparisons conducted in Phase 2.

Comparison Number	Parameter		Parameter	Interaction Effect	Order	Percentage
1	Corner Radius	vs.	Land Width	0.1835	1st	Ref 100%
2	Corner Radius	vs.	Petal Angle	0.0618	3rd	33.67% of Ref
3	Corner Radius	vs.	Rake Angle	0.0065	6th	3.54% of Ref
4	Land Width	vs.	Petal Angle	0.0805	2nd	43.86% of Ref
5	Land Width	vs.	Rake Angle	0.0084	5th	4.58% of Ref
6	Petal Angle	vs.	Rake Angle	0.01075	4th	5.86% of Ref

Table 4-35: Summary of the Interaction Effects in all 6 Phase 2 Comparisons

With reference to table 4-35 above, Comparison Number 1, between the corner radius and land width, gave the greatest magnitude of the interaction effect. For that reason, comparison number one was designated '1st' in the 'Order' column. The largest interaction effect of 0.1835GPa was used as a reference from which the other five smaller interaction effects were based. Therefore the 'percentage' column, in table 4-35, is established by comparing the magnitude of the interaction effects against the reference value of 0.1835GPa.

With reference to table 4-35 above, there was a definite interaction effect between comparisons 1, 4, and 2. These three largest interactions are grouped together and listed in table 4-36 below.

Comparison Number	Parameter		Parameter	Interaction Effect	Order	% Smaller
1	Corner Radius	vs.	Land Width	0.1835	1st	Ref 100 %
4	Land Width	vs.	Petal Angle	0.0805	2nd	43.86% of Ref
2	Corner Radius	vs.	Petal Angle	0.0618	3rd	33.67% of Ref

Table 4-36: The Three Most Important Interaction Effects From The Phase 2 Analysis

In summary of each comparison listed in table 4-36:

Comparison number 1: Corner Radius vs. Land Width

1 The greatest level of interaction occurred while the corner radius was small. Changing the land width from 0.2mm to 1.5mm, within a trim die having a corner radius of 0.1mm, caused the effective stresses to increase by approximately 11.5%.

2 When the corner radius was 0.4mm, the percentage change in the induced effective stress levels was only 3.39%

Comparison Number 4: Land Width vs. Petal Angle

1 The greatest interaction effect occurred while the land width was small. Changing the petal angle from 20° to 45 ° within a trim die having a land width of 0.2mm caused the effective stresses to increase by approximately 6.53%.

2 When the land width was held at 1.5mm, the percentage change was only 0.125%.

Comparison Number 2: Corner Radius vs. Petal Angle

1 The greatest interaction effect occurred while the corner radius was small. Changing the petal angle from 20° to 45° within a trim die having a corner radius of 0.1mm caused the effective stresses to increase by approximately 6.52%.

2 When the corner radius was held at 0.4mm, the percentage change was only 1.52%.

As previously discussed, the analysis conducted in Phase 1 varied only one parameter of the trim die profile at any one time, and any possible interaction between these parameters, was unknown.

The phase 2 results, summarised in tables 4-35 and 4-36, illustrated that the results obtained by changing a single parameter can be influenced by the level of another parameter, i.e. interaction has taken place.

4.3 Phase 3: The Final Trim Die Profile

The 'Optimum' values for the trim die profile, obtained from the Phase 1 analysis, did not consider any possible interaction between the parameters. The analysis conducted in the Phase 2 did consider the possible interaction effects between these parameters, while Phase 3 presented here, combines the conclusions from Phases 1 and 2 to establish the final optimum trim die profile.

4.3.1 The Problem With 'One-Factor-At-A-Time'

With reference to Section 4.2.2 on page 155, the first comparison between the corner radius and the land width caused the highest interaction effect. But more importantly, the lowest level of effective stress was induced within the trim die having a corner radius of 0.4mm and a land width of 1.5mm. This is highlighted in figure 4-74 on page 157 by the red line. This contradicts the conclusions made in phase 1. In the Phase 1 analysis, it was stated that using the smallest possible land width, in this case 0.2mm, would induced the lowest magnitude of effective stress. This example highlights the dangers of using the one-factor-at-a-time strategy.

This contradiction can be explained by the fact that in the FEA models simulated in Phase1 to investigate the effect of altering the land width, a fixed corner radius of 0.2mm was used. However in the Phase 2 tests, in Section 4.2.2 on page 155, it was shown that if the corner radius was increased to 0.4mm, the largest land width induced the lowest stress.

The other five comparisons from Phase 2 tend to back-up the conclusions from Phase 1 as outlined in Section 4.1.6, page 148. The lowest effective stresses induced within the trim die, during the forging process, occurred while using the following trim die parameter combinations:

- The largest corner radius (0.4mm) and a small petal Angle (20°). Comparison number 2.
- The largest corner radius (0.4mm) and the smallest Rake Angle (1°). Comparison number 3.
- The smallest Land Width (0.2mm) and a small Petal Angle (20°). Comparison number 4.

- The smallest Land Width (0.2mm) and the smallest Rake Angle (1°). Comparison number 5.
- The smallest Petal Angle (20°) and the smallest Rake Angle (1°). Comparison number 6.

Therefore if the largest fillet corner radius of 0.4mm is used, the optimum land width could be either 0.2mm or 1.5mm based on the Phase 1 and Phase 2 analysis. In terms of induced effective stresses, the 1.5mm land width would be optimum as it gave the lowest magnitude in comparison number 1 on page 156. With reference to figure 4-74, on page 157, changing the land width from 0.2mm to 1.5mm, while the corner radius was held constant at 0.4mm, caused the effective stresses to drop from 2.2125GPa to 2.1375GPa, which is a change of approximately 3.4%. However the Land Width tests in the Phase 1 analysis presented in Section 4.1.3 on page 106, showed that increasing the land width from 0.2mm to 1.5mm caused the maximum tensile radial stress to increase from 37.6MPa to 239.3Mpa respectively. This is an increase of approximately 636%. Because of this, it was concluded that the smaller land width was more beneficial in terms of the induced effective stresses and the tensile radial stresses.

Following discussions with the technical staff within the trim die manufacturing plant of SPS Hi-Life Tool, Shannon, the minimum land width value was increased from 0.2mm to 0.4mm. From practical experience it has been found, that a land width value smaller than 0.4mm causes the workpiece material to shear prematurely. As discussed in Section 2.1.1 on the fundamentals of trimming, premature shearing of the workpiece material, before the *Knock-Out* sequence, can cause damage to the trim die and bolt making machine.

Therefore by the combination of the conclusions from Phases 1 and 2, and taking into the consideration of the premature shearing of the workpiece material, the Optimum values for the parameters which make up the profile of the M6 trim die are listed in table 4-37 below:

Parameter	Optimum value
Corner Geometry: Fillet	0.4mm
Land Width	0.4mm
Petal Angle	25°
Rake Angle	1°

Table 4-37: Phase 3: Optimum Trim Die Profile Parameters

The analysis conducted in Phases 1 and 2 highlighted the influence of each parameter of the trim die profile on the induced stresses within the die. Table 4-38 below lists the effect that changing the trim die parameters had on the induced effective and tensile radial stresses within the trim die.

Parameter Altered	Percentage Change In Effective Stress	Percentage Change In Tensile Radial Stress
Corner Radius From 0.1 to 0.4mm	20.1%	84.23%
Land Width From 0.2 to 1.5mm	13.7%	84.29%
Petal Angle From 20° to 45°	1.68%	9.12%
Rake Angle From 1° to 3°	0.63%	2.1%

Table 4-38: Phase 3: The Effect Each Parameter Had On The Induced Stresses Within The Trim Die

With reference to table 4-38 above, changing the corner radius caused the greatest percentage change of 20.1%, in terms of the induced effective stresses, followed closely by the effects of changing the land width. Changing the Petal and rake angles caused only a small change in these effective stresses. In terms of the tensile radial stresses, the greatest change was 84.29%, and this occurred through altering the land width. From table 4-38, the influence of the value of the land width is clearly obvious. As previously explained, increasing the land width increases the aspect ratio. This increase in the aspect ratio traps a greater amount of workpiece material between the trim die and the top tool, which effectively increases the stresses within the trim die.

For the reasons outlined above, a new trim die profile, previously untested, was examined for which the land width surface is effectively 'removed'. This 'new' trim die profile has been designated a 'Reverse Compound' trim die.

The 'reverse compound' and optimum trim die profiles have been simulated and the results will now be presented in Phase 3.

4.3.2 Reverse Compound Trim Die

Figure 4-80 below illustrates a new and previously unconsidered trim die profile developed by the author and termed a 'Reverse Compound'. Basically, this new design uses the optimum parameters determined from the Phase 1 and 2 analyses but introduces a larger radius of 5.0mm which blends the optimum corner radius of 0.4mm to the petal surface, angled at the optimum value of 25°. The optimum trim die simulated in this Phase 3 analysis is shown in black while the new large blend radius of the 'Reverse Compound' trim die is shown in red.

The name 'Reverse Compound' comes from the fact that its profile is similar to that of the standard compound trim die, in that it has a large radius and a smaller blend radius. The name 'reverse' is due to the fact that the larger radius of 5.0mm is sloping to the right, instead of the Phase 1 compound models that sloped to the left.

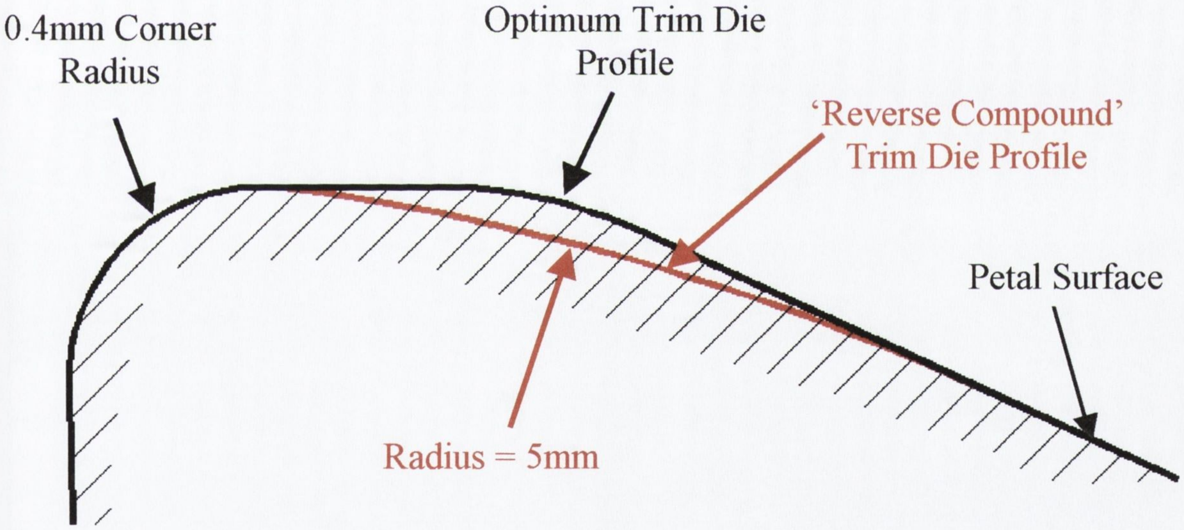

Figure 4-80: Comparison Between Optimum And Reverse Compound Trim Dies

In Section 4.1.3 on page 106 in the Phase 1 analysis, the models used to simulate alterations to the land width highlighted the significance of the geometrical shape of the top tool. It was found that the length of the flat contact surface on the top tool dictated the 'critical' value for the land width. For this reason, a large blend radius of 2.5mm was introduced to reduce the severity of stresses caused when the workpiece material became trapped between the trim die and top tool. The existing top tool geometry is shown in black in figure 4-81, while the new large blend radius of 2.5mm is shown in blue.

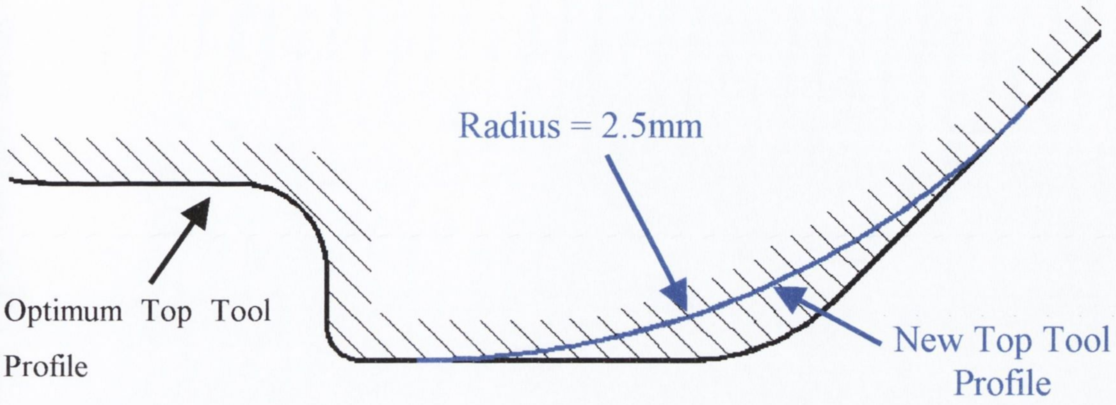

Figure 4-81: The Phase 3 Modification To The Top Tool Profile

Table 4-39 below details the various parameters of the Optimum and Reverse Compound trim die models analysed in this section.

	Parameter				
Trim Die	Corner Radius	Land Width	Petal Angle	Rake Angle	Modified Top Tool?
Optimum	0.4mm	0.4mm	25°	1°	No
Reverse Compound	0.4mm	None	25°	1°	Yes

Table 4-39: The Two Models Simulated in the Phase 3 Analysis

The effective and tensile radial stresses induced within the trim die for the two models listed in table 4-39 above will now be discussed.

4.3.3 Effective Stress Results

As with all the models analysed in Phase 1, the trim die stroke is divided into three stages 1, 2 and 3. These stages correspond to a trim die stroke of 0.3, 1.0 and 3.0mm respectively. For each of these stages the corresponding effective and tensile radial stresses are analysed and discussed.

Area 1: Trim Die Stroke = 0.3mm

Figure 4-82 below illustrates the effective stress plotted against the trim die stroke. In Area 1, which relates to a stroke of 0.3mm, the stresses in both the optimum and reverse compound trim die reach a peak value, and then tend to fall off as the stroke increases to 1.0mm. As previously explained in the Phase 1 analysis, the peak stress at this level of stroke corresponds to the yielding and plastic flow of the workpiece material.

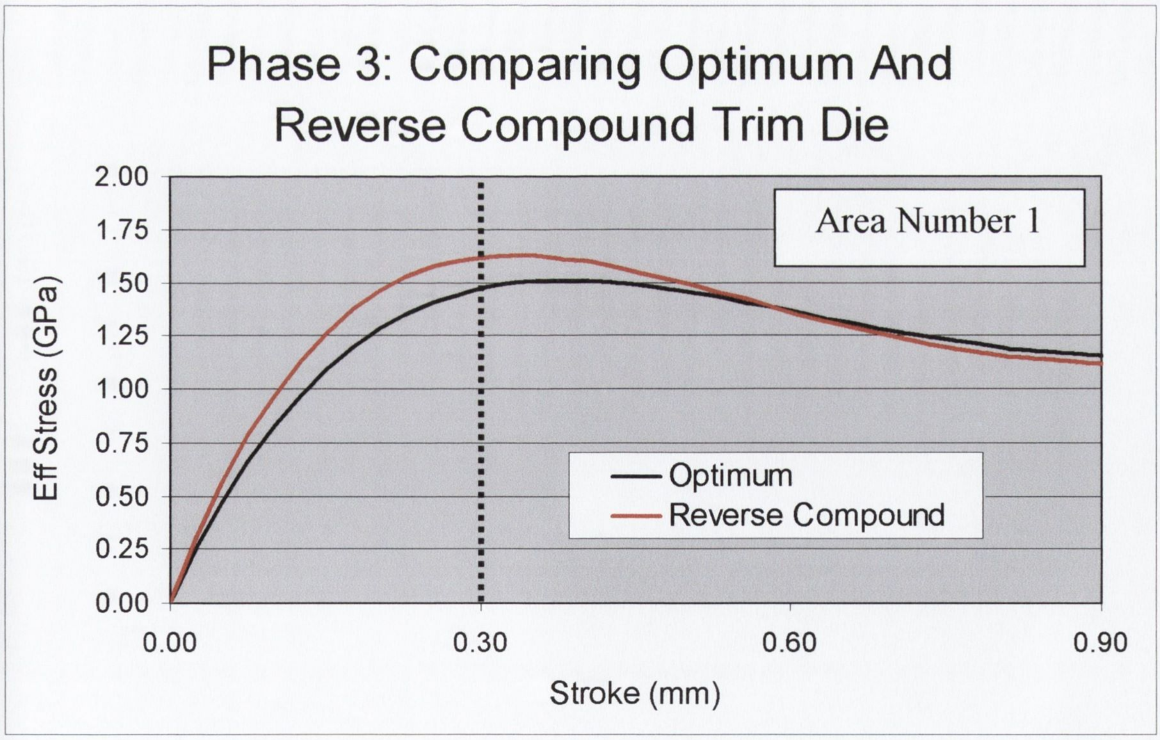

Figure 4-18237: Effective Stress vs. Stroke for the Optimum and Reverse Compound Trim Die at Area 1

With reference to figure 4-82, at a stroke of 0.3mm, the reverse compound and optimum trim die models induced an effective stress of 1.615GPa and 1.4695GPa respectively. Therefore at this level of stroke, the Optimum trim die profile induced an effective stress approximately 9% lower than the Reverse Compound trim die. Figures 4-83 and 4-84 illustrate the shaded plots of the effective stress distributions with the two trim die models. The Reverse compound trim die model causes a higher magnitude of effective stress due to the 'sharper' corner being forged into the workpiece. With reference to figure 4-84, the location of the maximum effective stress, within the workpiece, occurs at the intersection of the 0.4mm fillet and the larger 5.0mm blend radius. This blend radius effectively creates a sharper profile, which induces a higher magnitude of effective stress due to a reduction in the load bearing area.

In relation to Area 1, the Optimum trim die model was considered best as it induced the lowest effective stress values within the trim die material.

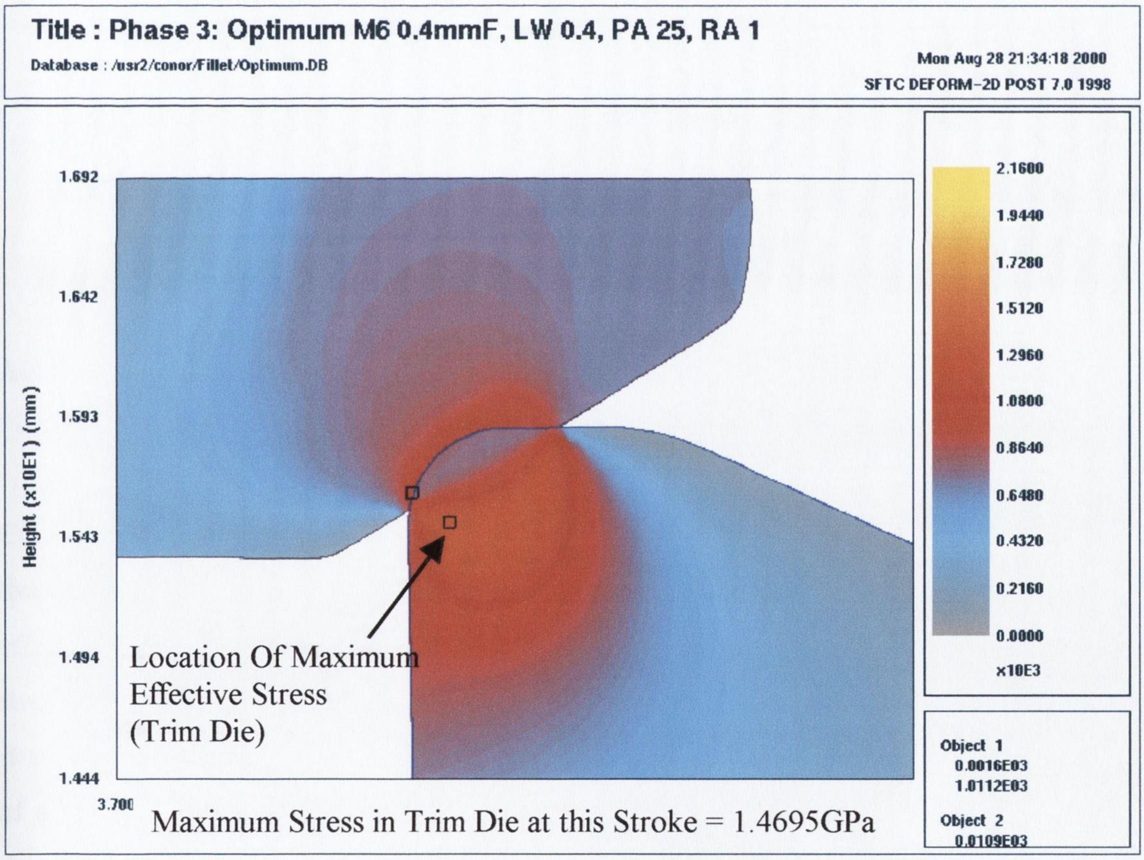

Location Of Maximum Effective Stress (Trim Die)

Maximum Stress in Trim Die at this Stroke = 1.4695GPa

Figure 4-83: Effective Stress in the Optimum Trim Die Model at 0.3mm Stroke

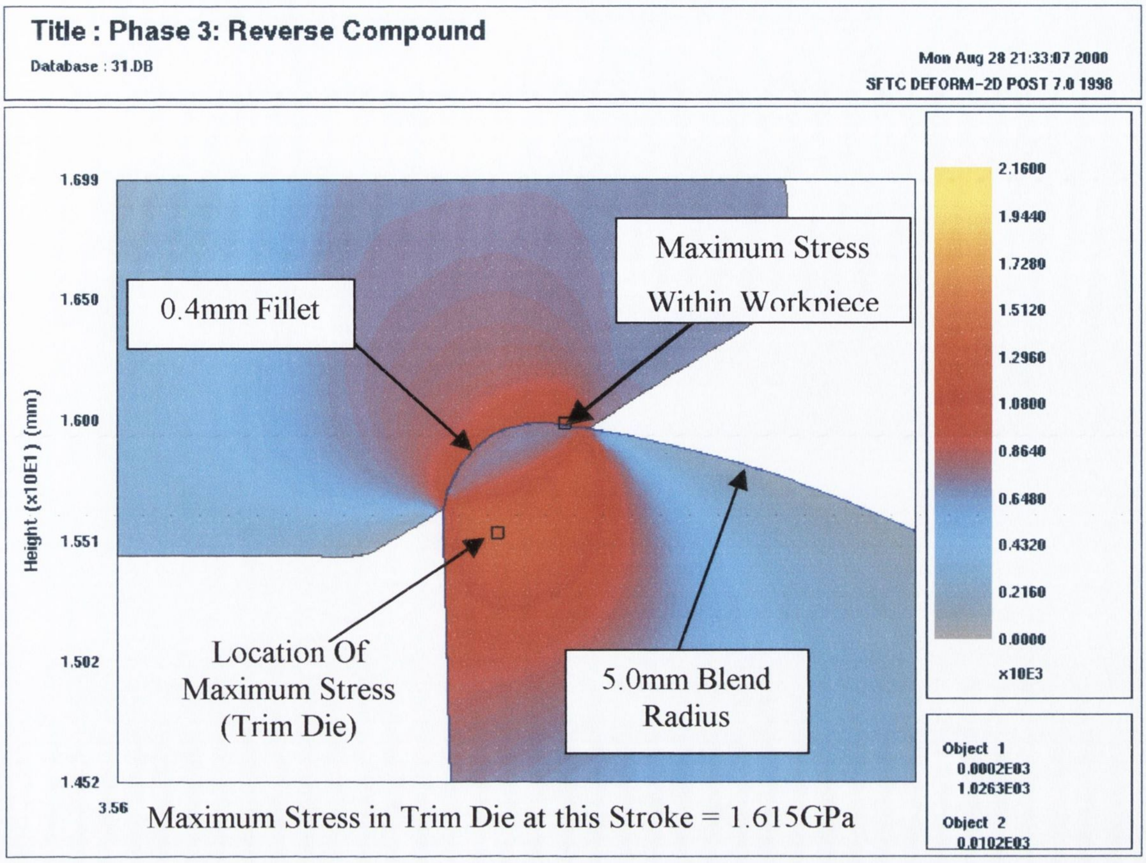

Figure 4-84: Effective Stress in the Reverse Compound Trim Die Model at 0.3mm Stroke

Area 2: Trim Die Stroke = 1.0mm

Figure 4-85 illustrates the effective stress results for the Optimum and Reverse Compound trim dies at the second stage, Area 2. The range of stroke on the x-axis allows the trends leading up to and following the 1.0mm mark to be visualised. The maximum effective stress induced in the Optimum and Reverse Compound trim dies, at this level of stroke is 1.1533GPa and 1.1153GPa respectively. Therefore at Area 2, which relates to a stroke of 1.0mm, the Reverse Compound trim die causes a reduction in the effective stress of approximately 3.3%. The percentage change between the two FEA models is relatively small, but with respect to figure 4-85, this small change is the start of a larger trend. As with the previous analyses conducted in Phase 1, once the stroke of 1.0mm has been passed, the level of effective stresses within both models start to increase. This increase is due to the workpiece material making contact with the top tool, see figures 4-86 and 4-87, which causes an additional resistance to the flow of the workpiece material.

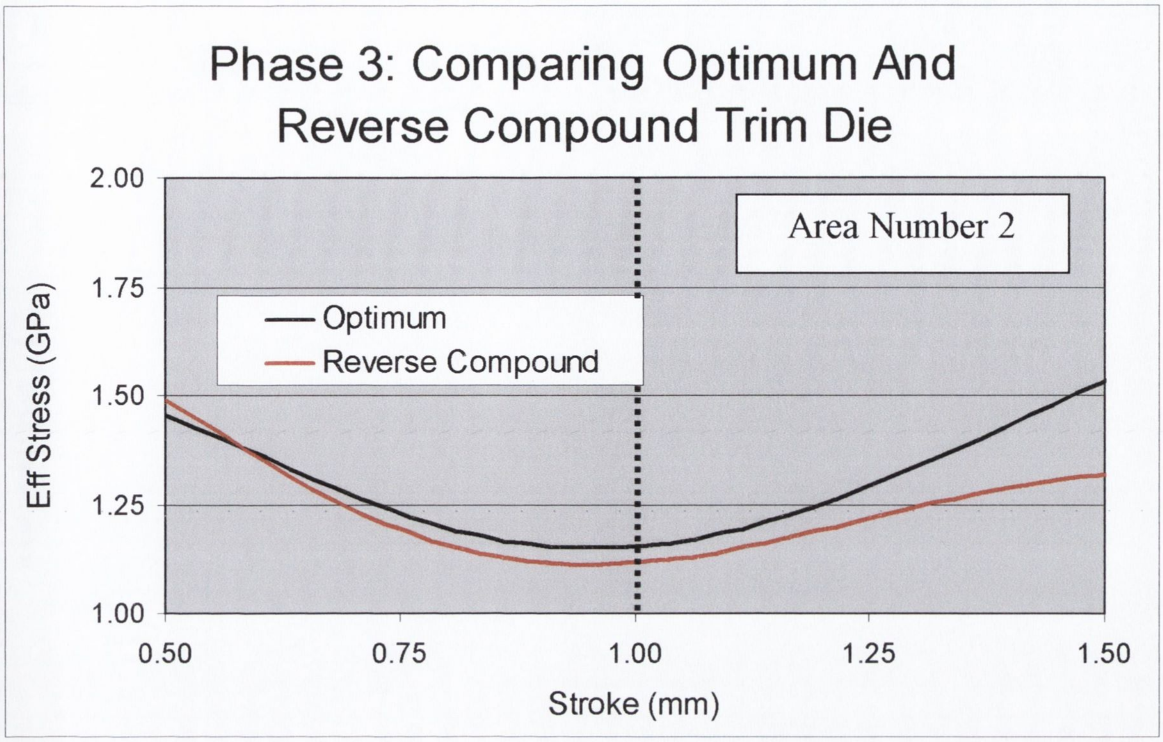

Figure 4-85: Effective Stress vs. Stroke for the Optimum and Reverse Compound Trim Die at Area 2

A comparison of figures 4-86 and 4-87 illustrate the very different trim die and top tool profiles simulated. The Optimum trim die, as illustrated in figure 4-86, induced the highest effective stress at this level of stroke because the workpiece material has to negotiate two sharp corners, one on the top tool and the second on the intersection between the land surface and the petal surface. In comparison, the Reverse Compound model, illustrated in figure 4-87, has replaced these sharp corners with two large radii, enabling the workpiece material to flow less restricted into the trimmed area. As the trim die stroke increases past 1.0mm, the difference between the two models becomes more exaggerated. The Reverse Compound trim die, due to the two large radii, causes a reduction in the normal pressure between the trim die, workpiece and top tool. This reduction in the normal pressure, reduces the level of tangential shear stress and friction at the interface between the workpiece, trim die and top tool. Hence at this position of trim die stroke, the Reverse Compound trim die induced a marginally lower level of effective stress and was considered best.

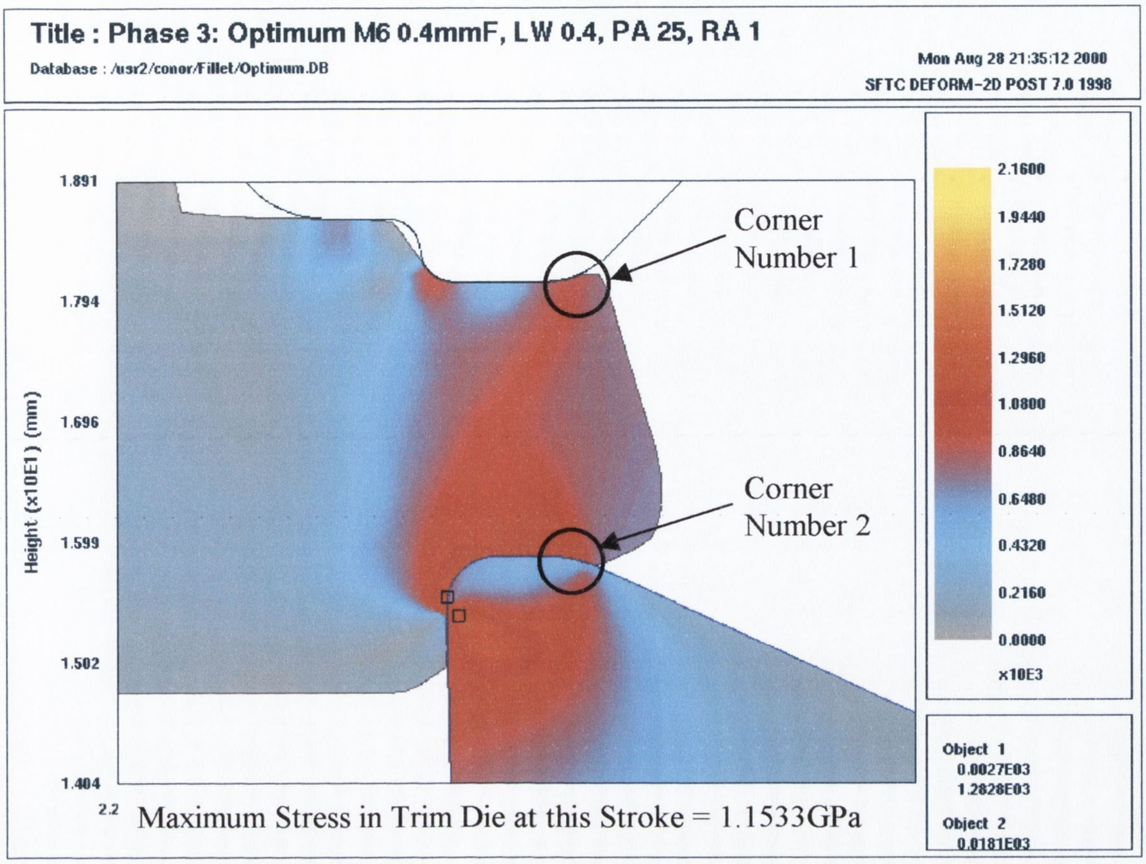

Figure 4-86: Effective Stress in the Optimum Trim Die Model at 1.0mm Stroke

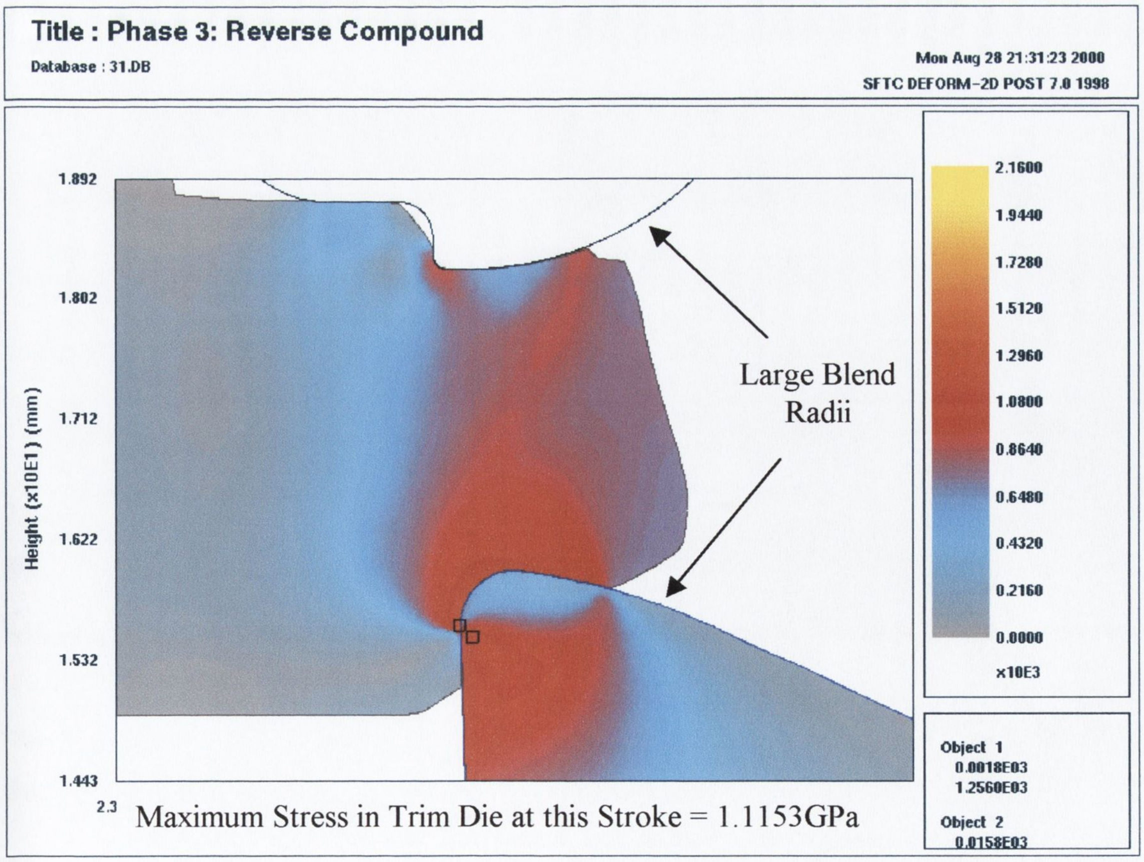

Figure 4-87: Effective Stress in the Reverse Compound Trim Die Model at 1.0mm Stroke

Area 3: Trim Die Stroke = 3.0mm

Figure 4-88 below illustrates the effective stress plotted trim die stroke for the Optimum and Reverse Compound trim dies at stage 3. As with all the analysis conducted in Phase 1, the final stroke of the trim die is dictated by the corner radius. This effect is explained in greater detail in Appendix D on page 238. Because both the Optimum and Reverse Compound trim die have a corner radius of 0.4mm, both incurred a stroke of 2.92mm. This final stroke of 2.92mm is highlighted in figure 4-88 below.

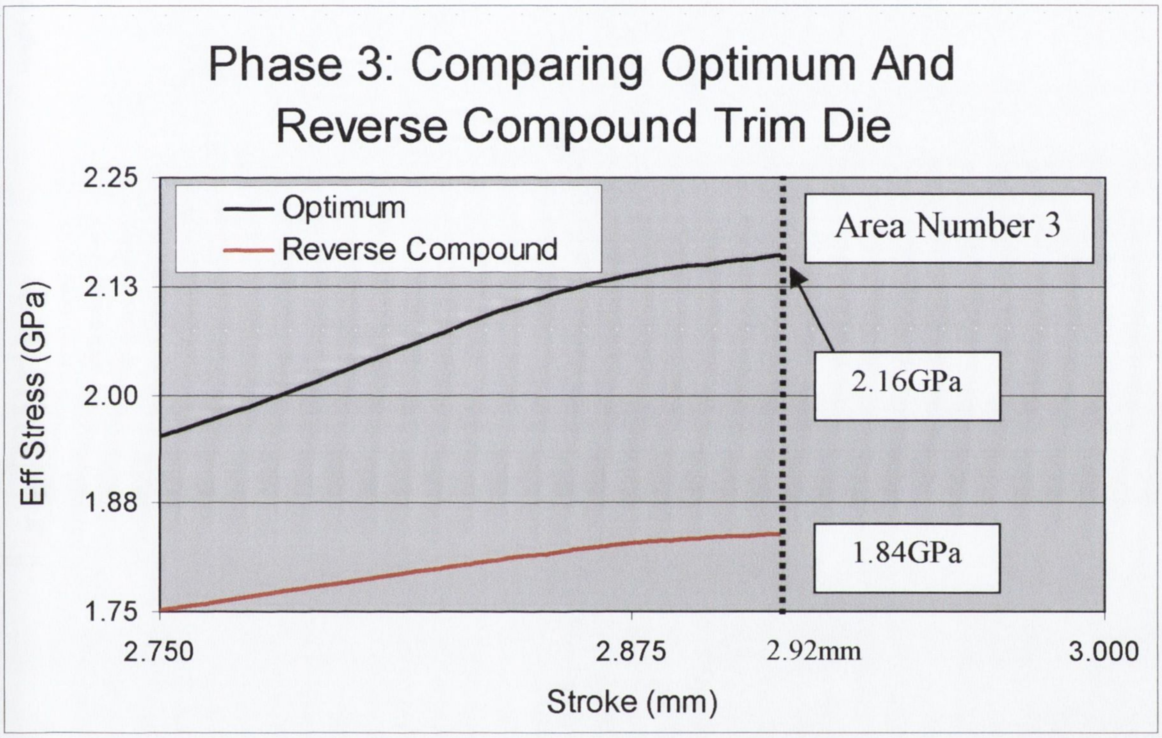

Figure 4-88: Effective Stress vs. Stroke for the Optimum and Reverse Compound Trim Die at Area 3

The Optimum and Reverse Compound trim die induced effective stresses of 2.16GPa and 1.84GPa respectively. This is a reduction of approximately 15%. Figures 4-89 and 4-90 illustrate the shaded effective stress plots in both the Optimum and Reverse Compound trim die models at the final stroke of 2.92mm. The yellow region within the trim die, shown in figure 4-89, highlights the higher effective stress of 2.16GPa. The aspect ratio in the Reverse Compound trim die model, i.e. the flash width divided by the flash thickness, is constantly changing due to the two large blend radii.

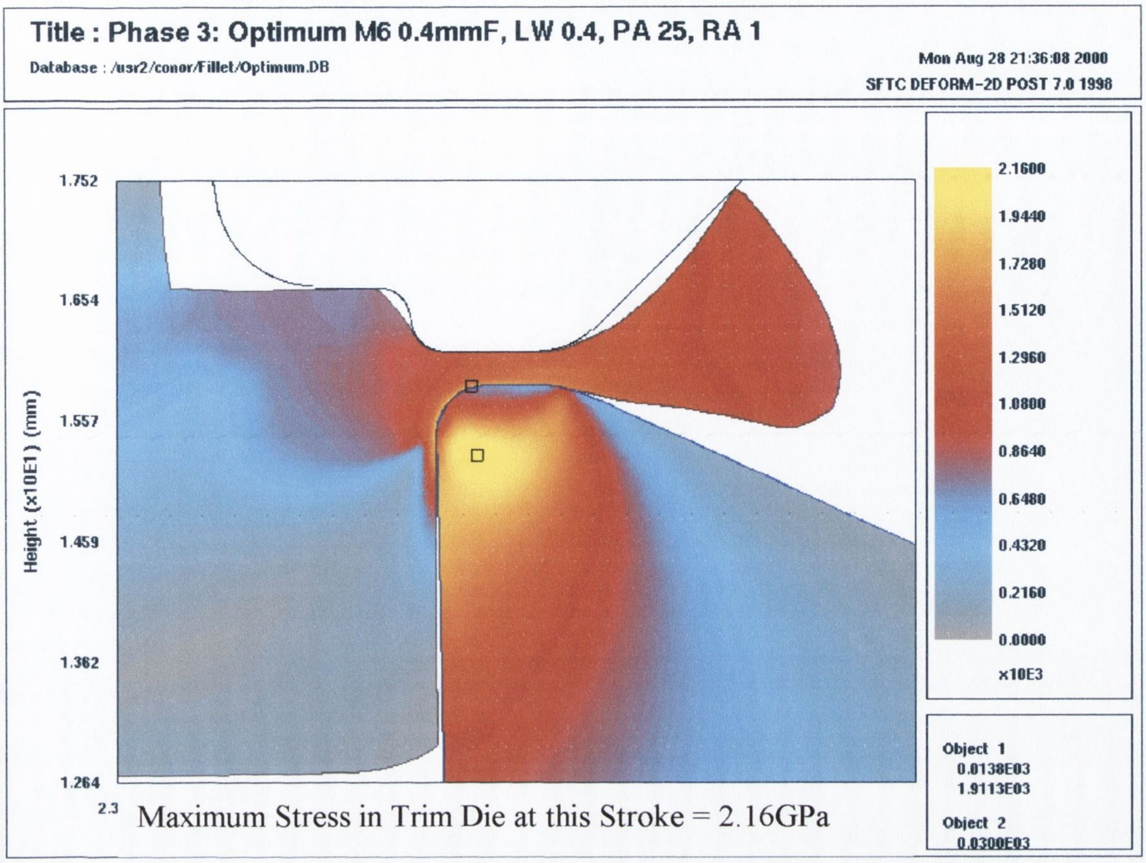

Maximum Stress in Trim Die at this Stroke = 2.16GPa

Figure 4-89: Effective Stress in the Optimum Trim Die Model at the Final Stroke

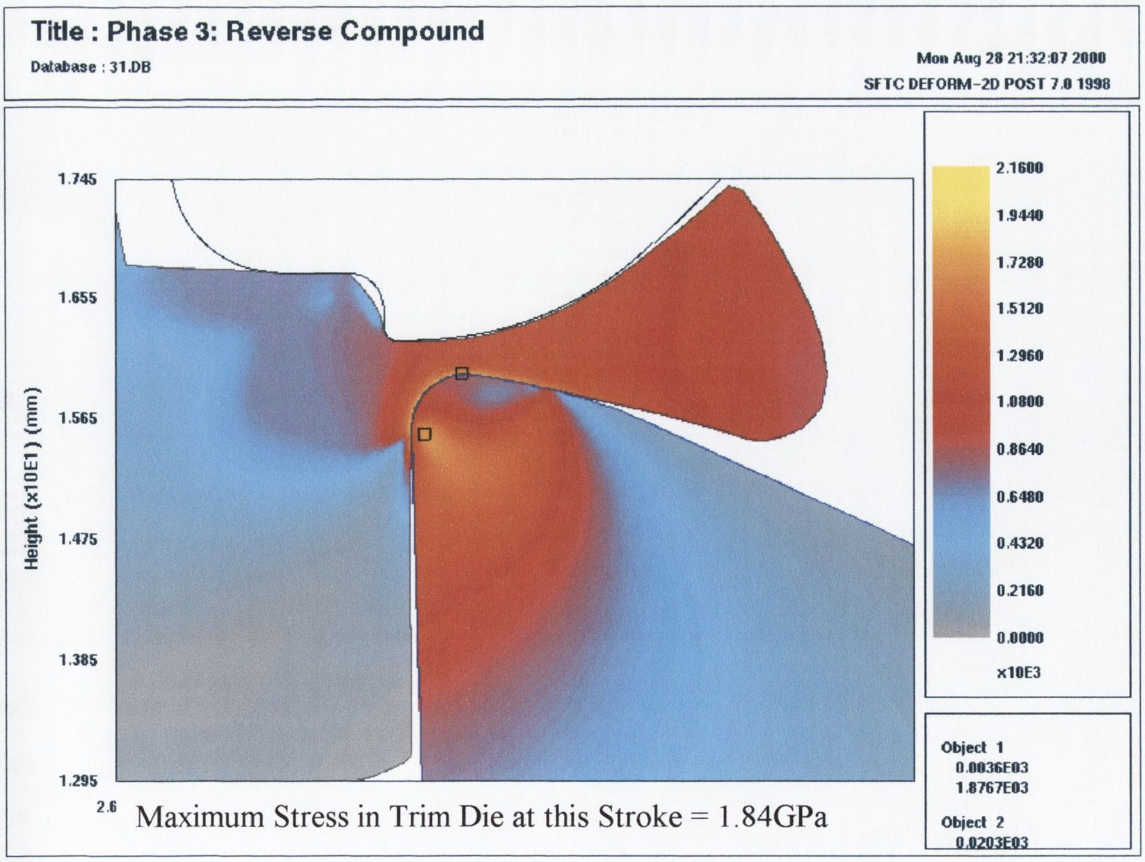

Maximum Stress in Trim Die at this Stroke = 1.84GPa

Figure 4-90: Effective Stress in the Reverse Compound Trim Die Model at the Final Stroke

With reference to figures 4-88, 4-89 and 4-90, the Reverse Compound trim die induced the lowest effective stress at Area 3. For this reason, the reverse Compound trim die was considered best at stage 3 of the trim die stroke.

In terms of the maximum tensile radial stresses, along the top surface of the trim die, the Optimum and Reverse Compound models induced values of 39.3MPa and 38.5MPa respectively. This is a difference of only 2%, therefore in terms of the tensile radial stress, there is virtually no difference between the two models.

4.3.4 Phase 3 Conclusions

Two FEA models were simulated in Phase 3. The first trim die profile modelled in Phase 3 was obtained by combining the conclusions from Phases 1 and 2. This new profile was designated 'Optimum'. The Phase 2 set of tests highlighted the significance of the land width, in terms of the induced effective and tensile radial stresses. For this reason, the second trim die modelled was a previously untested FEA simulation with a modified trim die and top tool profile. This new profile was designated 'Reverse Compound' due to it similarity to the standard compound trim die profile modelled in Phase1. Comparisons of the two models at the various stages of trim die stroke are listed in table 4-40 below.

Trim Die Name	Area Number	Trim Die Stroke (mm)	Lowest Induced Effective Stress (GPa)
Optimum	1	0.3	1.4695
	2	1.0	1.1533
	3	2.92	2.16
Reverse Compound	1	0.3	1.615
	2	1.0	1.1153
	3	2.92	1.84

Table 4-40: Phase 3 Conclusions

With reference to table 4-40 above, the truly optimum trim die profile, which induced the lowest magnitude of effective stress at stage 3 of 1.84GPa would be the Reverse Compound model. This effective stress value of 1.84GPa is approximately 15% lower than the 'Optimum' trim die modelled in this section and up to 33% lower than the worst model simulated in Phase 1.

4.4 Phase 4: 3D Analysis

In Section 3.1.2 on page 54, it was explained that a 'worst case scenario' was used to convert the 'real world' three dimensional (3D) trim die into a theoretical two dimensional (2D) model. The main advantage of using a 2D model is that the simulation process becomes simpler, but more importantly, the solution times are significantly reduced. A typical analysis procedure would be to first simulate the process in 2D and once the optimum parameters had been established, conclude the analysis by using the optimum parameters in a 3D simulation.

4.4.1 The Need For 3D

The 'worst case scenario' considered a plane through the trim die where the greatest amount of workpiece material would be trimmed, and consequently on which the greatest stress would occur. This plane, as explained in figure 3-3 on page 55, was through the center of the flats of the internal hexagonal hole. The negative aspect of simulating the trimming process as being axisymmetric is that the FE package considers the internal hole as being circular. This internal circular hole is illustrated in figure 3-6 on page 58. Because of this, the stress distribution at the corners of the hexagonal hole could never be established using an axisymmetric FE model. Therefore to simulate the stress distribution in the vicinity of the corners of the hexagonal hole, 3D analysis is required.

Once the 2D models had been completed, it was originally intended to simulate various trim die profiles in 3D, unfortunately, simulating the large plastic deformation, associated with the trimming process, proved to be very difficult. However, two 3D models have been simulated, using the 3D version of DEFORM, and will now be presented.

4.4.2 Rigid Trim Die Analysis

The first attempt to simulate the trimming process in 3D was simplified by making two changes to the model.

1. The trim die and top tool were considered as 'Rigid' within the FE model.
2. Due to symmetry, it was only necessary to model one quarter of the trim die.

With respect to point one, rigid objects are modelled within DEFORM as non-deformable bodies. During the deformation process, the object is represented by its geometric profile and not by a generated mesh. Running the simulation with rigid objects greatly reduces the running time but unfortunately, no stresses can be calculated within a rigid object. With respect to point two, there is another plane of symmetry, which would reduce the 3D model to a one-sixth simulation. This plane of symmetry was rejected due to difficulties in applying accurate boundary conditions.

Figure 4-146 on the following page, shows the one-quarter 3D FE model. In this analysis the workpiece was considered as a 'plastic' object, while the rigid trim die and top tool are represented in wire mesh form. Table 4-41 below, highlights that although the model was simplified to only one-quarter full size, the large number of elements within the workpiece resulted in the run time being considerably larger than that of an axisymmetric 2D model.

Object	Element Number		Run Time	Typical 2D Run Time
	Surface	Body	(Hours)	(Hours)
Workpiece	4664	24,518	≈ 60	1.5

Table 4-41: Phase 4: Workpiece Element Number and Run Time

With respect to table 4-41 above, the total number of elements in the workpiece, combining the surface and body elements, was 29,182. The time taken to simulate the model was approximately one week. When this run time is compared to a typical 2D model, the 3D run time was over 40 times slower. Figures 4-92 and 4-93 show the shaded effective stress distributions within the workpiece at 50% and 100% deformation respectively.

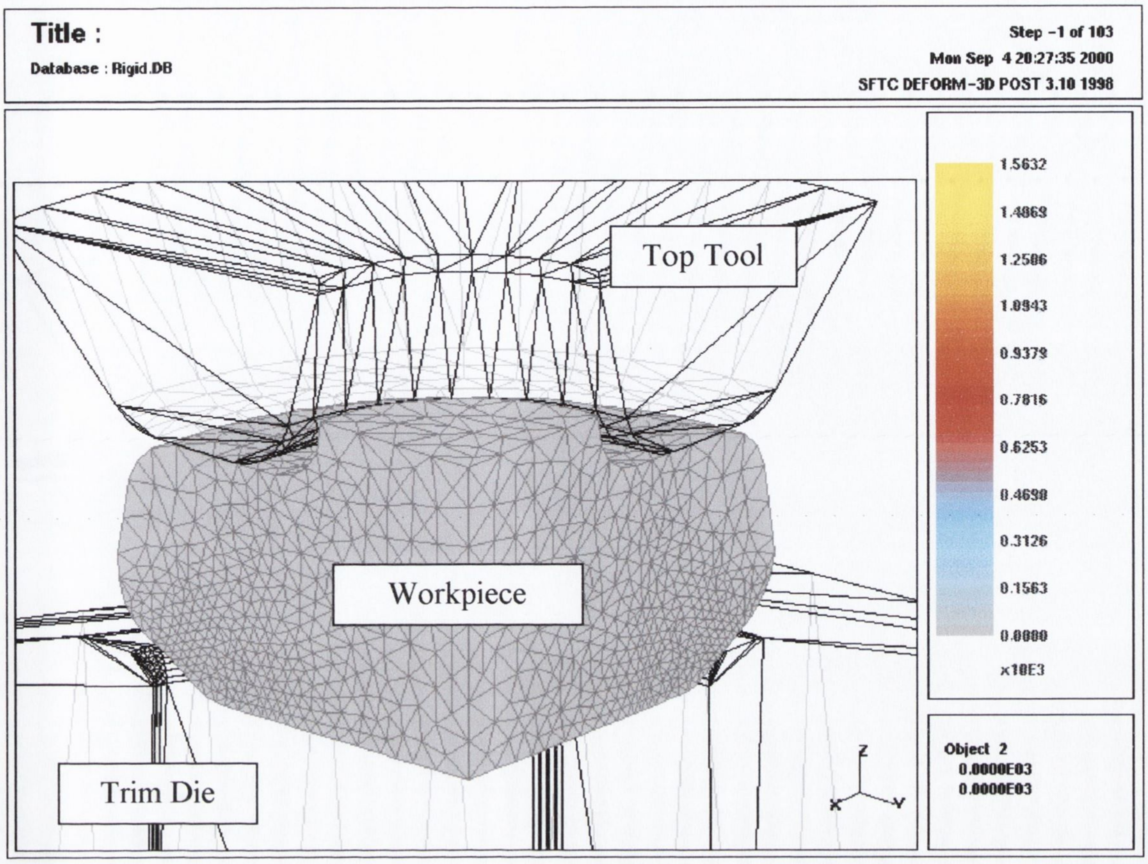

Figure 4-91: One-Quarter Model Showing Workpiece and Rigid Trim Die and Top Tool

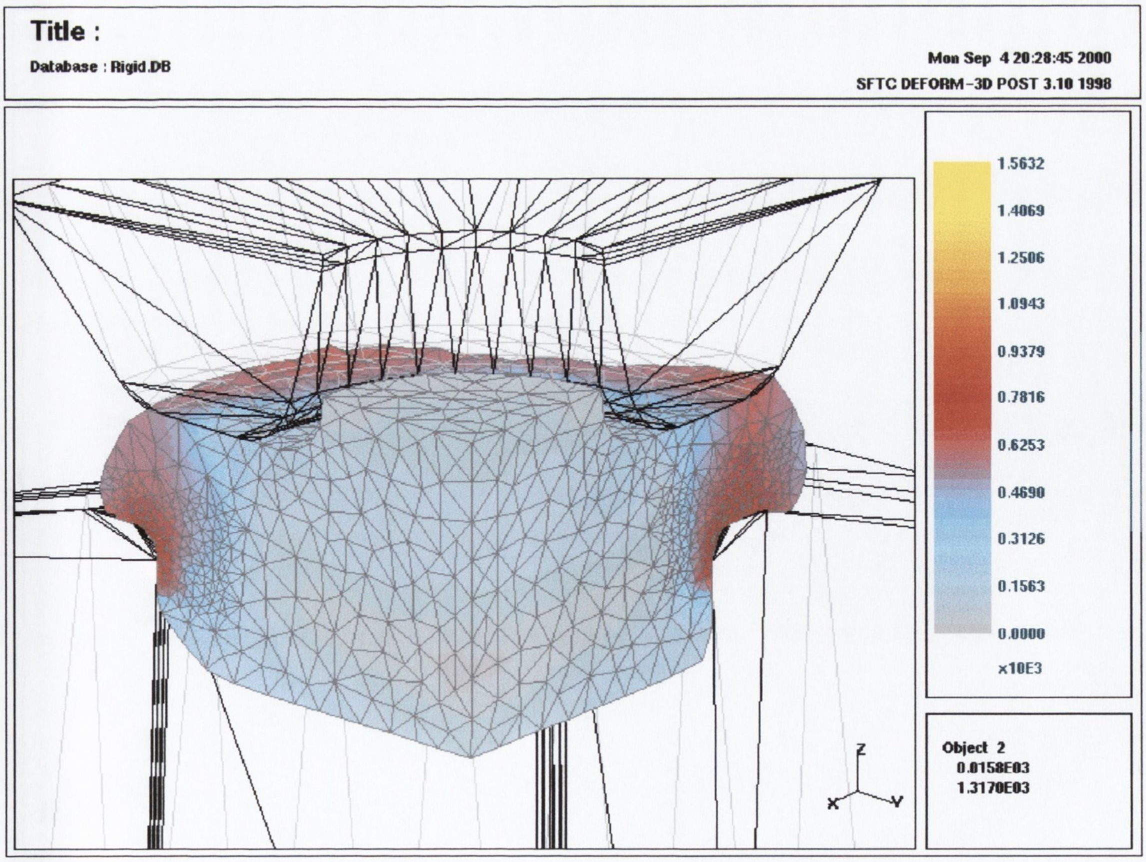

Figure 4-92: Phase 4: Effective Stress Distribution Within Workpiece at 50% Stroke

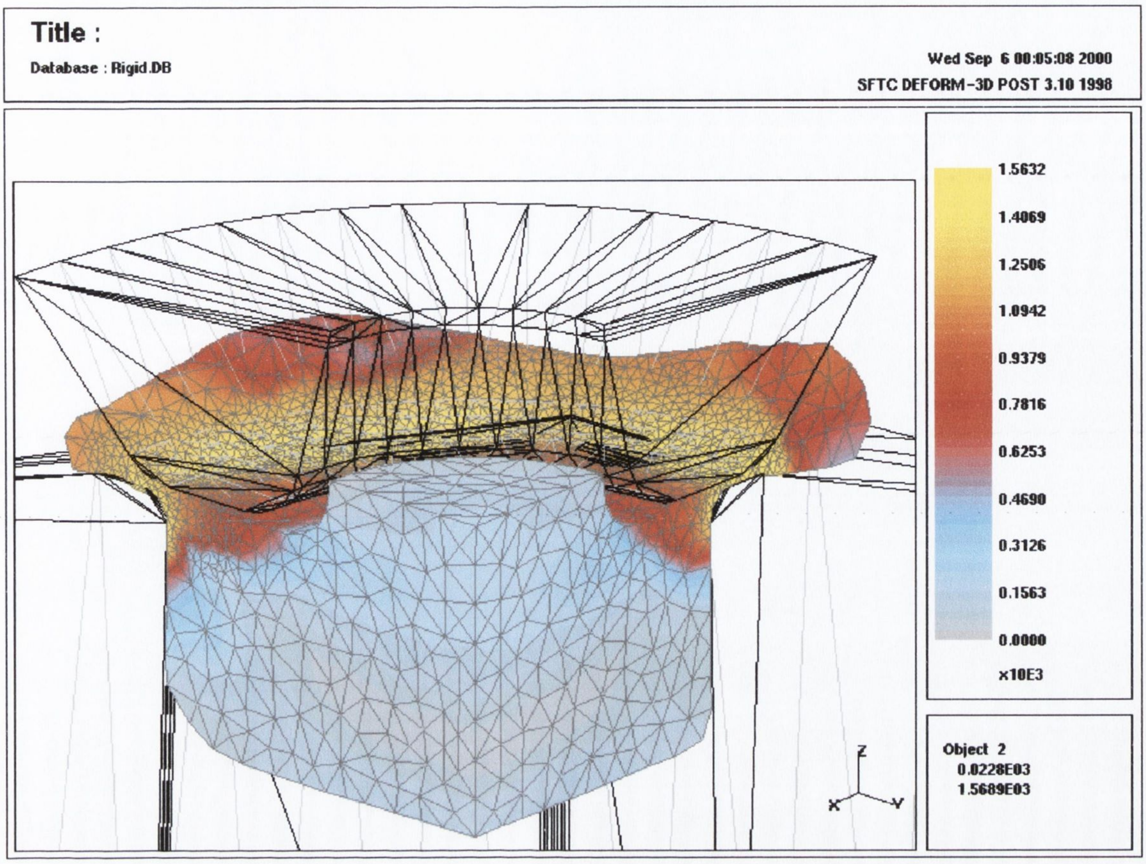

Figure 4-93: Phase 4: Effective Stress Distribution Within Workpiece at 100% Stroke

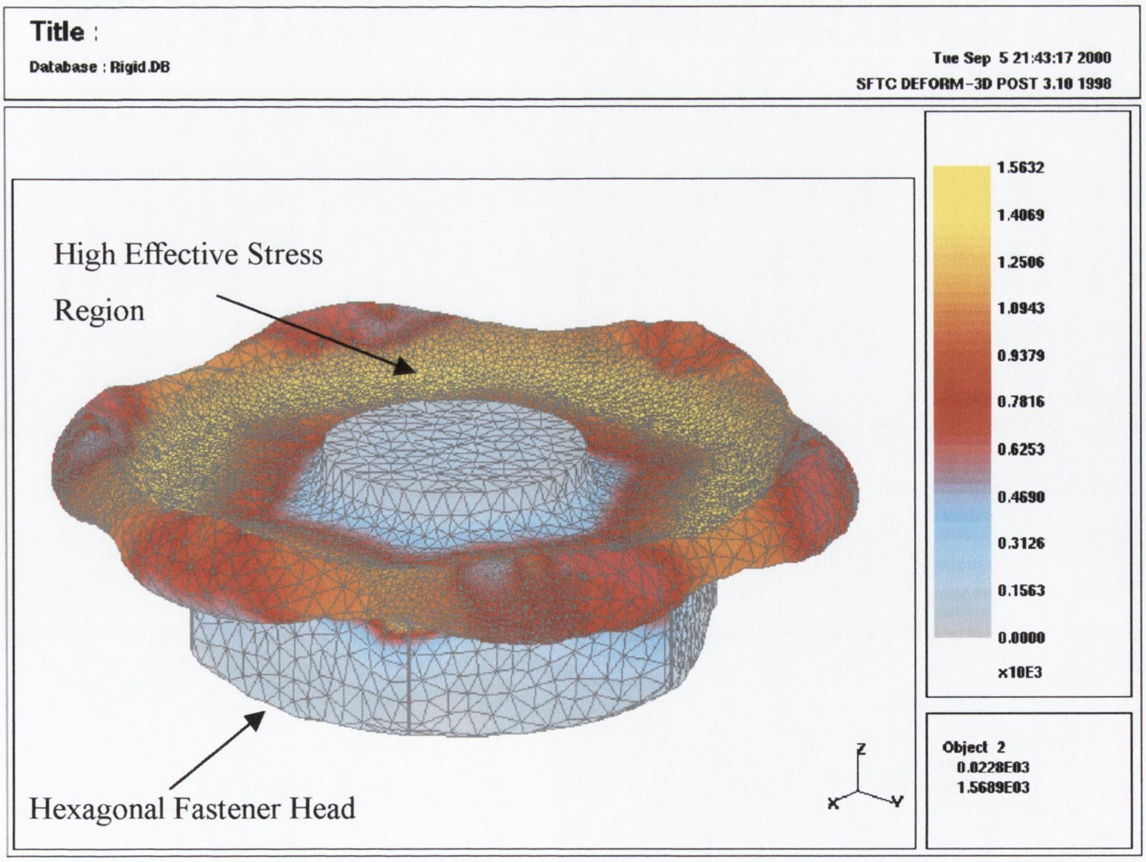

Figure 4-94: Phase 4: Effective Stress Distribution Within Workpiece at 100% Stroke. Tools Removed.

With respect to figure 4-94 on the previous page, the rigid trim die and top tool have been removed and the one-quarter workpiece has been mirrored to illustrate the entire workpiece at 100% deformation. Although the 3D model considered the trim die as being rigid, the final deformed profile of the workpiece coincided very well to an actual workpiece, as shown in figure 4-95 below.

Figure 4-95: Actual Bolt Head Showing Excess Trimmed Material.

4.4.3 Elastoplastic Trim Die

As previously explained, in the first 3D model the trim die was considered as a rigid tool, and therefore the stress distributions within the die were unknown. To address this situation a second 3D model was used in which the trim die was considered to be an elastoplastic object.

Figures 4-96 and 4-97 illustrate the shaded effective stress distributions in the 3D trim die at 5% and 100% deformation respectively. The deformable workpiece has been removed from these images for clarity. Both figures show that the region of highest effective stress occurs at the centre of the flat surface of the internal hexagonal hole. This result validates the 'worst case scenario' assumption detailed previously in Section 3.1.2.1 on page 53.

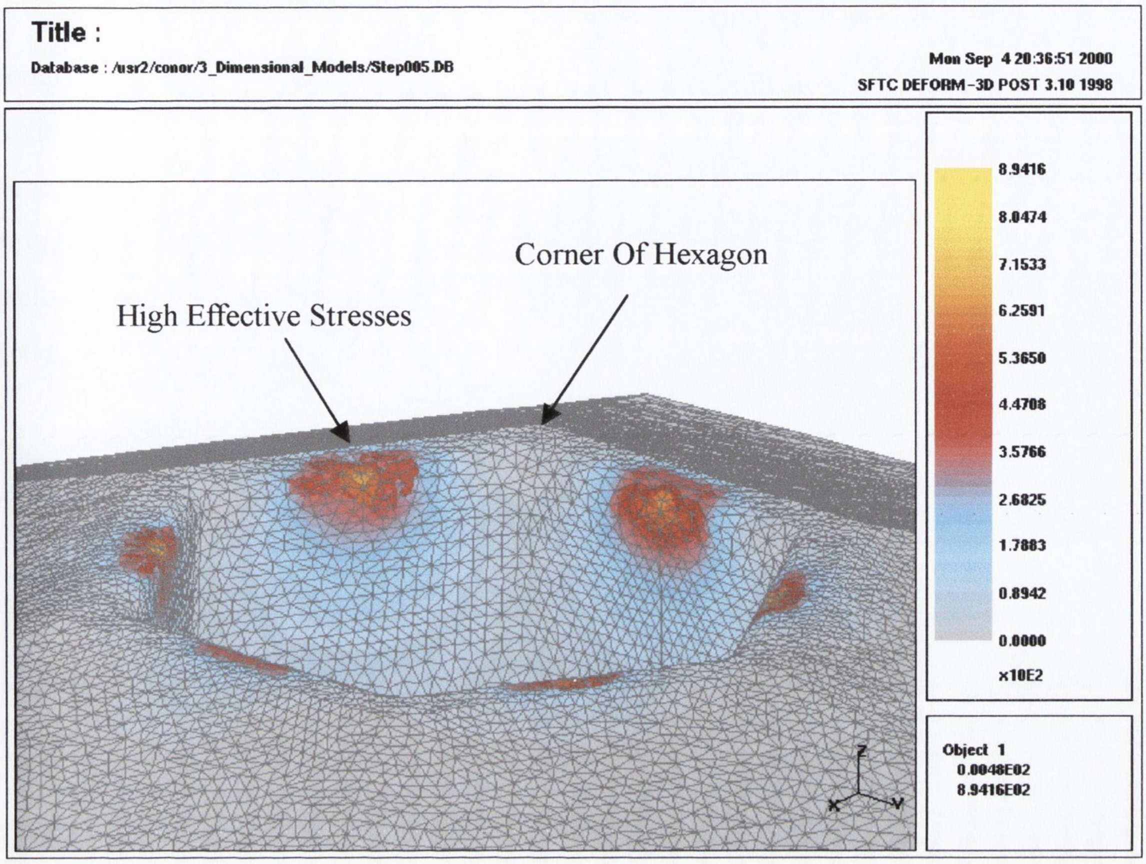

Figure 4-96: Phase 4: Elastoplastic Trim Die at 5% Deformation

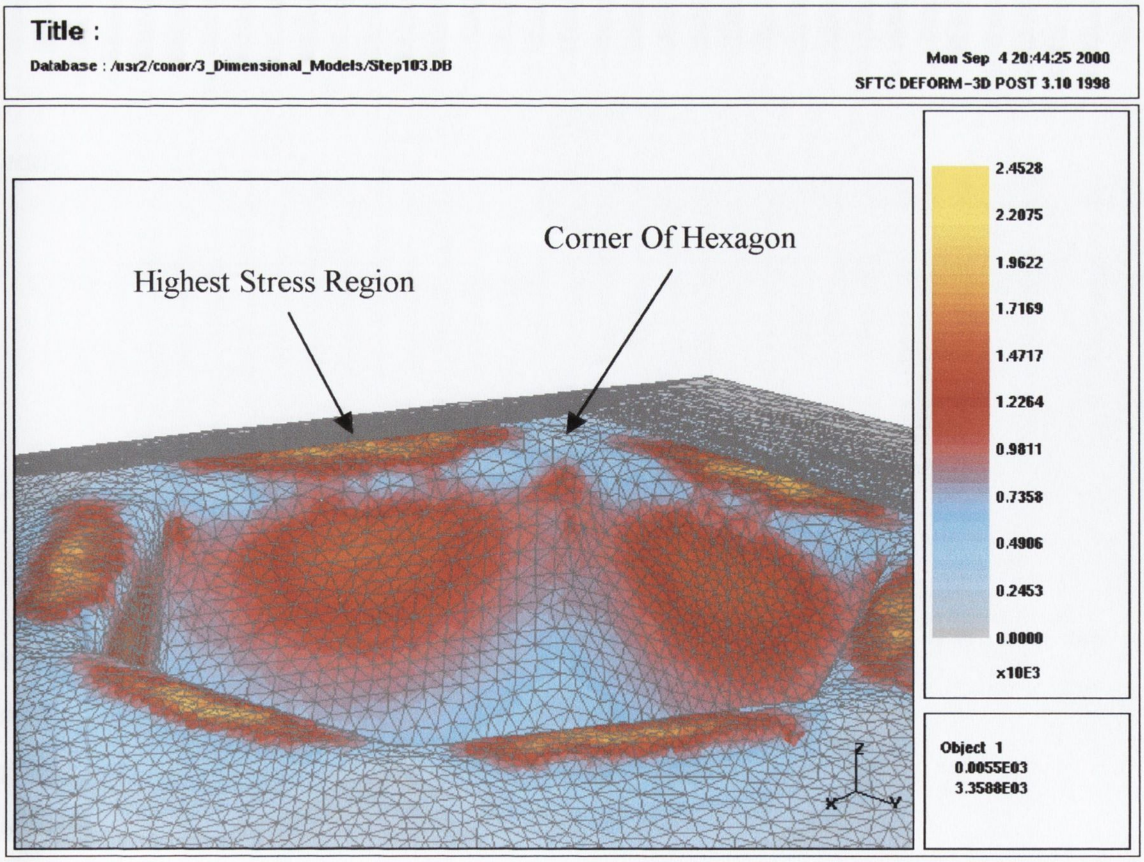

Figure 4-97: Phase 4: Elastoplastic Trim Die at 100% Deformation

Table 4-42 below shows the total number of elements and run times for the two 3D models simulated in Phase 4. As previously mentioned, the first simulation with rigid dies required a minimum of 29,182 elements within the workpiece to simulate the deformation process. The second 3D model required 52,467 elements within the trim die, which brought the total number of elements in the model to 81,649 (Trim Die and Workpiece). Table 4-45 also highlights that the second 3D model was twice as slow as the first and over 80 times slower than a standard axisymmetric 2D model.

Sim. No	Object	Element Number			Run Time (Hours)	Typical 2D Run Time (Hours)
		Surface	Body	Total		
1	Workpiece	4,664	24,518	29,182	≈ 59	1.5
2	Trim Die	8,880	43,587	52,467	≈121	1.5

Table 4-42: Phase 4: Workpiece and Trim Die Element Numbers and Run Time

4.4.4 Conclusions: Phase 4

The 3D analysis was useful in order to model as accurately as possible the 'real world' trim die, due to the internal hexagonal hole. The analysis was beneficial because:

1. The theoretical profile of the deformed workpiece, obtained in the FE model, closely matched the experimental profile, validating the FE set-up.
2. The selection of the 'worst case scenario', through the centre of the flats on the hexagon, as the plane for the axisymmetric 2D models was correct, because it was proved that the highest stresses occurred at this location.

However, simulating the trimming process in 3D is very demanding of computational power. Table 4-42 shows clearly that the second 3D model is over 80 times slower than a comparable model in 2D. Therefore due to the nature of the forging operation and the large scale deformation involved, 3D modelling of the trimming process is not yet practical.

4.5 Experimental Tests

4.5.1 Compression Test Results

As outlined in section 2.4.1, compression tests were carried out to ascertain the necessary flow stress data for input into the DEFORM pre-processor.

To investigate the influence of the hardness of an M2 specimen on the flow stress behaviour, compression tests were carried out on specimens having 3 different Rockwell hardness levels:

1) 57 – 59 HRc
2) 60 – 62 HRc
3) 62 – 64 HRc

The stress / strain curves for M2 at the three hardness ranges are provided in figure 4-98. The Rockwell hardness values listed in the three points above are represented in figure 4-98 by the coloured lines, black, red and blue respectively. A total of eight tests, for each hardness range, were conducted to establish confidence in the results.

Two main points can be concluded from these graphs.

1) A small reduction in the hardness value from 60~62 to 57~59 Rockwell, had a very large effect on the stress/strain curve. See red and black lines in figure 4-98.
2) Although the onset of yielding is dictated by the relative hardness of the tool steel, the elastic stiffness for all three hardness grades remains unchanged.

The hardness of the trim die after its final tempering, see section 2.1.5, was 60-62 HRc, i.e. the red line in figure 4-98. The stress and strain points where taken from this graph and used as the input data for flow stress curve for M2 within DEFORM. A standard accepted yield stress value for M2 tool steel, having a Rockwell Hardness of 60-62 HRc, is 2500MPa.

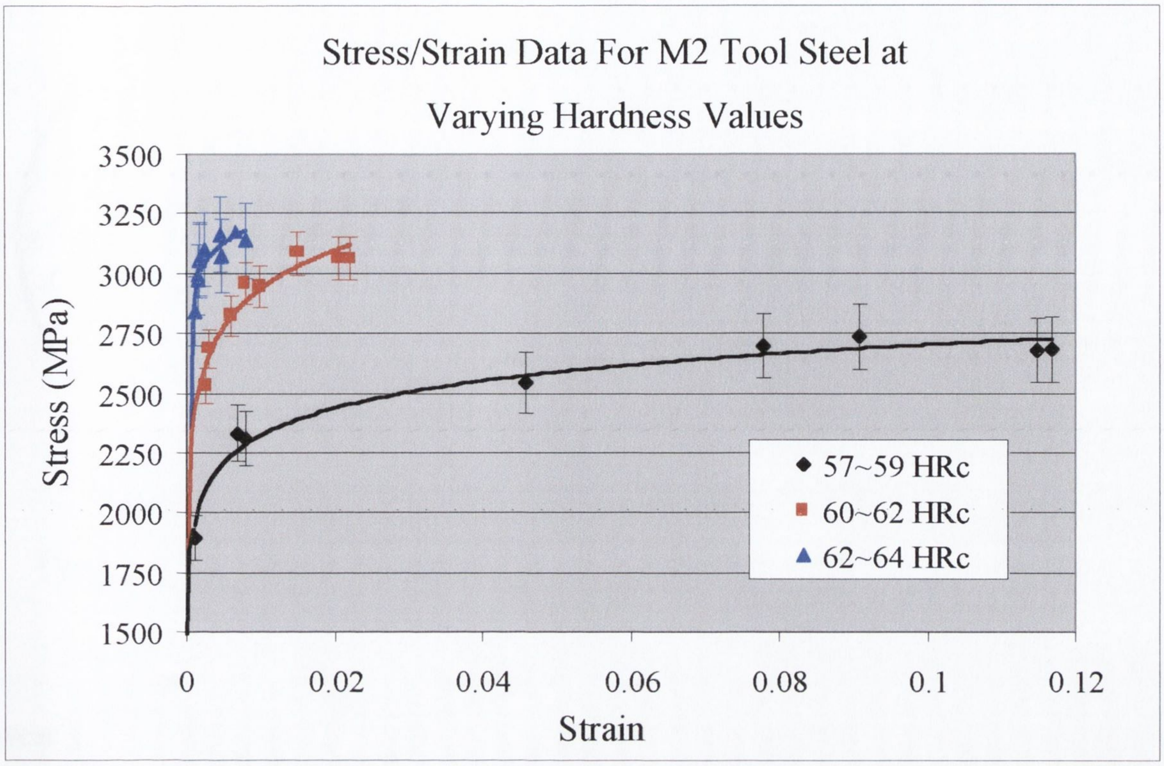

Figure 4-98: Experimental Stress / Strain Data Collected for the Tool Steel Material M2

4.5.2 Ring Compression Test Results

The ring compression test, as outlined in Appendix C on page 234, was conducted on the low carbon medium alloy heading material in the form of a steel ring compressed between two coated M2 anvils. The anvils were ground, heat treated and coated to accurately represent the trimming process between the trim die and workpiece. The same lubricant was used in the test as is used in the trimming process. During the tests it became apparent that the ring was not deforming homogenously. Instead of producing a flattened circular ring, an 'elliptical' ring was formed. Figure 4-99 illustrates the ideal circular flattened ring on the left and the elliptical ring obtained on the right. Although many materials employed in engineering applications possess mechanical properties that are direction-dependent, i.e. anisotropy [41], the elliptical deformation of a simple ring test on a low carbon, medium alloy steel would not be anticipated or expected. Closer examination of the coated M2 anvils revealed that the final grinding operation before the application of the coatings, left straight grooves on the surface. Therefore during the deformation of the ring, the material flowing in the same direction as the straight grooves would experience less resistance than the material flowing at 90° to the grooves.

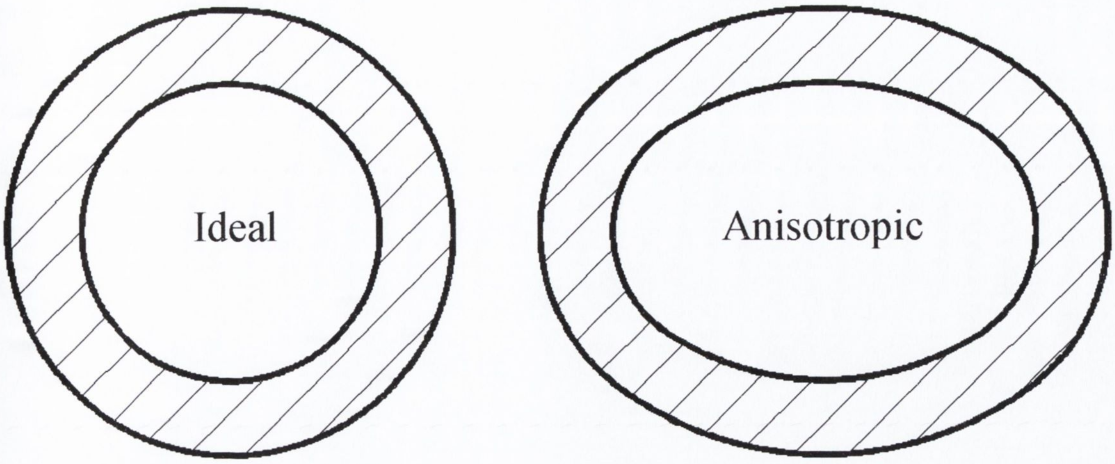

Figure 4-99: plan View Of Ideal Deformation on the Left and Anisotropic Deformation on the Right

Figure 4-100 below shows the M2 anvil, the grinding direction and the two distinct wear patterns on the anvil. These wear patterns were left behind by the workpiece material sliding over the anvil. These wear patterns show that the ring specimen had a higher deformation in that direction which lines up with the grinding direction on the anvil.

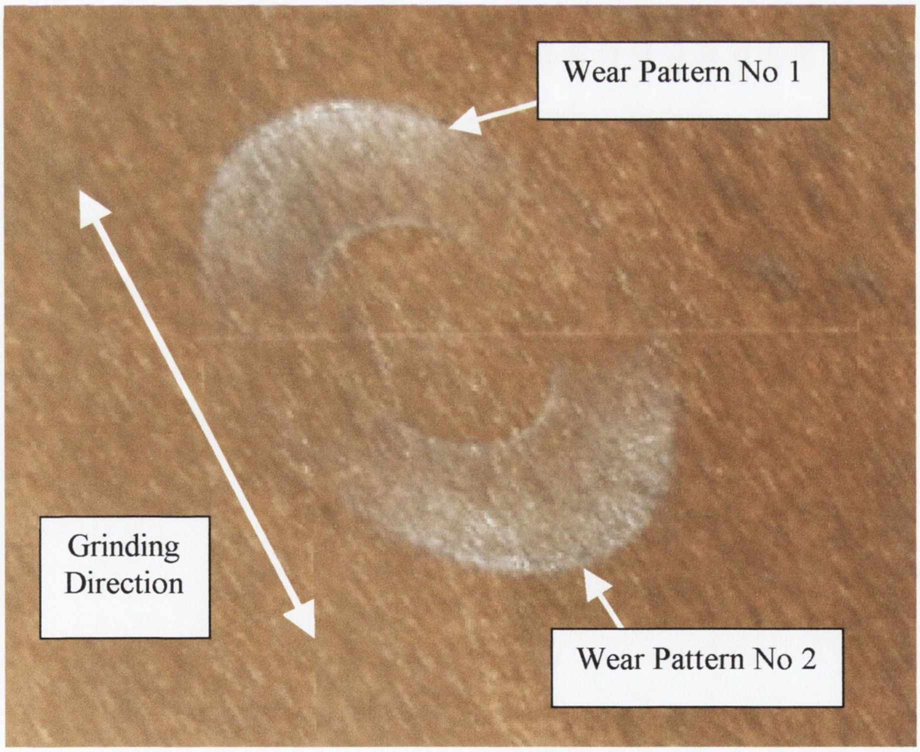

Figure 4-100: Orientation of the Grinding Grooves on the M2 Anvils and the Associated Wear Patterns

The end results of these findings was that the theoretical ring calibration charts, detailed in Appendix A could not be used because the internal hole of the deformed specimen had effectively a major and minor axis, and as a consequence both readings gave different friction factors (m).

The friction factor (m) for all the FE models simulated in this project used a value of 0.1. This friction factor value was taken from the established research work of Shiro Kobayashi, Soo-Ik OH and Taylan Altan [41], where it is stated that for cold forming of steels using lubricants or oils, a friction factor (m) in the range 0.08 to 0.1 is suitable.

4.5.3 Forging Load Test Results

As explained in Section 3.2.2.1, the forging load tests were conducted to validate the FE results. In Section 3.1.2.1 on page 54, it was explained that the 'real world' 3D trim die was reduced to a 2D representation by considering the 'worst case scenario'. This assumption transformed the internal hexagonal hole into a circular one. Therefore to compare the FEA and experimental results, the trim die and top tool needed to have circular internal holes. Figure 4-101 below shows a standard trim die on the left, with the hexagonal internal hole, along side the circular trim die and top tool.

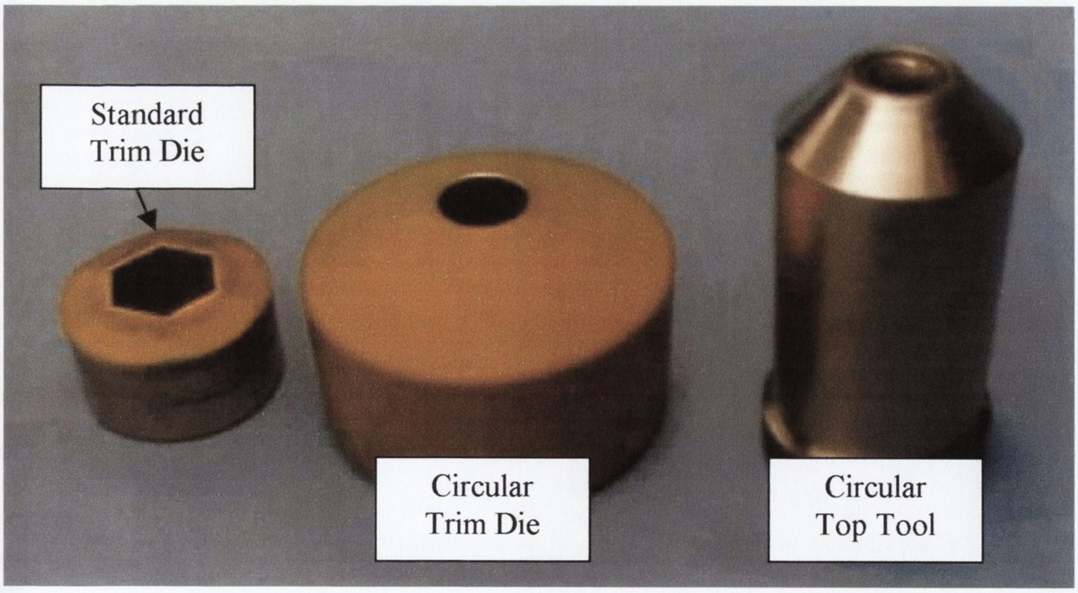

Figure 4-101: Forging load Validation Trim Die and Top Tool

A P.C. using the data acquisition software Lab view V5.1, was used to obtain the displacement of the press crosshead and the forming load recorded on the load cell. Figure

4-102 shows the first comparison between the experimental and theoretical FE models. Two points were concluded from figure 4-102:

1. The percentage difference between the theoretical and experimental results at the end of the trim die stroke was almost 30%
2. The initial path taken by the two curves, up to a stroke of 1.0mm, was very different.

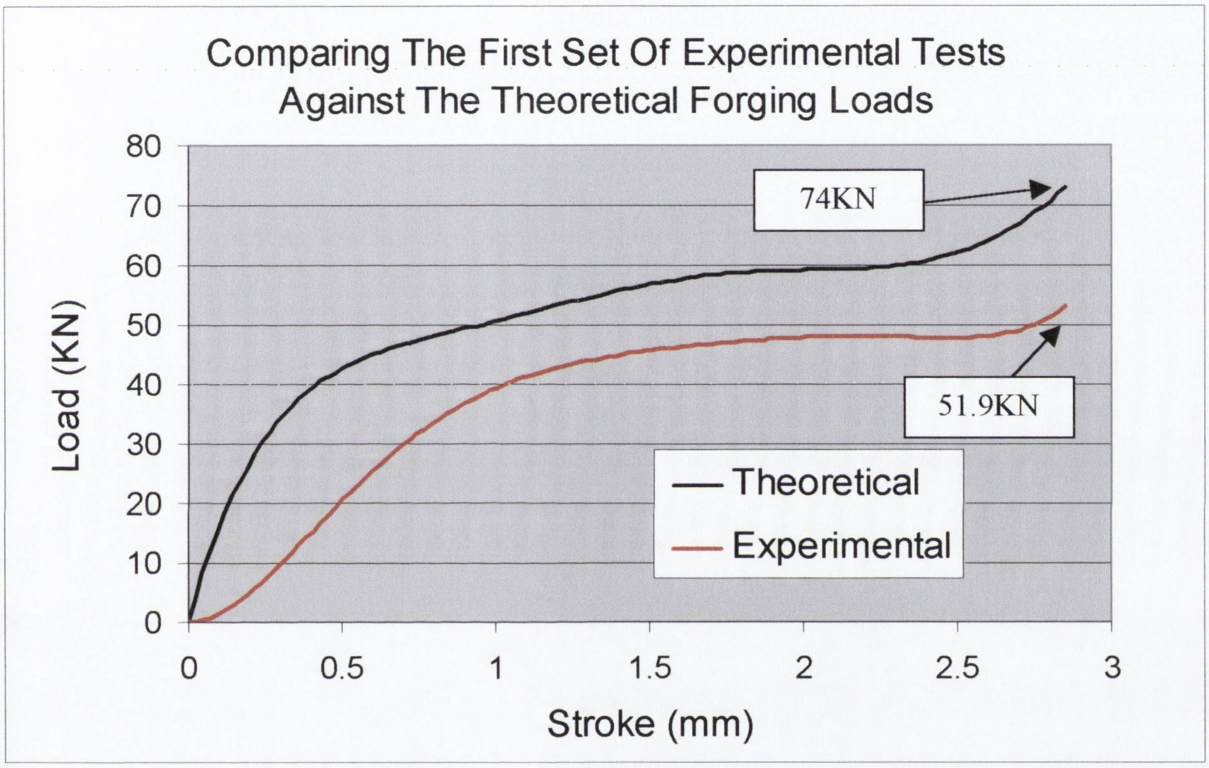

Figure 4-102: First Set Of Experimental Forging Load Validation Curves

An investigation into the possible cause for this large discrepancy between the theoretical and experimental forging loads curves concluded that the press crosshead was deflecting during the test, which induced an incorrect displacement reading. To overcome this problem a Linear-Variable Differential Transducer (LVDT) was used to accurately measure the displacement of the press crosshead. Figure 4-103 shows the second set of tests using the LVDT measuring device. Figure 4-103 illustrates that once the LVDT was used to measure the actual press crosshead displacement, the experimental and theoretical forging load curves were in very close agreement. The percentage difference at the end of the trim die stroke was then only 7.33%.

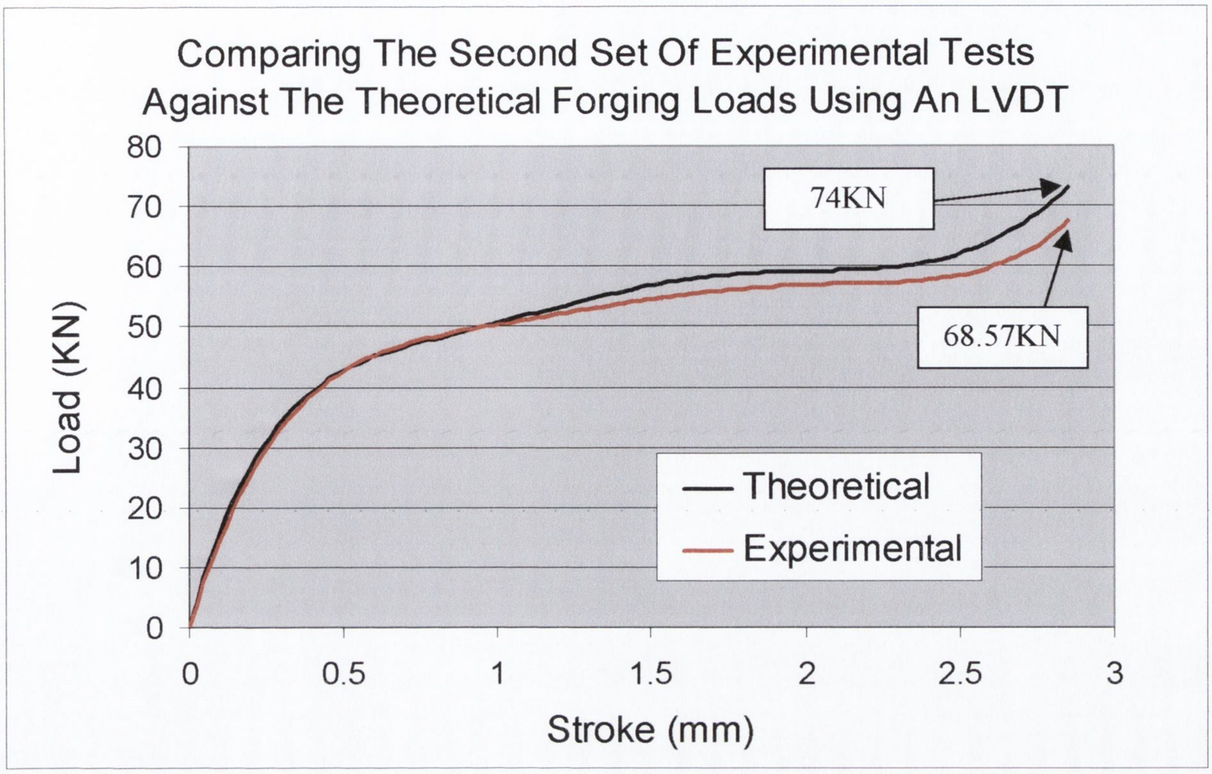

Figure 4-103: Second Set Of Tests Using The LVDT To Accurately Measure The Crosshead Displacement

With respect to figure 4-103, as the experimental forging load (Red line) was accurately predicted by the FE model (Black line), it was concluded that the FE results produced in this project could be relied upon with some confidence.

4.5.4 Failure Analysis

The main reason for the replacement of a trim die is due to cracking or chipping near the cutting radius. Cracking or chipping ultimately results in a section of the trim die breaking away and renders the tool useless. Figure 4-104 below shows a Scanning Electron Microscope (SEM) image of a chipped trim die.

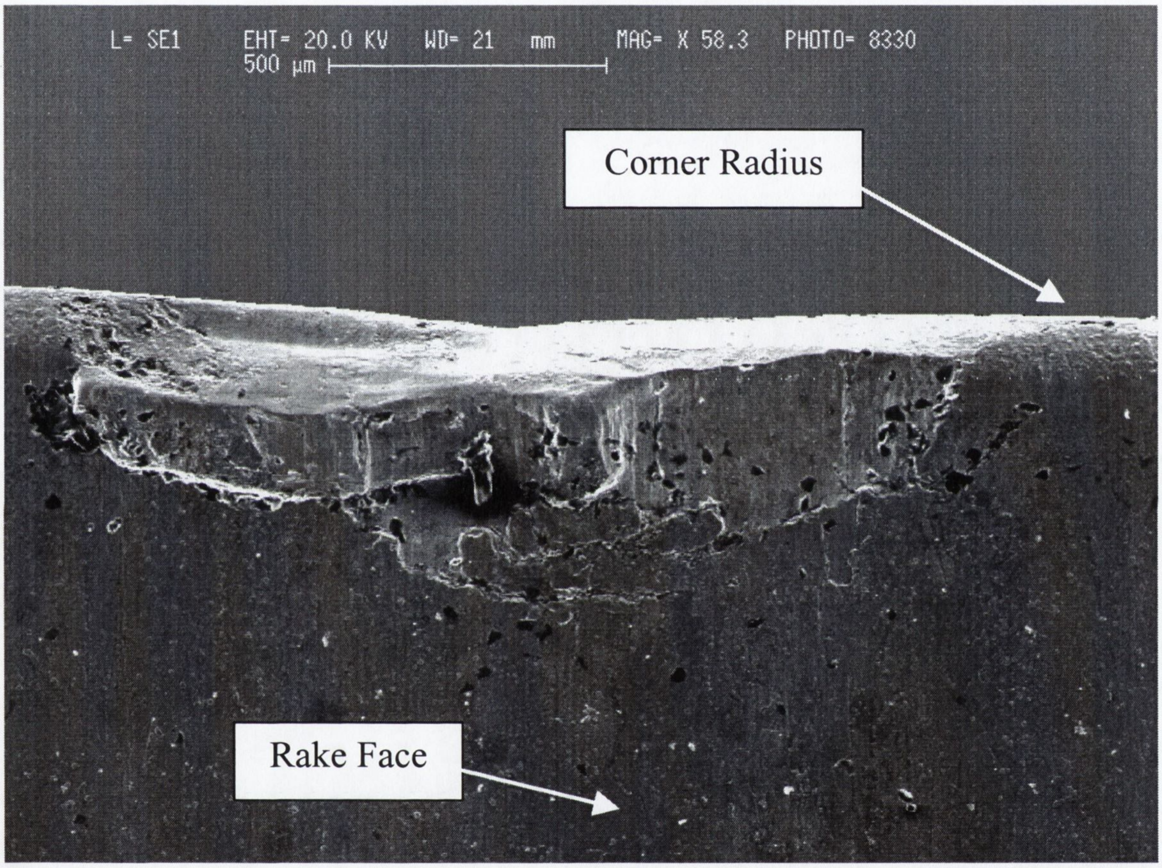

Figure 4-104: SEM Image Of Chipped Trim Die

In conjunction with the simulation of the trimming process, a failure analysis was conducted in an effort to understand the main factors influencing the failure of a trim die. From an early stage it was clear that failed trim dies could be divided into two categories, Misfeed and Non-Misfeed failure. It later transpired that the 'non-Misfeed failures' were most likely fatigue induced. Descriptions of the two categories of trim die failure, along with the reasons for their occurrence will now be discussed. The detrimental effect of coatings, in terms of fatigue resistance, will also be discussed.

4.5.4.1 Misfeed Failure

If a bolt making machine is running at full speed, and a situation arises where there is no workpiece present in the top tool, the momentum of the ram which drives the trim die, causes the trim die and top tool to make contact. The footprint of the top tool in hexagonal, therefore when the two collide, a hexagonal impression (called a witness mark) is left on the land surface of the trim die. Trim dies, having this witness mark, were grouped in the 'misfeed failure' category. These failed trim dies were sectioned, mounted, polished and etched as detailed in Section 3.2.5 on page 77. Figure 4-105 below shows a section through a typical trim die and the approximate locations of the cracks arising from the misfeed and non-misfeed failures. With respect to figure 4-105, the images shown in the following figures 4-106, 4-109 and 4-112 are viewed from direction 1, while figure 4-119 is viewed from direction 2.

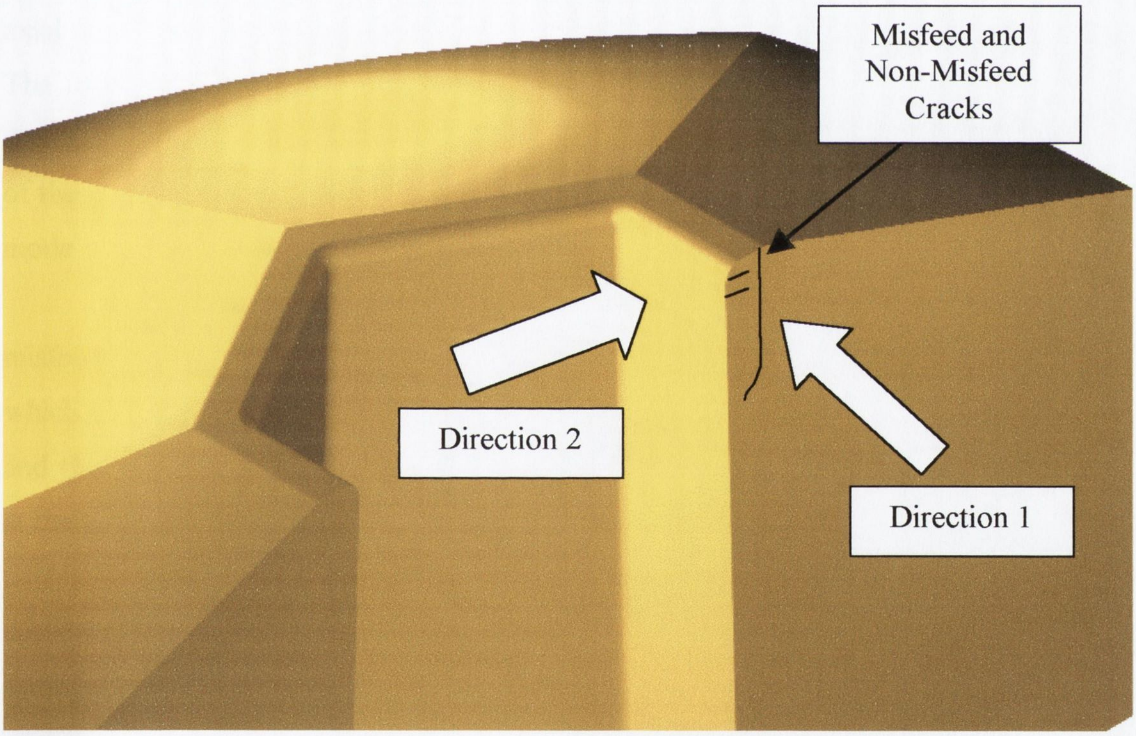

Figure 4-105: Section Through Trim Die Showing Location of Cracks

With the use of a light microscope, a particular crack pattern was evident. Figure 4-106 on the following page shows the crack location associated with a misfeed failure as viewed from direction 1. On the left hand side an image taken with the light microscope shows the physical cracks, while on the right hand side a drawing indicates where these cracks are located with respect to the trim die corner profile.

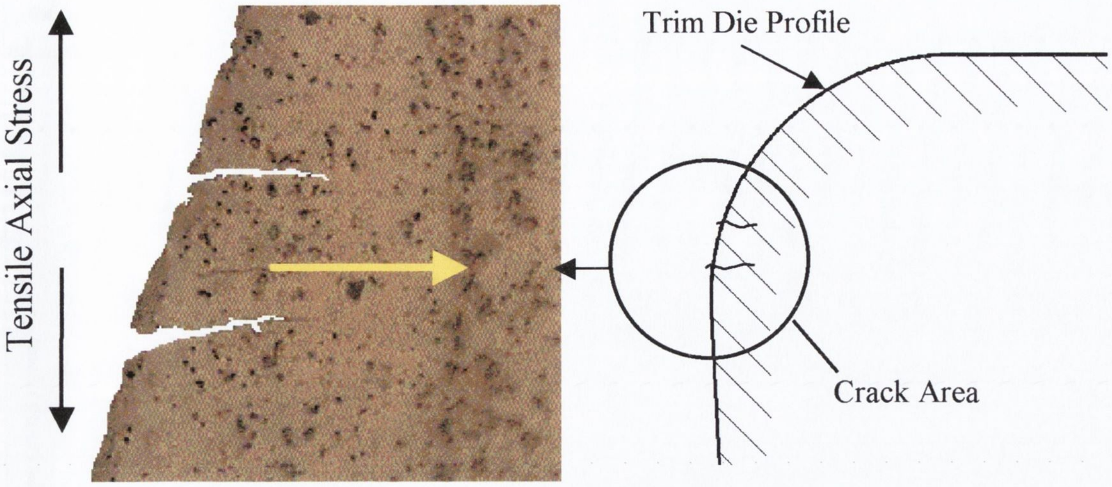

Figure 4-106: Misfeed Crack Location On Trim Die And Detail

The two cracks shown in figure 4-106 are propagating to the right, highlighted by the yellow arrow. Therefore these cracks are propagating in the radial direction. A tensile axial stress is required to drive these cracks in the radial direction shown in figure 4-106. The initial reaction to the concept of the trim die colliding with the top tool would be to consider that only compressive and not tensile axial stresses would prevail in the vicinity of the corner radius. Therefore to investigate the stress state within the trim die during this mode of failure, an FE model, which simulated a misfeed, was constructed and analysed.

Figure 4-107 shows the axial stress distribution within the trim die during the misfeed simulation. To simulate the misfeed failure, the workpiece material was removed which enabled the trim die to be forced upwards into the top tool. The small square symbol and the yellow region in figure 4-107 illustrate that the maximum tensile axial stresses act at the approximate location of the misfeed cracks observed using the light microscope.

The reasons for having tensile instead of compressive axial stresses at the trim die corner can be explained by considering the velocity vector plot of the trim die material during the simulation, as shown in figure 4-108.

With respect to figure 4-108, notice that there are two distinct directions for the trim die material to follow. The yellow arrow highlights the first direction, which is due to the FE model forcing the trim die upwards into the top tool. The red arrow highlights the second flow direction of the trim die material. Due to the rigid top tool, the upward movement of the trim die causes the material at the corner to flow radially inwards. This radially inward flow causes the maximum tensile axial stresses to occur close to the corner radius.

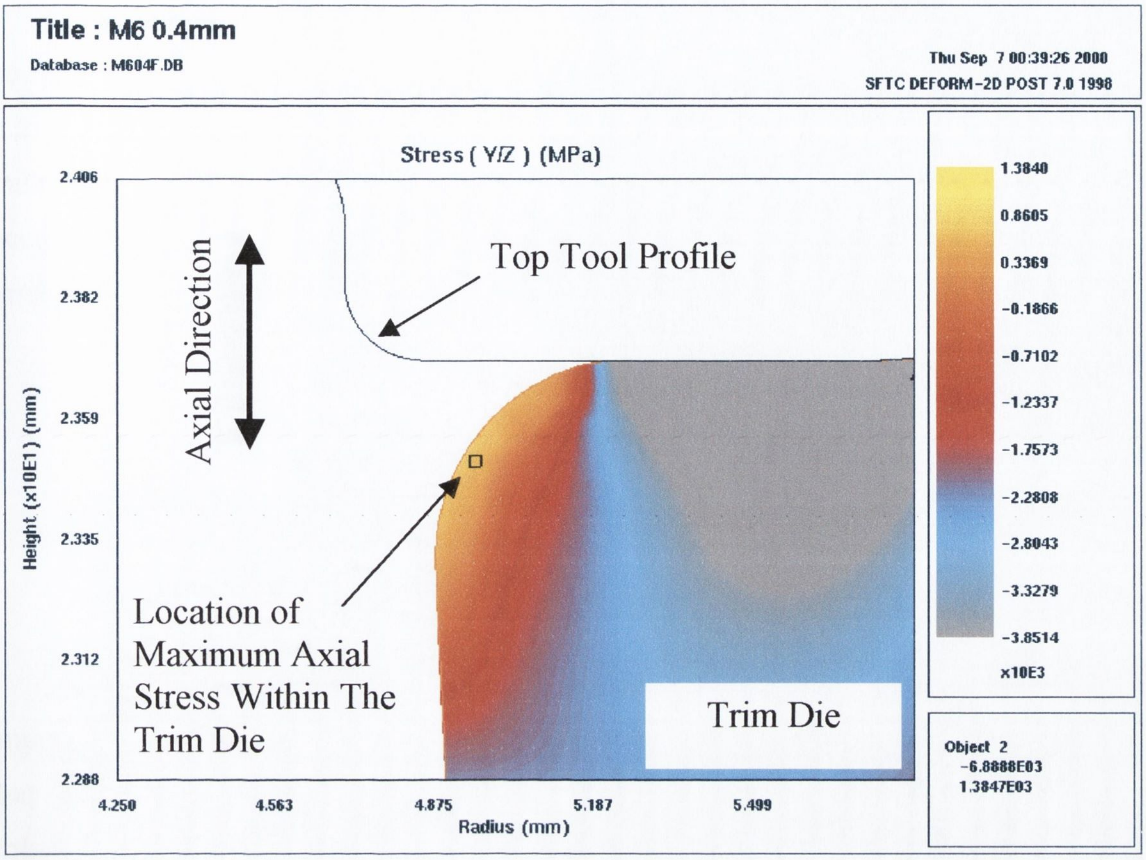

Figure 4-107: Axial Stress Distribution Within Trim Die During A Misfeed Simulation

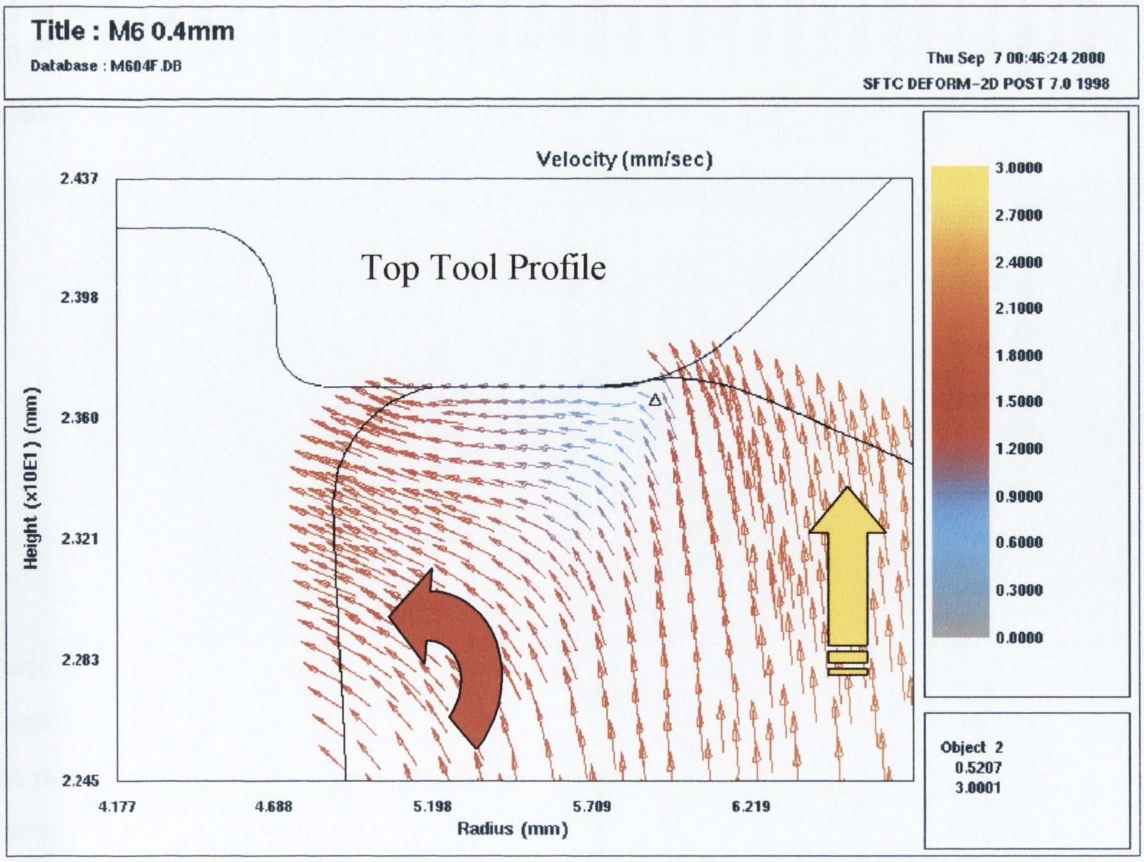

Figure 4-108: Velocity Vector Plot Of Trim Die Material Flow During A Misfeed

By using a FE model to simulate a misfeed, the stress state in the vicinity of the corner profile was established. Due to the trim die material flowing radially inwards, the maximum tensile axial stress was located in the same vicinity as the cracks observed in the failed dies. Therefore with the use of an FE model, a theoretical explanation for the occurrence of the radial cracks within the trim dies, that failed by misfeed, has been established.

4.5.4.2 Non-Misfeed Failure

As previously mentioned, during a misfeed, the top tool leaves a hexagonal impression, known as a 'witness mark', on the land surface of the failed trim die. Trim dies that failed, but did not have the tell tale witness mark, were sectioned, mounted and polished as outlined in Section 3.2.5 on page 77. Figure 4-109 shows an SEM image of the crack pattern associated with failed trim dies having no 'witness mark'.

It is obvious by comparing figures 4-106 and 4-109 that the two categories of failed trim dies produced very different crack patterns. A detailed examination of figure 4-109 posed some questions:

1. Why was the crack initiation site along the top 'Land Surface' of the trim die and not at the base of the corner radius as in the trim dies failed by 'misfeed'?
2. When the crack started to propagate, why was its initial direction perpendicular to the 'Land Surface'?
3. Why did this perpendicular crack direction change, near the end, to curve towards the inner 'Rake Surface' of the trim die?

As stated by other researchers [34], since World War II great progress has been made in understanding the ways in which materials fracture. This knowledge has proved essential in providing a better formulation of fracture mechanics. Nevertheless, it is still not possible to use this knowledge, together with other material properties, for predicting fracture behaviour in engineering terms with a high degree of confidence.

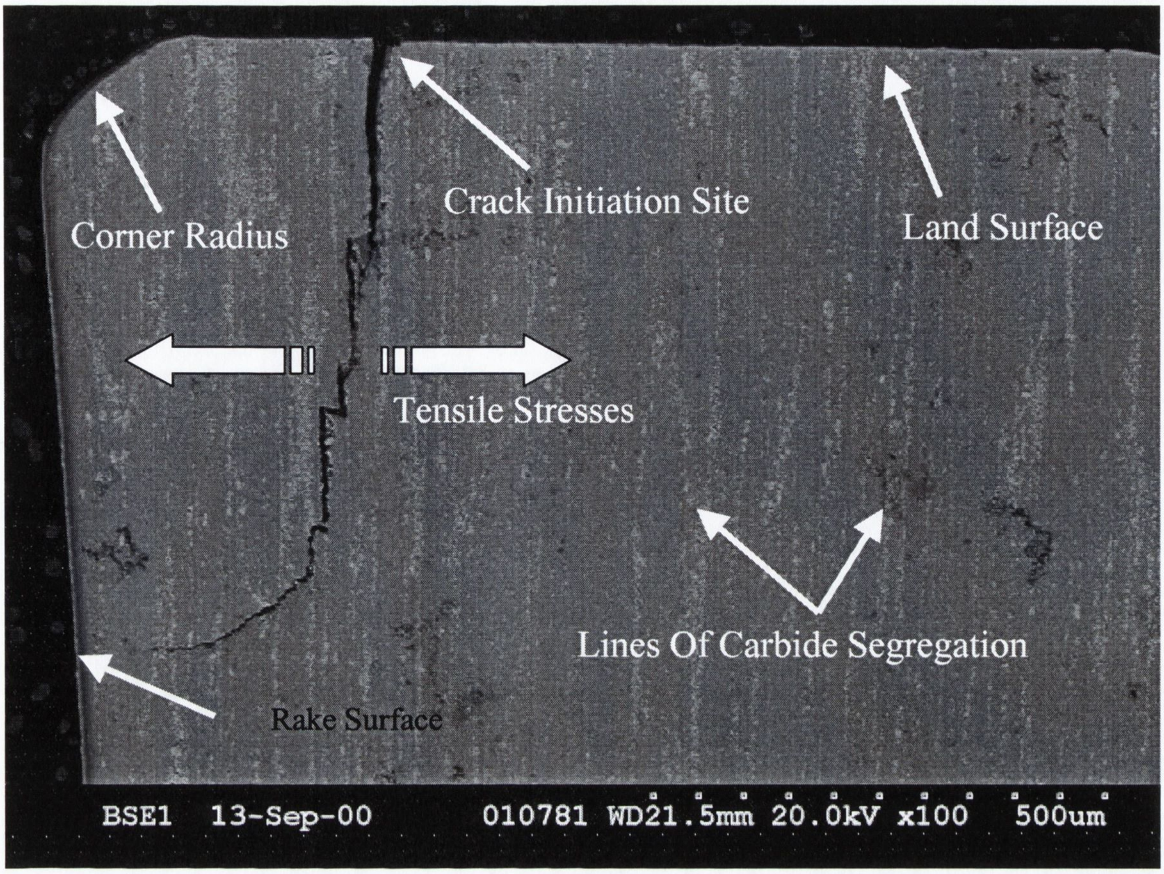

Figure 4-109: Non-Misfeed Crack In Failed Trim Die

The mechanism of fracture within the trim die would in itself require independent research, and is outside the scope of this project. However in an attempt to establish some of the reasons for failure, the most likely mechanisms based on the FE results and experimental findings will be presented.

Crack Location:

With reference to figure 4-109, the crack initiation site was along the top of the trim die, known as the land surface. The following explanation for possible reasons for this location of crack initiation assumes that a small defect or crack is present along this land surface. In Section 4.5.4.3 on page 208 it will be explained how coatings can have a detrimental effect in terms surface topography and induce small cracks and flaws on the surface of a trim die. However, for the time being, it is sufficient to assume that a small crack is present. This small crack will remain 'dormant' until a sufficiently high tensile stress acts upon it.

Figure 4-109 shows that once the crack starts, its direction is initially perpendicular to the land surface. It has been stated earlier that assuming that a crack is loaded in Mode I (see Section 2.4.3.3 on page 33), i.e. where the cracks sides move perpendicular apart, the opening stress driving the crack growth is the maximum principal stress (MPS) [27, 31, 36]. Figure 4-110 shows the shaded MPS distribution along the top surface of the trim die during a forging operation. The square in figure 4-110 highlights the location of the maximum tensile principal stress, which is approximately in the same vicinity as the actual crack initiation site shown in figure 4-109. However, the direction of the crack propagation should be perpendicular to the MPS [34]. Figure 4-111 is a close up image of the location of the maximum tensile principal stress. In this image, the principal stress vector plots are shown. The yellow and orange lines represent the tensile and compressive stress components σ_1 and σ_2 respectively. From figures 4-110 and 4-111, it is clear that along the top surface of the trim die is the location for the maximum tensile stress component, and its direction is perpendicular to the direction of the actual crack, i.e. straight downwards as highlighted by the white arrow. The direction of the maximum principle stress shown in figure 4-111 is aligned in the radial direction. It is for this reason that during the FE analysis conducted earlier in Phases 1 to 3, that both the effective stress component and the tensile radial stress was obtained.

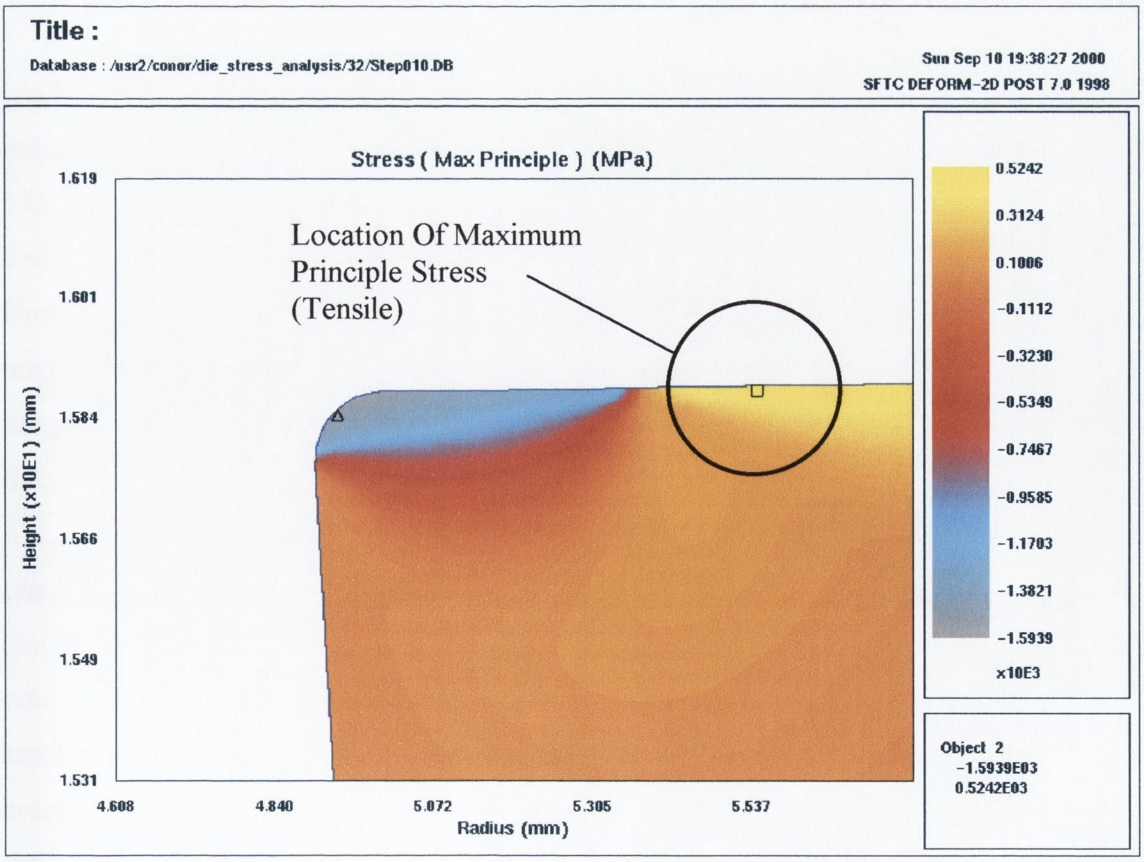

Figure 4-110: Maximum Principle Stress (MPS) Distribution Along the Top Surface Of the Trim Die

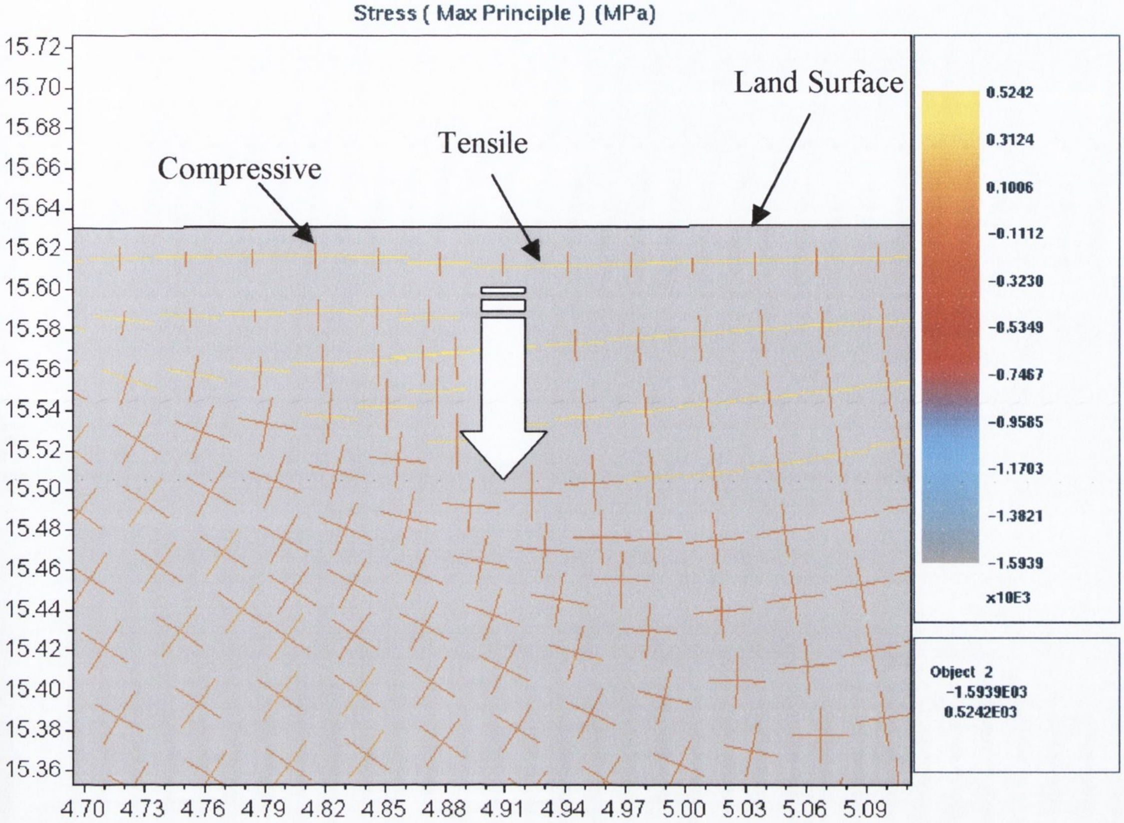

Figure 4-111: Maximum Principle Stress Vector Plot On Top Surface Of the Trim Die

The results presented in the previous pages have established, theoretically, how a crack could propagate initially from a small flaw or surface crack. The maximum tensile radial stress recorded along the top surface of the trim die during the Phase 1 analysis was 545.3MPa. The yield stress of the trim die material is approximately 2,500MPa. Therefore under static loading these stresses are not sufficient to cause rupture within the trim die. However, because the trimming process causes cyclic loading on the tool, these stresses might be sufficient to cause the crack to propagate by fatigue. It was for this reason that fatigue tests were conducted on M2 High Speed Steel material, the results of which are detailed in Section 4.5.4.4 on page 215.

Another feature of the cracks obtained from the non-misfeed cracks is that once the crack has started downwards, its initial path is very straight. It would be incorrect to assume that because the initial MPS drove the crack downwards, that it will remain on that course indefinitely because as the crack propagates, the stress state in the vicinity of the crack changes. Therefore the most likely explanation for the initial straight path of the crack is due to carbide segregation. The cause of the carbide segregation and how it effects the crack path will now be discussed.

Initial Crack Propagation Path

In figure 4-109, vertical straight lines within the M2 material can be observed. These lines are caused by carbide segregation. To verify this assertion an Elemental X–Ray Spectrum Analysis was conducted at two locations within the trim die material. Figure 4-112 below is a high magnification image at the initiation site of the crack shown in figure 4-109.

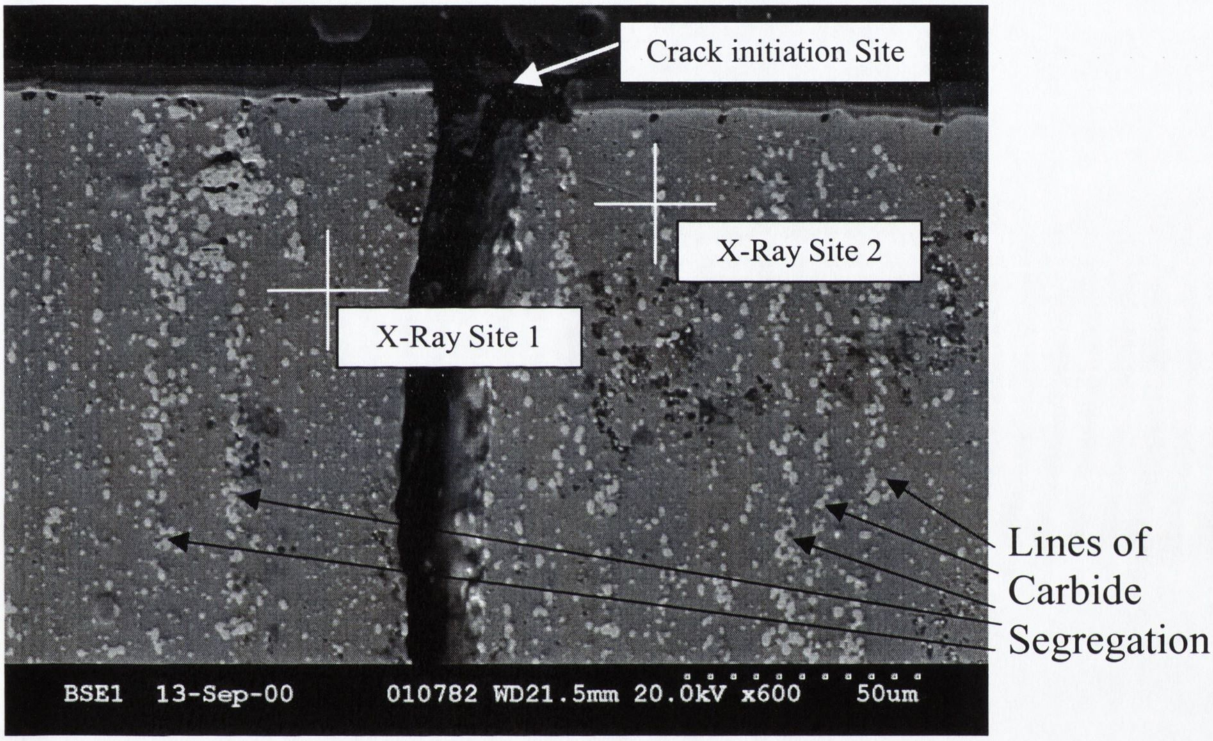

Figure 4-112: Crack Propagation Path Along Carbide Segregation

With respect to figure 4-112, the vertical carbide segregation lines are highlighted along with the two sites for the elemental X-ray spectrum analysis. X-ray site number 1 was within the matrix material, while X-ray site number two was over one of the small white particles, which combine to form the line of segregation. Figure 4-113 and 4-114 show the results from X-ray site number 1 and 2 respectively. The results from site 1 shown in figure 4-113 illustrate the high concentration of iron (Fe) that would be naturally expected in the matrix of the M2 steel. The results from site number 2, shown in figure 4-114, confirm that the lines highlighted in figure 4-112 above are indeed lines of carbide segregation due to the high concentration of tungsten, molybdenum and vanadium.

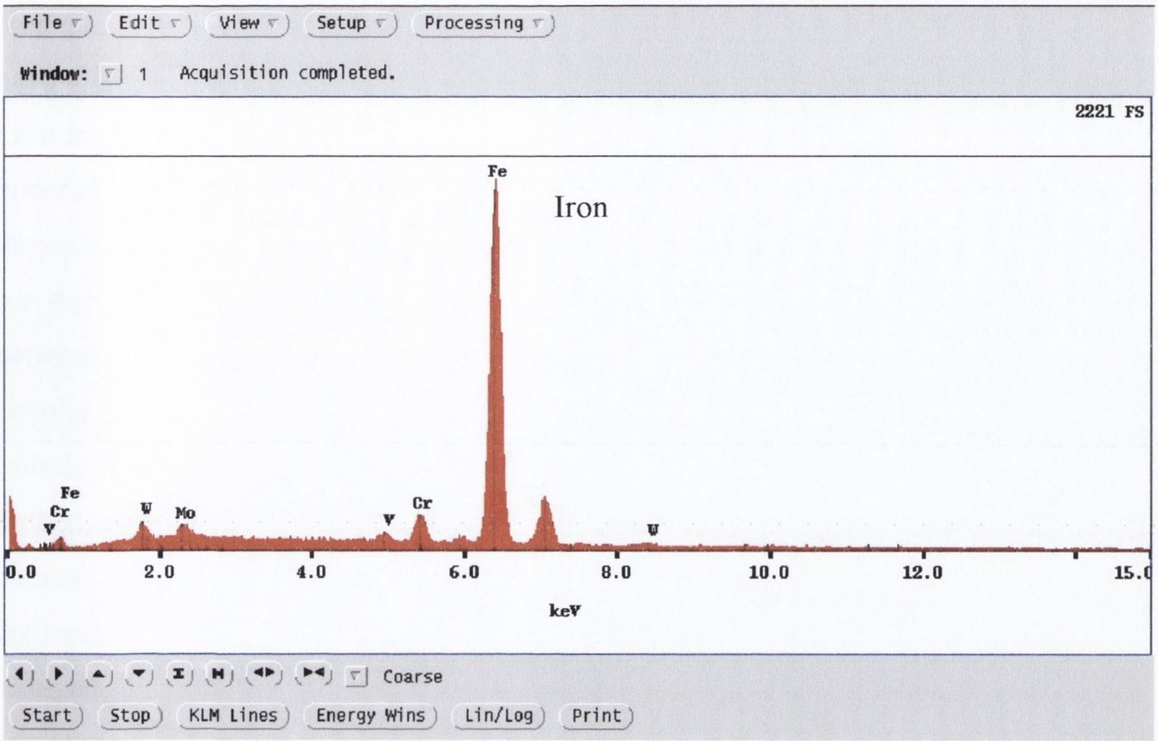

Window: 1 Acquisition completed.

Figure 4-113: Elemental X-Ray Spectrum Analysis At Site Number 1

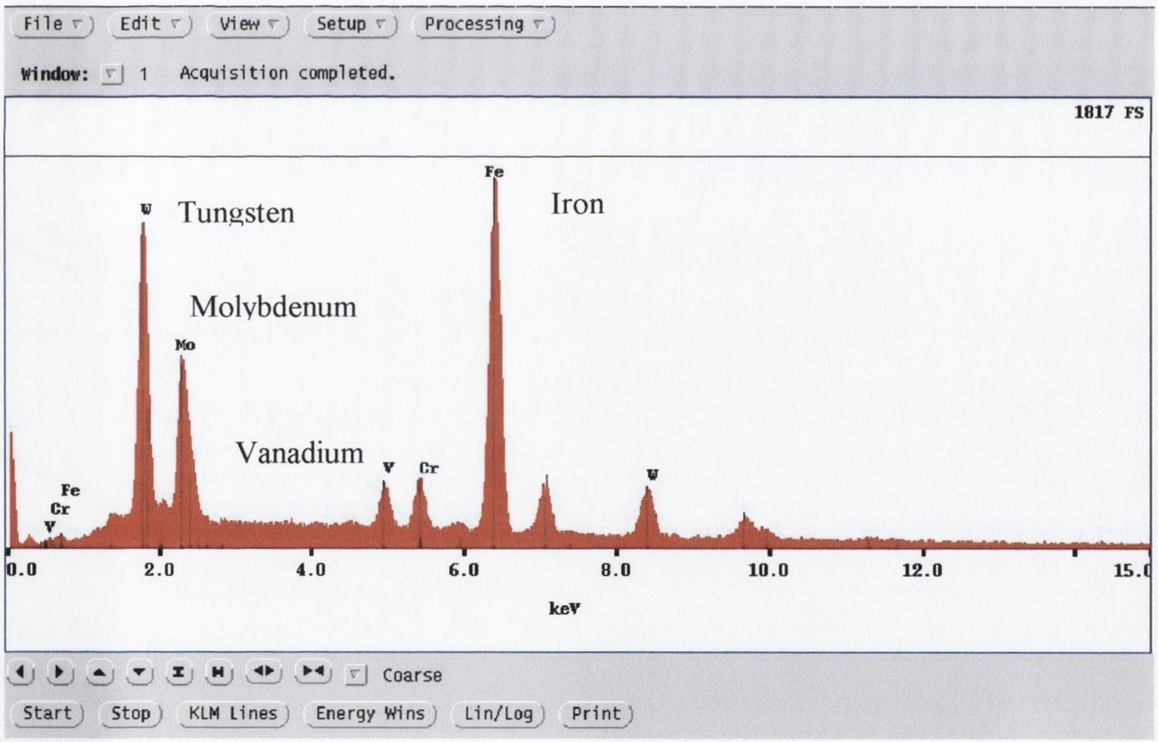

Window: 1 Acquisition completed.

Figure 4-114: Elemental X-Ray Spectrum Analysis At Site Number 2

In Section 2.2 on page 6, the manufacturing process of the trim die was explained. The trim die material M2 comes into the factory in round bar stock. During the manufacture of AISI M2, an appropriate amount of carbon is used to permit the formation of hard carbide particles. Depending on which element of the M2 alloy the carbon combines with dictates the hardness of the particle. Molybdenum and tungsten carbides have a hardness of up to approximately 75 HRc while the hardest of them all, vanadium carbides reach 80 to 85 HRc. Therefore these carbide particles are harder than the matrix material around it. The mechanical working of the M2 ingot into round bar stock causes the carbides to form circular rings [6]. Figure 4-115 shows a representation of a circular bar stock with the carbide rings present. Moving out from the centre of the bar, the space between the carbide segregation rings increases [72]. A cross section taken through the circular stock shows the vertical lines illustrated in figures 4-109 and 4-112. This type of carbide segregation is typical in AISI M2. The toughness achievable in high-speed steels is limited by the defects in the steel such these carbide segregation lines [7]. Obviously because of this carbide segregation, the material is anisotropic. Because of this fact, one of the world largest steel manufactures, Uddeholm, have stopped the production of M2 and changed to using the Anti-Segregation Process (ASP) for the production of steel that has a segregation free structure.

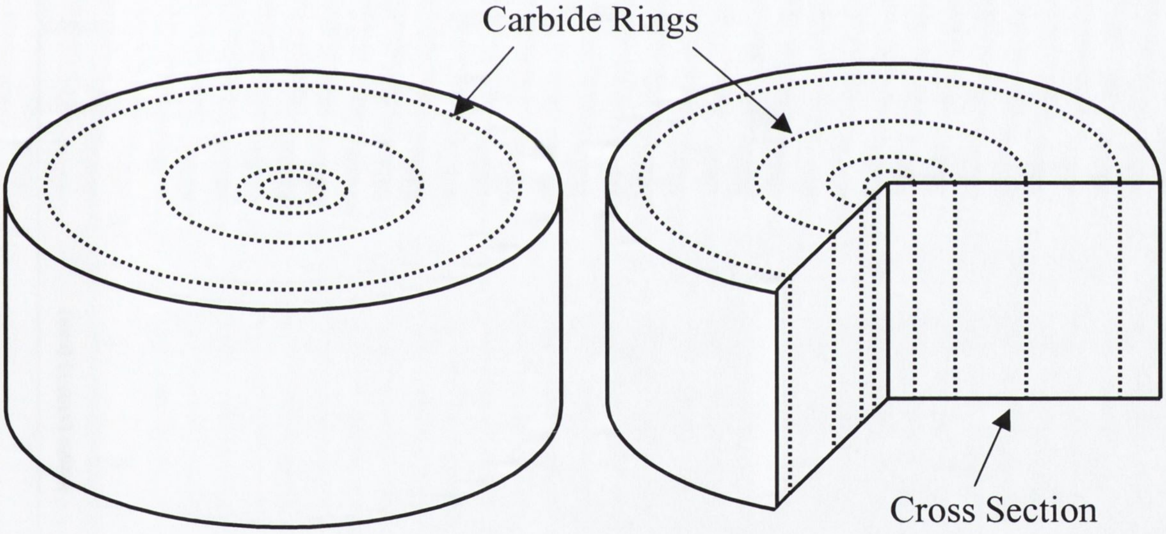

Figure 4-115: Carbide Segregation Rings In Bar Stock M2

Obviously if a crack starts to propagate in the vicinity of a carbide segregation line, the crack will follow this line, because as already mentioned, the carbide particles are very hard and therefore brittle. Now that a theoretical explanation for the perpendicular crack propagation path has been established, the last question posed by the crack pattern shown in figure 4-109 is why, does this crack path deviate from the brittle carbide segregation line and curve towards the inner rake surface. The most likely reason for this deviation of the crack path will now be discussed.

Final Crack Propagation Path

As previously explained, the crack path can be determined by considering the MPS directions, but as the crack propagates, the stress pattern changes and therefore so too will the MPS direction. Therefore in an attempt to establish the stress pattern in the trim die once the crack has travelled a certain straight distance, an FE model was simulated with a slot in the trim die to represent the crack. Figure 4-116 shows the Finite Element Mesh (FEM) of the trim die and the dimensions of the slot. The dimensions of the slot were established from an actual crack using a Series TM 300 Mitutoyo toolmakers microscope as shown in figure 3-14 on page 64.

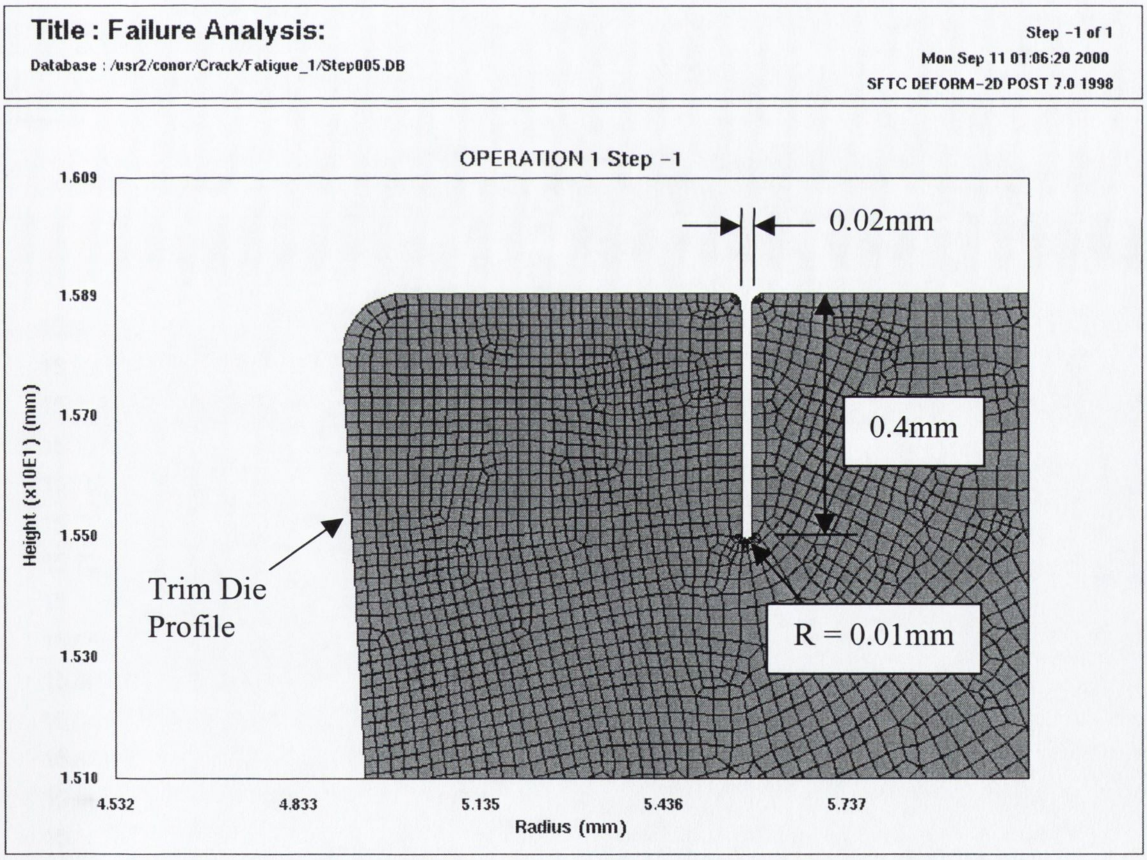

Figure 4-116: Trim Die With Slot To Represent Crack

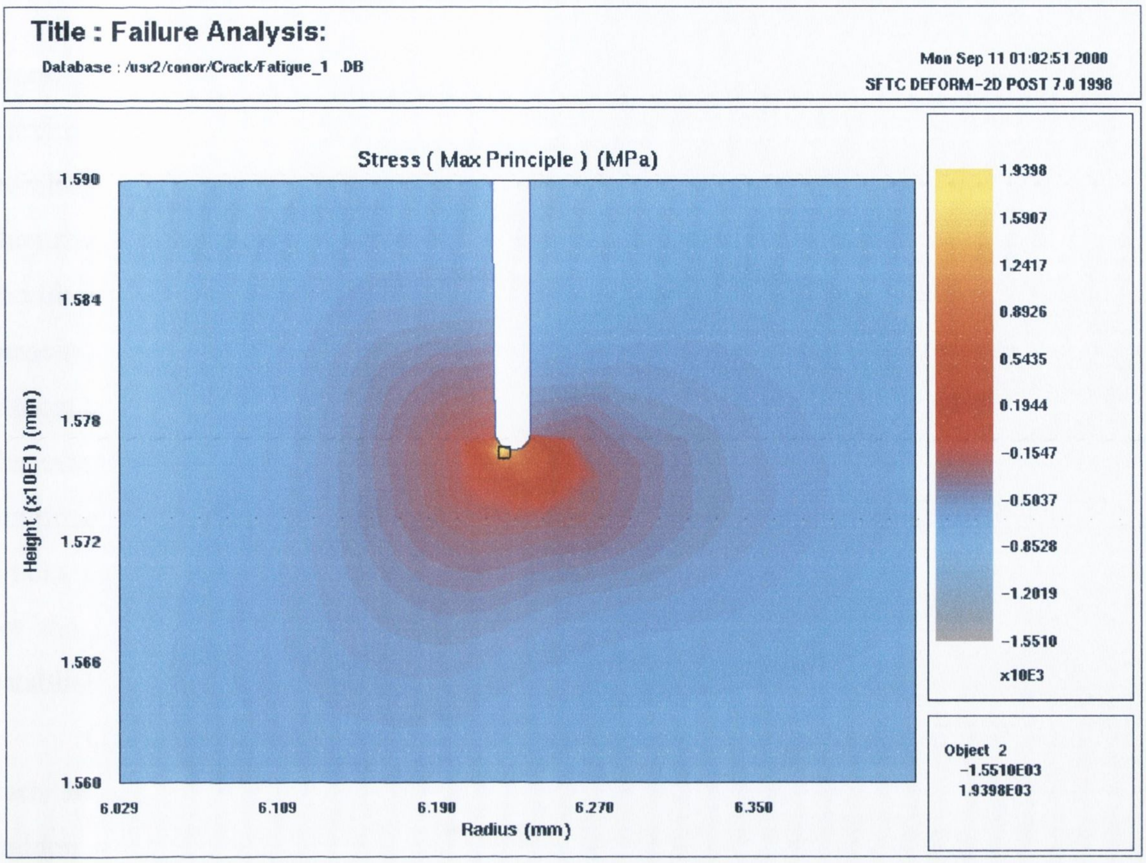

Figure 4-117: Maximum Principle Stress At Root Radius Of Crack

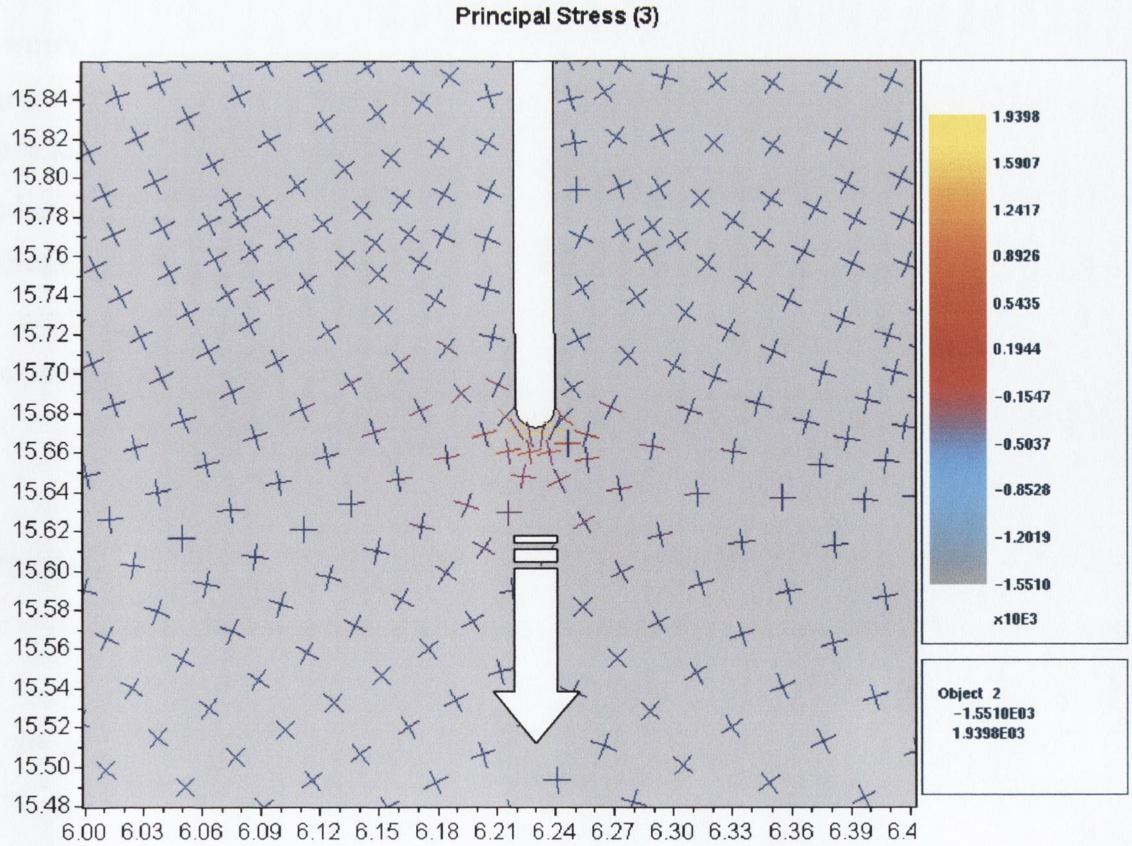

Figure 4-118: Principle Stress Vector plots Around The Crack Root Radius

The maximum principle stress (MPS) distribution around the root radius of the crack in the trim die is shown in figure 4-117. The square symbol indicates that the maximum tensile value of MPS in on the left hand side of the root radius. This is the side pointing towards the direction of the inner rake surface. However, when the directions of the principle stresses are analysed by considering the vector plots as shown in figure 4-118, the likely direction of crack propagation is ambiguous. Figure 4-118 shows that the tensile principle stresses around the crack root radius, highlighted in yellow, are symmetric and almost horizontal at the lowest point on the radius. Therefore using the previous theory that the crack will be driven perpendicular to the MPS would suggest that the crack would continue downwards. This might explain why some of the failed trim dies had vertical cracks that did not initiate in the vicinity of a line of carbide segregation. An explanation for the final curving of the crack into the inner rake surface has not been theoretically established.

One possible reason for the cracks curvature is that once the crack has grown to such an extent that the remaining net-section is insufficient to carry the forging load, a sudden fracture takes place. As the crack propagates downward, the distance from the crack tip and the inner surface is constantly decreasing due to the rake angle. Eventually, the crack will require less energy to curve to the inner surface than continue straight downwards and hence turn in that direction. Another important point to make in relation to figure 4-117 is that the highest tensile stress located at the corner of the crack radius was 1,939.8MPa, while the highest tensile stress along the top surface during the Phase 1 analysis was 545.3MPa, therefore as the crack propagates, the net section of the trim die is decreasing which effectively weakens the tool. The topography of a fractured surface can be used to establish what failure mechanism occurred. The next section attempts to decipher the complex fractured surface from an analysis of a failed trim die.

Fractured Surface Topography

As illustrated in figure 4-105 at the start of this failure analysis Section, the images of the crack pattern shown to date have been taken using the light microscope from direction number 1. However, with the use of a Scanning Electron Microscope (SEM), high-resolution images taken from direction number 2, which is basically ‘face-on’ to the crack, were obtained. Figure 4-119 illustrates an SEM image of the fractured surface.

With respect to figure 4-119, two distinct surfaces are highlighted. The top of the image is where the crack initiated, and it has a smooth surface topography. This smoothness could be attributed to fatigue crack closure, which has a tendency to smoothen out the contacting surfaces due to the constant cyclic loading. The bottom surface topography, caused by fast fracture due to overload, has the appearance similar to a fracture surface caused by Microvoid Coalescence. But as previously outlined in Section 2.4.3.1 on page 28, Microvoid Coalescence is the mechanism which causes dimpled rupture in steels that have a high ductility. However other researchers have stated that there a number of situations where dimpled rupture is observed for embrittled materials [94]. Comparing figure 4-119 below and figure 4-109 on page 195 there is a close correlation between the smooth surface shown below and the almost perpendicular crack path shown in figure 4-109, where fatigue has prevailed.

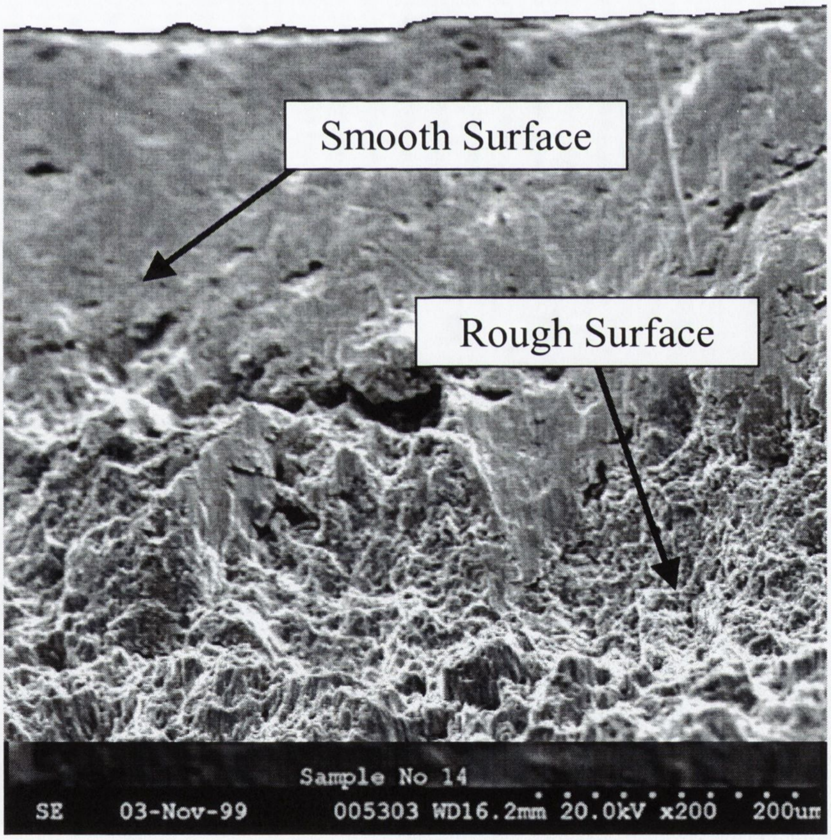

Figure 4-119: Fractured Surface Showing Signs Of Fatigue And Rapid Fracture

As previously outlined in Section 2.4.1.4 on page 25, repeated sliding or rubbing of one component over another, leads to spalling or microcracking that causes contact fatigue wear. During the trimming process, the workpiece material is constantly sliding over the land surface of the trim die. To investigate the possibility of contact fatigue being a possible mode of crack initiation, SEM images were taken along the land surface of a trim die which had produced approximately 30,000 bolt heads. Figure 4-120 shows a large crack that has formed on a plane parallel to the corner radius. The white arrow indicates the direction of workpiece material flow over the top of the trim die.

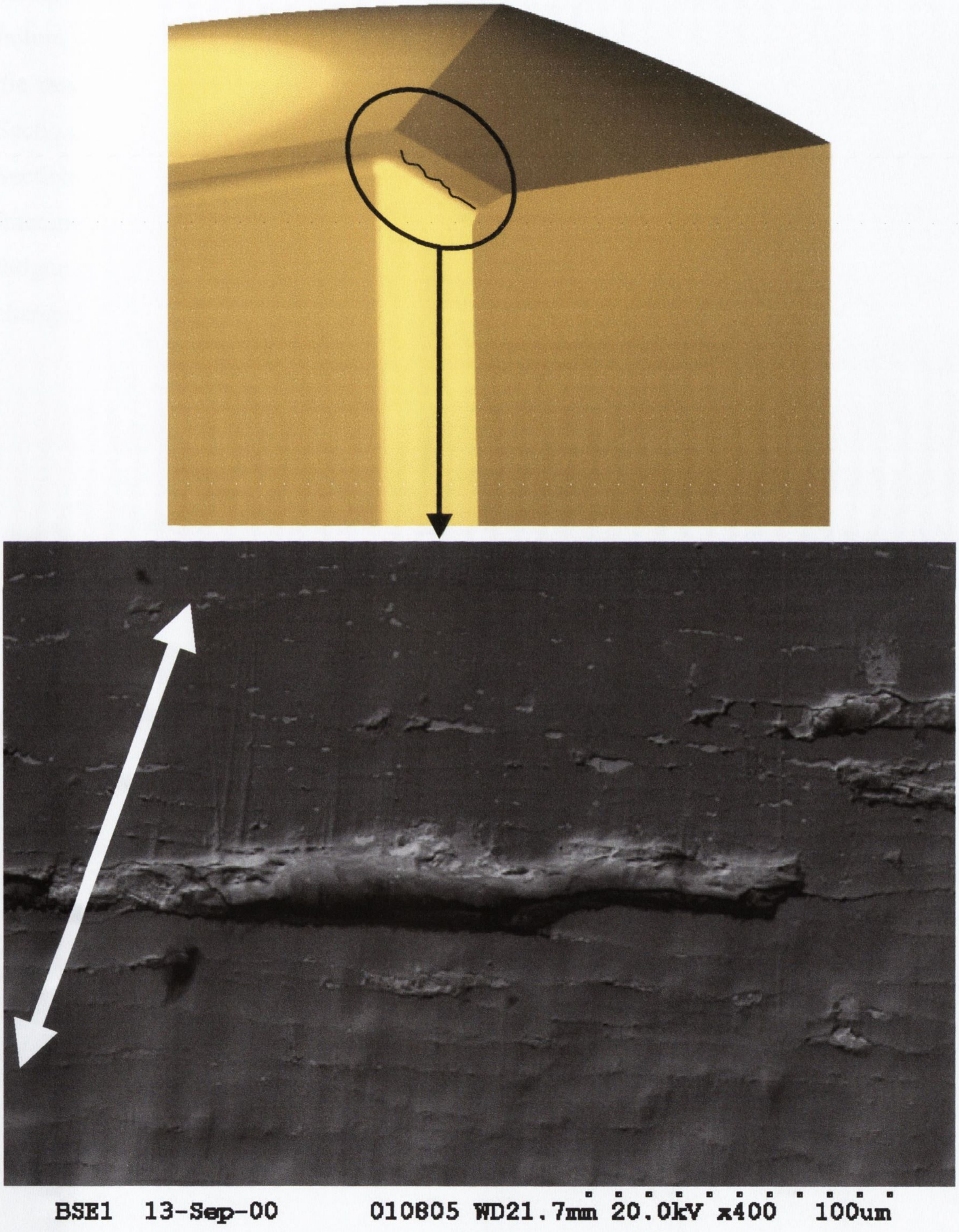

Figure 4-120: Transverse Crack Pattern Similar to that Caused By Contact Fatigue

A comparison between figure 4-120 and figure 2-15 on page 25, which shows cracks caused by contact fatigue [9], indicate a close similarity.

The failure analysis at this point had established, on a theoretical basis, the mechanism for fracture for both the 'misfeed' and 'non-misfeed' failures. The misfeed failure was caused by the trim die material being forced to flow radially inwards as the trim die made contact with the top tool. The non-misfeed failure mechanism described in this Section is more difficult to explain due to lack of evidence. As previously detailed in Section 2.4.3.3 on page 31, fatigue fractures may exhibit striation marks. None of the fractured surfaces analysed in this project exhibited striations. However, the absence of fatigue striations does not mean that the basic mechanism by which the crack advanced has changed [94]. A lack of striations on a fatigue surface may be caused by:

- The mechanism of 'crack-closure' could have a tendency to obscure striation marks caused by the rubbing together of the fractured surfaces.
- When the trim die fails, the operator of the boltmaking machine might not noticed immediately, therefore making it possible for a number of bolts (50 to 200) to be trimmed. This might explain why some of the fractured surfaces are relatively smooth as shown in figure 4-121 below.

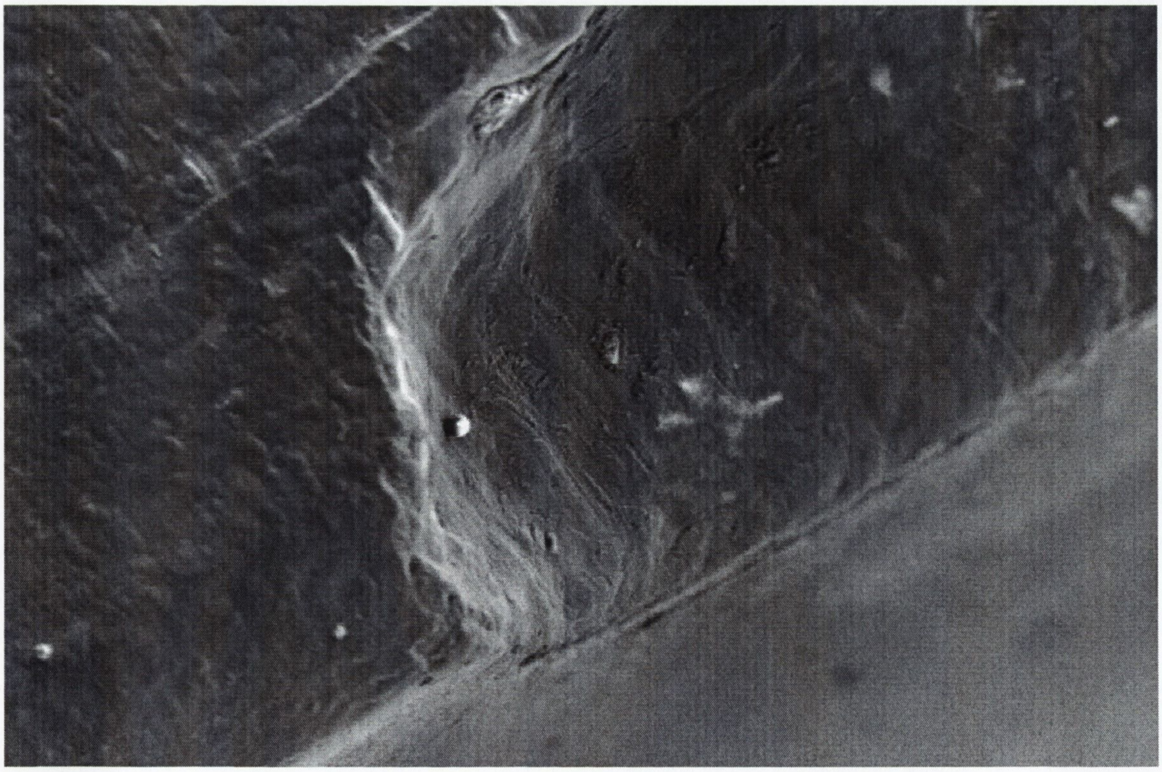

Figure 4-121: Smooth Fracture Surface on Failed Trim Die

The non-misfeed trim dies show no visible 'witness' marks, therefore failure caused by gross cracking or plastic deformation can be ruled out. The results from the FE models, detailed in Phases 1 to 3, have indicated that the theoretical maximum principal stress of 545.3MPa along the top surface of the trim die is insufficient to cause rupture in the M2 material having a yield stress of 2500MPa. Because of these two facts, and by a process of elimination, the most likely mechanism for crack propagation is fatigue.

The fatigue mechanism described in this Section was based on the premise that a small crack or flaw along the land surface of the trim die was acting as a stress raiser to initiate a fatigue crack. In the following Section 4.4.4.3 it is explained how the coatings of the trim dies, analysed in this project, develop flaws before forging a single bolt head.

4.5.4.3 The Effect Of Coatings

As detailed in Section 2.3.3 on page 17, the trim die analysed in this project are coated using a CVD process to improve its wear characteristics. However Section 2.3.4 on page 18 highlighted that the exact influence of coatings on metal substrates produced some contradictory results in terms of fatigue endurance.

There is general agreement that fatigue cracks initiate on the surface of components under cyclic loading. It has been stated that the single most prevalent initiator of brittle fracture is a fatigue crack, which conservatively accounts for at least 50% of all brittle fractures in manufactured products [20].

The results presented in the previous section indicated that the fracture of the trim die was most likely induced by fatigue, which originated from a surface flaw or small crack. Section 2.3.4.3 on page 21 gave details of research by Geiger et al [10] were an M2 substrate was fatigue tested to establish the exact influence of CVD coatings on tool steel, however these results could not be used in this project for the reasons outlined in Section 2.3.4.3 on page 21. It was for this reason that an analysis into the effects of coatings was conducted in this project.

Figure 2-14 on page 20 clearly indicated that a CVD process generates tensile residual stresses within the coating. The tensile residual stresses are caused due to a mismatch of the coefficients of thermal expansion between the coatings and the steel substrate [8, 16]. Table 4-42 below shows the difference in coefficients of thermal expansion between the M2 substrate and the various coatings.

Material	Coefficient of Thermal Expansion per °c
TiN	8×10^{-6}
Ti (CN)	8×10^{-6}
TiC	8×10^{-6}
M2 High Speed Steel	12×10^{-6}

Table 4-43: Coefficients of Thermal Expansion

Therefore as the trim die is heated in the heat treatment cycle, the M2 substrate wants to expand up to 50% more than the coating and this causes a tensile stress system within the coating. It has been stated that compressive residual stresses at the external surfaces generally enhance fatigue life, while tensile stresses are detrimental [18].

Section 2.2.4 on page 12 outlined the heat treatment process applied to the machined and coated trim dies. Because of the very high temperatures applied to the coated trim die, and the previously mentioned thermal mismatch, it was decided to conduct a surface topography analysis of a trim die pre and post heat treatment.

The following four figures 4-122 to 125 are taken from a coated trim die which was cut in half. The first two, figures 4-122 and 4-123, show the pre-heat treated surface topography. The other half of the trim die was then heat treated as outlined in Section 2.2.4 on page 12. Figures 4-124 and 4-125 shows its surface topography post-heat treatment.

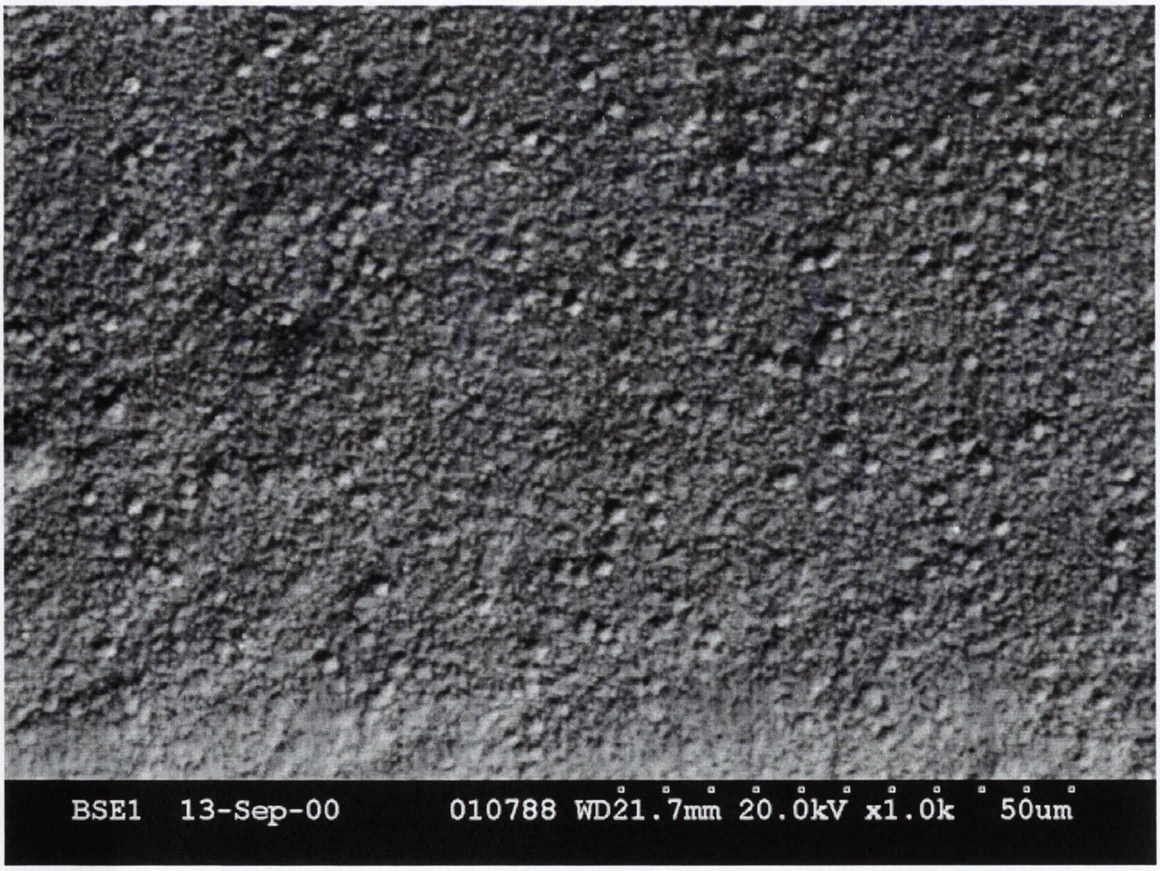

Figure 4-122: Surface Topography Pre-Heat Treatment at a Magnification of 1K

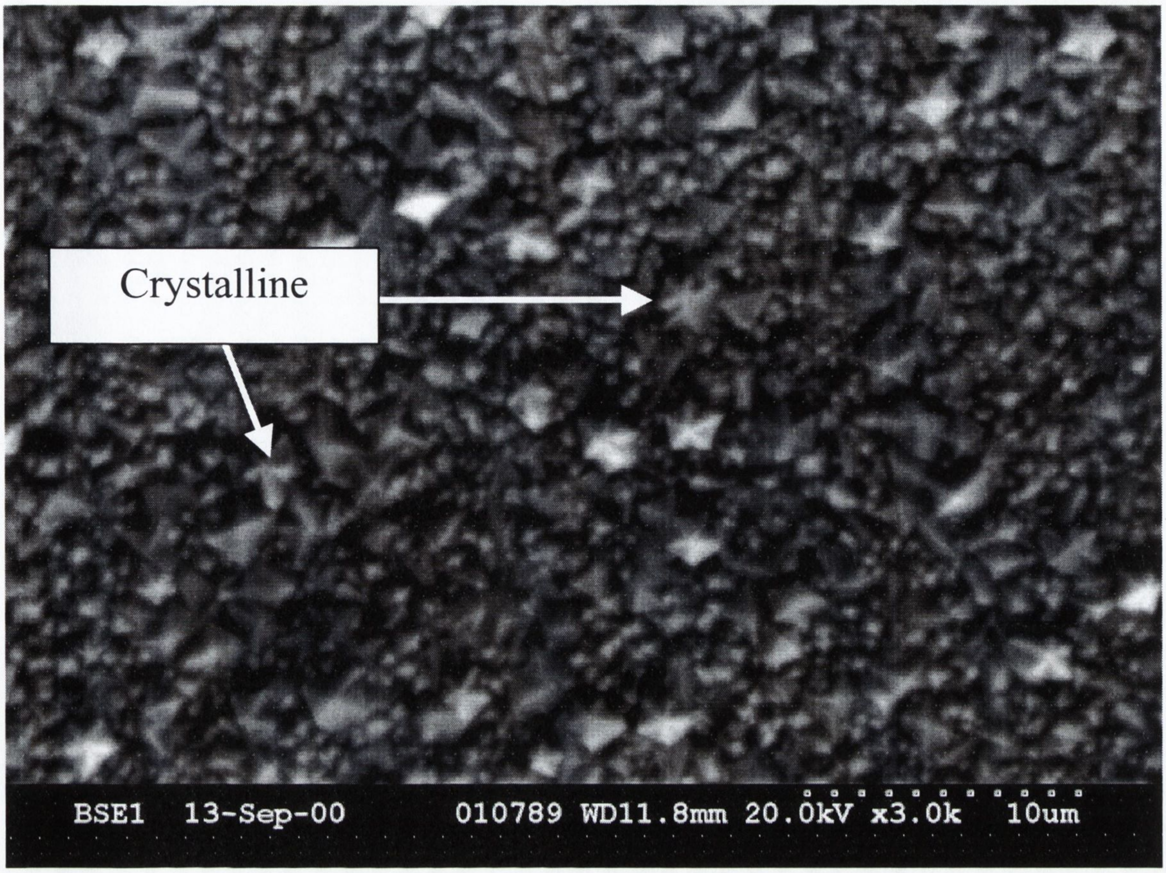

Figure 4-123: Surface Topography Pre-Heat Treatment at a Magnification of 3K

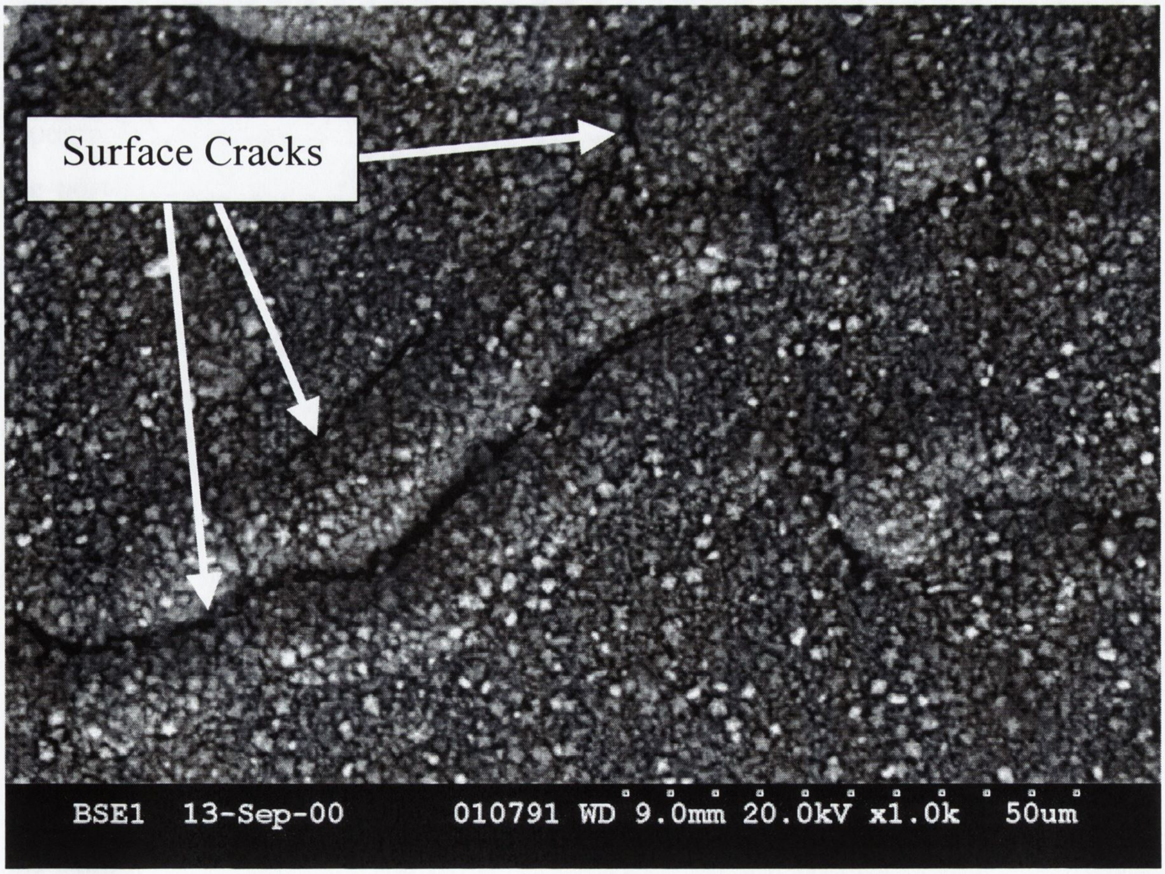

Figure 4-124: Surface Topography Post-Heat Treatment at a Magnification of 1K

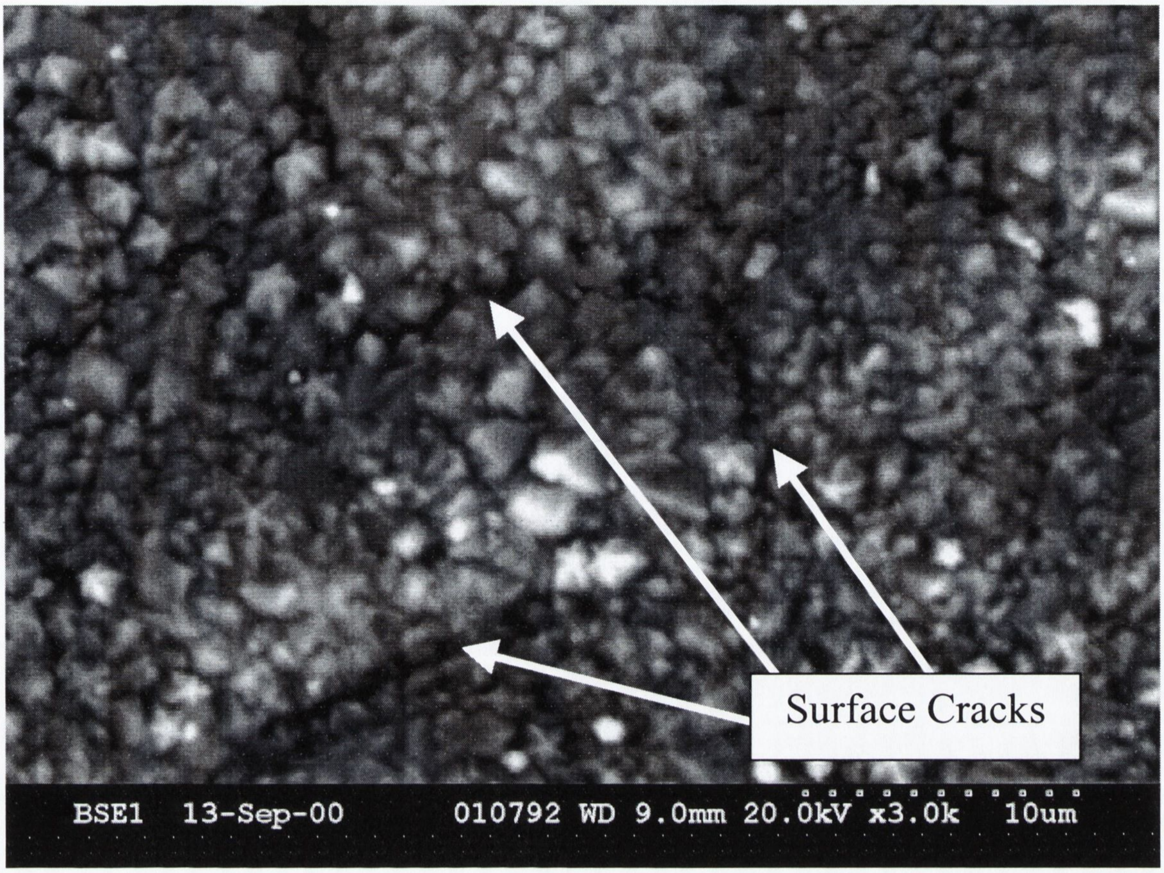

Figure 4-125: Surface Topography Post-Heat Treatment at a Magnification of 3K

Figures 4-122 and 4-123 show the SEM images of the pre-heat treatment surface topography at magnifications of 1K and 3K respectively. Figures 4-124 and 4-125 show the post-heat treated surface topography from the same trim die at magnifications of 1K and 3K respectively. The pre-heat treatment images shown in figures 4-122 and 4-123 indicate that the coating is very crystalline. The heat treatment cycle applied to the trim die between the conditions shown in figure 4-123 and 4-124, consisted of a pre heat to 870°c, high heat to 1120°c and then quenching in nitrogen under high pressure (3-6 bar). Following this, the trim dies were tempered at 560 °c for three soaks of 150 minutes each. When the surface topography of the trim dies after heat treatment was analysed, as shown in figures 4-124 and 4-125, a very distinct change in surface topography was observed. The crystalline structure visible in the pre-heat treatment images has disappeared. The post-heat treatment surface is more undulating, but more importantly, the surface is covered in surface cracks as highlighted in figures 4-124 and 1-125.

It has already been established that surface roughness has a significant influence on the fatigue endurance of a component. The pre and post heat treatment trim dies were placed into a series 100 Zygo white light profilometer, which uses phase shift interferometer to measure surface roughness. The results from the Zygo machine for the pre and post-heat treated trim dies are shown in figures 4-126 and 4-127 respectively.

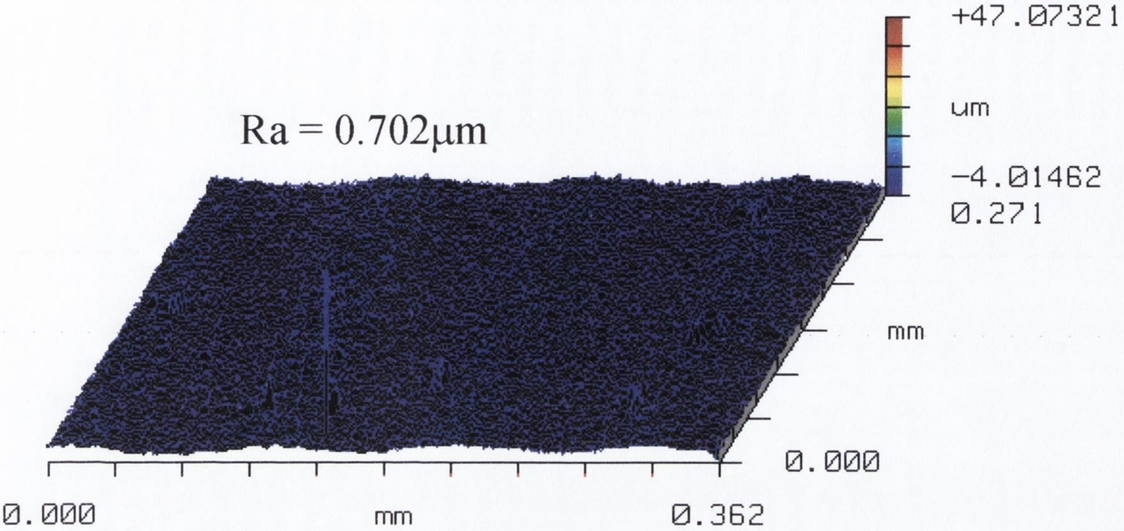

Figure 4-126: Results from the Zygo Machine For the Pre-Heat Treated Trim Die

Figure 4-126 above indicates that the pre-heat treated trim die had a surface roughness value Ra of 0.702μm. When this is compared to the post-heat treated image shown in figure 4-127, the Ra value has increased by approximately 3 times to 2.131μm.

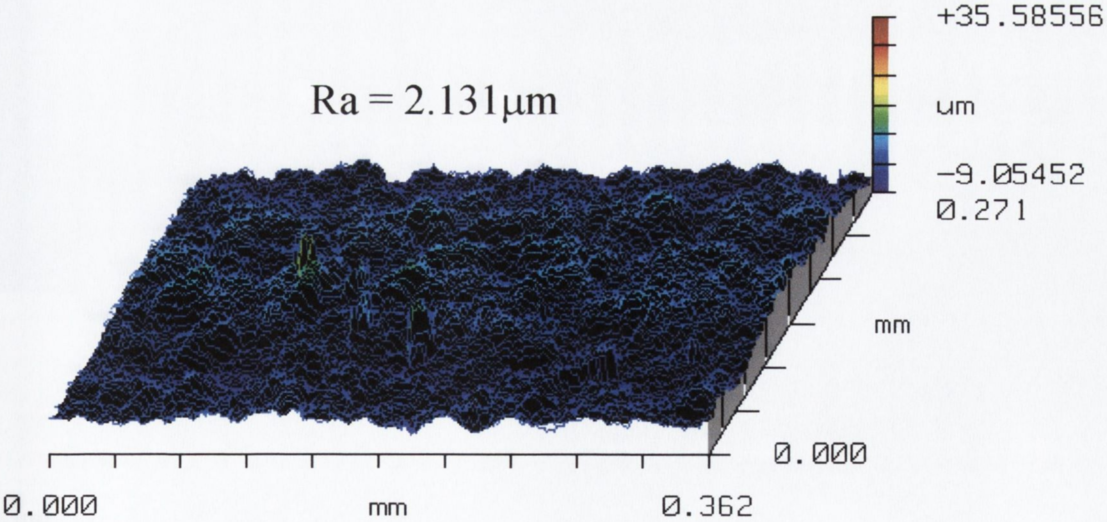

Figure 4-127: Results from the Zygo Machine For the Post-Heat Treated Trim Die

The images from the SEM and Zygo machine have proved that the heat treatment cycle causes a sever change in the roughness of the surface, but more importantly, considerable cracking within the coating. Whether it is the high temperature that causes the surface cracking or the rapid nitrogen quenching is unknown but it is sufficient to say that their combined effect can be detrimental in terms of the fatigue life of the tool.

Section 2.3.4.5 on page 22 highlighted research work that suggested that multi layers in a coating provide a barrier to crack propagation [16]. Given that the trim die coating consists of three layers, it was thought that even if the top layer had cracked, the second or third layer would act as a barrier. To investigate this, trim dies that had failed in service were sectioned, mounted and polished as outlined in Section 3.2.5. Figure 4-128 is a light microscope image of a crack, which has propagated from the surface through the three coatings and into the substrate.

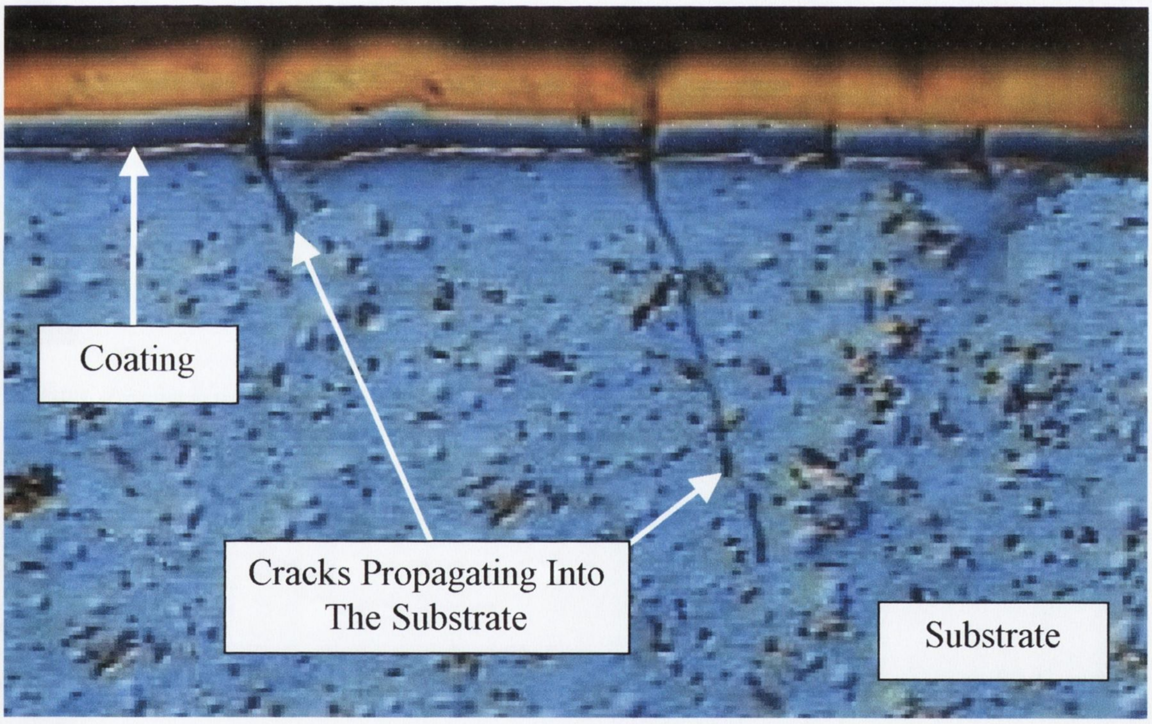

Figure 4-128 Surface Crack Propagating into the M2 Substrate

A possible explanation as too why a crack would propagate through the three coating layers would be that because of the high temperatures involved in the CVD process, a diffusion layer between each coating interface is established. This diffusion of the layers enables the crack to propagate from one coating to another and finally into the M2 substrate.

Finally, during the analysis of the coatings, using the light microscope, an unexpected image was discovered. Figure 4-129 below shows the appearance of what would appear to be 'corrosion pits' at the coating / substrate interface. Section 2.3.4.4 on page 22 detailed how other researchers [14, 15, 20, 21] have proposed a mechanism of the decrease in corrosion fatigue life.

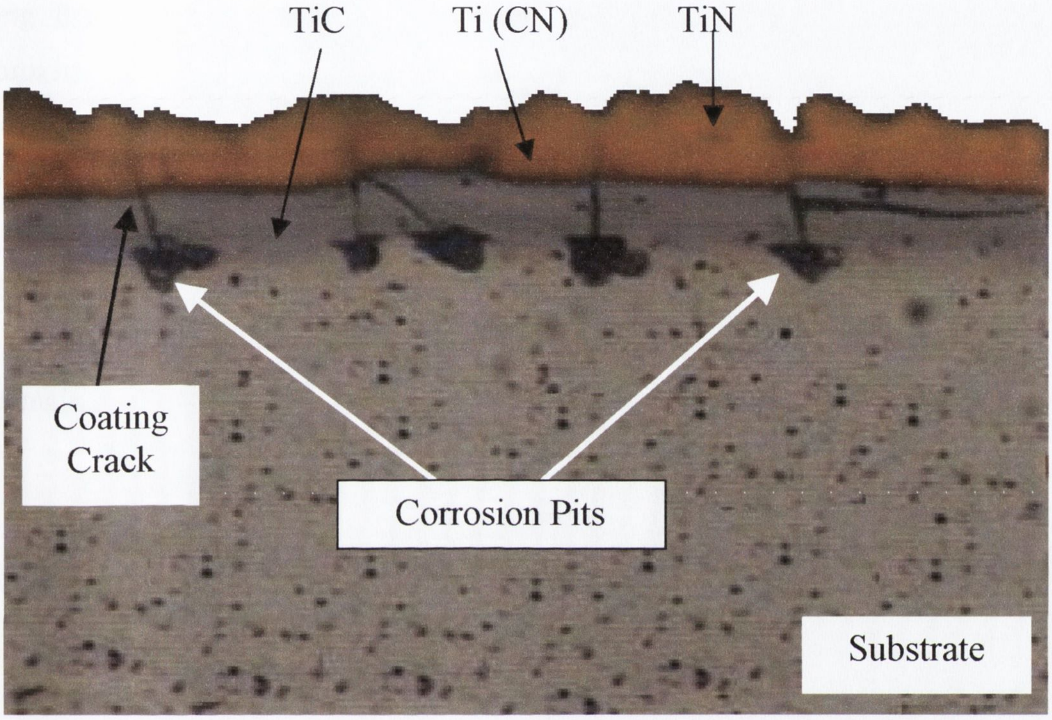

Figure 4-129: Light Microscope Image Of Corrosion Pits Between the Coating and Substrate Interface

With reference to figure 4-129, it can be seen that there is a crack above each corrosion pit. These corrosion pits act as initiation sites for fatigue cracks to propagate and will generally reduce the fatigue endurance of a component [15, 20]. However it is unlikely that the corrosion pits shown above caused failure within the trim die due to the short process times of the dies themselves. Instead a more likely explanation would be to assume that these corrosion pits formed after the die had failed over a far greater period of time.

4.5.4.4 Fatigue Results

As outlined in Section 4.5.4.2 on page 194, the 'non-misfeed' failures suggested that fatigue loading could cause the propagation of the small cracks from the top surface of the trim die. The FE analysis indicated that the maximum theoretical tensile radial stresses along the top of the trim die was 545.3MPa, while the yield strength of M2 is approximately 2,500MPa. Obviously the tensile radial stresses on the land surface are insufficient to cause rupture. However as explained in Section 2.4.3.3 on page 31, it is generally understood, that a component which experiences sufficient cyclic stresses below its yield stress can eventually fail due to fatigue [20]. For that reason four point bending fatigue tests, as detailed in Section 3.2.3, were conducted on the trim die material M2.

The previous Section 4.5.4.3 outlined some of the detrimental effects of coatings. The two main effects were:

1. The CVD coating process imparts tensile residual stresses within the coating due to thermal mismatch.
2. Once the trim die has been through the heat treatment cycle the surface of the coating had developed cracks before trimming a single bolt.

Because of the two points listed above, fatigue tests were conducted on coated and uncoated M2 to prove or disprove the negative effects of the trim die coating. The fatigue specimens were rectangular in cross section having dimensions of 10 x 20mm and a length of 135mm. The grinding parameters, heat treatment and coating application matched the specifications applied to the trim die during manufacture.

For all the fatigue tests conducted in this project, the stress ratio (R), which is given by the ratio of the minimum stress (σ_{min}) to the maximum stress (σ_{max}), was held constant at 0.1. A total of 56 fatigue tests were conducted, half of which using the coated M2 samples.

Figure 4-130 shows the resulting S / N curve, plotting the stress range against the log of the number of cycles to failure, for the uncoated and coated M2 specimens. The black line represents the uncoated specimens while the red line represents the coated specimens.

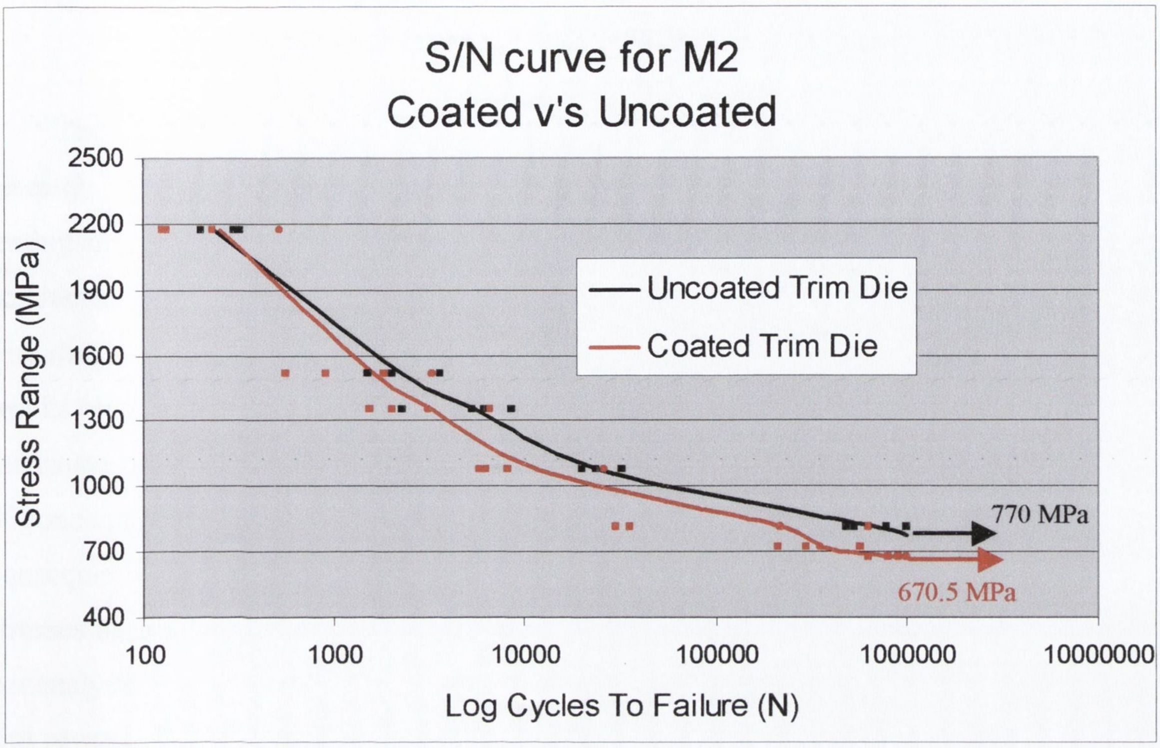

Figure 4-130: Fatigue Test Results for the Uncoated and Coated M2 at Room Temperature

With respect to figure 4-130 above, the fatigue limit for the uncoated and coated specimens was 770MPa and 670.5MPa respectively. Therefore, in the case of the uncoated samples, if a load were applied to the four point bending specimens, that induced a stress range of 770MPa, the sample would complete one million cycles without failure. The same stress range of 770MPa applied to the coated M2 specimen would cause failure between 226,000 to 359,000 cycles. The stress range had to be lowered to 670MPa before the coated specimens completed one million cycles.

Figure 4-130 clearly proves that for the test results presented here, the application of a CVD coating reduces the fatigue limit of the heat treated trim die material M2 by almost 13%.

4.5.4.5 Conclusions: Failure Analysis

The exact mechanism of fracture within the trim die would require independent research and was outside the scope of this project. An analysis based on experimental testing and observations coupled with other research work on fracture and fatigue has been conducted to establish the most likely failure mechanism within the trim die. The failed trim dies were divided into two categories, Misfeed Failure and Non-Misfeed Failure. The results obtained from a FE model of the trim die colliding with the top tool helps to explain the cause of 'misfeed' failures. The finite element analysis conducted in Phases 1 through 3 concentrated on optimising the various parameters of the trim die profile. As a consequence of this analysis it was discovered that the trim die experiences tensile radial stresses along the top 'land surface' where the 'non-misfeed' cracks are known to appear. An analysis of the maximum principle stresses in the vicinity of the known crack initiation site revealed that the tensile principle stresses were perpendicular to the trim die surface and hence promotes crack propagation.

Once the crack had started to propagate, its path was perpendicular to the surface on which initiation occurred. Images from the SEM highlighted vertical segregation lines through the M2 die material. An elemental X-ray spectrum analysis revealed that these lines were in fact carbide segregation lines. Due to the alloying elements of the M2 steel, these carbides are very hard and therefore very brittle. If a crack were formed in the vicinity of these carbide segregation lines its propagation path would follow a line through the brittle carbides.

In an effort to establish why the crack later changed course and veered towards the inner rake surface, an FE model that reproduced the crack, was used. The results obtained from this analysis did not confirm why the crack changed direction. However, the most likely explanation is that as the crack propagates vertically downwards the distance between the tip of the crack and the inner surface of the trim die is ever decreasing, due to the internal rake angle. Therefore at a certain point, the crack requires less energy to change direction and break to the surface through the reduced volume of the metal than to continue downward through the bulk of the trim die.

It was decided to conduct an analysis into the effects of applying a coating onto the trim die because other research in the area, outlined in Section 2.3.4.1 on page 18, produced contradictory results. SEM images revealed that the surface topography pre and post-heat treatment had very different appearances. The two main points arising from this analysis were:

1) The CVD coating process leaves residual tensile stresses which are known to reduce the fatigue life [34]
2) The heat treatment cycle causes cracks to form on the surface.

Four point bending fatigue tests were conducted on coated and uncoated M2 specimens in an effort to prove or disprove the detrimental effects of coatings and obtain fatigue data for M2. The results obtained proved that using a coating on the heat treated AISI M2 reduced the fatigue limit of the material.

As previously highlighted in the Phase 1 conclusion on page 148, the highest theoretical radial stress along the top land surface of the trim die was 545.3MPa. However the fatigue test results presented in this section have stated that the fatigue limit for the coated M2 material is 670.5MPa. Therefore an initial reaction might be to assume that none of the trim dies should have failed, as the maximum theoretical radial stress is below the fatigue limit of the material. However the percentage difference between the experimental fatigue tests and the theoretical FE estimation of maximum principal stresses is only 18.6%. With reference to figure 4-130, there is a scatter band of approximately 25% in the results, therefore taking the scatter in the fatigue results into consideration, incidences could arise were the theoretical radial stress is sufficiently high to cause fatigue in the trim die. The possible variation in the fatigue limit explains why not all the trim dies fail due to this fatigue mechanism.

In terms of fatigue testing with the inherent difficulty of scatter in the results, and the fact that the FE models are, by definition, an approximation of the actual trimming process, it can be concluded that the theoretical estimations are satisfactorily within the limits of experimental uncertainties.

Part V.

5 Conclusions

Numerous research programs have numerically and experimentally examined the stress distributions within cold forging processes, mainly cold extrusion [1,3,16,22,24,25, 27 – 30,32] However, to the author's knowledge, no theoretical or experimental investigation of the Trimming Process or Trim Die failure has been carried out previously. Therefore the objective of the work for this thesis was to analyse the effect of various trim die profile parameters on the stress distributions during the entire cold forming process, to determine an 'optimum' trim die profile and to suggest the likely mechanisms for tool failure.

The Influence of the Trim Die Profile parameters:

Corner Radius:

- A corner radius smaller than 0.2mm, in both the 'fillet' and 'compound' configurations, will cause yielding within the M6 trim die.
- The largest 'fillet' and 'compound' radii of 0.4mm and 0.25mm respectively, induced the lowest level of effective stress. However, comparing the two corner geometry configurations, the 'fillet' corner radius of 0.4mm induced an effective stress by almost 7.5% lower.

Land Width:

- The smallest land width of 0.2mm will theoretically induce the lowest effective stress in the trim die due to a reduction in the aspect ratio. However in terms of production on the factory floor, the lowest "practical land width" of approximately 0.2mm to 0.4mm would be advisable.

Petal Angle:

- An optimum petal angle of 25° induced the lowest effective stress within the trim die. Larger petal angles weaken the trim die, while the smallest angle of 20° offered the greatest resistance to the trimmed material.

Rake Angle:

- While varying the rake angle had little effect on the stresses within the trim die, however, the 1° rake angle induced the lowest effective stress and was therefore deemed 'optimum'.

Interaction Between Parameters:

The Phase 2 analysis concluded that interaction exists between some of the trim die profile parameters. The three interactions, compiled in order of severity are as follows:

- Corner Radius vs. Land Width
- Land Width vs. Petal Angle
- Corner Radius vs. Petal Angle

Failure Mechanisms of the Trim Die:

The combination of an experimental and theoretical investigation established the following:

- A theoretical explanation for the trim die failure known to be associated with a 'misfeed'.
- The crack location of the trim dies, categorised as 'non-misfeed' failures, requires a tensile radial stress to cause propagation. It is proposed that this tensile radial stress is the 'critical' stress component causing premature failure within the trim die.
- The magnitude of the theoretical 'critical' stress component is only 18.6% lower than the fatigue limit established by fatigue testing. Therefore it can be assumed that the crack propagates due to a fatigue type mechanism.
- An elemental X-Ray spectrum analysis verified that vertical straight lines of hard carbide particles exist within the trim die material structure, this line of carbides is caused by carbide segregation during the cooling of the M2 ingot. It is proposed that the fatigue resistance of the M2 high-speed steel will be reduced if a crack initiates in the vicinity of a line of carbide segregation.

- An investigation of the surface of a coated trim die, pre and post-heat treatment, highlighted surface defects caused by either thermal mismatch between the coatings and substrate, or due to the heat treatment processes such as rapid quenching during the austenitizing stage.

Optimum Trim Die Profile:

By combining the conclusion from the theoretical analysis performed in Phases 1 and 2, and the failure analysis, an 'optimum' trim die profile was established. The selection of the 'optimum' profile parameters was based on the magnitudes of minimum induced effective stresses and 'critical' tensile radial stresses. However, the analysis performed in Phases 1 and 2 highlighted the influence that the use of the 'Land Width' had on the induced stresses. Therefore a new and previously unconsidered trim die profile designated a 'Reverse Compound', was simulated and compared with the 'Optimum' trim die profile. The result from that comparison was as follows:

- At the final stroke of the trim die, the 'Reverse Compound' profile induced an effective stress of 1.84GPa compared to 2.16GPa obtained with the 'Optimum' profile. Therefore the Reverse Compound profile reduced the level of effective stress by approximately 15%.
- The 'critical' tensile radial stress induced by the 'Optimum' and 'Reverse Compound' profiles was 39.3MPa and 38.5MPa respectively, which corresponds to a difference of only a 2%. Therefore there is virtually no difference between the two models.
- Although the 'critical' stress component was virtually the same for both profiles, the value of 38.5MPa is approximately 92.95 % smaller that the worst profile simulated in Phase 1.

Overall Conclusions:

Based on the magnitudes and distribution, of the effective stress and the 'critical' tensile stress component, the use of the 'Optimum' or the untested 'Reverse Compound' profiles should, in theory, increase the life prediction of the trim die.

Part VI

Future Work

The Phase 4 analysis outlined on page 177 highlighted that due to the internal hexagonal hole within the trim die, 3D analysis is necessary to simulate the flow of workpiece material across the corners of the hexagon. Phase 4 also illustrated that at present the computational time required to simulate a one-quarter model of the trimming process is very intense. Until the FE packages become more efficient and personal computers more powerful, access to super computer mainframes would be the best approach to obtain a understanding of the 'real-world' trimming process.

In all the FE models presented in this thesis, the workpiece material is a medium carbon low alloy steel. However when forming Stainless Steel bolts, specific Trim Die profiles are required. Therefore a continuation of this research work would be to investigate how altering the workpiece material effects the selection of the 'Optimum' Trim Die profile.

References

1 Lange K, Hettig A and Knoerr M. *Increasing tool life in cold forging trough advanced design and tool manufacturing techniques.* Elsevier Science Publications. 1992. Page 495-513.

2 ASM Handbook. *Forming and Forging.* ASM International, Metals Park, OH. Vol. 14. 1988

3 Quinlan G. E., Monaghan J. *An investigation into the effect of tool fillet corner geometry on tool stresses in a cold forging process.* Irish Manufacturing Committee 15. 1994

4 ASM Specialty Handbook. *Tool Materials.* ASM International, Metals Park, OH. 1995

5 ASM Handbook. *Machining.* ASM International, Metals Park, OH. Vol. 16. 1989

6 Higgins R. A., *Engineering Metallurgy.* Published by Edward Arnold. ISBN 0340 28524 9. 1957

7 Uddeholm Tooling AB. *The ASEA-STORA Process.* Customer Publications.

8 Murphy M. J., *Planar Sputter Magnetron Technology.* Ph.D. Thesis, Department of Electronic Engineering, Dublin City University. 1996

9 ASM Handbook. *Friction, Lubrication, and Wear Technology.* ASM International, Metals Park, OH. Vol. 18. 1992.

10 Geiger M, Hinsel C. and Engel U. *Effects of PVD and CVD coatings on fatigue strength of tool steel for cold forging.* Production Engineering. Vol. V/1. 1998. Page 43-46.

11 Shiozawa K., Nishino S. and Handa K., *The influence of applied stress ratio on fatigue strength of TiN Coated carbon steel.* JSME International Journal, series I. Vol. 35/3. 1992. Page 347-353.

12 Murakami R., Takeuchi T., Yano T. and Katsumura M., *Fatigue properties of thin films on steel coated by dynamic mixing.* Proc of the 6th int conf on mechanical behaviour of materials. Vol. 2. 1991. Page 487-492.

13 Venkatesh V. C., Ye C. T., Quinto D. T. and Hoy D.E.P., *Performance studies of uncoated CVD coated and PVD coated carbides in turning and Milling.* Annals of CIRP. Vol. 40. 1991. 545-550.

14 Shoiozawa K., Tomosaka T., Han L. and Motobayashi K., *Effects of flaws in coating film on fatigue strength of steel coated with titanium nitride.* JSME International Journal, series A. Vol. 36. 1996. Page 142-150.

15 Ebara R., Nakajima H., Odohira T., Wada T. and Hayano M. *Application of ion plated cr-tin multilayer coating to steam turbine blades.* Proc of the 16th turbomachinery symp. 1987. Page 03-09.

16 Klocke F. and Krieg T. *Coated tools for metal cutting- Features and applications.* Annals of the CIRP. Keynote Paper. Vol. 48. 1999. Page 515-525.

17 Vijgen R. O. E. and Dautzenberg J. H. *Mechanical measurement of residual stress in thin PVD films.* Thin solid films. Vol. 270. 1995. Page 264-269.

18 Fernand Ellyin. *Fatigue Damage, Crack Growth and Life Prediction.* Published by John Wiley and Sons Chapman and Hall. ISBN 0 412 59600 8. 1997.

19 Kocanda A. *Die steel for warm working - An evaluation of resistance to cyclic loading.* Advanced Technology of Plasticity. Vol. 1. 1990. Page 349-354.

20 ASM Handbook. *Fatigue And Fracture.* ASM International, Metals Park, OH. Vol. 19. 1996.

21 Korhonen A. S. *Wear-and Corrosion resistant PVD coatings for tools and machine parts.* Annals of CIRP. Vol. 39/1. 1990. Page 573-575.

22 Geiger M., Hansel M., Engel U. *FEM simulation of mixed-mode fatigue crack growth in metal forming tools.* Mixed modes fatigue and fracture, ESIS 14, Mechanical engineering publications. 1993. Page 03-21.

23 Falk B., Engel U. and Geiger M. *Estimation of tool life in bulk metal forming based on different failure concepts.* Journal of materials processing technology. Journal of materials processing technology. Vol. 80-81. 1998. Page 602-607.

24 Sonsoz A., Tekkaya A. E. *Service life estimation of extrusion dies by numerical simulation of fatigue-crack-growth.* Int. J. Mech. Sci. Vol. 38. 1996. Page 527-538.

25 Cser L., Geiger M., Lange K., Kals J. A. G. and Hansel M. *Tool Life and tool quality in bulk metal forming.* IMechE. Vol. 207. 1993. Page 223-239.

26 Hettig A., Reiss W. and Lange K. *A study of tool fracture in cold extrusion.* Trans Namri / SME Michigan. 1989. Page 49-53.

27 Knoerr M., Lange K. and Altan T. *Fatigue failure of cold forging tooling: causes and possible solutions through fatigue analysis.* Journal of materials processing technology. Journal of materials processing technology. Vol. 46. 1994. Page 54-71.

28 Engel U. *Reliability analysis of cold forging tools.* Proc of the 9th international cold forging congress, Solihull, UK. Vol. 9. May 1995. Page 103-112.

29 Kusiak Jan, Thompson Erik G. *Optimisation techniques for extrusion die shape design.* Numiform. 1989. Page 569-574

30 Geiger M., Hansel M., Rebhan, T. *Improving the fatigue resistance of cold forging*

tools by FE simulation and computer aided die shape optimisation. IMechE. Vol. 206. 1992. Page 143-150.

31 Nago Yuichi, Knoerr M and Altan T. *Improvement of tool life in cold forging of complex automotive parts.* Journal of materials processing technology. Vol. 46. 1994. Page 73-85

32 Geiger M. and Hansel M. *An energy-based approach to the simulation of fatigue crack initiation in metal forming tools.* WIRE. Vol. 43. 1993. Page 271-277.

33 ASTM. *Standard Terminology Relating To Wear and Erosion.* Annual Book Of Standards. Vol. 3.02. 1987. Page 243-250.

34 Ewalds H. L. and Wanhill R. J. H. *Fracture Mechanics.* Published by Edward Arnold. ISBN 0 7131 3515 8. 1984.

35 Miller, Patricia. *Failure mechanisms in tool steels.* Manufacturing Engineering. January 1999. Page 82-87.

36 Wang. Ge. *Prediction of Fatigue Failure In Engineering Components Using The Finite Element Method.* Ph.D. Thesis, Department of Mechanical and Manufacturing Engineering, University Of Dublin, Trinity College. 1999.

37 ASTM. *Standard Practice For Presentation Of Constant Amplitude Fatigue Test Results For Metallic Materials.* Annual Book Of Standards. Vol. 3.02. 1995.

38 Wu W. T., Li G., Arving A. and Tang J. P. *Development of a three-dimensional finite element method based process simulation tool for the metal removal industry.* Proc of the 3rd biennial joint conf on Engineering systems design and analysis. Vol. 3. 1996. Page 143-150.

39 Knoerr M., Lee J. and Altan T. *Application of the 2D finite element method to simulation of various forming processes*. Journal of materials processing technology. Vol. 33. 1992. Page 31-55

40 Altan Taylan and Knoerr Markus. *Application of the 2D finite element method to simulation of cold forming processes.* Journal of materials processing technology. Vol. 35. 1992. Page 275-302.

41 Kobayashi S., Oh S. and Altan T. *Metal Forming and the Finite Element method.* Oxford University press. 1989.

42 Wu W.T., Oh S.I., Altan T and Miller R. A. *Automated Mesh Generation for forming simulation-1.* Proc Computers in Engineering ASME. Vol. 5. 1990. Page 507-515.

43 Altan T. Numerical Process simulation for tool and process design in bulk metal forming. Annals of CIRP. Vol. 45. 1996. Page 599-615.

44 Takahashi M. and Kobayashi S. *Some Aspects Of Finite Element Analysis of Plastic Compression.* Proc 5th North American Metalworking Research Conference. 1977. Page 87-94.

45 Matsumoto H., Oh S. I. and Kobayashi S. *A note on the Matrix Method For Plastic Analysis Of Ring Compression.* Proc 18th International Machine Tool Design Research Conference. 1977. Page 3-9.

46 Oh S. I. *Finite Element Analysis of Metal Forming Processes with Arbitrarily Shaped Dies.* Int. J. Mech. Sci. Vol. 24. 1982. Page 479-493.

47 Kobayashi S. A review of the Finite Element Method and Metal Forming Process Modelling. J. Applied Metal Working. Vol. 2. 1982. Page 163.

48 Kobayashi S. *Metal Forming and the Finite Element method - past and future.* Proc 25th International Conference on machine Tool Design. 1985. Page 17-32.

49 Osokada K. and Mori K. *The Use of micro- and supercomputers for simulation of metal forming processes.* Annals of CIRP. Vol. 34. 1985. Page 241-244.

50 Hussin A.A.M., Hartley P., Sturges C. E. N. and Rowe G.W. *Non-Linear Finite Element Analysis on Microcomputers For Metal Forging*. Journal of Strain Analysis. Vol. 21. 1986. Page 197-203.

51 Creus G.J. and Groehs A. G.. *Finite Element Analysis of large Plastic Deformations In Metals.* In Chenot J. L. and Onate E., editors, Modelling of metal forming processes. 1988. Page 27-36.

52 Mahrenholtz O. and Dung N. L.. *Mathematical Modelling of Metal Forming Processes by Numerical Methods.* Adv Tech. Of Plasticity. Vol. 1. 1990. Page 3-10.

53 Yan L., Xu S. and Li G. *Finite Element Analysis of Metal Forming Processes on Personal Computers.* Journal of Engineering for Industry. Vol. 113. 1991. Page 441-445.

54 Walters J., Tang J.T. and Wu W. T. *Recent Development and Applications of Finite Element Method in Metalforming.* Journal of materials processing technology. Vol. 46. 1994.

55 Barcellona A., Cannizzaro L., Forcellese A. and Gabrielli F. *Validation of frictional studies by double cup extrusion tests in cold forming.* Annals of CIRP. Vol. 45/1. 1996. Page 211-214.

56 Wanheim T. *Friction at high pressures.* WEAR. Vol. 35. 1973. Page 225-244.

57 Hartley P., Sturgess C.E.N., Rowe G.W. *Friction in Finite Element Analysis of Metal forming Processes.* Int. J. Mech. Sci. Vol. 21. 1979. Page 301-311.

58 Hartley P., Pillinger I. and Sturgess C.E.N. *Modelling Frictional Effects in Finite*

Element Simulation of Metals Forming. In I. Haque et al, editor, Friction and Material Characterisations, Winter Annual Meeting of ASME, MD 10. 1988. Page 91-96.

59 Haque I., Jackson J.E. and Gangee T.. *Some Numerical Aspects of friction modelling in material forming processes.* In I. Haque et al, editor, Friction and Material Characterisations, Winter Annual Meeting of ASME, MD 10. 1988. Page 39-46.

60 Raous M., Pinto Y. and Chadrand P.. *Numerical Modelling of friction for metal forming processes*. In Chenot J. L. and Onate E., editor, Modelling of Metal Forming Processes, pages 93-99. Kluwer Academic. 1988.

61 Ramakrishnan N., Ghantasala S. and Kutumba Rao V.V. *An Algorithm to incorporate friction in finite element analysis of metalworking.* Journal of materials processing technology. Vol. 23. 1990. Page 311-319.

62 Durham D. R., Von Turkovich B. F. and Assempoor A. *Fillet Design in Cold Forging Dies*. Annals of CIRP. Vol. 40. 1991. Page 235-238.

63 Altan, T., Oh., S. I. and Gegel, H. *Metal Forming: Fundamentals and Applications.* ASM International, Metals Park, OH. 1983.

64 Schey, J. A. *Metal Deformation Processes: Friction and Lubrication.* ASM International, Metals Park, OH. 1983.

65 Iwabuchi, Akira. Yunus, Ahmad bin Hj. Hayashi, Mitsuaki. Nisi, Jun-ichiro, Sato, Yuji. *Die life and workpiece properties under dry conditions in high-speed pressworking*. Trans of ASME / Journal of manufacturing science and engineering. Vol. 119. November 1997. Page 550-555.

66 DEFORM User Manual

67 ANSYS Theory Manual.

68 Walters John. *Simulation and analysis for forging companies - an industrial overview.* 39 H. R. Bergman Memorial Spring Seminar, ASM Milwaukee Chapter. 1997.

69 Mountgomery Douglas C. *Design and analysis of experiments. Published by John Wiley and Sons*. 4th Edition. 1997.

70 ASTM. *Compression testing standard.* Annual Book Of Standards. March 31, 1989.

71 Buehler Dialog Reference Manual. *Microstructural analysis reference manual.* Section 2. Appendix 1.

72 ASM Handbook. *Metallography and Microstructures.* ASM International, Metals Park, OH. Vol. 9. 1985.

73 ASM Specialty Handbook. *Carbon And Alloy Steels.* ASM International, Metals

Park, OH. 1996.

74 ASM Handbook. *Surface Engineering.* ASM International, Metals Park, OH. Vol. 5. 1994.

75 Male A. T. and Cockroft M. G. *A method for the determination of the coefficient of friction of metals under conditions of bulk plastic deformation.* Journal Inst. Of metals. Vol. 93. 1964. Page 121.

76 Lee C. H. and Altan T. *Influence of flow stress and friction upon metal flow in upset forging of rings and cylinders.* ASME. Journal of Engineering for Industry. Vol. 94. 1972. Page 775-782.

77 Male A. T. *Variations in Friction coefficients of metals during compressive deformation.* Journal of the institute of metals. Vol. 94. 1966. Page 121-125.

78 deMeester, B., Tozawa, Y. *Cold Upsetting Tests.* Annals of CIRP. Vol. 28/2. 1979. Page 577-580.

79 Freudenthal, A.M. The Inelastic Behaviour of Engineering Metals and Structures. Wiley, New York. 1950.

80 Cockroft, M.G. and Latham, D.J. *Ductile and Workability of Metals.* J. Inst. Metals. Vol. 96. 1968. Page 33-39.

81 Brozzo, P., Deluca, B. and Rendina, R. *A New Method for the Prediction of Formability Limits of Metal Sheets.* Proceedings of the 7th biennial congress of International Deep Drawing Research Group. 1972.

82 Osakada, K., Watadani, A. and Sekiguchi, H. *Ductile Fracture of Carbon Steel Under Cold Metal Forming Conditions:* Tension and Torsion Tests Under Pressure. Bulletin of JSME. Vol. 20. 1997. Page 1557-1565.

83 Ayada, T., Higashino, and Mori, K. *Central Bursting in Extrusion of Inhomogeneous materials.* Proceedings of 1st ICTP, Advanced Technology of Plasticity. Vol. 1. 1984. Page 553-558.

84 McClintock, F.A. *A Criterion for Ductile Fracture by the Growing of Holes.* J. Applied Mechanics. 1968.

85 Rice, J. R. and Tracey, D. M. *On the Ductile Enlargement of Voids in triaxial Stress Fields.* J. Mech. Phys. Solids. Vol. 17. 1969. Page 201-217.

86 Oyane, M. *Criteria of Ductile Fracture Strain.* Bulletin of JSME. Vol. 15. 1972. Page 1507-1513.

87 Lemaitre, J. *A Continuous Damage Mechanics Model Fro Ductile Fracture.* J. Of Engineering Materials and Technology. Vol. 17. 1985. Page 83-89.

88 Dawson, P., Lee, Y.S., and Kumar, A. *Void Growth in Drawing and Extrusion of*

Ductile Metals. J. of Materials Processing Technology. Vol. 32. 1992. Page 119-134.

89 Kim H., Yamanaka M. and Altan T.. *Prediction and elimination of ductile fracture in cold forgings using fem simulations.* Trans of NAMRI/SME. Vol. XXIII. 1995. Page 63-69.

90 Ceretti E., Taupin E. and Altan T. *Simulation of Metal flow and fracture applications in orthogonal cutting, blanking, and cold extrusion.* Annals of the CIRP. Vol. 46. 1997. Page 187-190.

APPENDIX A

Trim Die Material Characterisation

The trim die is made from high speed steel AISI M2. Table A-1 below shows the typical percentage chemical composition for M2.

Element	Chemical Composition
Carbon	0.83%
Tungsten	6.13%
Molybdenum	4.94%
Vanadium	1.95%
Chromium	4.33%

Table A-1: Typical Chemical Composition of AISI M2 (% wt)

The main features of a high-speed steel are its great hardness in the heat-treated condition and its ability to resist softening at relatively high working temperatures.

The alloying elements listed in table A-1 have different influences on the properties of M2. The effects of one alloying element on a steel may be affected by the presence of other elements [73]. The effects of a particular element may be beneficial to steel in one respect but detrimental in others. General effects of the various alloying elements found in high-speed steels are summarised below.

Carbon is the most important single alloying element in steel. It is essential to the formation of cementite, pearlite, spheroidite, bainite and iron-carbon martensite. Microstructures comprising one or more of these components can provide a wide range of mechanical properties and fabrication characteristics.

Tungsten and Molybdenum improve the red hardness retention and high temperature strength of the matrix material. They also combine with the carbon atoms to form carbides with an approximate hardness of 75 HRc.

Vanadium is generally added to steel to inhibit grain growth during heat treatment. In controlling grain growth, it improves both the strength and toughness of hardened and tempered high-speed steels. When vanadium combines with carbon to form a carbide, its hardness is approximately 80-85 HRc.

Chromium is generally added to increase resistance to corrosion, oxidation, to increase hardenability and improve abrasion resistance in high carbon compositions.

APPENDIX B

Coating Application Techniques

B1. Chemical Vapour Deposition (CVD)

Chemical vapour deposition of hard wear resistant coatings such as Titanium Carbide or Titanium Nitride onto cemented carbide cutting tools was first introduced in the 1960's.

CVD can be defined as a process in which gaseous chemical reactants are transported to a reaction chamber, activated thermally or by other means in the vicinity of the substrate, and made to react to form a solid deposit on the substrate surface. Figure B-1 below schematically represents a thermally assisted CVD coating process.

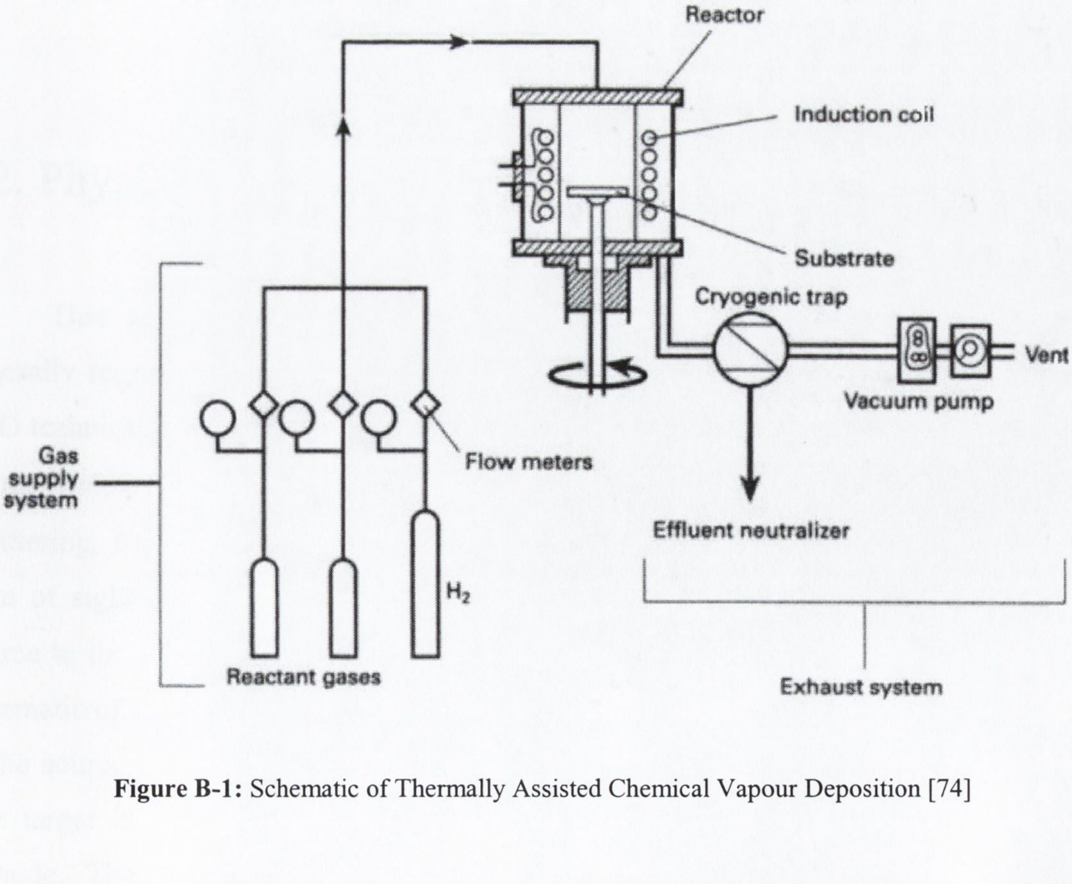

Figure B-1: Schematic of Thermally Assisted Chemical Vapour Deposition [74]

]

In the CVD coating process a gas mixture is introduced into a reactor in which the tools to be coated are heated to approximately 1000°c. The gaseous atmosphere envelops them and a chemical reaction takes place on the surface of the parts providing a solid material coating.

The chemical reactions, along with the coating temperatures required to produce Titanium Carbide (TiC), Titanium Carbonitride (Ti (CN)) and Titanium Nitride (TiN) are given below,

To produce a TiC coating layer:

$$TiCl_4 + CH_4 + H_2 \xrightarrow{1020°c} TiC + 4HCl + H_2$$

To produce a Ti (CN) coating layer:

$$TiCl_4 + CH_4 + N_2 + H_2 \xrightarrow{1000°c} Ti\ (CN) + 4HCl + H_2$$

To produce a TiN coating layer:

$$TiCl_4 + N_2 + H_2 \xrightarrow{975°c} TiN + 4HCl + H_2$$

With respect to the three chemical reactions listed above, the Hydrogen gas does not take part in the reaction and is referred to as the 'carrier'.

B2. Physical Vapour Deposition (PVD)

Due to the high temperatures involved in the CVD process heat treatment is generally required after the coating has been deposited. This led to the development of PVD techniques. In comparison with the CVD process, the temperatures are relatively low, in the order of 550°c. The basic PVD processes fall into three general categories, Sputtering, Evaporation and Ion plating. The PVD method is sometimes referred to as a 'line of sight' process. This means that the hard coating material is transferred from a source to the tool, travelling in a straight line. Figure B-2 on the following page shows a schematic of the Sputtering PVD process. In the Sputtering PVD process, the target, which is the source of the coating material, and the substrate are placed in a vacuum chamber. The target is connected to a negative voltage supply, which causes it to become the cathode. The substrate material generally faces the target. The coating material is transported from the target to the substrate by a bombardment of the target by gas ions that have been accelerated by the high voltage supply. Momentum transfer between the incoming ions and the target ejects atoms of the coating material. These ejected particles move across the vacuum chamber to be deposited on the substrate. This process of building atoms of the coating material on substrate causes high compressive stresses within the PVD coating.

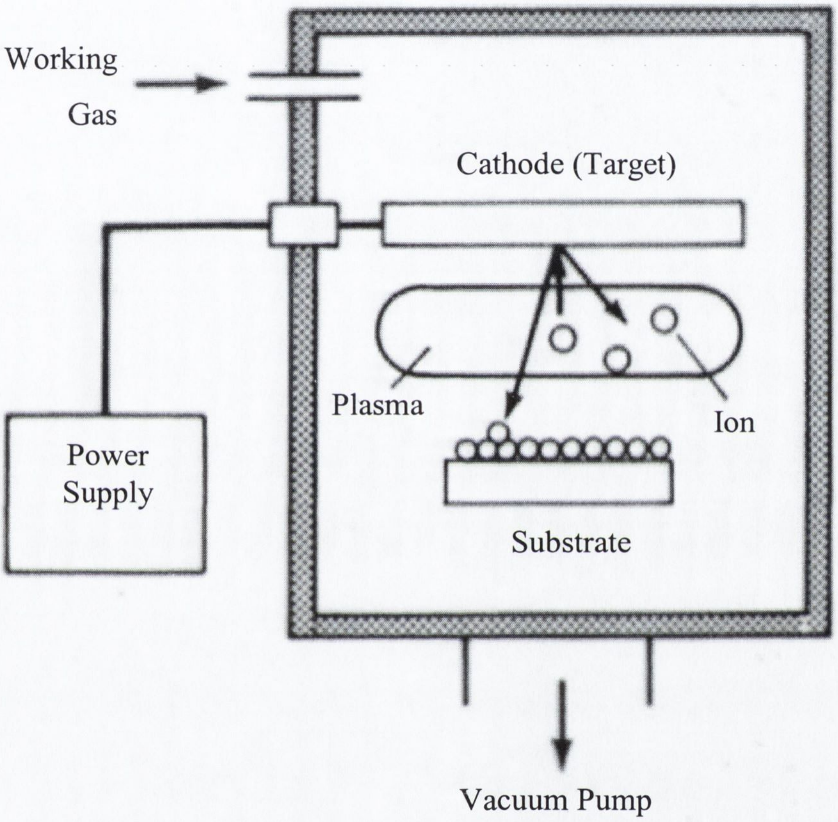

Figure B-2: Schematic of A Sputtering PVD Process [74]

APPENDIX C

Ring Compression Tests

A ring compression test was used to determine the friction factor between the fastener material, a low carbon medium alloy steel, and the trim die material, which is M2 tool steel. Figure C-1 below illustrates a cross section through the ring compression specimen and anvils, before any deformation has taken place. The ring compression specimen is shown hatched. R_i = inner radius, R_O = outer radius and T_0 = original height. The two anvils, shown above and below the specimen in figure C-1 where made from M2 and ground to the same surface conditions as the trim die, and they were coated with the triple layers of TiC, Ti (CN) and TiN, hardened and heat treated as outlined in Section 2.2.4 on page 12. The grinding, coating and heat treatment of the anvils was consistent with the manufacturing process applied to the trim die to ensure good correlation between the ring test and the trimming process.

The anvil-specimen-anvil sandwich shown in figure C-1 was then placed into an INSTRON 1196 testing machine, which is rated to 250 KN. Reducing the initial height of the specimen by the application of pressure onto the M2 anvils, an incremental decrease of (ΔT_0) was recorded.

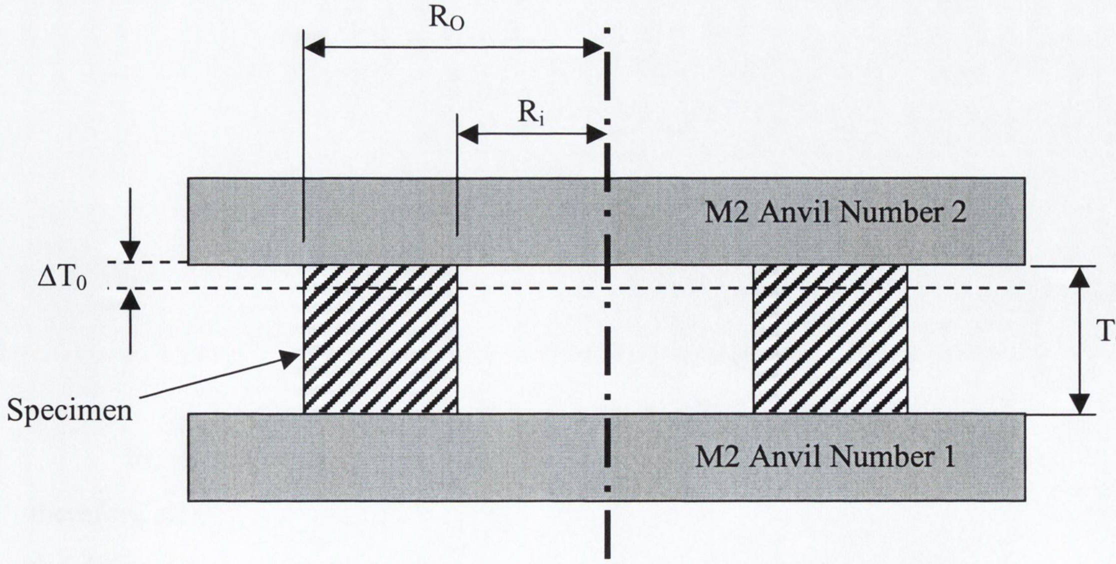

Figure C-1: Deformation Behaviour During A Ring Compression Test

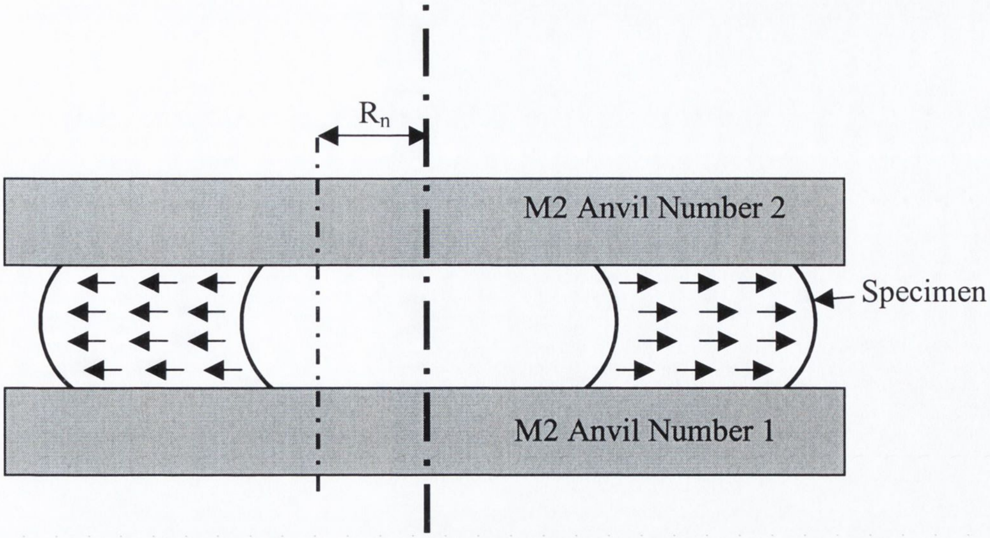

Figure C-2: After Deformation With Low Friction

The change in internal and eternal diameters is very dependent on the friction conditions at the die-workpiece interface. For low values of friction, the ring would deform in the same way as a solid disk, with each element flowing radially outward at a rate proportional to its distance from the axis of symmetry. Figure C-2 illustrates such a deformation, assuming low friction values, where (R_n) is the neutral radius. Any point on the neutral radius (R_n), the material is assumed to be stationary.

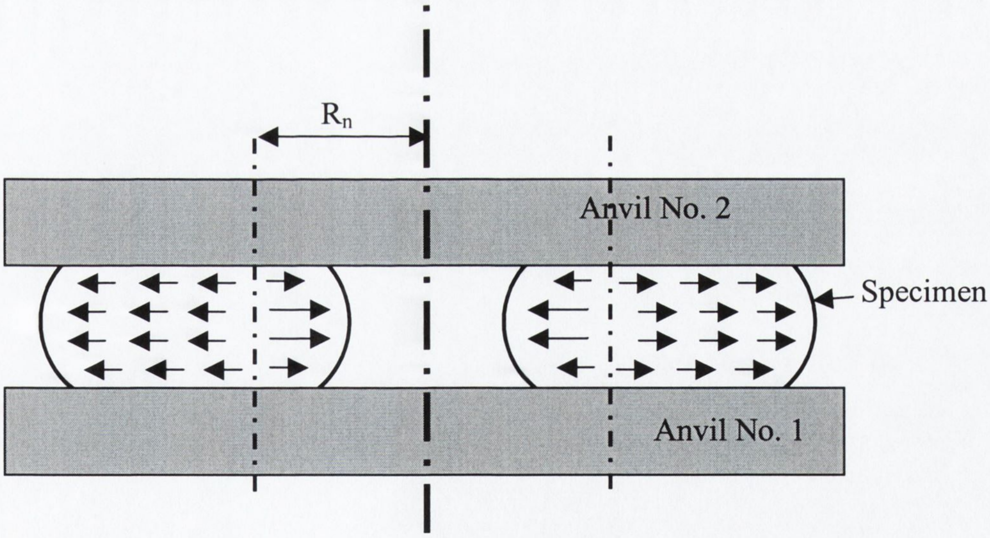

Figure C-3: After Deformation With High Friction

In relation to figure C-2, the neutral radius is smaller than the inner radius, therefore all the workpiece material flows radially outward. In figure C-3, which represents the deformation during high friction, all points with a radius greater than the neutral radius will flow radially outward, however all points with a radius smaller than the neutral radius, flow radially inward. Thus the change in internal diameter provides a simple method for evaluating interface friction. The ring test has an advantage when applied to the study of friction [63] as the force necessary to deform the ring and the flow stress of the specimen material do not have to be known. To obtain the magnitude of the friction factor, theoretical calibration curves, based on work by [75, 76 and 77] as shown in figure C-4 below, were utilised.

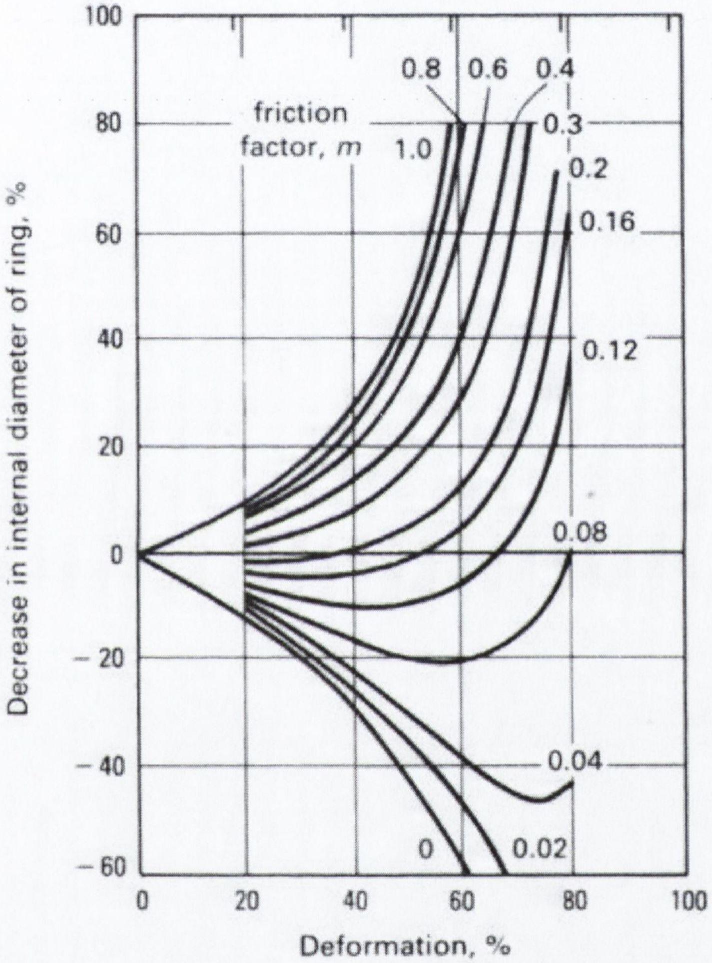

Figure C-4: Theoretical Calibration Curve to Determine the Friction Factor (m)

With reference to figure C-4, it can be seen that only two variables are required to calculate the friction factor (m). The first variable is the percentage deformation in the height of the ring, which is plotted on the x-axis. The second variable is the percentage decrease in internal diameter, which is plotted on the y-axis. For example with reference to figure C-4, if a 40% deformation in the height of the ring resulted in a decrease in the internal diameter of 20%, the friction factor (m) for that experimental test would be approximately 0.6.

The theoretical calibration curve shown in figure C-4 varies depending on the initial dimension of the ring specimen. The dimensions of a typical ring test specimen, as standardised by other research [75, 76 and 77] should follow the ratio of eternal diameter to internal diameter to thickness of 6:3:2. The dimensions of the ring compression specimen tested within this thesis are shown in figure C-5 below.

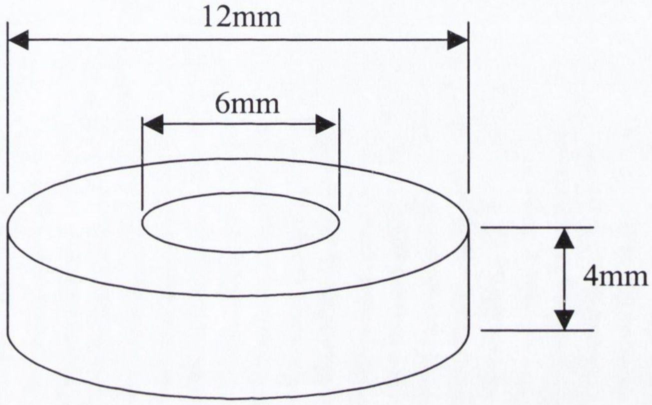

Figure C-5: Typical Ring Compression Specimen

The results from these ring compression tests are detailed in section 4.5.2 on page 185.

APPENDIX D

Corner Radius and Trim Die Stroke

Figure D-1 below shows a 0.1mm Fillet trim die, workpiece and top tool. The dimension labelled 'X' has to remain constant as this dictates the distance across the flats of the trimmed bolt head. Dimension 'Y' is designated the 'final stopping distance', which is effectively equal to the flash thickness. As previously mentioned in the Phase 1 finite element results in Section 4.1 on page 79, once the user defined reference points on the top tool and trim die reach the value 'Y' the simulation is given the signal to stop. The final stopping distance 'Y' remained constant at 0.25mm for all the FE models simulated in this project.

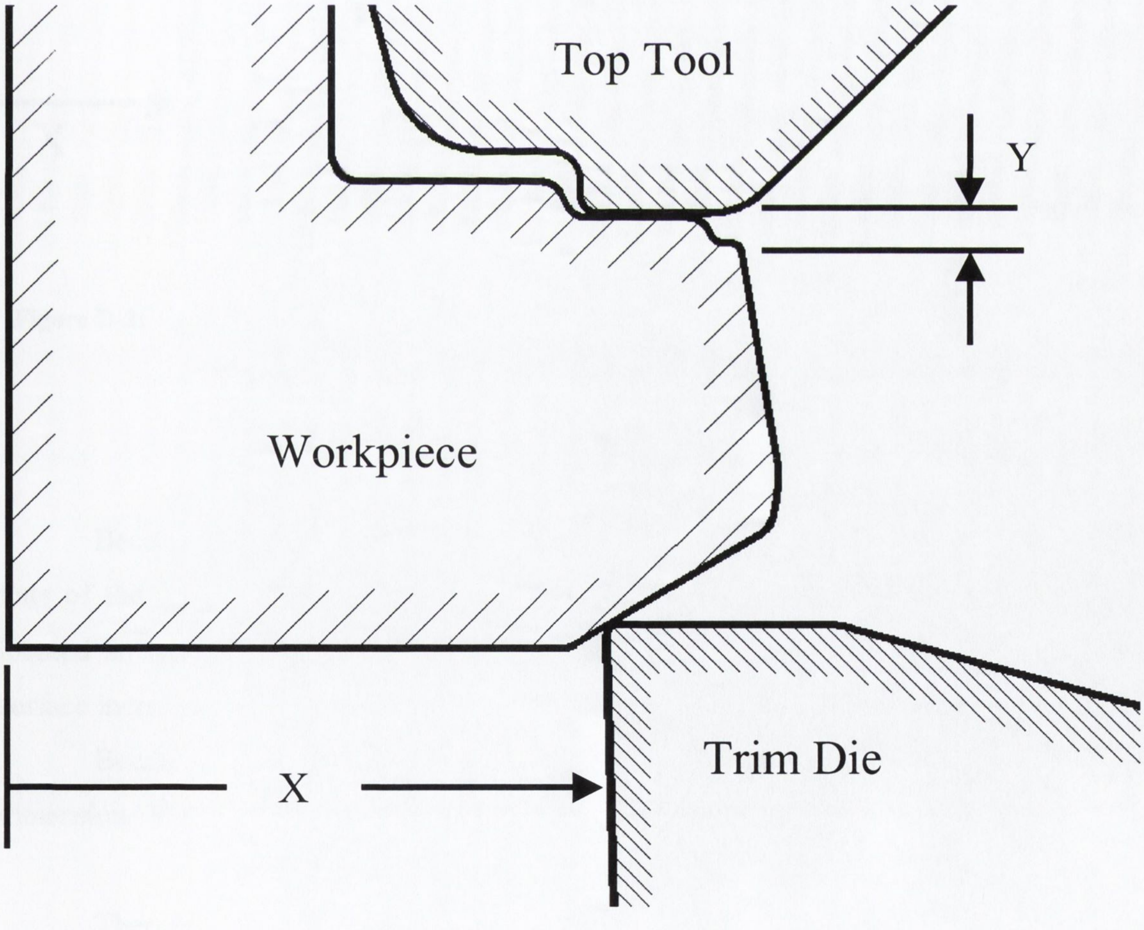

Figure D-1: Top Tool, Workpiece and Trim Die Showing Stopping Distance and Across Flats Dimension

Figure D-2 below shows a close up view of the contact area between the trim die and workpiece. The workpiece is highlighted by the hatched pattern. The 0.1mm fillet trim die profile is shown in black, while the 0.4mm fillet trim die profile is highlighted in red.

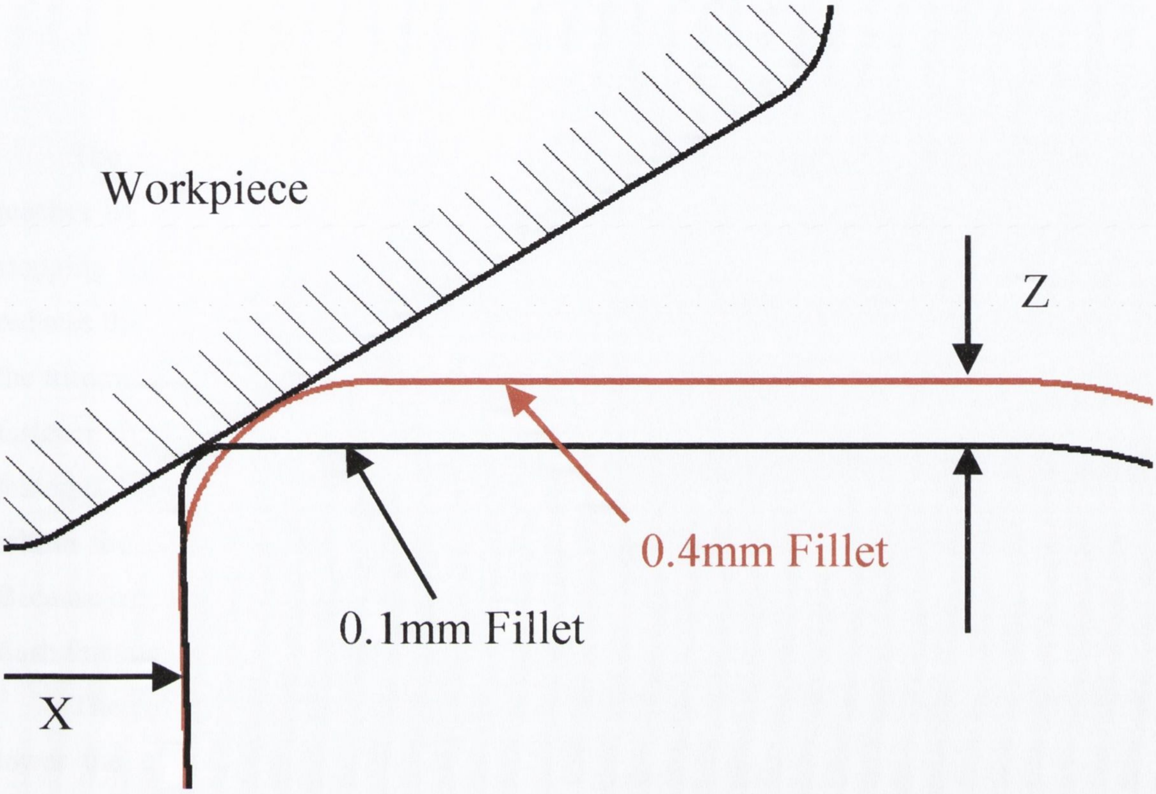

Figure D-2: Close-up of Trim Die and Workpiece Showing the Variation in the 0.1mm and 0.4mm Trim Dies

Because the inner distance 'X' has to remain constant so that the distance across the flats of the bolt hexagon are accurate, when the 0.4mm fillet trim die (shown in red) is located so that the inner rake face lines-up with the dimension 'X' the top of the land surface increases by a distance 'Z'.

Because of the 0.1mm and 0.4mm trim dies are both terminated when the reach the dimension 'Y' (see figure D-1), the 0.4mm trim die has less of a distance to travel.

Therefore, the greater the corner radius, the smaller the actual travel of the trim die.

APPENDIX E

Fracture Within The Workpiece Material

The results presented in Phases 1, 2 and 3 have highlighted that as the trim die reaches its final stroke, the effective stresses within the trim die rise sharply. Obviously stopping the trim die further from the top tool reduces the aspect ratio and consequently reduces the induced stress. As explained in Section 2.1.1 dealing with the fundamentals of the trimming process, once the trim die reaches its final stroke, a *Knock-Out* pin forces the fastener through the centre of the trim die, and in doing so shears the excess trimmed material. Naturally, increasing the flash thickness lowers the magnitude of effective stress within the trim die, but it also increases the shearing or knockout (KO) load required. Because of this it was decided to conduct an investigation into the effects of increasing the flash thickness in terms of KO load and the fracture surface topography.

The conclusions from Phase 3 stated that using a Reverse Compound trim die would lower the effective stresses within the trim die by up to 15%. Although the Reverse Compound trim die is purely conceptual, and its potential advantages have not been validated experimentally, it was considered advantageous to investigate how this new profile would perform during the final knockout sequence to determine if the 15% difference in effective stress could be further increased. A standard 0.25mm compound trim die was used to compare to the results obtained from the Reversed Compound model.

As previously mentioned in Section 4.1 on page 79, the FEA package DEFORM was instructed to end the simulation once the flash thickness, defined as the distance between two user defined points, reached a value of 0.25mm. Figure 4-2 on page 80 illustrates this final stopping criterion. The term ‘stopping distance’ is equivalent to the ‘flash thickness’, and will be considered as such from here onwards. A total of eleven FEA models were constructed, were the flash thickness was altered from 0.25mm to 0.75mm in steps of 0.05mm.

E1. Effective Stress Results

Figure E-1 presents the effective stresses plotted against the flash thickness for the Reverse Compound and Standard trim die. As previously explained, increasing the flash thickness reduces the aspect ratio, which in turn reduces the magnitude of the induced effective stresses. With respect to figure E-1, at a flash thickness of 0.25mm the maximum effective stresses recorded for the Reverse Compound and Standard trim die FE models were 1.84GPa and 2.381GPa respectively. Increasing this flash thickness to 0.75mm caused the maximum effective stresses within the Reverse Compound die to drop to 1.382GPa, which is a reduction of just under 25%. In the case of the Standard trim die, increasing the flash thickness to 0.75mm caused the effective stresses to drop to 1.846GPa, which is a drop of over 22%. It would be advantageous, in terms of the effective stresses, to increase the flash thickness to 0.75mm instead of 0.25mm, but increasing the flash thickness also increases the necessary shearing or knockout (KO) load. This increase in the required Knock-Out (KO) load must be determined.

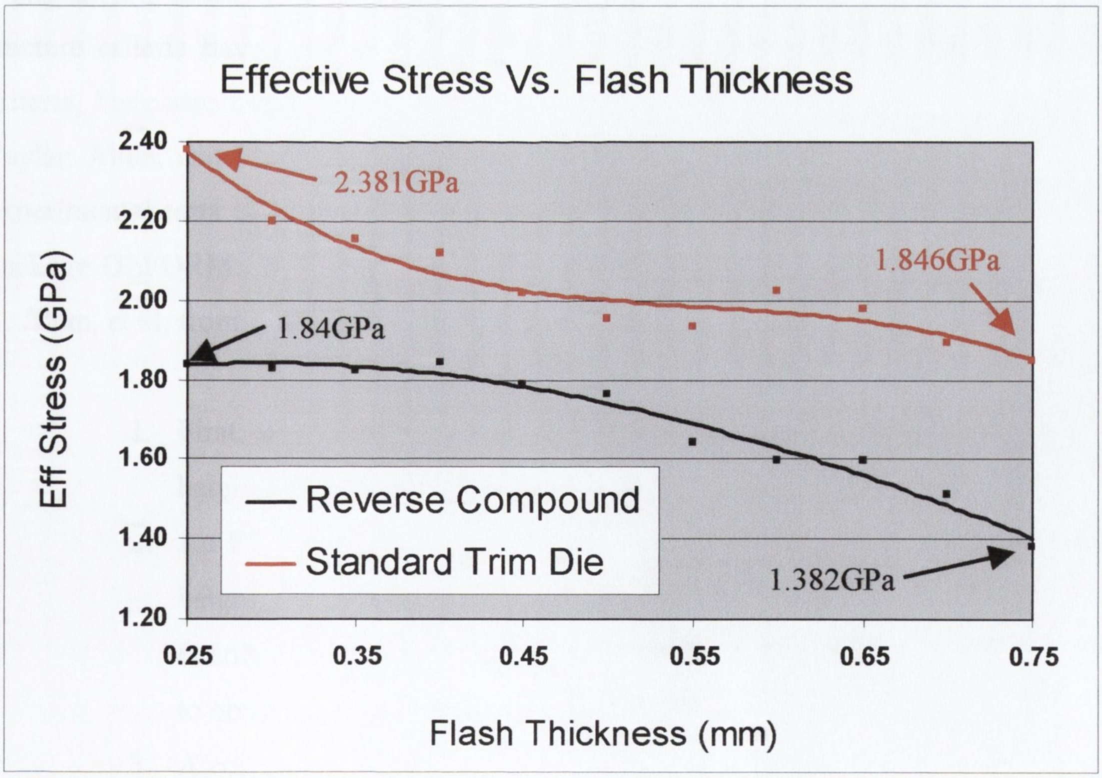

Figure E-1: The Effects Of Increasing The Flash Thickness On The Effective Stresses

E2. Fracture Module

In industry, the last sequence or knockout sequence, after the trim die has reached its final stroke, is the shearing of the excess trimmed material around the head of the fastener. DEFORM has a fracture module built into its pre-processor. The DEFORM user manual states that once elements reach a critical 'damage' value, fracture will occur [66]. The term 'damage' can be calculated within DEFORM using any one of seven different ductile fracture criteria. Once an appropriate ductile fracture criterion has been selected, the user specifies a critical value 'C' for the damage parameter. When the workpiece material is being deformed, during the knockout sequence, any elements that sustain a damage value equal to the predefined critical value 'C' will be deleted, hence simulating fracture. At the present time, fracture is simulated within DEFORM by element deletion, however future release versions of DEFORM promise element splitting and element separation. Obviously the selection of the ductile fracture criterion and critical damage value 'C' is of utmost importance.

Many previous experimental studies, not conducted by the author, have been undertaken to determine formability and/or fracture limit diagrams [78], and several ductile fracture criteria have been suggested [79 - 83]. Mathematically derived ductile fracture criteria, have also been proposed based on experimental observations [84 - 88]. In 1995, Taylan Altan, and Hyunkee Kim [89] conducted extensive research combining FEA and experimental tests to validate the seven ductile fracture criteria available within the FEA package DEFORM. The procedure to determine the critical damage value, as outlined by T. Altan, et al, from a compression test is as follows:

1. First, a compression test, with grooved dies, is conducted to measure the height of the specimen at the occurrence of surface fracture.
2. An FE simulation of the compression test is performed and stopped at the height reduction determined experimentally in point 1. One of the seven ductile fracture criterions within DEFORM is chosen in the post-processor, to obtain the distribution of damage value within the workpiece.
3. A comparison is made between the location of the maximum damage value, predicted by the FE model, with the experimental determined fracture site. If the maximum damage value location coincides with the actual fracture

site, the maximum damage value is therefore taken as the critical damage value 'C' for the material under test.

4. If the location of maximum damage, predicted by the FE model, does not coincide with the experimental location, then the selected ductile fracture criterion, in point 2, is considered inappropriate and another criteria is used until the results coincide.
5. The FE simulation is then run again, but this time with the fracture module within the pre-processor, activated. The critical damage value, obtained from point 3 or 4, is then used during the simulation determine which elements are to be deleted.

The conclusion from the extensive research programme of T. Altan et al, was that three of the seven ductile fracture criteria's within the pre-processor of DEFORM, predicted the height reduction at fracture with acceptable accuracy. Of the three successful fracture criterions, proposed by Cockroft and Latham, appeared to be the best choice for practical applications because its integrand is simple and no material constant other than the flow stress curve was required to determining the damage value [89, 90]. The Cockroft and Latham ductile fracture criterion is given as follows:

$$\int^{\bar{\varepsilon}_f} \frac{\sigma^*}{\bar{\sigma}} d\bar{\varepsilon} = C \qquad \text{Eqn E1}$$

Where $\bar{\varepsilon}_f$ = Effective Fracture Strain, σ^* = Maximum Principle Stress, $\bar{\sigma}$ = Effective Stress and $\bar{\varepsilon}$ = Effective Strain.

E3. Shearing Or Knockout (KO) Load

When each of the eleven FEA simulations had ended at their predetermined stopping distance, a new object was introduced into the model to represent the action of the knockout pin. The Cockroft and Latham ductile fracture criterion, within DEFORM, was activated and the knockout pin which makes contact with the base of the bolt shank, was instructed to move in a downward direction. This downward movement causes the workpiece material to flow back over the corner radius of the trim die. The trim die at this point is locked in position, and therefore the workpiece material, in the vicinity of the corner radius, experiences high stresses. Figure E-2 illustrates the location of the knockout pin within the DEFORM model. The downward movement of the knockout pin, as outlined above, is highlighted in figure E-2 by the yellow arrow. This downward movement causes the workpiece material to shear along the line 'A-A'. In this section E3, the critical damage value 'C' was chosen to be equal to 0.5. The selection of this value will be discussed in section E4.

Figure E-3 is a close-up view of the effective stress distributions within the workpiece and trim die just prior to the onset of fracture for a flash thickness of 0.75mm. Notice that due to the downward displacement of the workpiece material, caused by the knockout pin (not shown), a gap is generated between the top tool and the workpiece.

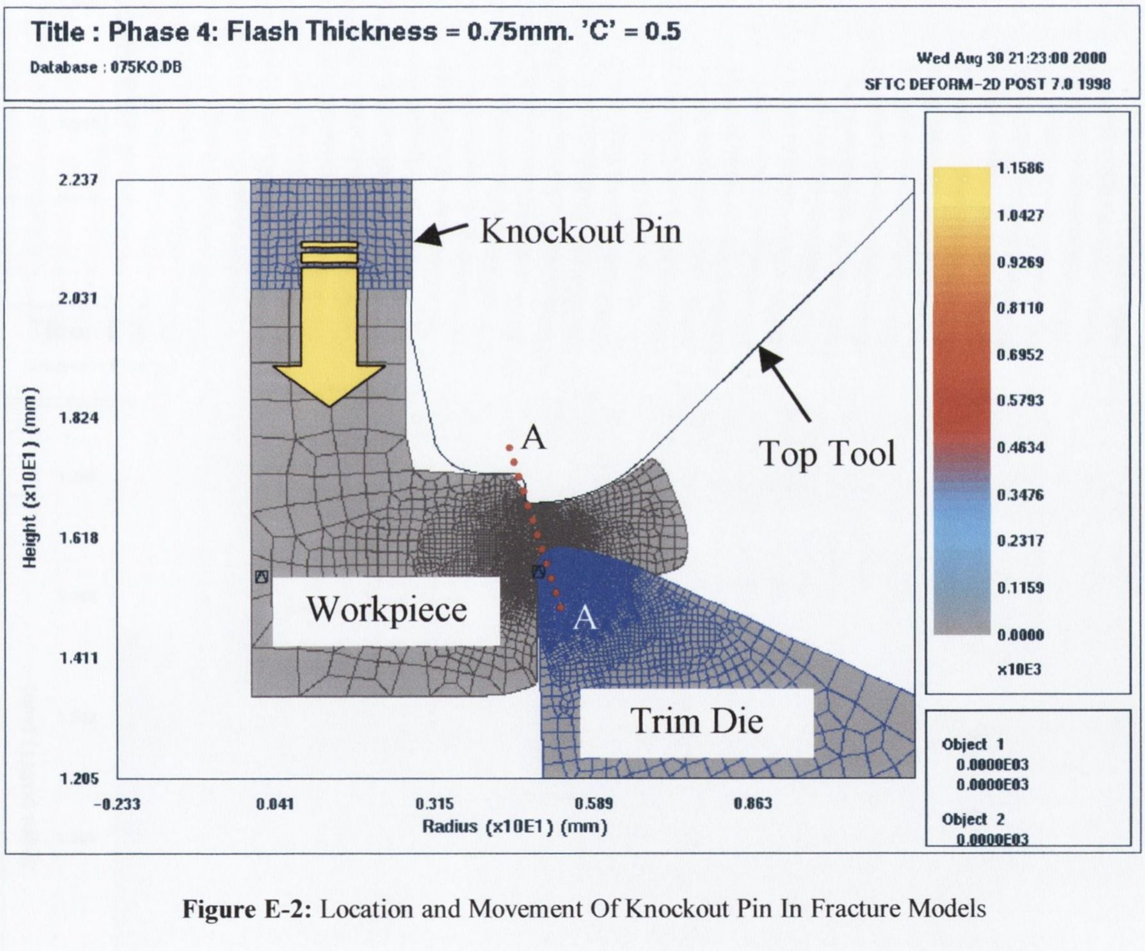

Figure E-2: Location and Movement Of Knockout Pin In Fracture Models

In figure E-4, the predetermined critical damage value 'C' of 0.5 has been reached within some elements within the highly stresses region, and these have consequently been deleted.

Figure E-5 plots the KO load required to shear off the excess material in all eleven FEA models as a function of the flash thickness.

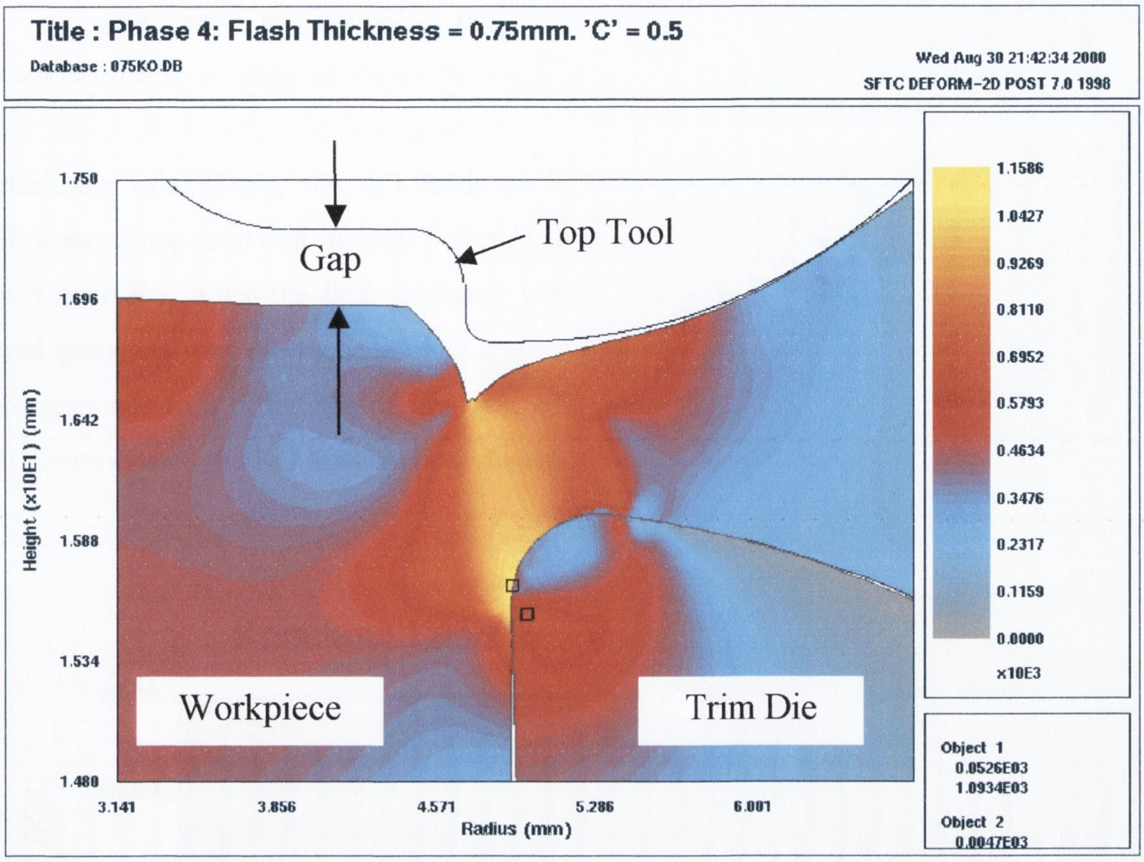

Figure E-3: Effective Stress Distribution Before Fracture

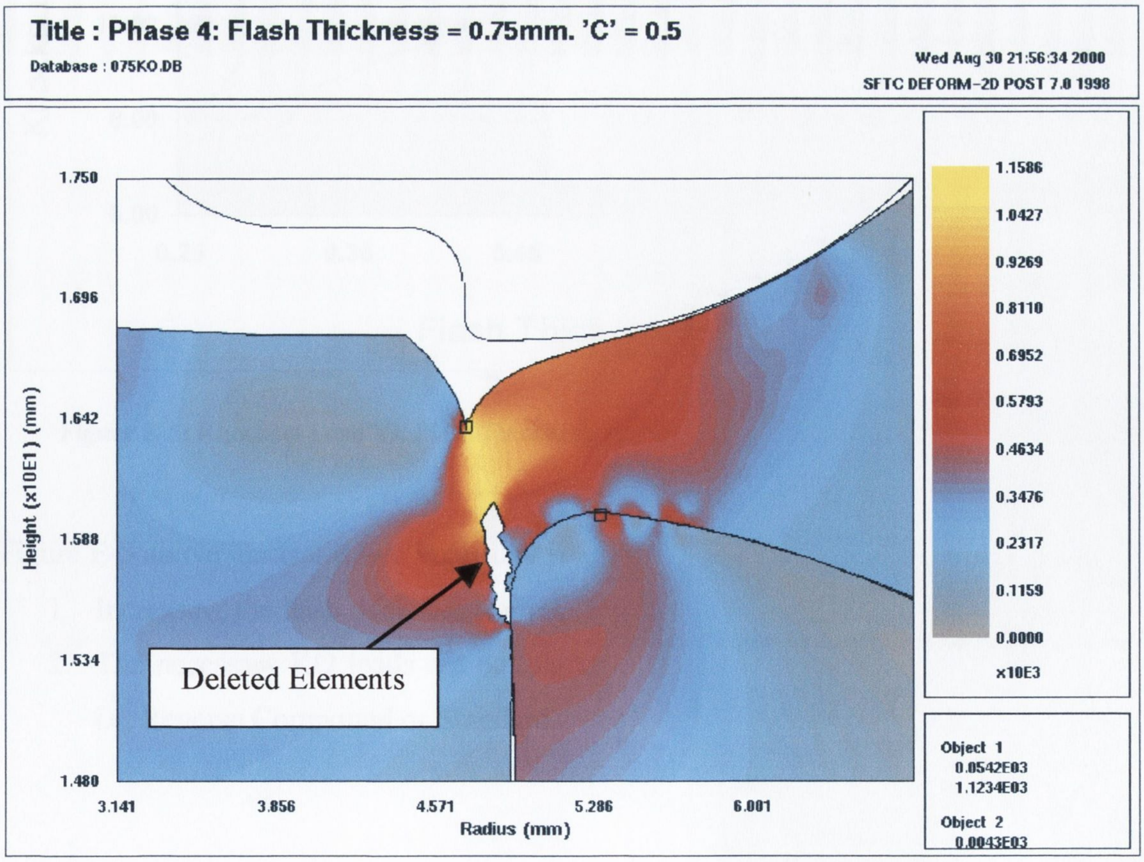

Figure E-4: The Effective Stress Distribution During Fracture Of the Workpiece Material

Obviously, by increasing the flash thickness, a greater amount of workpiece material has to be sheared, hence the corresponding load required to cause this shearing or knockout (KO) action is increased. With reference to figure E-5, at the minimum flash thickness of 0.25mm, the KO loads of 7.461KN and 7.286KN were recorded for the Reverse Compound and Standard trim die respectively. This corresponds to a difference of just over 2%. When the flash thickness was increased to 0.75mm, the Reverse Compound and Standard trim die recorded KO loads of 15.762KN and 14.739KN respectively. This corresponds to a difference of just over 6%. Varying the flash thickness from 0.25mm to 0.75mm caused the KO loads in both dies to double in magnitude.

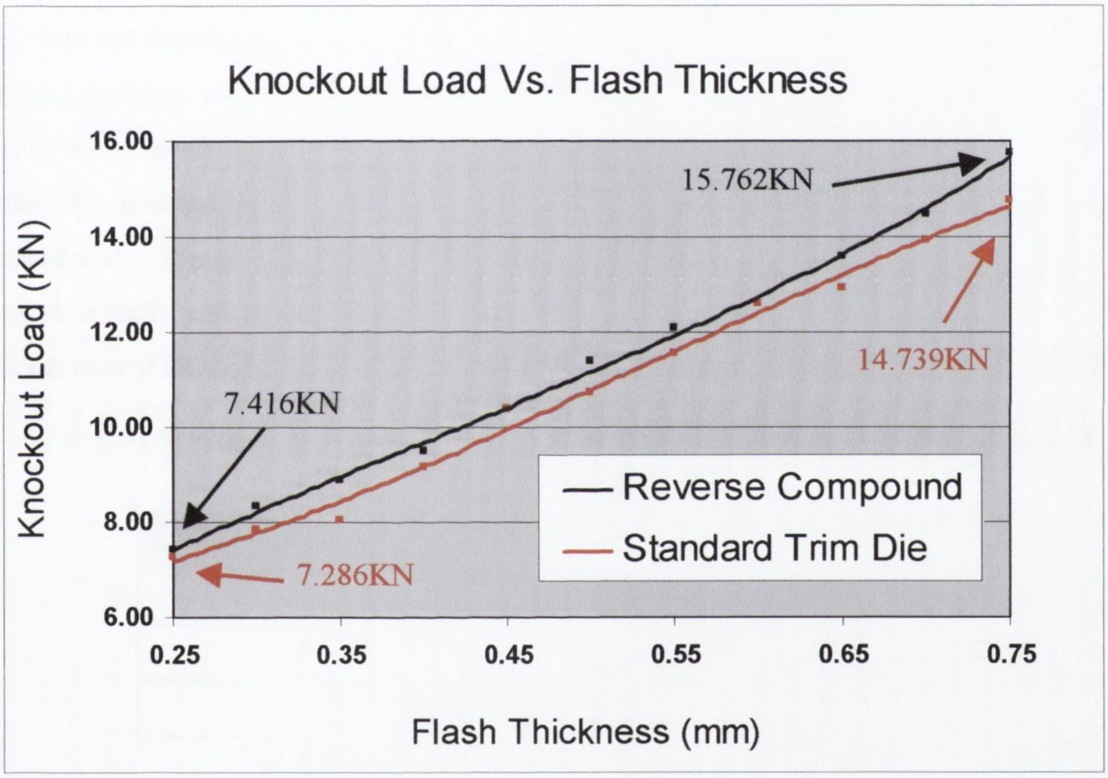

Figure E-5: Knockout Load Vs. Flash Thickness For Reverse Compound and Standard Trim Die

Figure E-5 above illustrates two important points.

1. Increasing the flash thickness from 0.25 to 0.75mm doubled the KO loads
2. The necessary KO loads are not significantly affected by the trim die profile used, i.e. Reverse Compound or Standard.

E4. Critical Damage Value ‘C’

As previously mentioned in section E2, the critical damage value ‘C’ used to determine the KO loads, plotted in figure E-5, was arbitrarily chosen at 0.5. An important consideration in relation to the experimental determination of the critical damage value ‘C’ is that the experimental test conducted should represent, as closely as possible, the actual process being simulated. It was not practical to conduct experimental trials on the factory floor to determine the location and onset of fracture within the workpiece material during the final knockout sequence. For this reason experimental validation of the critical value ‘C’ was not conducted for this project. Therefore to investigate the effect that altering the critical damage value ‘C’ had on the KO load and fracture surface topography, the ‘C’ value was altered from 0.5 to 0.25 and 0.1. Table E-1 illustrates how varying the critical value ‘C’ affected the predicted KO Load. In all three models, the flash thickness was held constant at 0.75mm. Table E-1 shows that although the critical damage value ‘C’ was not experimentally validated, changing its value from 0.5 to 0.1 had only a very small effect on the necessary KO load.

Critical Damage Value ‘C’	Flash Thickness	KO Load (N)
0.5	0.75mm	15762.54
0.25	0.75mm	15748.66
0.1	0.75mm	15735.58

Table E-1: The Effect of ‘C’ on the Knockout (KO) Load

With reference to table E-1, it might be concluded, that in terms of the KO load, the selection of the critical damage value ‘C’ had no significance. But as will be illustrated in the following Section E5, altering the critical damage value ‘C’ has a large effect on the topography of the fractured surface.

E5. Fracture Surface Topography

As outlined in table E-1, changing the critical damage value ‘C’ has apparently only a small effect on the KO load required to cause shearing off of the excess workpiece material. Figures E-6, E-7 and E-8 illustrate the final fractured surface topography for the critical damage values ‘C’ of 0.5, 0.25 and 0.1 respectively for a flash thickness of 0.75mm. With reference to these figures it is clear that although altering the ‘C’ value does not affect the KO load, it does affect the topography of the fractured surface.

With reference to figure E-6, when a critical value ‘C’ of 0.5 is used, the elements within the workpiece material experience large plastic deformation before the damage value of 0.5 is reached. This produces a large curved surface on the trimmed material, highlighted by the red line in figure E-6. A comparison between figures E-6, 7 and 8 illustrates that as the critical value ‘C’ is reduced from 0.5 to 0.1, the amount of plastic deformation, along the top surface of the trimmed material, is also reduced. Consequently, as the ‘C’ value is reduced, the fracture angle α, shown in figure E-6, approaches zero.

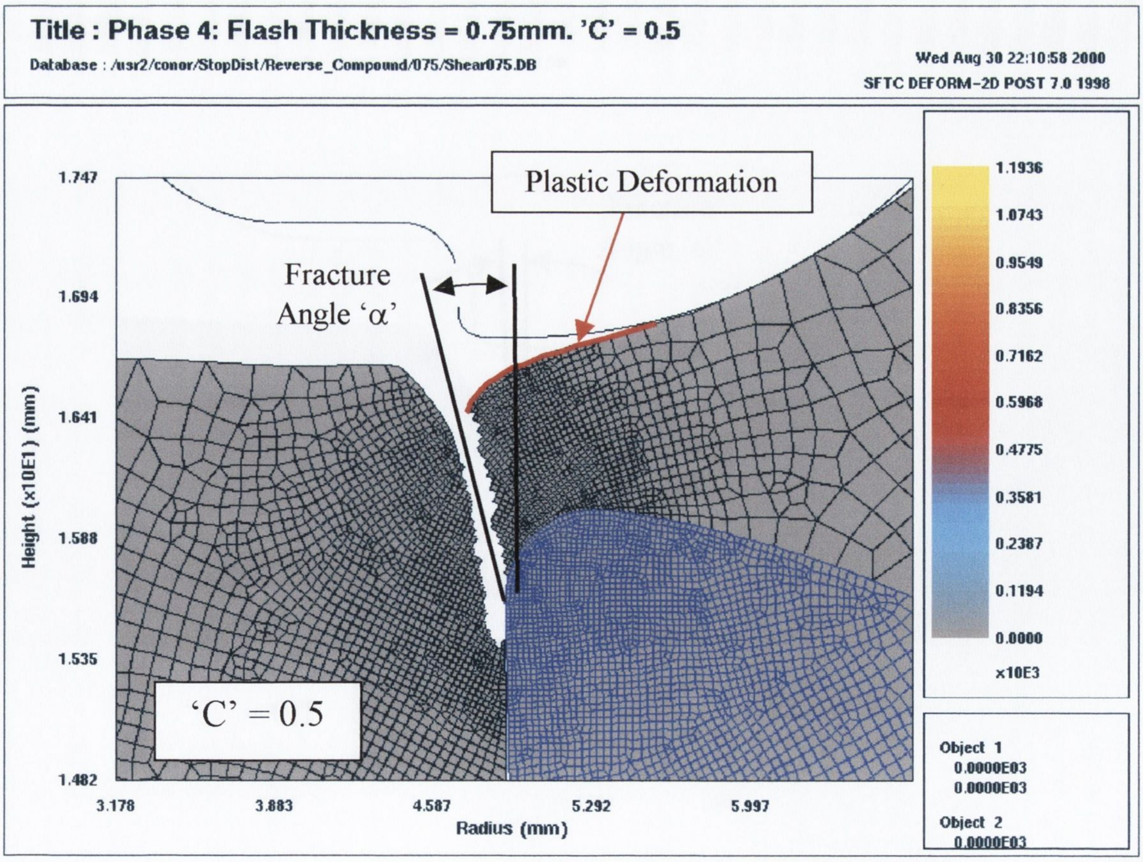

Figure E-6: Fractured Surface Topography When Critical Damage Valve ‘C’ = 0.5

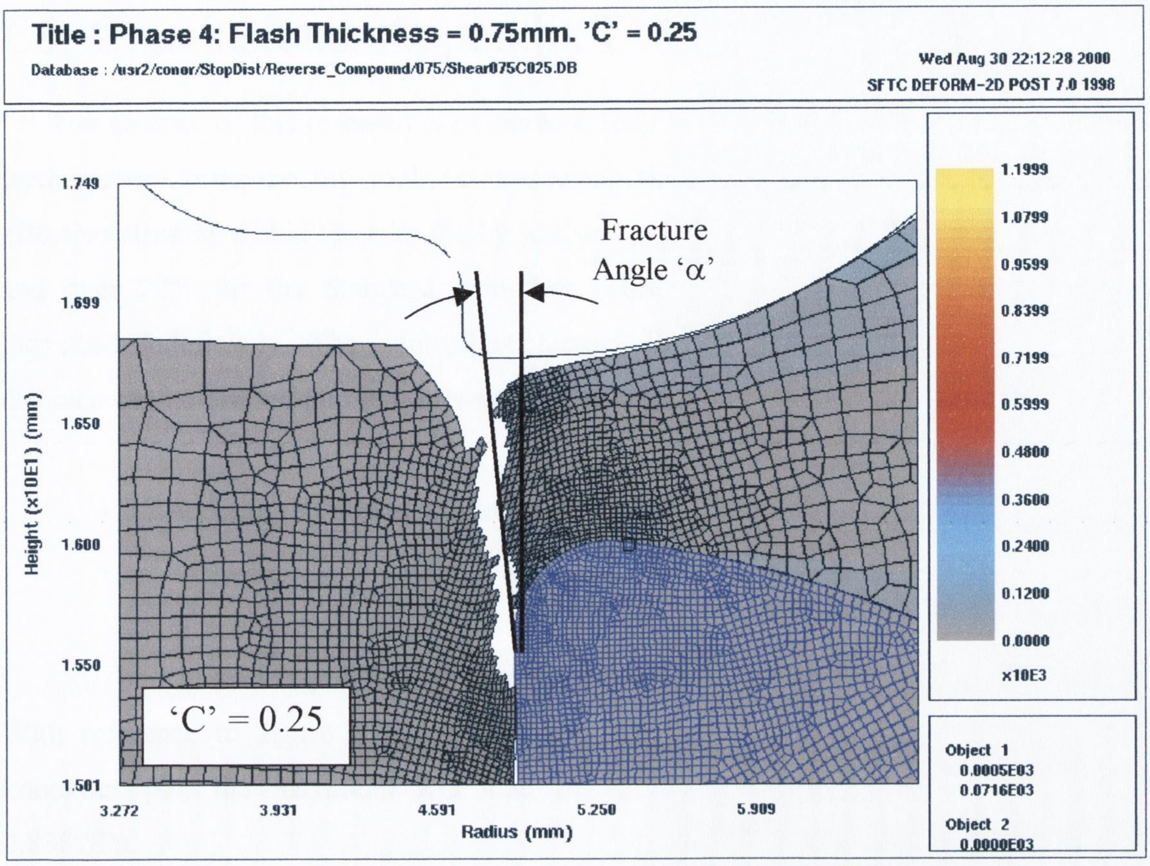

Title : Phase 4: Flash Thickness = 0.75mm. 'C' = 0.25

Database : /usr2/conor/StopDist/Reverse_Compound/075/Shear075C025.DB

Wed Aug 30 22:12:28 2000

SFTC DEFORM-2D POST 7.0 1998

Figure E-7: Fractured Surface Topography When Critical Damage Valve 'C' = 0.25

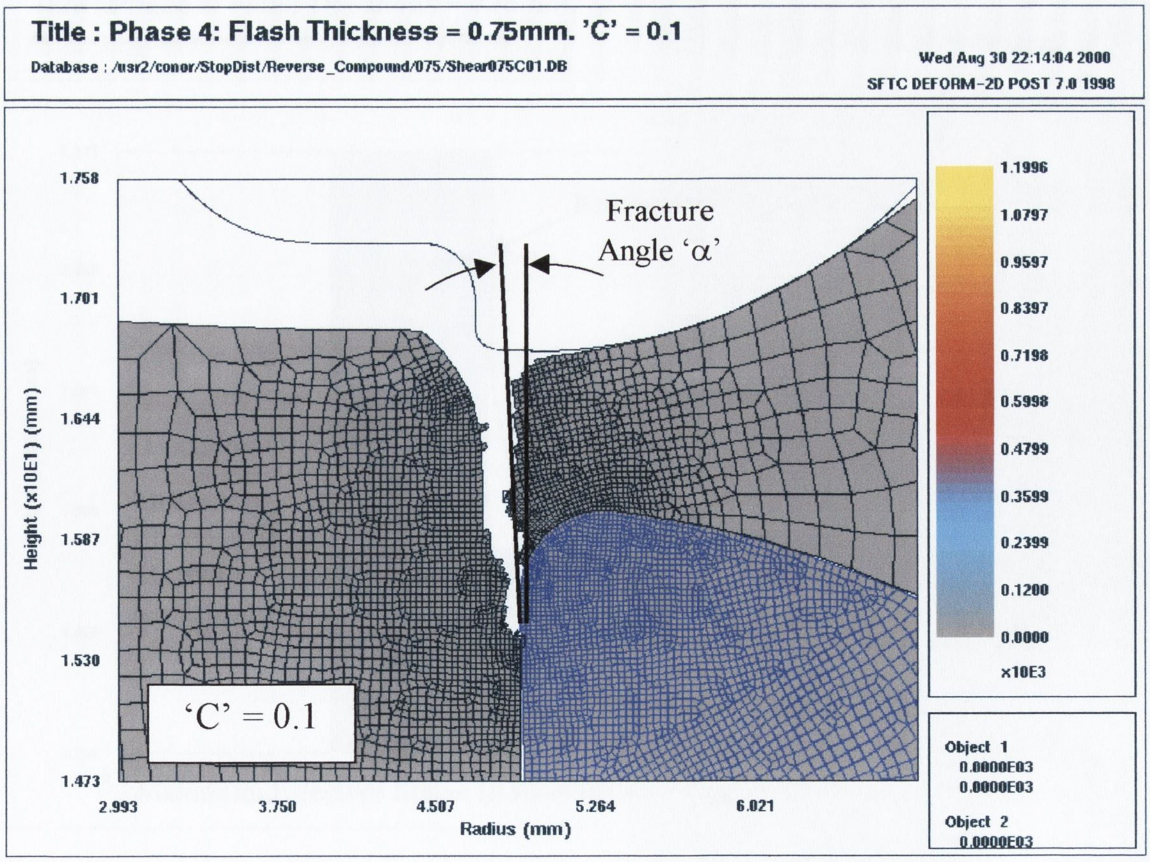

Title : Phase 4: Flash Thickness = 0.75mm. 'C' = 0.1

Database : /usr2/conor/StopDist/Reverse_Compound/075/Shear075C01.DB

Wed Aug 30 22:14:04 2000

SFTC DEFORM-2D POST 7.0 1998

Figure E-8: Fractured Surface Topography When Critical Damage Valve 'C' = 0.1

E6. Conclusions: Appendix E

The essence of this research is to increase the life of the trim die. Stopping the trim die further away from the top tool, i.e. increasing the flash thickness, reduced the induced effective stresses within the trim die by just under 25% in the Reverse Compound trim die and over 22% for the Standard Trim Die. This stopping distance cannot however be increased indefinitely. The controlling factors for determining the optimum stopping distance can be divided into two areas.

- Knockout (KO) load required.
- The quality of the fractured surface.

The KO load required is directly proportional to the stopping distance, as expected. With reference to figure E-9, which shows the effective stress distribution within the knockout pin, the maximum KO load of 15.762KN induced an effective stress of 0.838GPa.

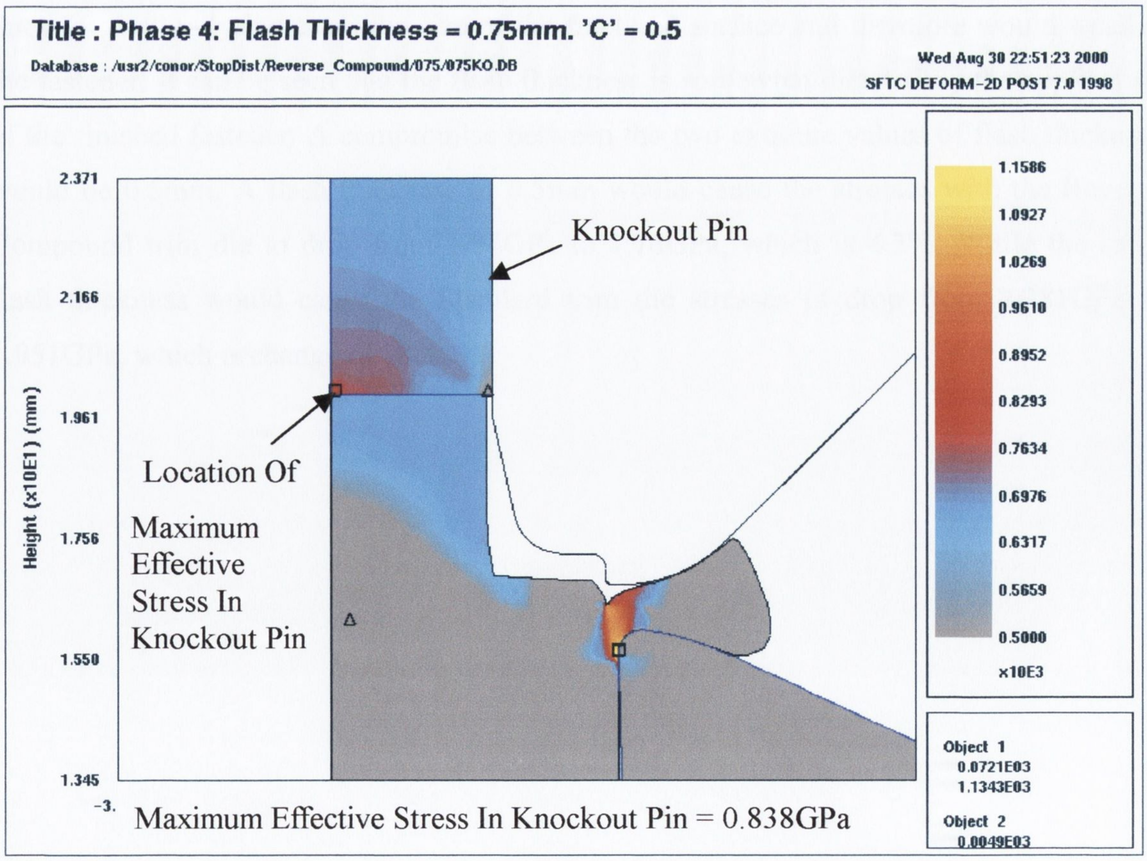

Figure E-9: Effective Stress Distribution Within Trim Die, Workpiece and Knockout Pin

From discussions with the technical staff in SPS, Hi-Life Tools in Shannon, it was established that the knockout pin is 'virtually never' replaced in a bolt-making machine. The knockout pin is generally made from the same material as the trim die, M2. Because the yield strength of M2 is 2.5GPa, it was concluded that doubling the KO load from 7.268KN to 15.76KN, the maximum effective stress of 0.838GPa within the knockout pin was not sufficient to cause any damage.

By comparing the KO load against critical damage value 'C', it was established, that although the 'C' value wasn't experimentally validated, the necessary KO loads remained virtually unchanged and could be accepted as accurate.

Finally, figures E-6 to E-8 showed that altering the value of 'C' did affect the fractured surface topography. Therefore, if the shape of the fractured surfaces produced within the FEA model were crucial, experimental validation of the critical damage value 'C' would be necessary.

Therefore taking into consideration the points outlined above, it was concluded that the final stopping distance between the trim die and top tool could be increased from the industrial standard of 0.25mm. However increasing the flash thickness to 0.75mm would not be acceptable for fasteners used in high strength applications, as increasing the flash thickness naturally increases the size of the fractured surface and therefore would weaken the fastener. It can be seen that the flash thickness is somewhat dictated by the application of the finished fastener. A compromise between the two extreme values of flash thickness would be 0.5mm. A flash thickness of 0.5mm would cause the stresses with the Reverse Compound trim die to drop from 1.84GPa to 1.76GPa, which is 4.3%. While the same flash thickness would cause the Standard trim die stresses to drop from 2.381GPa to 1.951GPa, which is change of 18%.